

Université Libre de Bruxelles
Faculté des Sciences



Measurement of the
Proton Structure Function $F_2(x, Q^2)$
with the H1 Detector at HERA

Dissertation présentée en vue
de l'obtention du titre de
Docteur en Sciences

Arkadi PANITCH

Octobre 1996

Abstract

In this thesis a measurement is presented of the proton structure function $F_2(x, Q^2)$ for momentum transfers squared Q^2 between 1.5 GeV^2 and 120 GeV^2 and for Bjorken x between $3 \cdot 10^{-5}$ and 0.32 , using data collected by the H1 experiment at HERA during the year 1994. The integrated luminosity is 2.7 pb^{-1} , which represents a tenfold increase in statistics compared to the previous analysis, based on the 1993 data. Low Q^2 values are reached using data with the ep interaction vertex shifted from the nominal position during special data taking period (SV data), and with the “satellite bunch” data sample. The systematic effects affecting the F_2 measurement are in the focus of the present analysis, since statistical uncertainties become insignificant. A measurement precision of the order of 10% is achieved, which is a factor two better than in 1993. The structure function is found to increase significantly with decreasing x , even in the lowest accessible Q^2 region, $Q^2 \sim 1.5 \text{ GeV}^2$. The data are well described by a Next to Leading Order QCD fit.

Contents

1	Introduction	3
2	Accelerator, beams and luminosity measurement	9
2.1	Accelerator	9
2.2	Longitudinal structure of the proton beam	11
2.3	H1 luminosity measurement	17
2.3.1	Luminosity in the satellite bunches	21
3	The H1 detector	31
3.1	Tracking system	33
3.1.1	Central tracker	33
3.1.2	Backward proportional chamber (BPC)	35
3.1.3	Forward tracker	35
3.2	Calorimetric system	35
3.2.1	The backward electromagnetic calorimeter (BEMC)	36
3.2.2	The liquid argon calorimeter (LAC)	43
3.3	Scintillators	43
3.4	Trigger	44
3.4.1	The BEMC single electron trigger (BSET)	46
3.5	Data acquisition	48
3.6	Monte Carlo simulation	48
4	Experimental method and DIS event selection	49
4.1	Experimental procedure	49
4.2	Deep inelastic scattering kinematics	52
4.3	Event samples	58
4.3.1	Backgrounds	58
4.4	DIS event selection	63
4.4.1	Electron identification	63
4.4.2	Background rejection	64
4.4.3	Run selection	71
4.4.4	Events per luminosity unit	72
4.5	Summary	75
5	Detector calibrations and resolutions	77
5.1	Space point measurement in the BEMC	77
5.2	BEMC energy scale and corrections	80
5.2.1	Double angle method	82
5.2.2	Crack corrections	82
5.2.3	Double angle recalibration	86

5.2.4	BEMC energy resolution	87
5.2.5	Systematic uncertainty of the BEMC energy scale	88
5.2.6	Summary	89
5.3	Systematic effects affecting the θ_e measurement	90
5.3.1	θ_e resolution	90
5.3.2	Vertex bias for the shifted vertex data	92
5.3.3	Preshowering and BPC-BEMC matching	94
5.4	y_Σ measurement	97
6	Selection efficiencies	101
6.1	Vertex reconstruction efficiency	101
6.1.1	Vertex efficiency measurement	102
6.1.2	Vertex efficiency for the “electron” kinematics	103
6.1.3	Vertex efficiency for the “sigma” kinematics	107
6.1.4	Vertex efficiency at low x - low Q^2	108
6.1.5	Forward vertex efficiency	112
6.2	BPC hit association losses	112
6.3	ECRA requirement losses	115
6.4	Summary	115
7	F_2 measurement	119
7.1	Event samples and data to Monte Carlo comparisons	119
7.1.1	Reweighting of the z -vertex distribution	119
7.1.2	Reweighting of the input F_2 parameterisation	122
7.1.3	Implementation of the electroweak radiative corrections	125
7.1.4	Final Monte Carlo to data comparisons	126
7.2	Kinematic plane coverage	128
7.2.1	Binning of the $x - Q^2$ kinematic plane	128
7.2.2	Kinematic measurement resolution and systematic bias	130
7.2.3	Smearred acceptance, purity and stability	133
7.3	F_2 measurement results	139
7.3.1	Systematic errors	139
7.3.2	Structure function F_2 measurement from the SV and satellite bunch data samples	140
7.3.3	Combining the SV and satellite bunch data samples	143
7.3.4	Final $F_2(x, Q^2)$ measurement results using the full combined 1994 data samples	148
7.3.5	Discussion	148
	Conclusions and Outlook	159
	Bibliography	i
	List of Figures	vii
	List of Tables	viii

Chapter 1

Introduction

Since 1991, the electron-proton collider HERA delivers collisions between 27.5 GeV electrons (positrons) and 820 GeV protons. The centre of mass energy of the ep collision \sqrt{s} was 296 GeV in 1994, which is an order of magnitude higher than the energy available in fixed target experiments. The high centre of mass energy allows on one side for a very high momentum transfer¹ Q^2 , making possible to resolve structures down to 10^{-18} m, and on the other side to study a region of high parton density in the momentum space (low x)². We are thus entering a kinematic region of special significance for QCD effects.

Deep Inelastic Scattering (DIS) is a fundamental process for measuring quark and gluon densities in the proton and to make quantitative tests of perturbative QCD [1, 2, 3]. One of the first analyses based on the HERA data was the determination in 1992 of the proton structure function in the previously unexplored region of low $x < 10^{-2}$. Although affected by large errors, this first measurement [4, 5] showed a fast rise of F_2 with decreasing x at low Q^2 , being an indication for a fast growing of the gluon density in the proton towards low x . This result was confirmed with larger statistics for Q^2 down to 4 GeV² in 1993 [6, 7].

In this thesis an analysis is presented of inclusive deep inelastic data taken by the H1 collaboration in 1994. To reach lower x values and correspondingly lower Q^2 values, special samples were analysed here of events with the ep interaction vertex shifted from the nominal position in special data taking period (SV data), and with the “satellite bunch” data sample. The accessible kinematic range has been extended down $Q^2 \sim 1.5$ GeV² and $x \sim 3 \cdot 10^{-5}$ and the structure function F_2 has been measured at a new level of precision compared to previous H1 measurements. The understanding of systematic effects affecting the F_2 measurement is of special importance as the statistical errors become negligible. Numerous technical studies presented here are intended to provide a detailed coverage of the F_2 measurement analysis, as recently published by H1 in [8].

Theoretical overview

In addition to Q^2 and x the following kinematic quantities are used in DIS studies: W is the (γ^*p) invariant mass and y is the inelasticity parameter ($Q^2 = xys$).

In DIS the measured quantity is a differential cross section in x and Q^2 . The differential Born cross section of a charged lepton off a proton can be parametrised in the following

¹ Q^2 is minus the square of momentum transferred from the electron to the proton.

²Bjorken x is, in a frame rapidly moving with respect to the proton, the fraction of the proton momentum carried by the struck quark.

way (neglecting the incoming proton and lepton masses):

$$\frac{d^2\sigma(l^\pm)}{dx dQ^2} = \frac{2\pi\alpha_{em}^2}{Q^4 x} \left[\left(2(1-y) + \frac{y^2}{1+R(x, Q^2)} \right) F_2(x, Q^2) \mp \left(2y - \frac{y^2}{2} \right) x F_3(x, Q^2) \right], \quad (1.1)$$

with

$$R(x, Q^2) = \frac{F_2(x, Q^2)}{2x F_1(x, Q^2)} - 1 = \frac{\sigma_L}{\sigma_T}, \quad (1.2)$$

where F_1 , F_2 and F_3 are the proton structure functions and R accounts for the longitudinal component in the total (γ^*p) cross section. $R(x, Q^2)$ has so far been measured only in fixed-target experiments, but even here information is scarce. The value of $R(x, Q^2)$ used for the measurement presented here is that predicted by QCD. Even in the highest Q^2 range accessed by the present data ($Q^2 \sim 5000 \text{ GeV}^2$) the contribution of the structure function $x F_3$ is still a small correction.

In the leading order approximation (LO) of perturbative QCD³, the structure function $F_2(x, Q^2)$ is directly related to the quark and antiquark momentum distributions $q_i(x, Q^2)$ and $\bar{q}_i(x, Q^2)$:

$$F_2(x, Q^2) = \sum_{flavours} e_i^2 x [q_i(x, Q^2) + \bar{q}_i(x, Q^2)], \quad (1.6)$$

where i labels the quark flavours and e_i are the quark charges. For large values of Q^2 the quark and the antiquark distributions exhibit approximate Bjorken scaling mildly violated by the QCD corrections. Relation 1.6 acquires corrections proportional to $\alpha_s(Q^2)$ in the next-to-leading order approximation.

In dealing with low Q^2 data one needs to introduce the concept of ‘‘higher twists’’. The Wilson operator product expansion (OPE: see for example [9])⁴, exploiting the renormal-

³In the renormalisation group formalism, the scheme-dependent renormalisation group functions β (Gell-Mann-Low) and γ (anomalous dimension) are calculated perturbatively using a power series expansion in g (QCD coupling constant):

$$\beta(g) = -\beta_0 g^3 - \beta_1 g^5 + \mathcal{O}(g^7), \quad (1.3)$$

$$\gamma(g) = \gamma_0 g^2 + \gamma_1 g^4 + \mathcal{O}(g^6), \quad (1.4)$$

where one-loop, two-loop, ... diagrams are relevant to determine (β_0, γ_0) , (β_1, γ_1) , etc. Renormalised physical quantities are expressed in terms of power series in $1/\ln(Q^2/\Lambda)$, where Λ is the QCD *scale parameter*. For example, the running coupling constant writes:

$$\frac{\alpha_s(Q^2)}{4\pi} = \frac{1}{\beta_0 \ln(Q^2/\Lambda^2)} - \frac{\beta_1 \ln \ln(Q^2/\Lambda^2)}{\beta_0^3 \ln^2(Q^2/\Lambda^2)} + \mathcal{O}\left(\frac{1}{\ln^3(Q^2/\Lambda^2)}\right). \quad (1.5)$$

Retaining the first term of the expansion corresponds to the leading order approximation. The second term represents the next-to-leading correction which corresponds to the two-loop effects [9].

⁴The inclusive cross section for DIS scattering is expressed in terms of the Fourier transform of the expectation value of the electromagnetic current product $J_\mu(x)J_\nu(0)$

$$W_{\mu\nu} \sim \frac{1}{2\pi} \int d^4 x e^{iq \cdot x} \langle p | [J_\mu(x), J_\nu(0)] | p \rangle. \quad (1.7)$$

This expression is not well defined since the integral is divergent for $x = 0$. The Wilson technics consists in expanding the product of currents $J_\mu(x)J_\nu(y)$ in a series of well-defined local operator $\mathcal{O}(x)$ with singular

isation group properties of scattering amplitude, leads to the representation:

$$F_2(x, Q^2) \propto \sum_{n=0}^{\infty} \frac{C_n(x, Q^2)}{(Q^2)^n}, \quad (1.9)$$

where the functions $C_n(x, Q^2)$ depend weakly (i.e. logarithmically) on Q^2 . The various terms in this expansion are referred to as leading ($n = 0$) and higher ($n \geq 1$) twists. Physically the higher twist effects arise from the struck parton's interaction with target remnants, thus reflecting confinement. For Q^2 of the order of 1 GeV², contributions of the “higher twists” may become detectable.

Thus, one can express the structure functions either in terms of the parton model where the leptons scatter off the quark in the target, or in terms of a bilocal product of quark operators

$$\int_0^1 d\xi \xi^{m-2} F_2(\xi, Q^2) = \int_0^1 d\xi \xi^{m-1} \sum_f e_f^2 [q_f + \bar{q}_f] = \sum_i C_{2,m}^{(i)}(Q^2) A_{2,m}^{(i)}, \quad (1.10)$$

where coefficient functions $C_{2,m}^{(i)}$ are of short-distance nature and are calculable by QCD, while the constants $A_{2,m}^{(i)}$ are related to the matrix elements of the long-distance operator and have to be determined experimentally. Relation 1.10 is known as the moment sum rule of order m for the structure function F_2 . The parton model interpretation is equivalent to the OPE only at the leading twist level. Beyond leading twist more general quantities – parton correlation functions – emerge.

The low Q^2 region should join smoothly onto the non-perturbative photoproduction limit, $Q^2 \rightarrow 0$, successfully described by the Regge-inspired models. F_2 can be related at low x for finite Q^2 ($W \simeq \sqrt{Q^2/x}$) to the total cross-section of the proton-virtual photon interaction $\sigma_{tot}(\gamma^*p)$ via

$$F_2(W, Q^2) \simeq \frac{Q^2}{4\pi^2 \alpha_{em}} \sigma_{tot}(\gamma^*p). \quad (1.11)$$

The Regge-type expectation has an essentially flat in x behaviour of the form $x^{-0.08}$, while the present surprise is that the strong rise of F_2 with decreasing x is still quite prominent even at values of Q^2 as low as 1.5 - 2.0 GeV². The transition from the “soft” to the “hard” regime thus appears to be rapid.

Small x physics

The behaviour of the proton structure function $F_2(x, Q^2)$ at small x reflects the behaviour of the gluon distribution, since the gluon is by far the dominant parton in this regime. A

complex coefficients $C_i(x)$:

$$J_\mu(x) J_\nu(y) = \sum_{i=1}^{\infty} C^{(i)}(x-y) \mathcal{O}\left(\frac{x+y}{2}\right) \quad (1.8)$$

where the choice of $(x+y)/2$ is arbitrary. The local operator is regular in the sense that the singularity of the product $J_\mu(x) J_\nu(y)$ for $x=y$ is fully contained in the coefficient functions $C^{(i)}(x-y)$. This enables us to extract a short distance piece in the scattering cross section, characterised by the singular c-numbers calculable in the framework of perturbative QCD, while the regular local operators include full information on the long distance properties (hadronisation) of the theory and are unimportant in the short distance region [9].

growth of the gluon density is transmitted via quark pair production $g \rightarrow q\bar{q}$ to the sea quarks probed by the photon. Perturbative QCD does not predict the absolute value of the parton distributions, but rather determines how they vary from a given input. For instance from given initial distributions at some scale Q_0^2 , we may evolve up to large Q^2 using the Altarelli-Parisi (DGLAP) [10] equations which are typically of the form

$$\frac{\delta g}{\delta \log Q^2} = P_{gg} \otimes g + \dots \quad (1.12)$$

where the convolution is over the longitudinal momentum fraction or x . The splitting function P_{gg} has the perturbative expansion in α_s ,

$$P_{gg} = \alpha_s P_{gg}^{(1)} + \alpha_s^2 P_{gg}^{(2)} + \dots \quad (1.13)$$

where $P_{gg}^{(i)}$ are in principle, calculable functions, though, to date, only $i \leq 2$ terms are known. In Leading Logarithmic Approximation (LLA: see for example [11]) the DGLAP evolution resums the $\alpha_s \ln Q^2$ terms to all orders of perturbative QCD expansion

$$P_{gg}^{(1)} \propto \sum_{n=0}^{\infty} c_n(x) \left(\alpha_s \ln Q^2 \right)^n. \quad (1.14)$$

In the *axial* gauge, the $\alpha_s^n \ln^n Q^2$ contribution is associated with a chain of n gluon emissions in which the successive gluon transverse momenta are strongly ordered along the chain, that is

$$q_{\perp 1} \ll q_{\perp 2} \ll \dots \ll q_{\perp n-1} \ll q_{\perp n} \ll Q^2. \quad (1.15)$$

Physically this means that partons of the (logarithmic) field theory are not point-like particles: an attempt to localise the parton of the i^{th} generation, which has typical transverse size $\Delta \rho_{\perp}^i \sim 1/k_{\perp i}$, reveals its substructure at smaller distances $\Delta \rho_{\perp} \sim 1/k_{\perp} \ll \Delta \rho_{\perp}^i$. In the next-to-leading order (NLO) logarithmic correction a logarithm is lost and $P_{gg}^{(2)}$ resums the $\alpha_s^n (\ln Q^2)^{n-1}$ terms. The DGLAP predictions in the HERA range depend on the shape of the starting distributions and on the starting scale. If started at a very low scale $Q_0^2 \leq 0.4 \text{ GeV}^2$, the evolution is sufficiently long for the gluon, quark and F_2 to develop a steep x behaviour in the HERA regime. In this case the distributions mimic an $x^{-\lambda}$ behaviour with $\lambda \sim \lambda(Q^2)$ and $\langle \lambda \rangle \sim 0.33$ in the HERA regime.

At sufficiently high electron-proton c.m. energy a second large variable, $1/x \sim s/Q^2$, is encountered. In leading order the resummation of $\alpha_s \ln 1/x$ terms is accomplished by the BFKL equations [12] and

$$x g(x, Q^2) \propto \sum_{n=0}^{\infty} f_n(Q^2) \left(\alpha_s \ln \frac{1}{x} \right)^n. \quad (1.16)$$

In contrast with the DGLAP evolution there is no restriction on transverse momentum in the summation but rather a strong ordering in longitudinal momenta or x :

$$x_1 \ll x_2 \ll \dots \ll x_{n-1} \ll x_n \ll x. \quad (1.17)$$

The singular $x^{-\lambda}$ growth with fixed λ is characteristic of the BFKL evolution, at variance with the DGLAP evolution, where it is incorporated in the starting distributions or generated by the evolution from a low scale and λ varying with Q^2 .

Ciafaloni, Catani, Fiorani and Marchesini [13] have proposed a unified evolution equations which embodies the BFKL evolution at small x and the DGLAP evolution at larger x . The CCFM equation is based on the coherent radiation of gluons, which leads to an angular ordering of gluon emissions. Outside the ordered region there is destructive interference between the emissions.

Finally one should mention that the rise of the gluon density at small x has to be damped at some sufficiently small values of x by saturation effects when the parton density is so large that the partons can no longer be considered as independent. The Gribov Levin Ryskin (GLR) equation is the first attempt to describe the saturation corrections to the BFKL evolution equations. Saturation effects are however expected to be relatively weak in the HERA kinematic domain.

The theory cannot predict so far the precise domains of validity of the different approaches since there is no scale in the $\ln Q^2 - \ln 1/x$ plane of evolution mechanisms. This is the task of experiments.

In deep inelastic experiments the low x region is correlated with low values of Q^2 . Thus a completely satisfying explanation of the observed rise at small x cannot avoid investigating the transition at high energies from the DIS structure function F_2 at small x to the photoproduction cross section. The interest is on the W -dependence at low Q^2 , since on one side for $Q^2 \sim 0$ the non-perturbative regime is successfully described by the Regge-inspired models, and on the other side for finite Q^2 , perturbative QCD predictions are given by the evolution equations. It remains also to see if a singular F_2 growth with decreasing x is evidence for the singular BFKL behaviour of the gluon or just evidence of the need for a different input parameterisation in the conventional DGLAP evolution. Acceptable DGLAP-based description (including next-to-leading order $\ln Q^2$ terms) are possible down to at least $Q^2 \sim 1 \text{ GeV}^2$. Within the current F_2 measurement precision the small x data can equally well be described by the BFKL leading order evolution. Last but not least, the DGLAP analysis is constrained to leading twist only, and for large Q^2 this approximation is well justified. However, once we are approaching the low- Q^2 region, the neglect of higher-twist contribution becomes more and more questionable.

Thesis organisation

This thesis is organised as follows.

In chapter 2, we introduce the layout of the HERA machine. The longitudinal structure of the proton beam is then discussed and a qualitative overview of the phenomena leading to the creation of the so-called "proton satellite bunch" is presented. One of the satellite bunches is observed in the H1 detector at $\approx +70 \text{ cm}$ with respect to the nominal interaction point and can be used for the measurement of the proton structure function F_2 at low Q^2 . An estimate of the integrated luminosity originating from the satellite bunch is performed, and a correction to the H1 luminosity is provided.

The H1 detector is shortly described in chapter 3, with an emphasis on the detector components used for this analysis.

In chapter 4 the experimental method used for measurement of the DIS cross-section and the structure function $F_2(x, Q^2)$ is introduced first. Next are briefly presented different ways of measuring the DIS event kinematics used in the present analysis. Then, after a short discussion of backgrounds, the DIS event selection is described.

Systematic effects affecting the measurements of the scattered electron energy and angle and of the hadronic final state are studied in detail in chapter 5.

The event losses are discussed in chapter 6. Particular attention is paid to the efficiency of reconstructing the event interaction vertex.

Finally, after a careful study of the accessible kinematic range using different methods of reconstructing the DIS event kinematics, chapter 7 presents the measurement of the structure function F_2 .

The thesis is summarised in the last chapter.

Chapter 2

Accelerator, beams and luminosity measurement

In this chapter, the layout of the HERA machine is first introduced. The longitudinal structure of the proton beam is then discussed and a qualitative overview of the phenomena leading to the creation of the so-called "proton satellite bunch" is presented. One of the satellite bunches is observed in the H1 detector. An estimate of the integrated luminosity originating from this satellite bunch is performed, based on the analysis of the distribution of the reconstructed z -vertex position. This allows this data sample to be used for the measurement of the proton structure function F_2 , which is the main topic of the present thesis. Finally, combining this satellite luminosity estimate with an analysis of the Forward Time of Flight (FToF) scintillator data, a correction to the H1 luminosity accounting for the total satellite bunch effect is provided.

2.1 Accelerator

The Hadron Elektron Ring Anlage (HERA) [15] consists of two separate 6.3 km long storage rings, designed to accelerate respectively 820 GeV protons and 30 GeV electrons (or positrons). The collisions take place in four interaction points from which three are actually occupied by the H1 (North Hall), ZEUS (South Hall) and HERMES (East Hall) detectors. The layout of the HERA machine together with its injection system is shown in Fig 2.1.

Injection system

The electrons¹ from a 500 MeV linear accelerator are injected into a small storage ring where they are accumulated into a ~ 60 mA single bunch. They are then injected into the DESY II synchrotron which brings the energy up to 7 GeV. From DESY II they are transferred to the PETRA ring where the energy is ramped up to 14 GeV after accumulating up to 70 bunches. At this energy the bunches are transferred to HERA. This is repeated until HERA has been filled with 210 (170 in 1994) bunches.

A whole new chain of preaccelerators has been built in order to inject protons into HERA. A linear accelerator delivers a 50 MeV negatively charged hydrogen ion beam which is stripped upon entering into the DESY III synchrotron. Inside DESY III the protons are captured into 11 radio frequency (rf) buckets with the final bunch spacing and the final total number of particles per bunch, unless losses happen during transfers

¹In this chapter, "electron" refers to electron and positron: in 1994 HERA has collided e^+ against protons for most of the time.

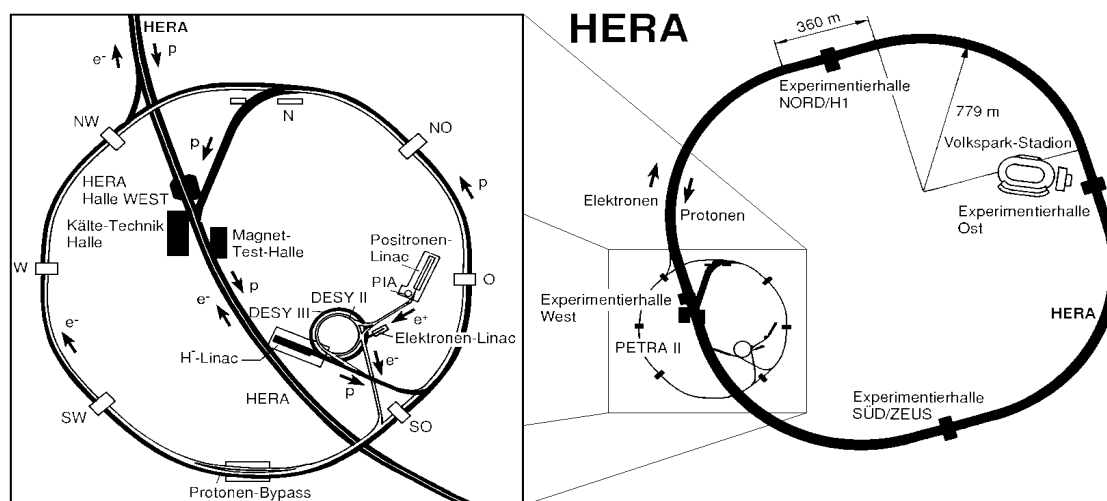


Figure 2.1: *Layout of HERA and injection system.*

and ramping. The protons are then accelerated up to 7.5 GeV and transferred to PETRA which can accumulate up to 70 bunches and accelerate them up to 40 GeV. They are finally transferred to the HERA proton ring.

HERA collider

In HERA, eight super-conducting cavities are necessary to accelerate the electrons up to 30 GeV energy. Electrons are bent inside the ring by a modest field of 0.165 T which is achieved with conventional magnets. The synchrotron energy loss is compensated by 500 MHz rf cavities.

Conventional rf cavities are used to accelerate the protons from 40 GeV to 820 GeV and to maintain them at this energy. A much higher 4.68 T bending field is required to keep the 820 GeV protons on orbit. The proton ring is equipped with a total of 1819 super-conducting magnets and correction coils. The quality of the magnets is such that it is possible to rise the strength of the magnetic field up to 5.8 T, which would correspond to 1 TeV proton beam.

The main nominal parameters of the HERA rings are listed in Table 2.1. In 1994, the third year of HERA operation, the lepton beam energy was fixed at 27.5 GeV. At this energy, the ep centre of mass energy is

$$\sqrt{s} \simeq \sqrt{4E_e E_p} = 296 \text{ GeV.}$$

The maximum number of bunches was 170 for the electrons (or positrons) and 168 for protons instead of the designed number of 210 bunches. Among them, 17 lepton bunches and 15 proton bunches are unpaired, so that they do not collide. They are commonly called

	p-ring	e-ring	units
Nominal energy	820	30	GeV
Beam polarisation	(70% ?)	70%	
Polarisation time		28	minutes
Magnetic field	4.68	0.165	T
Total number of particles	2.1	0.8	10^{13}
Number of bunches	210	210	
Injection energy	40	14	GeV
Filling time	20	15	minutes
σ_x/σ_y at I.P.	0.29/0.07	0.26/0.02	mm
σ_z	110	8.0	mm
Energy loss/turn	6.26×10^{-6}	127	MeV
RF-frequency	52.033/208	499.776	MHz
RF-power	1	13.1	MW
Luminosity	$1.5 \times 10^{31} \text{ cm}^{-2} \text{ s}^{-1}$		
Integrated Luminosity	50 pb $^{-1}$		

Table 2.1: Nominal (design) HERA parameters (from [15]).

”pilot bunches” and permit to measure the rate of beam interactions with the beam-pipe walls and with the residual gas inside the beam-pipe. The performance of the HERA proton acceleration system in 1994 is listed in Table 2.2 and compared to the average performance during the two preceding years since HERA commission in 1992 [16].

	Average 1992	Average 1993	Average 1994	Best 1994	Design Goal
Beam energy [GeV]	820	820	820	820	820
Beam current [mA]	1.4	12.5	40	60	159
Number of bunches	10	90	170	170	210
Particles per bunch/ 10^{10}	1.8	1.8	3.1	4.7	10
Bunch length [ns]	1.27	0.46	0.42	0.34	0.5
Beam loss (ramping)	30%	7%	7%	1%	0%
Beam lifetime [h]	100	100	200	1000	20

Table 2.2: HERA proton acceleration system performance (from [16]).

An upgrade is envisaged which will allow for a 4 times increase of luminosity resulting in $\sim 180 \text{ pb}^{-1}/\text{year}$ of total integrated luminosity.

2.2 Longitudinal structure of the proton beam

In HERA, proton and electron beams are composed of packets of particles, spaced by 96 ns (28.8 m) in the longitudinal direction. Electron packets are composed of a short single bunch with an approximately Gaussian shape, and length $\approx 2.5 \text{ cm}$ (0.08 ns). Proton packets have a more complex structure with a central (main) bunch of high intensity,

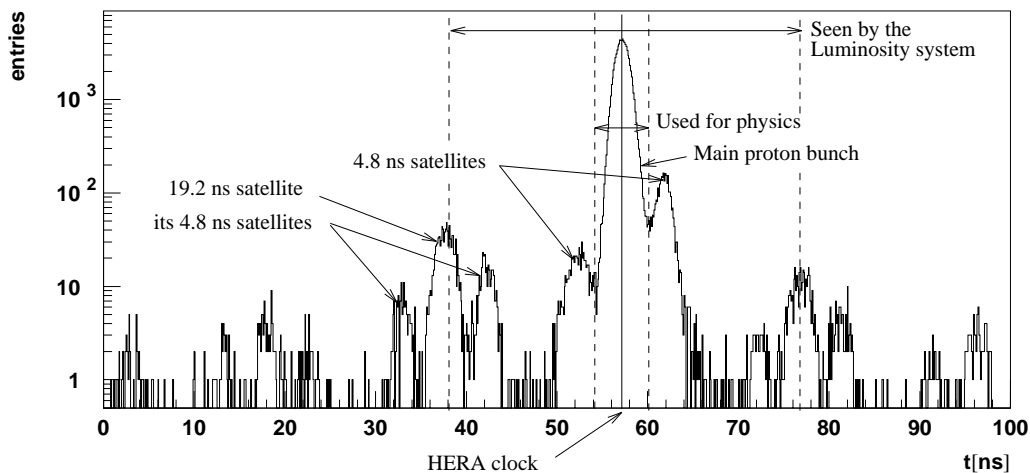


Figure 2.2: *Longitudinal profile of a proton bunch as observed in the forward time of flight scintillator FToF.*

surrounded by several extra (satellite) bunches of much less intensity, at ± 4.8 ns and ± 19.2 ns, thus filling the 96 ns interval between interactions. Fig 2.2 illustrates the longitudinal profile of a proton packet as observed in the forward time of flight scintillator FToF (see section 2.3.1 for details on the FToF data analysis). The HERA clock is synchronised with the arrival of the main proton bunch and the positron bunch in the nominal interaction point (IP) of the detector (H1, ZEUS and HERMES).

The distribution of the interaction position along the z -axis observed with the H1 detector (see section 2.3.1) reflects roughly the longitudinal structure of the proton beam, resolved by the much shorter electron bunch. The distribution of the observed interaction z -vertex position (see Fig 2.8-*a*) due to collisions between the main proton bunch and the electron beam has a width of ≈ 10 cm. It is essentially half the length of the proton bunch.

Another peak in the vertex distribution appears at $\approx +70$ cm from the main peak and corresponds to the satellite bunch arriving 4.8 ns before the main bunch. Other satellite bunches are not observed in the detector due to acceptance effects.

Only interactions corresponding to the main proton bunch are usually used for physics analysis. However, the H1 luminosity system, based on the detection of bremsstrahlung events ($ep \rightarrow ep\gamma$) (see section 2.3), is sensitive to the total amount of protons contained within ± 19.3 ns of the main bunch centre. As a consequence, the integrated luminosity \mathcal{L} should be corrected to account for the satellite bunch effect.

The rest of this section is dedicated to a qualitative overview of the phenomena leading to the occurrence of this complicated proton bunch structure.

The next section is devoted to an analysis of the available data and to the determination of the integrated luminosity originating from the satellite bunch, and thus to the correction

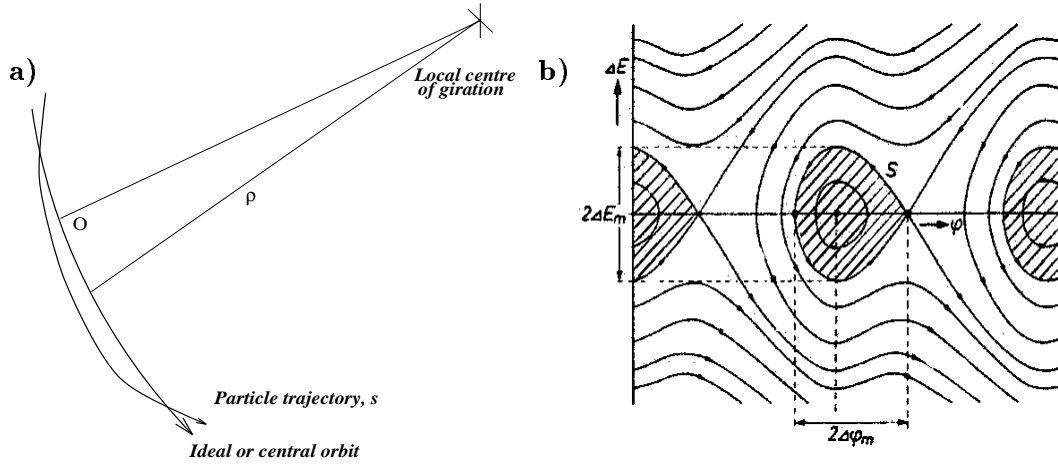


Figure 2.3: a) Curvilinear coordinate system following the beam through the accelerator; b) particle trajectories in the longitudinal phase space representation (from [17]).

to the integrated luminosity used for the physics analysis.

Longitudinal phase space. Rf buckets

The operating principle of synchrotron acceleration consists in imparting higher and higher energies to particles as they move in a stable orbit of constant radius. The actual particle acceleration is accomplished with resonators (cavities) operating with radio-frequency (rf) voltage. Since particles attain velocities close to the velocity of light c at relatively small energies (especially electrons), their frequency of revolution is approximately constant. Hence the frequency of the accelerating voltage can also have a constant value.

The movement of particles inside an accelerator can be described in a multi-dimensional phase space. The longitudinal deviations (synchrotron oscillations) from the trajectory of the ideal (synchronous) particle crossing the cavity at the correct phase of the accelerating voltage can conveniently be represented in a *longitudinal phase space* in which the abscissa is the phase φ when a particle crosses a cavity ($\varphi = 0$ at a peak voltage) and the ordinate is the deviation ΔE from the synchronous particle energy E_0 . The phase φ is related to the curvilinear particle coordinate along the accelerator. Similarly, the ordinate ΔE can be related to the deviation $\Delta\rho$ from the radius ρ_0 of the equilibrium orbit, perpendicular to the trajectory along the accelerator (see Fig 2.3-a). The trajectory of particles in this phase space is determined by the properties of the rf cavities.

For small deviations from the synchronous trajectory, a particle behaves as if it was submitted to a harmonic oscillator, and its trajectory is an ellipse in the longitudinal phase space representation. If, however, the deviations are not small, the trajectories are no longer elliptical. Fig. 2.3-b shows several trajectories. One of these is the critical trajectory, the *separatrix* S . In the hatched zone inside the separatrix loop, trajectories are closed and the acceleration is stable. The particles with trajectories outside the separatrix loop diverge indefinitely and get lost.

The loops within the separatrix can be considered as forming *rf buckets*. Particles with

trajectories belonging to a bucket form a *bunch* circulating coherently around the ring.

The bucket length defines the maximum phase spread of the accelerated particles ($2\Delta\phi_m$) and, similarly, the bucket width is equal to their maximum energy spread ($2\Delta E_m$) [17].

PETRA–HERA transfer. The 19.2 ns satellites

The relative bucket height, $2\Delta E_m/E_0$ (see Fig 2.3-*b*), is a particularly important factor when particles are transferred from one accelerator to another, in our case from the PETRA preaccelerator to HERA.

In PETRA, the bunching is done using the rf cavities operating at 52.03295 MHz. At HERA, bunches are first trapped in buckets with almost the same length (phase spread) $2\Delta\phi_m$, created by the 52.03426 MHz rf cavities. However, due to a different design, the HERA 52 MHz rf system is operated at a much higher voltage. A bucket in HERA is thus ≈ 2.8 times as large (energy spread) as a bucket in PETRA. After injection from PETRA to HERA, particle bunches tend to fill the whole HERA bucket and are diluted in phase space. The beam appears to be unstable in this configuration [18].

A technical solution to this problem, used by the HERA crew, consists in imparting to the bunch a rotation in the PETRA bucket longitudinal phase space, and in injecting it into the HERA bucket when the rotation angle is 90° with respect to the initial position. This allows for a much better filling of the phase space of the HERA bucket and preservation of the bunch compactness. Fig 2.4 illustrates this bunch rotation technique used to inject protons from PETRA to HERA. The bunch is first pushed on the knot between two rf buckets (*a* – *b*). There it undergoes electromagnetic forces which tend to stretch it (*c*). Then it is returned back to the centre of the bucket and rotated (*d* – *f*). At this stage it is transferred to HERA (*g* – *j*) [18].

As a side effect, when the bunch is stretched on the knot between two buckets, some small fraction of the protons escapes to neighbouring buckets. These particles are transferred to HERA and accelerated together with the main proton bunch. They form the 19.2 ns satellites, this value being the delay between buckets created by the 52 MHz rf cavities [18].

Another way to inject efficiently protons from the PETRA to the HERA 52 MHz rf system is presently under study. It consists in inducing energy spread oscillations, so that the proton envelope in the phase space is modulated and oscillates between the initial state (Fig 2.4-*a*) and a state with reduced phase ϕ spread but stretched energy spread, corresponding roughly to Fig 2.4-*f*. This technique should avoid the 19.2 ns satellites [18].

Longitudinal bunch compression in HERA. The 4.8 ns satellites

When the beam has been transferred to HERA, it can be accelerated up to the designed energy of 820 GeV. However, the beam intensity is limited by the onset of *collective instabilities*. Such instabilities appear, for instance, when the mutual forces between the particles in the beam or between the two beams inside the collider become comparable to the focusing forces. These focusing forces are provided transversely by the beam optics and longitudinally by the rf bucket which insures the longitudinal stability.

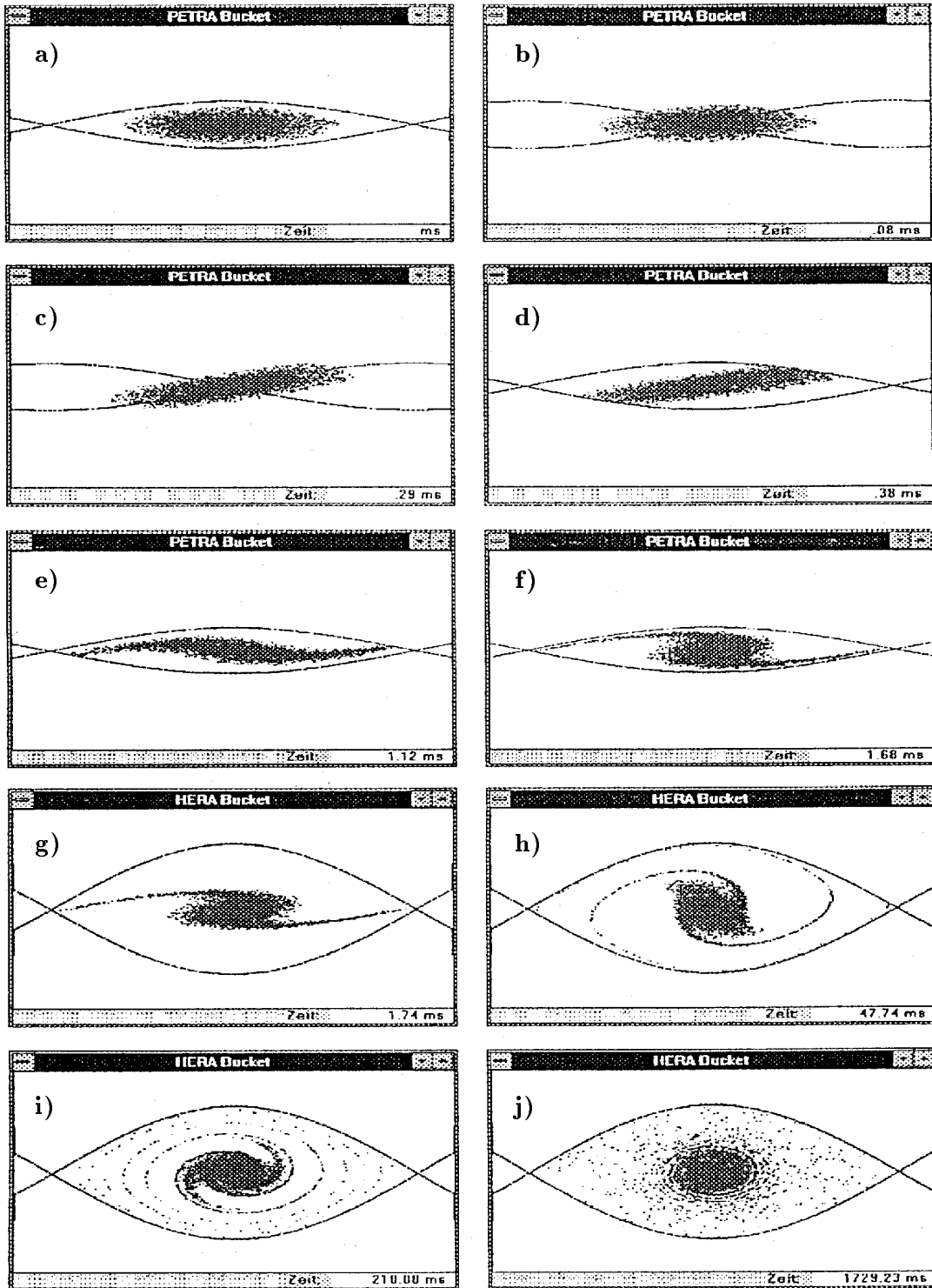


Figure 2.4: Simulation of the bunch rotation technique in the longitudinal phase space representation (x -axis is the phase spread and y -axis is the energy spread), used to transfer protons from PETRA (a – f) to HERA (g – j); time (“Zeit”) in ms; (from [19]).

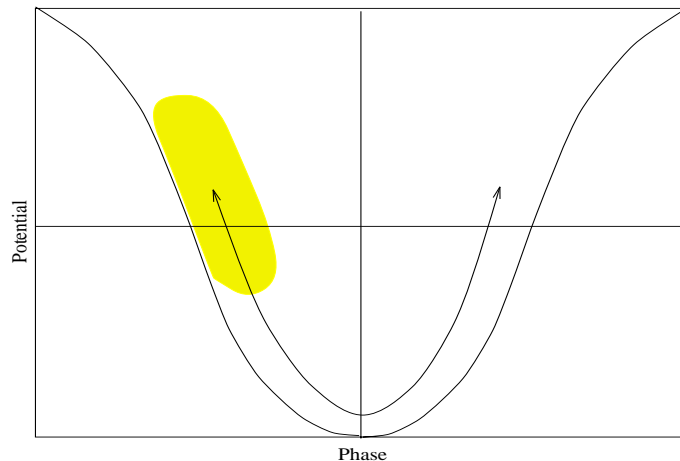


Figure 2.5: Illustration of the longitudinal instability of a single bunch, provoked by collective oscillations of the bunch around the equilibrium position in the potential gap created by the rf-system and corresponding to a bucket.

Another kind of collective instabilities is provoked by interactions between the beam and the electromagnetic waves it generates in the vacuum chambers. Since the vacuum chamber walls have a finite impedance, the electromagnetic image of the beam has a feedback effect on the beam itself. A resonance can appear under given conditions and at given frequencies. Fortunately, these resonance effects, which tend to destabilise the beam, are normally suppressed by the so-called *Landau damping*. A simple physical interpretation can be given to this damping mechanism. A proton beam has a natural energy spread. Thus only a very small fraction of the protons fall inside the exciting frequency ω of the feedback loop corresponding to the beam and its electromagnetic image. These protons are coupled to the external source and steadily absorb energy. Their oscillation amplitudes grow, but since the fraction of protons for which this happens decreases with time, the global response of the ensemble is limited and the feedback loop remains stable [17].

However, this natural damping mechanism breaks down in HERA during the ramping if the beam intensity is too high. In this case, the fraction of protons which fall inside the exciting frequency ω starts to increase. Thus, protons begin to oscillate coherently around the equilibrium position in the potential gap created by the rf system and corresponding to a bucket (Fig 2.5). The longitudinal bunch length grows and the whole system becomes unstable.

Here again, a procedure has been designed by the HERA crew in order to suppress this longitudinal bunch length grow and thus accelerate a high intensity beam. During ramping time (around 300 GeV), a longitudinal focusing system using 208 MHz rf cavities is progressively brought into operation, superimposed to the 52 MHz rf system. At some intermediate energy, the 208 MHz cavities take over completely the task of accelerating the beam and of insuring its longitudinal stability. The effect of this mixing is illustrated on Fig 2.6. A steep potential gap is created (see right column Fig 2.6), increasing the energy spread and thus reintroducing the Landau damping mechanism.

As a consequence, the length of the proton bunches is reduced. However, the tails of the bunches are trapped in neighbouring buckets (see Fig 2.6 $g-j$) of size 4.8 ns in the 208

MHz rf-system. Protons trapped inside these neighbouring buckets are therefore known as the 4.8 ns satellite bunches [18].

2.3 H1 luminosity measurement

Introduction

- The H1 luminosity measurement procedure is first presented in this section. The 1994 data samples are then presented.
- The H1 luminosity system does not allow for a separate luminosity measurement for ep interactions in the satellite bunches. Therefore, a procedure has been developed, in order to estimate the integrated luminosity accumulated in the so-called ‘forward satellite bunch’ observed in the H1 detector at $\approx +70$ cm with respect to the nominal interaction point. The achieved precision allows these data to be used for physics analysis. The measurement of the proton structure function F_2 , based on these data, is presented in chapter 7.
- Combining the forward satellite bunch luminosity measurement with the analysis of FToF data, the luminosity correction accounting for the total satellite bunch effect is thus established. This correction corresponds to the total integrated luminosity for all satellites, including those which are not observed in the H1 detector but contribute to the H1 integrated luminosity measurement.

H1 online luminosity monitor

The luminosity² is measured online from the rate (typically a few kHz) of bremsstrahlung (or Bethe-Heitler, BH) interactions $ep \rightarrow ep\gamma$. A process which has a large and precisely known cross section.

Online, the luminosity measurement is based on the detection of the scattered electron and outgoing photon in coincidence. The luminosity system contains two arms: an electron tagger (ET) and a photon detector (PD), situated respectively at -33.4 m along the e -ring and -102.9 m in the direction tangent to the incoming e -beam from the nominal interaction point. Fig 2.7-a illustrates the position of the H1 luminosity monitor components.

²In this section, the term *luminosity* refers to the *instantaneous* luminosity measurement \mathcal{L}_{inst} expressed in $\text{cm}^{-2}\text{s}^{-1}$. The *specific luminosity* is the instantaneous luminosity normalised to the beam currents (or number of colliding particles): $\mathcal{L}_{sp} = \mathcal{L}_{inst}/I_e I_p$. It describes purely geometrical properties of the beams. The *integrated luminosity* is defined as: $\mathcal{L}_{integrated} = \int \mathcal{L}_{inst} dt$. It is typically integrated over a detector *run* period, characterised by uniform detector and beam conditions. A short run can last only a few seconds and a long run a few hours. The luminosity defined in this way represents the HERA-*delivered* luminosity. It has to be corrected for the H1 trigger dead-time effect, defining the H1-*gated* luminosity. Each individual H1-run is classified according to the detector and the beam conditions as *poor*, *medium* or *good* quality run. The H1-*collected* luminosity usually corresponds to the fraction of the H1-gated luminosity with *medium* or *good* run quality. Finally, one has to take into account that during part of the run some subdetectors can be out of operation, reducing the data taking efficiency. After correcting the H1-gated luminosity for the requested detector status, one obtains the H1-*physics* luminosity, used for physics analysis. The last number depends on the choice of the subdetectors that are requested to be operating.

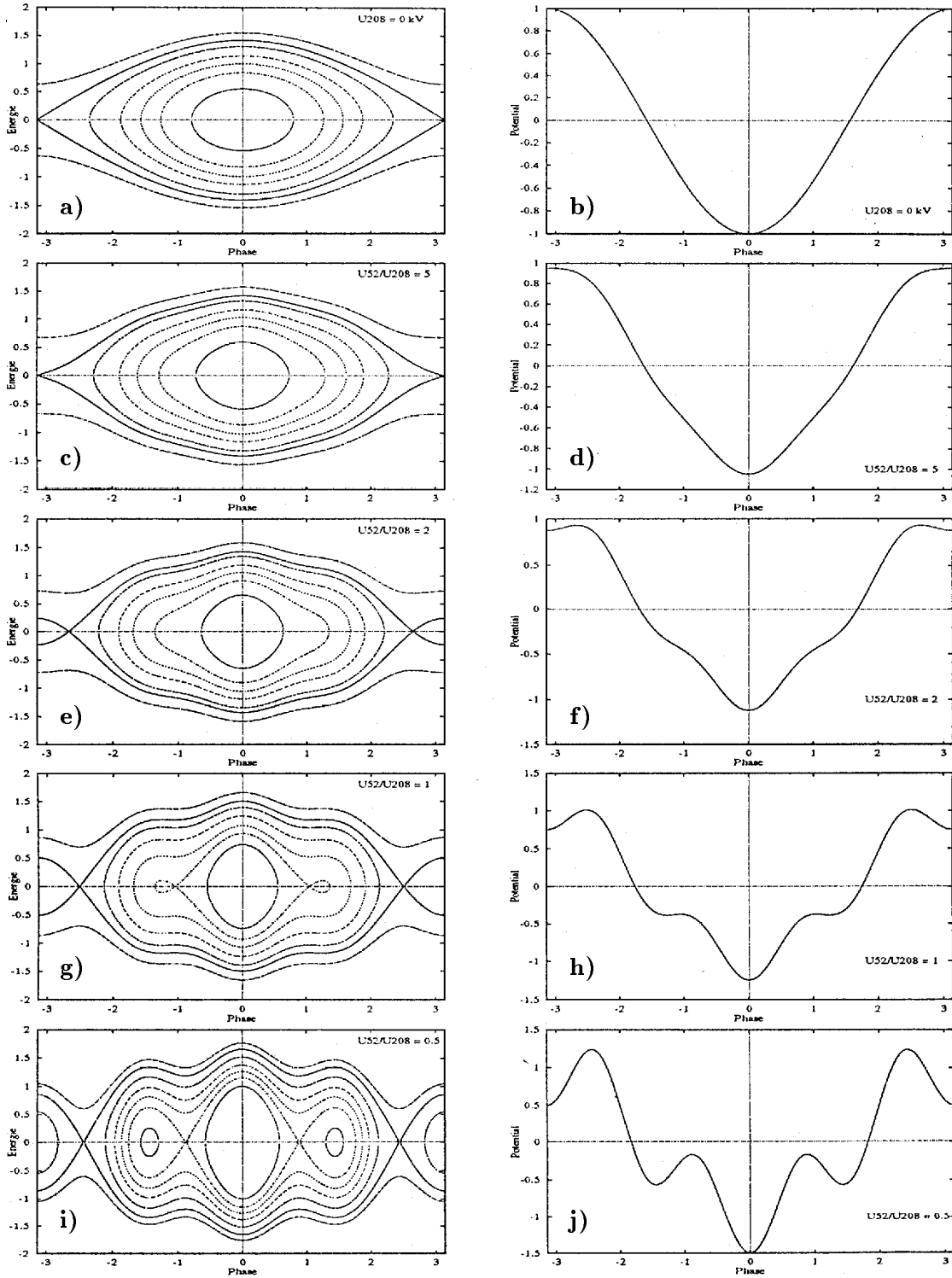


Figure 2.6: Evolution of the bucket (left column) and the potential gap (right column) shapes, created by mixing the 52 and 208 rf systems in HERA. Note the change of the scale of the ordinate in the right column (from [19]).

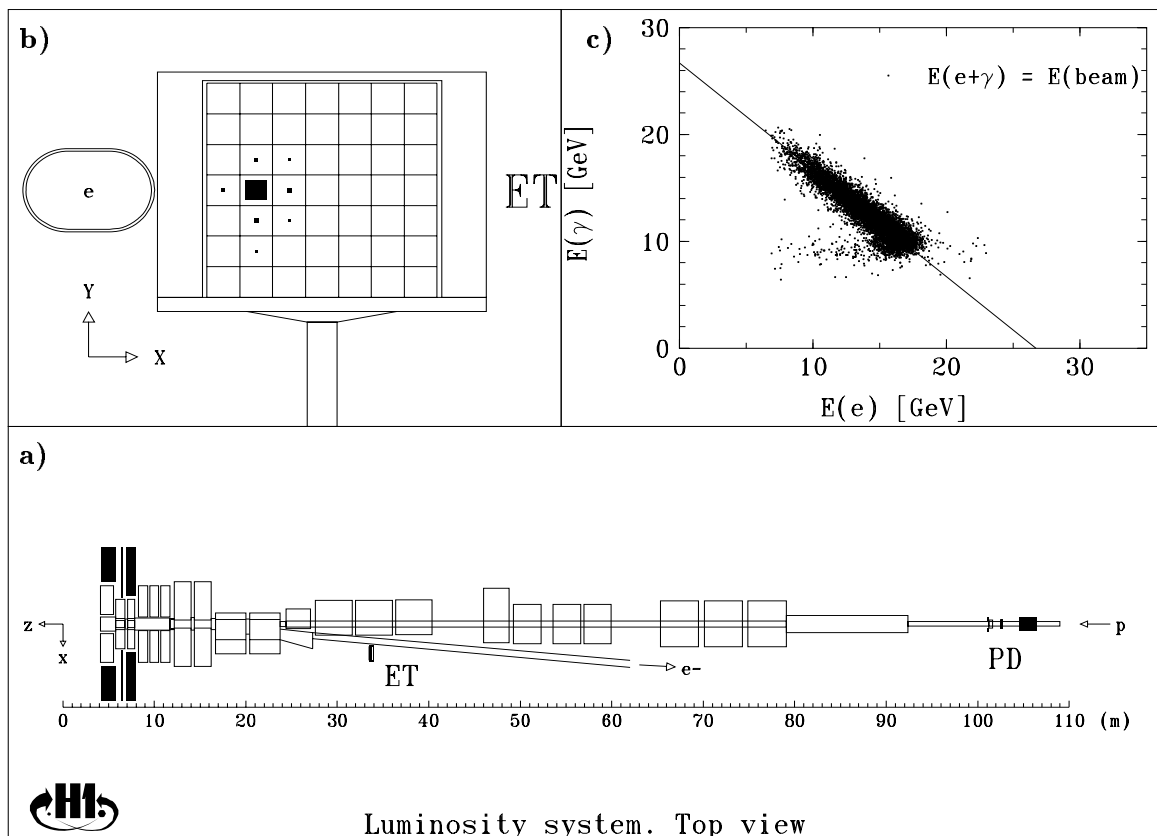


Figure 2.7: *Sketch of the H1 luminosity system: a) general view of the luminosity system ($z=0$ corresponds to the nominal interaction point IP); b) example of a reconstructed energy deposition in the ET detector; c) energy correlation between the e and γ arms (from [20]).*

The electron tagger (ET) electromagnetic calorimeter consists of 7×7 cells with a total area of $154 \times 154 \text{ mm}^2$. Electrons scattered with an energy different from the beam energy are deviated in the spectrometer-like electromagnetic field created by the focusing magnets. They leave the beam-pipe and are detected in the electron tagger if their energy is between 10 and 20 GeV (for emission angle $\rightarrow 0$). An example of reconstructed energy deposition in the ET detector is shown in the transverse view (Fig 2.7-b). The photon detector (PD) consists in a synchrotron radiation filter, followed by a Čerenkov water counter and an electromagnetic calorimeter. The PD calorimeter is made of 5×5 cells with transverse total area of $100 \times 100 \text{ mm}^2$.

Both the ET and PD calorimeters are permanently calibrated during data taking, using the energy constraint for the selected events: $E_{ET} + E_{PD} = E_{e\text{-beam}}$. Fig 2.7-c illustrates the energy correlation between the e and γ arms. The energy resolution obtained for the ET and PD is $\sigma/E = 10\%/\sqrt{E} \oplus 1\%$.

The luminosity is defined as:

$$\mathcal{L}_{inst} = \frac{N^{total} - (I_e^{total}/I_e^{pilot}) \times N^{pilot}}{\sigma_{visible}}(1 + \delta), \quad (2.1)$$

where N^{total} is the total number of detected bremsstrahlung events, N^{pilot} is the number of bremsstrahlung events originating from the beam-gas interactions; I_e^{total} and I_e^{pilot} are respectively the total electron beam current and the electron pilot bunch current, and $\sigma_{visible}$ is an estimate of the total $ep \rightarrow ep\gamma$ cross-section, taking into account the electron arm acceptance and the trigger efficiency. A small correction term δ is applied in order to take into account the superposition of several bremsstrahlung interactions occurring in the same bunch crossing.

The systematic error in this luminosity measurement is dominated by the uncertainty on the electron tagger acceptance, which depends strongly on the precise knowledge of the electron trajectory in the HERA magnetic fields, up to the entry of the electron tagger. The overall normalisation error can reach 10% in extreme cases of large variations of the beam optics. However, the precision achieved using this method can be improved offline by verifying the time dependence of the electron tagger acceptance and correcting the overall normalisation used in the online measurement.

Offline luminosity measurements

A different selection of the bremsstrahlung events detected by the luminosity monitor is used for the offline luminosity measurement. The luminosity is computed using the so-called *hard γ sample* [20], i.e. high energy photons ($E_\gamma > 10 \text{ GeV}$), detected in the photon arm. The main advantage of this method over the coincidence method used for the online luminosity measurement is that the selection efficiency is insensitive to possible variations of the beam optics. On the other hand, it requires a precise absolute energy calibration and detailed understanding of the resolution of the photon detector, and therefore must be performed offline.

The luminosity is defined in the same way as for the coincidence sample (using eq. 2.1). The dominant contribution to the systematic error is the absolute energy calibration and resolution of the γ -arm. The total uncertainty in the measured integrated luminosity with the hard γ method for e^+p interactions in 1994 is 1.40%. This method provides the

most precise estimate of the integrated luminosity and is used for the final measurement for the 1994 run period.

The total integrated luminosity can also be measured from the rate of *QED Compton events* [22]. The cross-section is precisely predicted by the QED theory, but is small compared to the bremsstrahlung cross-section. This method is however an important cross-check of the methods described above since it does not rely on the luminosity system detectors, the event selection being based on the central detector alone. The precision of this method was limited by statistics.

Another cross-check of the integrated luminosity measurement is provided by the so-called *random coincidence method* [23]. The integrated luminosity is determined from the rate of bremsstrahlung events superimposed with an independent class of events, for instance DIS events. The selection is independent of the electron tagger and photon arm triggers, providing a cross-check of their efficiencies.

Integrated luminosity in 1994

In 1994, HERA delivered a total of $\approx 6 \text{ pb}^{-1}$ of luminosity for lepton-proton collisions. Part of this luminosity corresponds to e^-p collisions. However, after 2 months of operation it was decided to use positrons instead of electrons. This allowed for a significant decrease of the background rate and thus an increase of the data taking efficiency³. Therefore, most of the 1994 luminosity was collected with e^+p interactions. During the last days of HERA running in 1994 data were also taken with the nominal interaction point shifted by ≈ 65 cm downstream the proton beam. In what follows, these data are referred to as the *shifted vertex* (SV) data.

Table 2.3 summarises the total collected luminosities for these three different HERA configurations, together with the different sources of errors contributing to the uncertainty in the absolute luminosity measurement using the hard γ sample events.

2.3.1 Luminosity in the satellite bunches

Introduction

Different methods can be used to estimate the satellite bunch contribution to the measured integrated luminosity. A straightforward method would be based on a direct measurement of the proton current I_p in the satellite bunches, \mathcal{L}_{sat} being extracted using the theoretically expected specific luminosity $\mathcal{L}_{sp}(z)$ according to:

$$\mathcal{L}_{sat} = \mathcal{L}_{sp}(z) \sum (I_e I_p) \quad (2.2)$$

³The difference between e^+ and e^- has a purely technical origin: it is related to the presence of ionised (i.e. positively charged) micro-dust particle “clouds” inside the beam-pipe. Thus, the negative e^- beam gas attracted and scattered on them to much more extent than the positive e^+ beam. At HERA the effect is particularly large since the pumping system heavily ionises the rest gas. It is now claimed to be improved, but even in an ideal case, e^+ will always behave better than e^- (this is experimentally proved at all e^+e^- machines) since the rest gas gets ionised in any case by the beam itself [21].

⁴Total integrated luminosity for *good* and *medium* quality runs. No subdetector operation status correction is applied.

⁵Statistical error on the selected bremsstrahlung events and statistical error on the e -gas background subtraction using the pilot bunch events.

Data	e^-p	e^+p	SV
HERA delivered luminosity (nb^{-1})	846	4665	78
H1 collected luminosity (nb^{-1}) ⁴	494	3424	65
H1 efficiency (%)	58	73	83
Errors			
Theoretical value for σ_{BH}	0.5%	0.5%	0.5%
Trigger efficiency	0.3%	0.3%	0.3%
Statistics, e -gas bgr. subtraction ⁵	1.3%	0.4%	3.3%
γ -arm energy scale (calib. & resol.)	1.1%	0.9%	1.7%
Geometrical acceptance of γ -arm	0.5%	0.5%	0.5%
Multiple photon pile-up	0.3%	0.4%	0.3%
Counting and rounding errors	0.5%	0.5%	0.5%
Total error from lumi. system	1.96%	1.4%	3.84%
Satellite bunch correction (see section 2.3.1)	0.34%	0.38%	0.66%
Overall error	1.99%	1.48%	3.90%

Table 2.3: Total integrated luminosities delivered by HERA and contributions to the experimental error on luminosity. (Final values for the 1994 run period [20].)

where the sum is taken over all pairs of colliding bunches, the specific luminosity $\mathcal{L}_{sp}(z)$ describing purely geometrical properties of the beams: beam sizes and their matching⁶.

Unfortunately this direct measurement was not possible during the 1994 data taking period due to the absence of an adequate hardware device. An indirect measurement of the longitudinal structure of the proton beam could be provided by the Forward Time of Flight scintillator detector. But, for reasons that will be given later (see section “FToF data analysis”), the extraction of the proton current in the satellite bunch using the FToF data alone is affected by a systematic error of the order 20 – 50%. However, an estimate of the relative intensities $I_p^{-4.8}/I_p^{+4.8}$ or $I_p^{-19.2}/I_p^{+19.2}$ can be reliably obtained using the FToF data.

On the other hand, the -4.8 ns satellite is observed in the H1 detector and its contribution to the global luminosity can be estimated directly by analysing the z_{vertex} distribution of selected classes of events.

A combined approach is thus used to estimate the satellite luminosity.

- The z_{vertex} distribution of the low Q^2 DIS events is used to estimate the integrated luminosity for the forward (-4.8 ns) satellite. This satellite is observed in the H1 detector with a z_{vertex} distribution centred around $\approx +69$ cm in the H1 coordinate system⁷.

⁶The specific luminosity as a function of z for head-on collisions of beams with a Gaussian spatial shape (which is a good approximation for HERA), can be written as

$$\mathcal{L}_{sp}(z) = [2\pi e^2 f_H \sigma_x(z) \sigma_y(z)]^{-1} = \frac{13.1 \times 10^{25}}{\sigma_x(z) \sigma_y(z)} \text{cm}^{-2} \text{s}^{-1} \text{mA}^{-2}, \quad (2.3)$$

where e is the electron charge and $f_H = 1/(220 \cdot 96 \text{ ns}) \approx 47.35 \text{ kHz}$ is the HERA revolution frequency. The definition of the transverse beam sizes $\sigma_x(z)$ and $\sigma_y(z)$ relies on the optical parameters of the beams at the IP with coordinate z : the emittance ϵ and the beta function β^* [24].

⁷It can be noted that this value does not correspond to the expected $\approx +75$ cm for the mean position

This distribution is similar to the one from the shifted vertex data sample with the nominal interaction point shifted to $\approx +67$ cm. Therefore, detector effects are expected to be similar for both samples. If there was no shifted vertex data sample, it would be necessary to compare the satellite bunch z_{vertex} distribution to the one of the main bunch and this analysis would be less reliable since one would have to take into account different detector acceptances for the two data samples.

The integrated luminosity corresponding to the forward satellite bunch can thus be measured in a straightforward way by comparing the numbers of selected events in the forward satellite and in the shifted vertex sample:

$$\mathcal{L}_{fw\ sat} = \mathcal{L}_{sv} \cdot N_{fw\ sat} / N_{sv} \quad (2.4)$$

where identical criteria were used to select low Q^2 DIS events and \mathcal{L}_{sv} is measured with the H1 luminosity system.

- From the known ratio R_{tof} between the FToF signals from forward and backward p -satellites allows to compute their relative luminosities. Thus,

$$\mathcal{L}_{sat} = \mathcal{L}_{fw\ sat} \cdot (1 + R_{tof}) \quad (2.5)$$

- Finally, a second order correction for the small luminosity tail from ± 19.2 ns satellites is made using equation 2.2. The absolute contribution of this satellite bunch to the overall luminosity error is small, because the specific luminosity \mathcal{L}_{sp} , entering equation 2.2, drops fast outside the interaction region [24].

Analysis of the z -vertex distributions

Low Q^2 DIS events are used in order to determine the fraction of the total integrated luminosity corresponding to electron collisions with the early (-4.8 ns) p -bunch satellite.

The criteria used to select a clean DIS sample will be described in details in section 4.4. Fig 2.8 shows the z -vertex distribution for the low Q^2 ($Q^2 < 5.5$ GeV²) e^+p events. Q^2 is estimated from the polar angle θ_e and the energy E'_e of the scattered electron. In Fig 2.8-*a*, ‘forward’ satellite events are clearly visible in addition to the main bunch events. It should be noted that the $Q^2 < 5.5$ GeV² cut strongly favours satellite bunch events, because their θ_e angular acceptance and thus their Q^2 acceptance ($Q^2 \sim \theta_e$) is increased⁸ compared to that of the main bunch events.

Fig 2.8-*b* presents the z -vertex distribution for the shifted vertex events, obtained by applying the same criteria as for the nominal vertex sample selection. The results of Gaussian fits to the central part of the peaks are shown on Fig 2.8-*a* for the satellite bunch and in Fig 2.8-*b* for the shifted vertex data. Note again that the average z -vertex position

of this satellite ($z_{sat} - z_{IP} = c\tau_{sat}/2 = \pm 72$ cm). We think that since the satellite bunch appears from the tails of the main bunch during ramping (see previous section), it does not necessarily sit in the bottom of the rf bucket, and therefore, it can be observed in a position slightly different from that corresponding to the centre of the bucket.

⁸The angular acceptance in the backward region is limited by the size of the beam-pipe. Satellite bunch interactions take place further away from the backward electromagnetic calorimeter BEMC than the main bunch events. Therefore lower polar angles θ_e can be reached for these interactions.

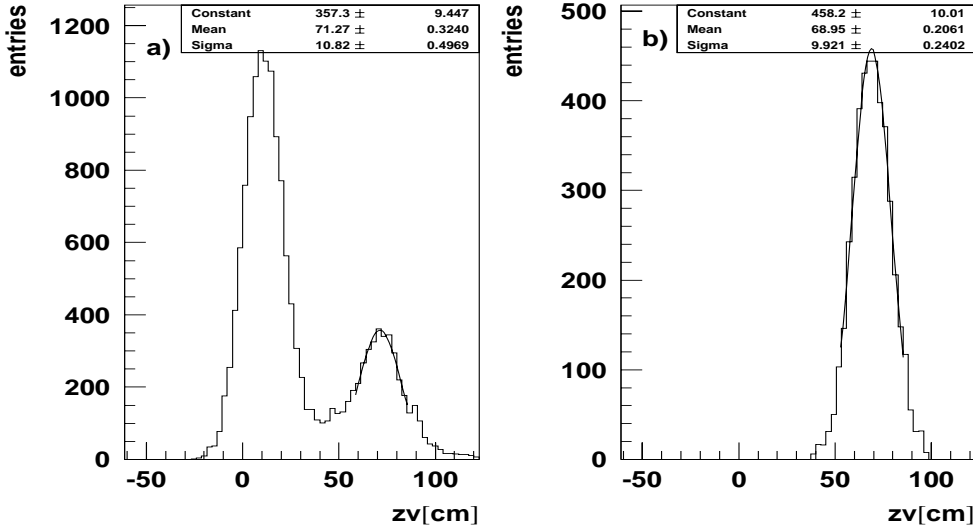


Figure 2.8: z -vertex distribution for low Q^2 DIS events ($Q^2 < 5.5 \text{ GeV}^2$) for the a) nominal vertex sample; b) shifted vertex sample.

of this last sample is approximately the same as for the satellite bunch sample. The mean positions for both peaks is slightly shifted compared to the values quoted before (by ≈ 2 cm) due to the particular Q^2 selection in the present case. Note also that the satellite bunch z -vertex distribution is slightly wider than the shifted vertex sample distribution. This widening is due to the fact that the nominal interaction point position has moved with time by a few centimetres in the case of the nominal vertex interaction runs (see Table 7.1).

An absolute estimate of the integrated luminosity corresponding to the forward satellite bunch is determined by comparing the numbers of events obtained by applying identical selection criteria⁹ to the satellite and the shifted vertex samples. In addition, special cuts were applied in order to take into account the slightly different trigger configuration in the

⁹The following selection criteria were applied to both samples:

- run selection:
 - run quality: Good or Medium
 - trigger phase: 3, 4
 - detector status: correction to the run luminosity $< 20\%$ when the following subdetectors are required to be on: BEMC, BPC, CIP, CJC, COP, LAC, ToF.
- event selection:
 - z -vertex reconstructed within 20 cm from the average $\langle z_{vertex} \rangle$ value for the given run range
 - error on reconstructed z -vertex position < 5 cm
 - standard identification criteria for the scattered electron in the backward electromagnetic calorimeter (see section 4.4).

shifted vertex sample versus the nominal vertex satellite bunch sample (trigger configurations: see subsection “Trigger performance”, page 46; event selection: see section 4.4).

The systematic uncertainty was estimated by varying the selection criteria. In addition, the integrated luminosity of the SV sample itself is corrected for the satellite bunch effect, thus leading to an extra systematic error for the satellite bunch luminosity normalisation. A special minimum bias γp sample was used in order to determine the contribution $\Delta\mathcal{L}_{sat}$ of the satellite bunch in the shifted vertex sample. This contribution was estimated to be [25]:

$$\Delta\mathcal{L}_{sat} = 2.26 \pm 0.66\% \quad (2.6)$$

Finally, the integrated luminosity $L_{sv} = (59.6 \pm 2.3) \text{ nb}^{-1}$ was obtained as a normalisation value for equation 2.4.

For 1994 e^+p collisions, the total integrated luminosity for the forward (-4.8 ns) satellite is

$$\mathcal{L}_{fw\ sat} = (73.8 \pm 5.2) \text{ nb}^{-1} \quad (2.7)$$

corresponding to a total luminosity of 2592 nb^{-1} . The luminosities quoted above are obtained after applying run selection and correcting the run luminosity for the detector status. Table 2.4 summarises the sources of uncertainties.

a) event selection	5.7%
b) luminosity error in the SV sample $\delta\mathcal{L}_{sv}$	3.9%
c) error on satellite correction for the SV sample	0.7%
d) statistics	1.2%
Total error	7.1%

Table 2.4: Contributions to the experimental error for the ‘forward’ satellite luminosity measurement (from [24]).

FToF data analysis

The forward time of flight detector FToF is a pair of scintillators situated at $z = +7.0 \text{ m}$ downstream the proton beam from the nominal IP. Collected signals are proportional to the number of secondary charged particles hitting the FToF scintillators. They originate primarily from the proton remnant of ep interactions, but also from p -gas or p -wall interactions and e -beam related background.

To obtain informations on the p -beam structure, it is first of all necessary to separate signals due to the p -beam from signals related to the e -beam or to ep collisions. This is done by using a high threshold readout, which selects p -gas or p -wall interactions characterised by very high secondary particle densities and discriminates them from other types of interactions.

If the thus selected FToF events were originating from the p -gas contribution alone, the FToF response would be proportional to the proton beam current and the FToF data

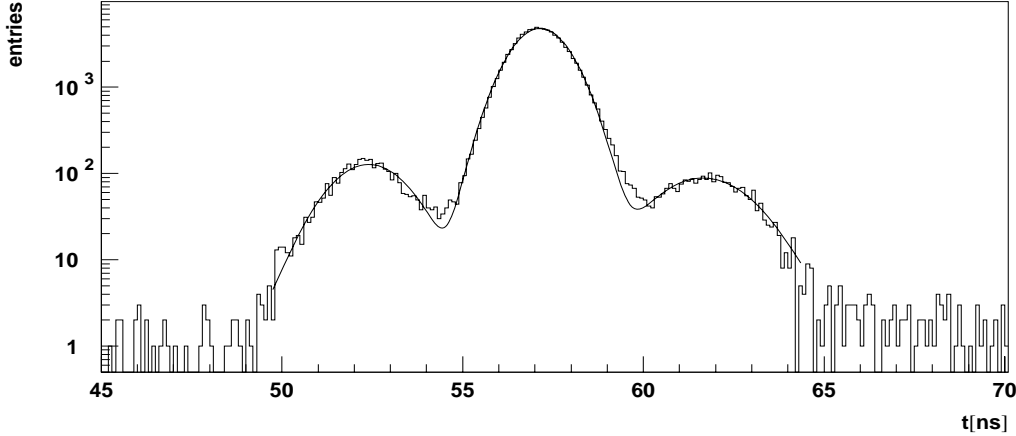


Figure 2.9: Example of a fit to the central part of the FToF spectra. The fit is a superposition of 3 Gaussian distributions over a constant background.

could be directly used to measure the longitudinal p -beam structure. However, there is always some p -wall contribution to the FToF signal caused by protons leaving the bunch. The problem is that the amount of protons per unit current leaving the beam is in general different for the main proton bunch and its satellites. The number of FToF counts is thus also related to the *a priori* unknown behaviour for each particular bunch. Therefore, we can not deduce directly the proton current in the satellite bunches using the FToF data.

However, since the beam optics are in a good approximation symmetric in z around IP, this behaviour should be similar for the forward and backward satellites. It is thus possible, using the FToF data to measure reliably the ratio of the currents in the forward and backward satellites.

High threshold FToF signals are stored in the so-called FToF ‘qvt’ histograms [26] and written together with non-event data in a special ‘KEEP’ event file. A typical example of an accumulated FToF ‘qvt’ spectrum is presented on Fig 2.2.

In order to estimate the ratio R_{tof} between the -4.8 ns and $+4.8$ ns satellites¹⁰, to be used in relation (2.4), the central parts of the FToF spectra were fitted as the superposition of 3 Gaussian distributions over a constant background. An example of a FToF spectrum accumulated during ≈ 20 min of data taking is shown in Fig 2.9. It should be noted that the tails of the bunches are not fully described by a Gaussian fit. This is a known feature and a second order effect for our purpose.

The time evolution of the fit parameters is illustrated on Fig 2.10 for ≈ 3.7 days of data taking. On Fig 2.10-*a* and *b* are shown respectively the total positron and proton currents as measured by HERA. The intensity of the e -beam drops rapidly due to synchrotron radiation. The e -beam was injected and accelerated eight times in HERA, corresponding to 8 *luminosity runs* (*a*). During the same time period, the p -beam was injected only 3 times (*b*).

¹⁰The -4.8 ns and $+4.8$ ns satellites are created by mixing the 208 MHz rf system to the 52 MHz rf system (see section 2.2). Their relative size depends on the phase-shift between these two rf systems and varies from one proton fill to another.

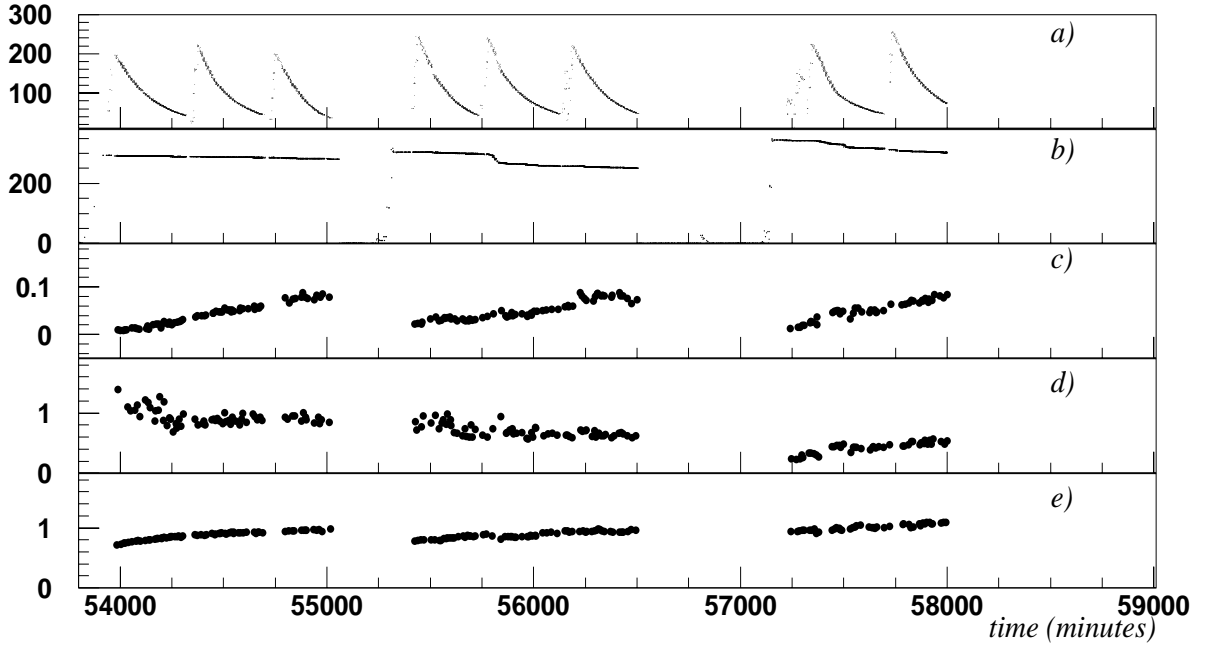


Figure 2.10: Time evolution (in minutes), of the: a) electron beam current b) total proton beam current c) ratio of the -4.8 ns satellite current to the main bunch current (see text) d) ratio of the -4.8 ns to the +4.8 ns satellite currents e) half-width of the Gaussian fit to the main bunch.

Fig 2.10-c shows the ratio of the -4.8 ns satellite current to the main bunch current defined as the ratio of the areas below the Gaussian fits to the corresponding peaks on the FToF ‘qvt’ histograms. The ratio increases slowly during each proton fill until the proton beam is dumped. It is difficult to make a reliable interpretation of this phenomenon [27]. We think that this grow is due to the faster increase of the p -wall contribution to the FToF signals in the satellite bunch than in the main bunch. In other words, we think that the amount of protons per unit current leaving the satellite bunch and contributing to the FToF ‘qvt’ spectra increases faster for the satellite bunch than for the main bunch.

An alternative hypothesis would be that of a real growth of the satellite bunch intensity with time, due to protons escaping from the main bunch and trapped in the satellites, thus increasing their population. This hypothesis would be supported by a growing longitudinal size of the main bunch, as can be observed in Fig 2.10-e. However, this phenomenon is unlikely to provide a significant increase of the satellite current [18].

The small value of the satellite current just after the proton beam ramp is probably due to the small phase and energy dispersion of protons inside the satellite bunch immediately after their creation. Thus few of them can leave the bunch phase space and be detected by the FToF.

Fig 2.10-d shows the ratio of the -4.8 ns to the +4.8 ns satellite currents obtained in the same way as for Fig 2.10-c. The ratio is relatively stable during each proton fill, tending to confirm the hypothesis that the background conditions are symmetric in z around the IP. It can however vary significantly from one proton fill to another. The ratio R_{tof} between

the -4.8 ns and $+4.8$ ns satellites, to be used in relation 2.5, is finally obtained by adding up FToF ‘qvt’ histograms for each luminosity run. The result is shown in Fig 2.11 as a function of the luminosity run number.

The systematic uncertainty on R_{tof} is estimated by varying the fitting procedure and, for instance, by using a polynomial representation for the background in place of the constant value. The uncertainty corresponds to $\delta R_{tof} = 5,5\%$ [24].

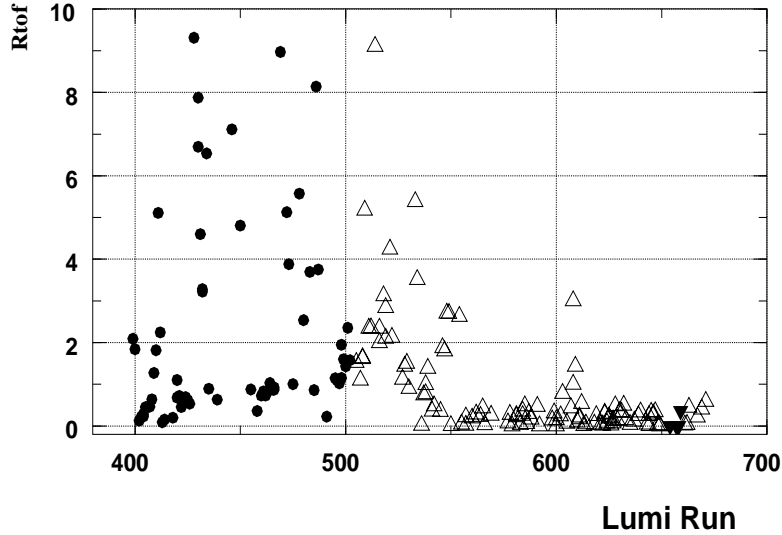


Figure 2.11: Ratio R_{tof} of the 4.8 ns to the $+4.8$ ns satellite currents as obtained from the FToF data in function of the luminosity run number (see text). Full points correspond to the e^-p data, open triangles to e^+p and full triangles to the SV data (from [24]).

Results

The total satellite bunch luminosity is obtained by multiplying the forward satellite luminosity $\mathcal{L}_{fw\ sat}$ with the forward to backward satellites ratio $R_{tof} = I_p^{-4.8}/I_p^{+4.8}$ and by adding a second order correction to account for the ± 19.2 ns satellites. The final values for the luminosity correction for the proton satellite bunch is shown in Fig 2.12. The total error determination for the full e^+p data sample is presented in Table 2.5. The errors

a) forward satellite luminosity	7.1%
b) backward/forward satellite ratio (FToF data) δR_{tof}	5.5%
Total error	9.0%

Table 2.5: Contributions to the experimental error in the total satellite luminosity determination (from [24]).

in Fig 2.12 also account for an extra statistical uncertainty coming from dividing the full data into subsamples with similar beam conditions and thus with similar satellite bunch corrections. On average, the corrections amount to:

$$\mathcal{L}_{sat}(e^-p - 1994) = (3.90 \pm 0.34)\% \quad (2.8)$$

$$\mathcal{L}_{sat}(e^+p - 1994) = (4.22 \pm 0.38)\% \quad (2.9)$$

In both cases the effect is larger than the total error from the luminosity system: 1.96% and 1.4% in e^-p and e^+p collisions respectively (see Table 2.3). Therefore, it definitely cannot be neglected. The period with high satellite level, emphasised as the shaded area in Fig 2.12, was found to be in direct correlation with the time (17-31/08/94) when a proton transmitter was not operational.

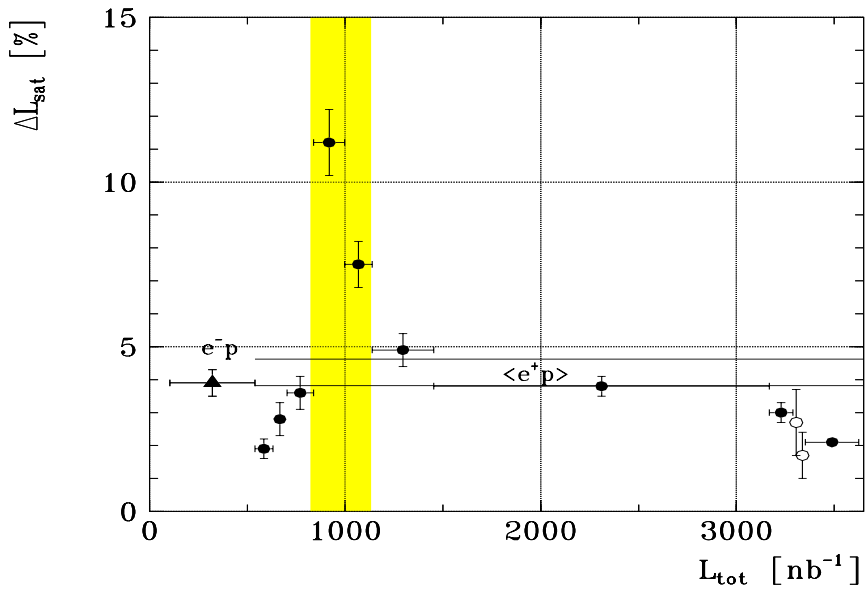


Figure 2.12: Satellite bunch correction to the measured luminosity in the H1 interaction region for different periods of 1994, presented as function of the total integrated luminosity. Empty points correspond to the shifted vertex data. The shaded area corresponds to the period with a broken transmitter (from [24]).

A special tool was provided to the H1 collaboration which allows the satellite bunch luminosity correction to be applied for physics analysis [24]. It provides integrated luminosity as a function of a fiducial cut along the z -axis in a run dependent way.

The relatively small error of the integrated luminosity measurement for the forward satellite ($\delta\mathcal{L}_{fw\ sat} = 7.1\%$, compared to $\delta\mathcal{L}_{sv} = 3.9\%$) makes possible to use these events for physics analysis on a comparable basis as the SV data sample.

Chapter 3

The H1 detector

The H1 detector [28] was designed in order to investigate high-energy interactions of electrons and protons at HERA. The structure function measurement presented in this thesis relies essentially on the central and backward tracker chamber systems and on the backward electromagnetic calorimeter which will be described hereafter in some detail. A brief description of the other H1 components will also be provided. At the end of this section the H1 trigger system will be introduced with a particular attention to the low Q^2 DIS trigger of prime importance for this analysis.

General description

The H1 detector is cylindrically symmetric around the beam axis. The imbalance in energy of the two colliding beams implies that the detector is more instrumented in the outgoing proton direction. In the H1 conventional reference system this direction defines the positive z -axis. The components of the detector situated on the positive side of this axis (relative to the interaction region) are referred to as the "forward" detector. The negative side, corresponding to the outgoing electron direction, is referred to as the "backward direction".

Starting the description from the interaction region, the detector (Fig 3.1) is composed of a central and a forward tracker (section 3.1), containing in turn several layers of drift and proportional chambers. The tracker is surrounded by a calorimetric system (section 3.2), composed of a liquid argon calorimeter (LAC-section 3.2.2) in the central and the forward directions and of a conventional electromagnetic lead-scintillator sandwich calorimeter (BEMC-section 3.2.1) in the backward part. A superconducting coil outside the liquid argon calorimeter provides an uniform magnetic field of 1.15 T. The iron return yoke surrounding the whole detector is laminated into several layers of streamer tubes used for the measurement of the hadronic shower tails by means of an analog readout system, and for muon tracking by means of a digital readout system. The latter is complemented with additional wire chambers inside and outside the iron. This allows measurement of muons with momenta greater than 1.5 GeV/c. A muon spectrometer is placed outside the iron in the forward direction ($3 < \theta < 17^\circ$), where the particle density is highest. The aim of the spectrometer is to measure the muon momentum between 5 GeV/c and 200 GeV/c. Two scintillator planes, located behind the backward calorimeter, are used to reject the background produced outside the H1 interaction region (section 3.3). A small scattered electron angle calorimeter, the "electron tagger", is situated at $z = -33$ m from the interaction point. Lastly a photon detector at $z = -103$ m, operating in coincidence with the electron tagger, monitors the luminosity by the bremsstrahlung process (section 2.3).

A more detailed description is provided in the rest of this section.

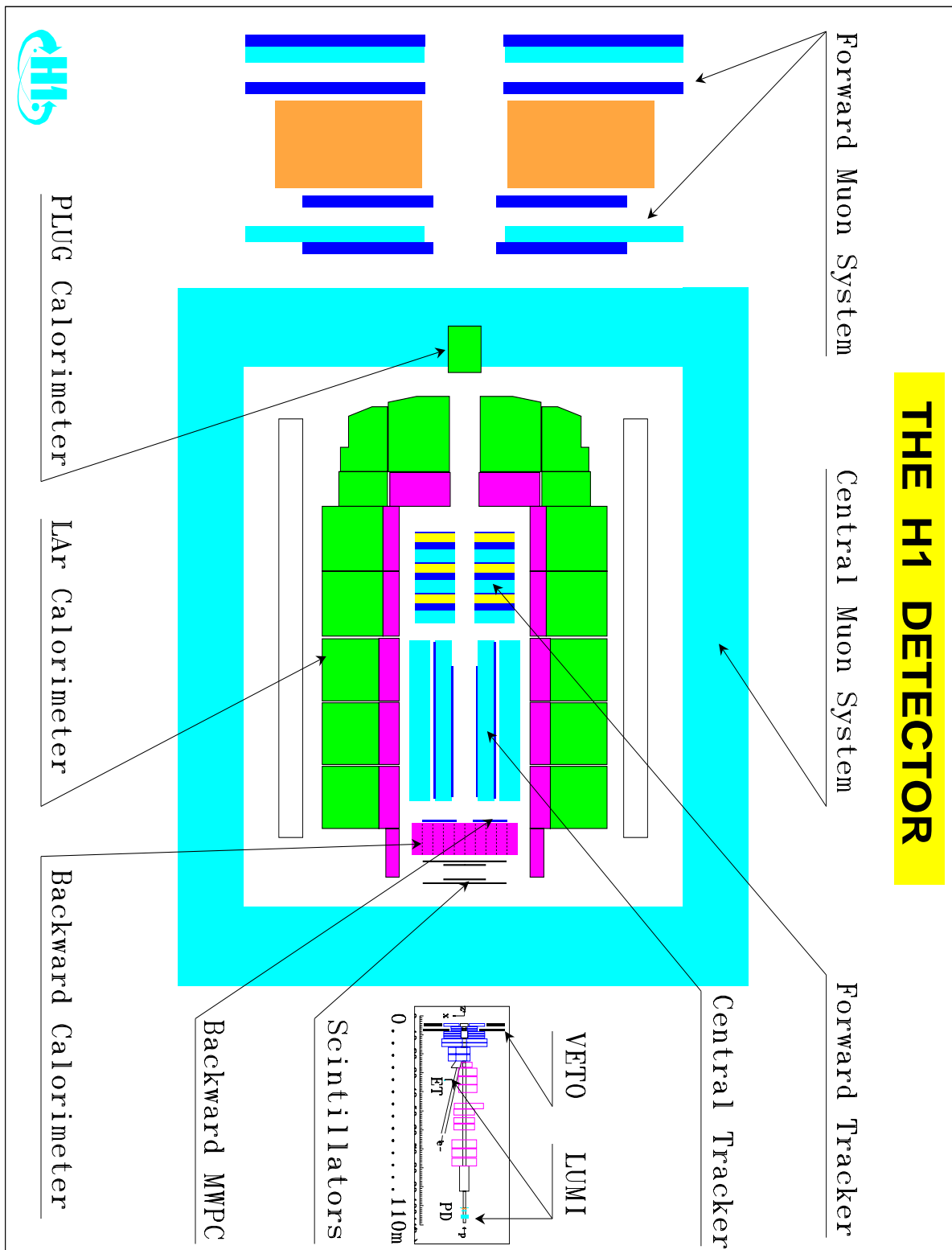


Figure 3.1: Longitudinal cut through the H1 detector along the beam line.

3.1 Tracking system

The H1 tracking system has been designed in order to provide charged particle track triggering, reconstruction and momentum measurement. The latter is made possible by the bending of particle trajectories in the magnetic field. Because of the asymmetry between the electron and proton beam energies, charged particles are mainly produced at small angles θ to the incident proton (forward) direction. To maintain good efficiency for triggering and reconstruction over the whole solid angle, two mechanically distinct detectors have been constructed, the central (CTD) and forward (FTD) trackers, respectively. Each is optimised for tracking and triggering in its angular region. The main parameters of the H1 tracking detectors are listed in table 3.1.

Central tracking		
Angular - radial coverage	$25 < \theta < 155^\circ$	$150 < r < 850$ mm
Jet chamber: spatial resolution	$\sigma_{r\phi} = 170$ μm	$\sigma_z = 22.0$ mm
z-chambers: spatial resolution	$\sigma_{r\phi} = 25$ and 58 μm	$\sigma_z \approx 350$ μm
Momentum - dE/dx resolution	$\sigma_p/p^2 < 0.01$ GeV^{-1}	$\sigma(dE)/dE = 10$ %
Forward tracking		
Angular - radial coverage	$7 < \theta < 25^\circ$	$120 < r < 800$ mm
Spatial resolution	$\sigma_{r\phi} = 170$ μm	$\sigma_{x,y} = 210$ μm
Backward tracking		
Angular - radial coverage	$155.5 < \theta < 174.5^\circ$	$135 < r < 650$ mm
Spatial resolution	$\sigma_{x,y} = 1$ mm	
Trigger proportional chambers		
Angular coverage - channels	$7 < \theta < 175^\circ$	3936

Table 3.1: Summary of the H1-tracking detector parameters (from [28]).

3.1.1 Central tracker

- **Central jet chambers: CJC1 and CJC2**

Track reconstruction in the central region is based on two large cylindrical coaxial drift chambers, CJC1 and CJC2. The active length of these chambers is 2200 mm. The active radial length is 224 mm for CJC1 and 296 mm for CJC2. The wires are oriented parallel to the beam axis (z -direction). The drift cells are inclined with respect to the radial direction by about 30° , such that in the presence of the magnetic field the ionisation electrons drift approximately perpendicular to stiff, high momentum tracks originating at the nominal interaction point. This gives optimum track resolution. A space point is measured with a resolution of 170 μm in the drift coordinate ($r\phi$ plane). By comparing the signal amplitudes readout at both wire ends, a resolution of one percent of the wire length is achieved in z . These chambers allow the measurement of the transverse particle momentum with precision $\sigma_p/p^2 < 0.01$ GeV^{-1} . The specific energy loss dE/dx is used to improve particle identification. The event interaction vertex determination relies essentially on CJC reconstructed tracks.

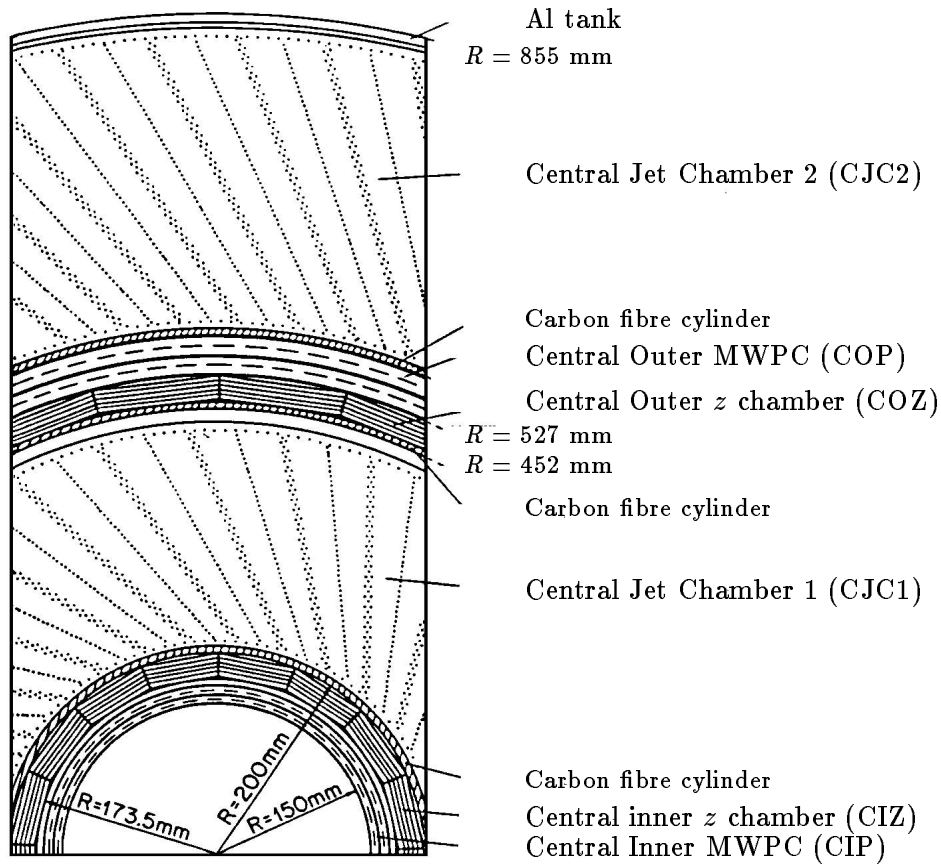


Figure 3.2: Radial view of the H1 central tracker (from [28]).

- **Central z -chambers: CIZ and COZ**

Two thin drift chambers, the central inner and outer z -chambers, surround the inner half of the jet chamber and complement the measurement of charged tracks in the latter chamber. In these chambers, the drift direction is parallel to the beam axis, the sense wires being perpendicular to the latter. The tracks elements are measured with a resolution of $300 \mu\text{m}$ in z and 1 to 2 % of 2π in ϕ .

Linking these track elements to those obtained from the jet chambers with accurate $r\phi$ and moderate z -measurement gives the final accuracy on both longitudinal and transverse momentum components. Finally it allows an improved z -determination of the event interaction vertex position.

- **Central proportional chambers: CIP and COP**

The inner multiwire proportional chamber (CIP) is closest to the interaction region (average $R = 161$ mm) and covers the largest solid angle ($8 < \theta < 172^\circ$). It is composed of 60 sectors in the z -direction ($\Delta Z = 3.65$ cm) and of 8 sectors in ϕ ($\Delta\phi = 45^\circ$).

The COP chamber [29] (average $R = 507$ mm) has an angular acceptance of ($25 < \theta < 156^\circ$). It is composed of 18 sectors in the z -direction ($\Delta Z = 12.1$ cm) and of 16 sectors in ϕ ($\Delta\phi = 22.5^\circ$).

Both chambers deliver a fast timing signal with a time resolution better than the separation between two successive HERA bunch crossings (75 ns for CIP and 60 ns for COP). In addition, in the central and forward regions, the combinations of pad hits in CIP and COP and in the forward proportional chambers (FWPC) are used to trigger on particles coming from the nominal interaction vertex region.

3.1.2 Backward proportional chamber (BPC)

The backward multiwire proportional chamber is situated right in front of the backward electromagnetic calorimeter (BEMC) and is of a great importance for this analysis since it allows the precise measurement of the impact point of the scattered electron entering the BEMC, and thus of the electron emission angle in the low Q^2 kinematic region studied here. It is made of four planes of wires with vertical, horizontal and $\pm 45^\circ$ orientations. The wires are strung every 2.5 mm, but signals from two wires are fed to one preamplifier.

For high energy electrons an efficiency of 87% per plane was measured from extrapolated jet chamber tracks. Three out of four planes are required in coincidence in order to reconstruct a space point with ≈ 1 mrad θ angular resolution. However, several hits are reconstructed in case of preshowering in material in front of the BPC, degrading significantly the θ angular resolution.

The intrinsic plane efficiency and the quoted single hit resolution cannot be used for the structure function analysis without further investigations, since effects as preshowering in the dead material are not correctly taken into account in the detector simulation. An analysis of the BPC resolution and efficiency for the ep data will be presented respectively in sections 5.3.1 and 6.2.

3.1.3 Forward tracker

The forward tracking detector consists of an integrated system of three identical supermodules. Each supermodule includes, in increasing z : three planar wire drift chambers, rotated by 60° to each other in azimuth, designed to provide accurate θ measurements, a multiwire proportional chamber (FWPC) for fast triggering (the time resolution is ~ 20 ns), a passive transition radiator and a radial wire drift chamber which provides accurate $r\phi$ (drift coordinate) information, moderate radius measurement by charge division and limited particle identification by measuring the transition radiation produced immediately upstream (see Tab 3.1).

3.2 Calorimetric system

The H1 calorimetric system consists of a liquid argon calorimeter (LAC) covering the polar angular range ($3 \leq \theta \leq 153^\circ$) and a backward electromagnetic calorimeter (BEMC) located in the electron direction and covering ($151 \leq \theta \leq 177^\circ$). The calorimetric coverage is complemented with a small calorimeter in the proton direction (PLUG), covering the region between the beam-pipe and the liquid argon cryostat ($0.6 \leq \theta \leq 3^\circ$) and by the

tail-catcher system (TC). The latter is used to provide a rough calorimetric measurement ($\sigma/E \simeq 100\%/\sqrt{E}$) of hadronic particles leaking out of the main calorimeter and is based on the analog readout of the pads of the limited streamer tubes that instrument the iron yoke.

3.2.1 The backward electromagnetic calorimeter (BEMC)

BEMC is a conventional electromagnetic lead-scintillator sandwich calorimeter [31].

The calorimeter is composed of 88 stacks aligned parallel to the beam pipe and mounted in an aluminium barrel of diameter 162 cm. The calorimeter front face is located at a distance of 144 cm from the nominal interaction point. The transverse structure can be seen in Fig 3.3-a. 56 stacks have a $\sim 16 \times 16 \text{ cm}^2$ quadratic cross-section. The remaining stacks have trapezoidal and triangular shapes in order to provide an approximation to the annular shape of the barrel support.

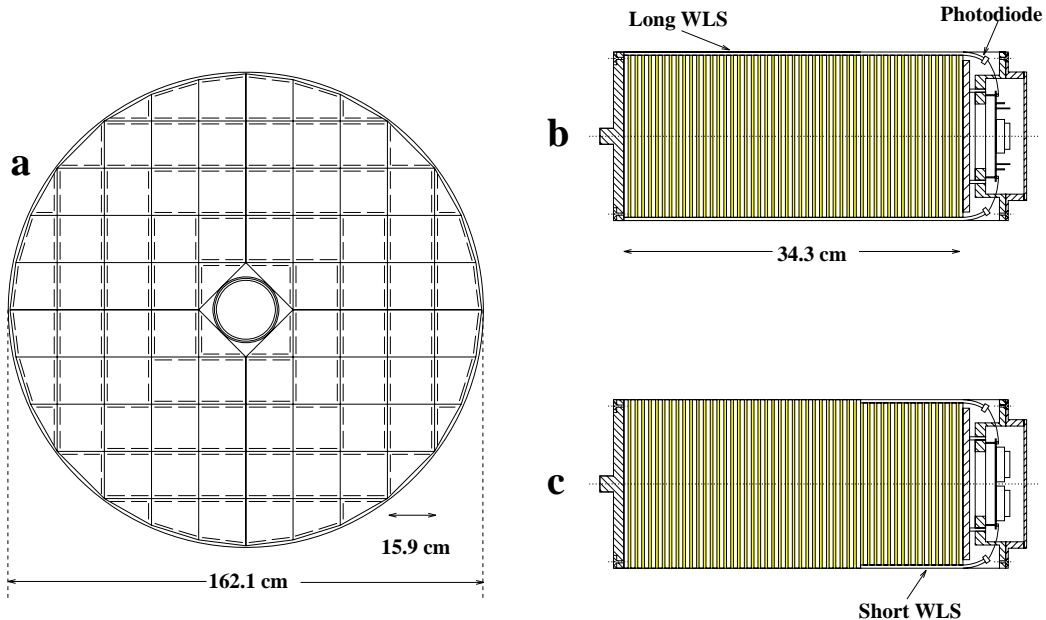


Figure 3.3: a) Transverse view of the backward electromagnetic calorimeter (BEMC). The orientation of long wavelength shifters is indicated by horizontal and vertical lines; b),c) longitudinal views of BEMC stacks in two perpendicular planes. The scintillating light is read out transversely via long WLS covering the full length of BEMC stacks (b). In square and trapezoidal stacks the last 15 sampling layers are also read out via short WLS (c) (from [31]).

The stacks are multilayer lead-scintillator sandwich structures with 50 active sampling layers made of plastic scintillator of 4 mm thickness (Fig 3.3-b,c). The active layers are interleaved with 49 layers of 2.5 mm lead. The entire structure corresponds to an average of 22.5 radiation length or 0.97 hadronic interaction length.

The scintillation light is coupled to wavelength shifter bars. Two pairs of 8 cm wide bars cover two opposite sides of a quadratic stack extending over the full active length.

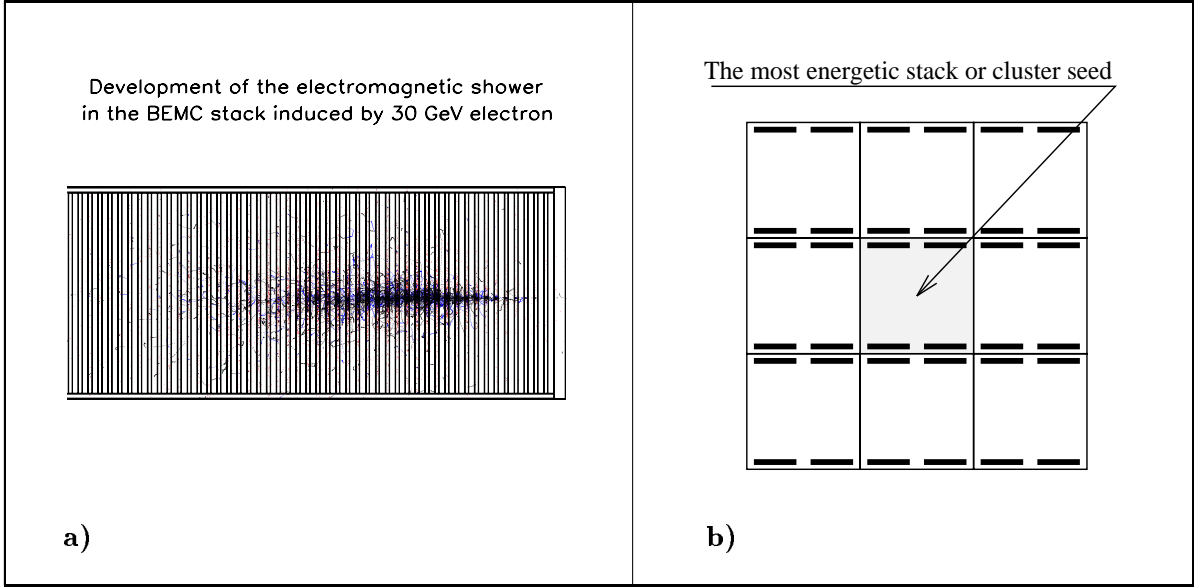


Figure 3.4: a) *Development of the electromagnetic shower in the BEMC (Monte Carlo simulation) induced by a 30 GeV electron*; b) *typical BEMC cluster composed of the most energetic stack (cluster seed) and its eight neighbouring stacks.*

The remaining two sides are covered with 16 cm wide bars extending only over the last 15 sampling layers in the stack.

The light emitted in the wavelength shifters is detected by photodiodes. Each long bar is equipped with one diode connected to a charge sensitive preamplifier. The short bars are connected to a pair of diodes, because of their double width. In total there are 472 read-out channels in the BEMC. The stack energy deposition is defined from the average signal of the four long wavelength shifters:

$$E_{stack} = \sum_{i=1}^4 WLS_i/4. \quad (3.1)$$

The electromagnetic shower induced by a scattered electron (see Fig 3.4-a) is normally confined inside one stack¹, which is called the most energetic stack, with a small energy leakage in the neighbouring stacks. The scattered electron cluster energy is therefore defined as the energy sum of the most energetic stack with its neighbour stacks:

$$E_{cluster} = \sum_{stack=1}^n E_{stack}. \quad (3.2)$$

¹The Molière-radius of an electromagnetic shower ($\rho_M = 21X_o/\epsilon_c$; describes the average lateral deflection of electrons after traversing one radiation length; ϵ_c is the critical shower energy; the maximum shower radius is $R \approx 2\rho_M$) in the BEMC is 3.4 cm, while the stack size is $\sim 15.9 \times 15.9$ cm.

A typical BEMC cluster is composed of the energy deposition in 9 stacks: the most energetic stack or cluster seed and its 8 neighbours (see Fig 3.4-*b*). Depending on the most energetic stack position the total number of stacks in the cluster can be less than 9.

BEMC Calibration

For the measurement of the structure function $F_2(x, Q^2)$ presented in this work, the determination of the kinematic variables x and Q^2 relies on the measurement of the scattered electron energy and polar angle θ_e . The electron energy is measured in the BEMC and the polar angle θ_e is measured using the backward proportional chamber BPC situated right in front of it.

A precise energy calibration of the BEMC is crucial. It was performed in two steps: initial calibration in test beams, improved calibration using ep data.

The initial BEMC energy calibration is based on 3 different methods:

1. electron beam data obtained at DESY;
2. electron, pion and muon beam runs at the CERN SPS;
3. high statistics cosmic muon data.

During the transfer of the initial electron energy scale into the H1 environment a calibration precision better than 10% was achieved. More details on the energy calibration at this stage can be found in [32].

For the next step three methods using ep data were used to improve the BEMC energy calibration:

1. the kinematic peak method, using the pronounced peak of quasi-elastically scattered electrons in the region close to the beam energy [33, 34];

The individual stacks absolute energy scale calibration is performed using this method. For the total cluster energy scale, the effects of the presence of dead material in front of the BEMC (up to two radiation lengths) and of cracks between the BEMC stacks are taken into account by a Monte Carlo simulation.

2. the double angle method, using an indirect energy estimate obtained from the measured polar angles of the scattered electron θ_e and the hadronic final state θ_{jet} (see section 5.2);

It provides an independent cross check of the total cluster energy scale and of its uniformity over the whole BEMC and allows to perform additional corrections in the crack region, which is difficult to calibrate with sufficient precision.

3. the QED Compton method. The physical process corresponds to the Compton scattering of a quasi-real photon on an incident electron, with the dominant contribution due to the elastic channel ($ep \rightarrow ep\gamma$). The energy and the angle of the scattered electron and of the photon are constrained by the QED theory, making this process well suited for calibration of the BEMC [22, 25].

This method allows to test the energy scale over the whole range of electron energies detected in the BEMC. The cross section of the elastic QED Compton process is approximately two orders of magnitude smaller than the DIS cross section, which is a drawback of this method in comparison with both the previous ones.

Energy scale

For the 1994 luminosity period it was possible to achieve, using the kinematic peak method, an average precision of 1% [31] for the global BEMC energy scale for electrons in DIS.

In the meantime, the local miscalibrations due to the effects of dead material and of cracks were improved using the double angle method in the most inner and outer BEMC parts (see section 5.2). With this improved energy reconstruction, the geometrical nonuniformity of the energy scale for the 1994 luminosity period is found to be less than 1% [31].

Using the QED Compton events the linearity of the BEMC response is determined to be better than 1% [31].

Energy resolution

A single quadratic² stack BEMC energy resolution has been measured at CERN and DESY test beams (Fig 3.5). Three terms determine the characteristics of the energy resolution. The readout by photodiodes and preamplifiers leads to a constant noise term (93 MeV for a single stack). Sampling fluctuations are proportional to \sqrt{E} . The leakage out of the stack contributes to the resolution with a term proportional to E . A fit to the measured points gives the resolution function to be: $\sigma/E = 0.097(6)/E \oplus 0.100(3)/\sqrt{E} \oplus 0.010(3)$ (E in GeV) [31].

In the H1 environment the energy of an electromagnetic cluster is reconstructed on basis of the energy measurement in the hottest stack and its eight neighbours. This increases the noise term by a factor 3 with respect to a single stack. In addition, it was found that single stack contributions are slightly higher compared to the one measured in the beam tests (130 MeV). Therefore the noise contribution term is 390 MeV. Stack-by-stack variations of the calibration and inhomogeneities of the energy response near the stack borders deteriorate the resolution and increase the constant term. Finally, the energy resolution function for the BEMC energy response is $\sigma/E = 0.39/E \oplus 0.1/\sqrt{E} \oplus 0.017$ (E in GeV) [31]. The corresponding curve is shown (dashed line) on Fig 3.5.

A measurement of the resolution performed directly from ep data at the electron beam energy using the double angle method (see section 5.2). is in a good agreement with this prediction, as shown on Fig 3.5.

Space point reconstruction

The energy deposited in each stack is reconstructed from the light collected by the four photodiodes, which, due to light attenuation, depends strongly on the position of the shower inside the stack. This dependence of light collection on the electron impact point

²The BEMC stacks have several basic transverse geometries: most of them are quadratic but there are few triangular and trapezoidal stacks in the most inner and outer BEMC parts (see Fig 3.3).

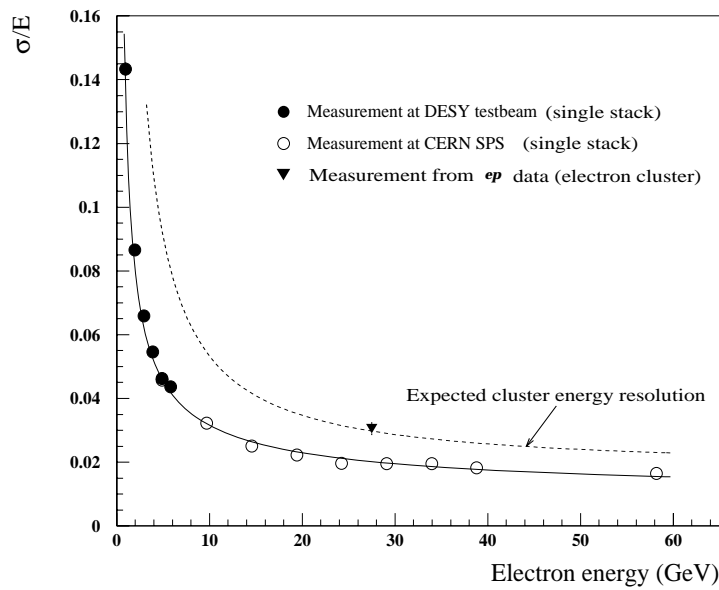


Figure 3.5: Energy resolution measured at the DESY test beam and at the CERN SPS for a single quadratic stack and direct measurement of an average cluster energy resolution from ep data using the double angle method. The solid curve is a fit to the test beam single stack energy resolution measurements. The dashed curve indicates the electromagnetic cluster energy resolution as extrapolated from the single stack energy resolution measurement.

has been studied and parameterised. The energy weighted average of the energy deposition in each stack of a cluster defines the centre of gravity of the cluster. The space point resolution obtained with this method is shown in Fig 3.6 [31]. A dedicated study will be presented in section 5.1.

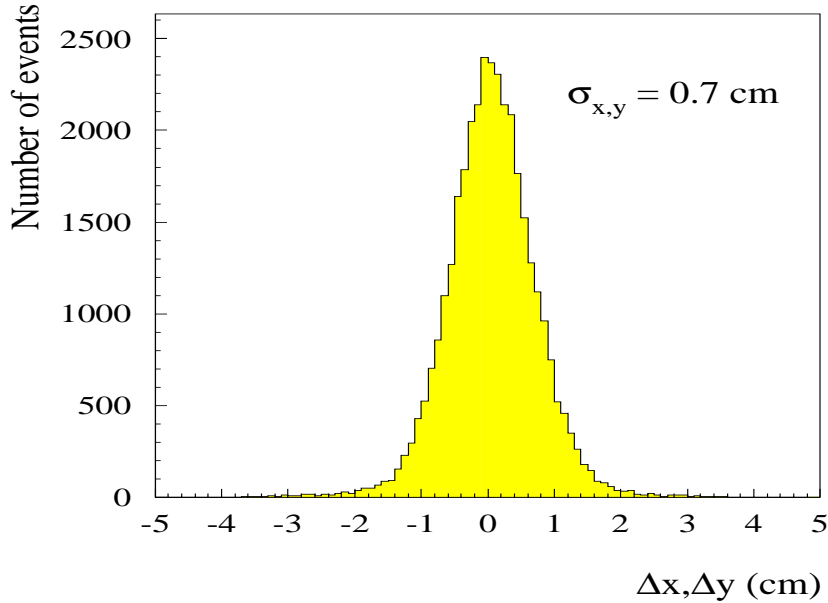


Figure 3.6: *Space point reconstruction resolution for electrons scattered into the BEMC (from [31]).*

Response to hadronic particles

The depth of the BEMC is approximately 1 hadronic interaction length λ_{int} . In Fig 3.7 the BEMC response to 30 GeV pions is shown. The data were measured at the CERN SPS and compared to a Monte Carlo simulation based on the GEANT package [36]. The simulation is normalised to data at the minimal ionising particle response peak (left peak on Fig 3.7). 40% of the charged pions traverse the BEMC as minimal ionising particles. In average, pions deposit $\approx 45\%$ of their energy in the BEMC. The good agreement between the test beam data and the shower simulation justifies the use of the BEMC in measurements of the backward hadronic energy flow.

Summary

The main parameters of the BEMC calorimeter are listed in table 3.2.

³Since the space point measurement provided by the BEMC is rather approximative, the impact point of the scattered electron is always measured in the backward proportional chamber BPC situated right in front of the BEMC.

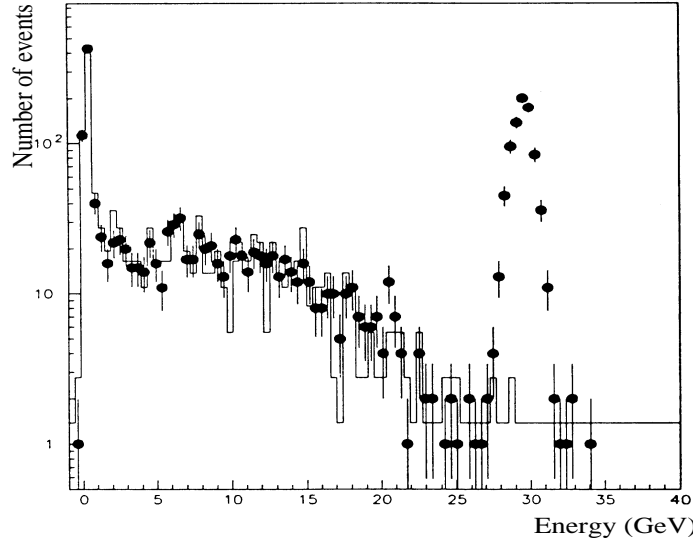


Figure 3.7: *Energy spectrum reconstructed in the BEMC for a 30 GeV mixed positron/pion beam (solid points) compared to the Monte Carlo simulation based on the GEANT package for pions (histogram). The positron contribution is visible as a peak at 30 GeV (from [31]).*

Distance interaction point–BEMC front plane	144.0 cm
Average density of sampling structure	4.98 g/cm ³
Sensitive length (total)	22.5 X_0 , 0.97 λ , 34.25 cm
Sensitive length (short WLS only)	6.8 X_0 , 0.29 λ , 10.35 cm
Molière-radius	3.4 cm
Maximum sensitive radius	≈ 79 cm
Electromagnetic energy resolution σ/E	$0.39/E \oplus 0.1/\sqrt{E} \oplus 0.017$
Geometrical nonuniformity of the energy scale	$< 1.0\%$ ($15 \leq R_{bpc} \leq 64$ cm)
Nonlinearity of the energy response	$< 1.0\%$ ($15 \leq R_{bpc} \leq 64$ cm)
Space point reconstruction resolution $\sigma_{x,y}$	7 mm

Table 3.2: *Summary of the BEMC calorimeter parameters.*

3.2.2 The liquid argon calorimeter (LAC)

The LAC calorimeter [30] is situated inside the large H1 coil, minimising in this way both the amount of dead material in front of it and the overall size and weight of the calorimeter. It uses liquid argon as the active material and is divided in two parts: an inner electromagnetic part (EMC) and an outer hadronic part (HAC). The segmentation along the beam axis is done in eight self-supporting ‘wheels’. Each of the six barrel wheels is segmented in ϕ into eight identical stacks or octants.

The total thickness of the electromagnetic calorimeter varies between 20 and 30 radiation lengths (X_0) or 1.0-1.4 interaction lengths (λ_{int}) for hadrons. The hadronic part has a thickness of 5 to 9 interaction lengths.

The energy resolution of the EMC varies between $\sigma/E = 10\%/\sqrt{E} \oplus 0.01$ and $13\%/\sqrt{E} \oplus 0.01$, depending on the stack. The hadronic calorimeter has an energy resolution of $\sigma/E \approx 50\%/\sqrt{E} \oplus 0.02$. Both the resolution and the overall energy scale have been verified using beam tests and H1 data. By comparing the measured track momentum of positrons and electrons with their corresponding energy deposition in the LAC, the electromagnetic energy scale is presently known to 3%. The absolute scale of the hadronic energy measurement is known to 4%, as determined from studies of the transverse momentum (p_t) balance in DIS events.

3.3 Scintillators

There were three scintillator detectors in the H1 detector during the 1994 data taking period. Two of them, a time of flight counter and a veto wall, are located in the backward region. They contribute greatly to the suppression of the proton beam related background (beam gas and beam wall interactions producing background showers of energetic penetrating hadrons and halo muons) in deep inelastic scattering. With a proton beam life time of 10 h the H1 sensitive detector volume is hit by this background with a frequency of 2.6 MHz. Another time of flight counter is situated in the forward part of the H1 detector (see section 2.3.1).

Backward time of flight counter (BToF)

The backward time of flight device is located upstream of the interaction region at $z \approx -2$ m. It consists of two planes of 3 cm plastic scintillator mounted perpendicular to the beam pipe. The plane nearest to the interaction point (ToF1) lies at $z = -1.95$ m and has 16 cells of 317×317 mm², thus matching the size of four BEMC stacks. The outer plane lies at $z = -2.25$ m and has eight larger counters (317×634 mm²). Each scintillator plane is sandwiched between two foils of lead (6.5 mm, 1.1 X_0) to absorb synchrotron radiation, both to protect the counters from damage and to limit the number of low energy triggers.

Signals are collected by 24 photomultiplier tubes, amplified and sent to the readout and the trigger system. The BToF total trigger decision time is 250 ns, from which 190 ns are due to the delay from the readout cables.

The device as a whole has a resolution of 4 ns which allows for a significant suppression of the proton beam related background (see Fig 3.8) since the mean separation time of particles from proton background and those from ep collisions is ~ 13 ns.

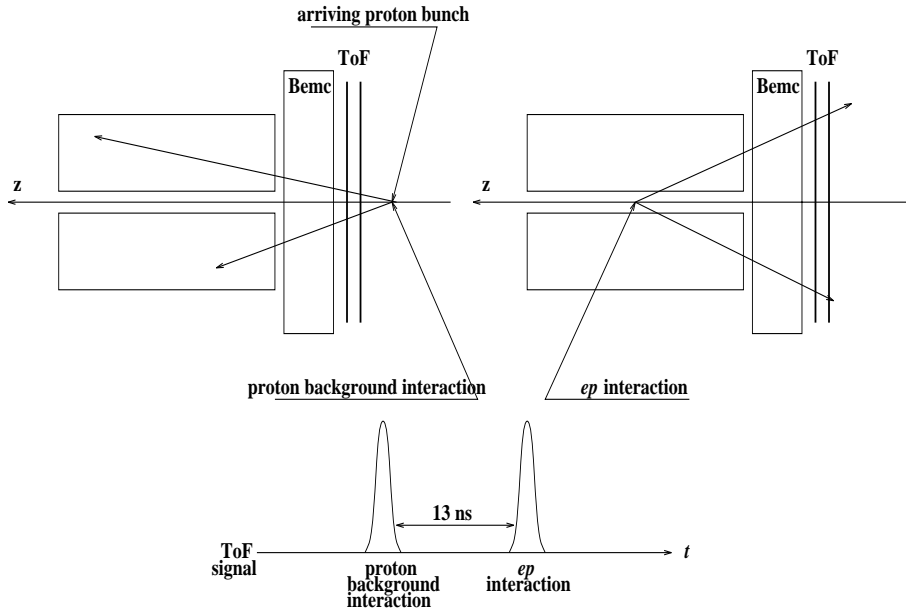


Figure 3.8: Proton related background identification using the BToF signal.

Veto wall

In addition to the BToF device two “backward” double scintillator veto walls are installed at $z = -6.5$ and $z = -8.1$ m.

The smaller inner veto wall covers the near beam area down to a radius of 11 cm. It is built out of four scintillator pairs and the total area covered is 100×90 cm². Hard penetrating background particles (i.e. halo muons) are identified in coincidence between scintillators with a time resolution of ~ 3 ns.

The large outer veto wall with an area of 5×4 m² overlaps the inner veto wall and nearly all of the liquid argon calorimeter and the instrumented iron end caps. It is made up of 10 large scintillator pairs of up to 2.1×0.90 m² each. The coincidence time resolution is ~ 8 ns, which allows for a clear time separation between the background of the passing proton bunch and event correlated hits.

3.4 Trigger

The purpose of the H1 trigger system is to select interesting ep events and to reject high rate background events. At the designed luminosity of 1.5×10^{31} cm⁻²s⁻¹, the rate of DIS events is ~ 5 Hz and the rate of the dominant physics process (photoproduction) is ~ 100 Hz. In 1994 the rate of genuine DIS events was less than 0.5 Hz.

The interesting physics channels are inundated by a $\times 1000$ higher background rate, consisting in three basic types: synchrotron radiation from the electron beam, proton gas interactions in the beam pipe vacuum of about 10^{-9} mbar and proton interactions on the beam pipe walls and surrounding equipments.

The background conditions as well as the short bunch time interval of 96 ns and the request for low deadtime of the readout system result in a four level (L1-L4) centrally

clocked trigger system, from which only L1 and L4 were operational in 1992-1995.

The first level trigger is supplemented by a front end *pipeline* keeping all detector informations for each bunch crossing (BC) until the final L1 trigger decision is available. The L1 trigger thus turns out to be deadtime free. The total pipeline length varies between 27 and 35 BC depending on the subdetector.

Level 1 The trigger level 1 system consists of nine different trigger systems, each based on the informations of a given subdetector. The outputs of these systems are called trigger elements, i.e. *yes/no* decisions encoded in bits. Most of these elements rely either on the geometrical origin of the events (BToF veto, hit patterns for the multiwire proportional chambers, etc.) or on the calorimetric triggers (energy thresholds for calorimeters, for instance the BEMC single electron trigger BSET (see section 3.4.1 for more details), etc.). Trigger elements are then used in the central trigger logic and combined to various so called subtriggers (e.g. $E_{BEMC} > E_{threshold}$ and good *BToF timing*).

Up to 128 subtriggers can be defined in order to select interesting physics events (physics triggers) but also to monitor detector efficiencies (monitor triggers) or to select cosmic ray events for calibration purposes (cosmic triggers).

The rate of each subtrigger is computed separately and can be prescaled if needed. The final L1 level decision is given by the logical OR of all subtriggers and is distributed to the front end electronics of all subsystems to stop the pipeline. At this point the primary deadtime begins.

Level 2 The L2 trigger starts the readout of the subdetectors. Complex decisions based on more detailed informations can thus be achieved. After a time of typically 20 μs the decision of the level 2 trigger defines whether a fast reject should happen or whether the event is to be treated further. For level 2 decision processors, various hardware solutions are under construction, including a neural network approach.

Level 3 If the event is accepted by the level 2 trigger, more precise and more time consuming readout operations like calorimeter analog to digital conversions are started, on basis of which a level 3 decision is available after typically a few hundred μs . In case of reject, the readout operations are aborted and the experiment is alive again.

Level 4 The level 4 filter farm is a software trigger based on fast RISC processor boards. It is integrated in the central data acquisition system and has the raw data of the full event available as a basis for its decision making algorithms. One of the most important rejection algorithms relies on the event (x, y, z) vertex constraint. Another algorithm is designed to reject events with a faked energy deposition in the BEMC due to a synchrotron shower particle hitting a BEMC-readout photodiode. As reconstructed data of the whole detector merge in L4 for the first time, it is well suited for monitoring and calibrations: numerous monitor histograms are filled there, which can be inspected online.

3.4.1 The BEMC single electron trigger (BSET)

The event selection used for the present analysis is based on electron (positron) identification in the backward electromagnetic calorimeter (BEMC). This identification relies on the BEMC single electron trigger (BSET) formed by several subtriggers derived from the BEMC, BToF and tracker trigger elements. Its basic function is to select events with localised energy deposition (cluster) in the BEMC stacks (see section 3.2.1). A detailed description of the BSET trigger is given in [35].

Analog signals from the photodiodes connected to the long wave length shifters in one stack are first summed up to form the stack response. Stack responses are then equalised to the same energy scale using known calibration factors. Two sets of thresholds controlled and monitored by threshold modules are applied to the stack signals. A low stack threshold (typically 1.3 GeV) is used to suppress noise contribution to cluster energies and to the total BEMC energy. A high threshold is used for cluster building initiation, with typical value of 2.3 GeV.

The trigger logic is separated into two independent branches: the analog branch, which forms analog sums (cluster and total energies), and the digital branch, based on stack threshold bit patterns. The trigger elements of the analog branch form the basis of the BSET subtriggers.

Predefined hardware cluster topologies based on simulation studies are put into the cluster separation (builder) module, which detects the cluster seeds and assigns neighbouring stacks above the noise threshold to form trigger clusters. The corresponding energies are summed up, and for each cluster the obtained sum ($E_{cluster}$) is compared to three thresholds to form three cluster trigger element labelled CL1, CL2 and CL3.

The lowest energy trigger element (CL1) was employed in coincidence with track trigger elements. To obtain a reasonable rate, it was most of the time prescaled in 1994. The medium threshold (CL2) was used together with a timing veto from the ToF as the standard DIS trigger of low Q^2 events. The highest threshold (CL3) was used for triggering of events with quasi-elastic scattered electrons, to be used mostly for BEMC calibration and monitoring.

Trigger performance

The efficiency of the BEMC trigger was determined using a sample of events triggered by independent triggers (liquid argon calorimeter trigger, z -vertex trigger and their coincidences). Fig 3.9 shows the efficiency of the two lowest thresholds labelled CL1 and CL2 used to trigger the low Q^2 physics sample (CL2 as a stand-alone calorimeter trigger and CL1 in coincidence with tracker trigger). The 50% trigger efficiencies (referred as thresholds) were set to 4.3 GeV, 7.7 GeV and 16.9 GeV for CL1, CL2 and CL3 respectively. These thresholds were set on the basis of rate contributions to the L1 trigger.

Two main sources of undesired triggers were identified. The most difficult one was caused by protons escaping the beam and hitting the synchrotron radiation mask situated just below the BEMC. These interactions were not vetoed by the BToF system. In addition, they had very large track multiplicities causing a large dead time due to the tracker readout. In the BEMC these events were triggered mostly by the inner triangular stacks near the beam pipe. To reduce this background interaction rate, the four innermost triangular

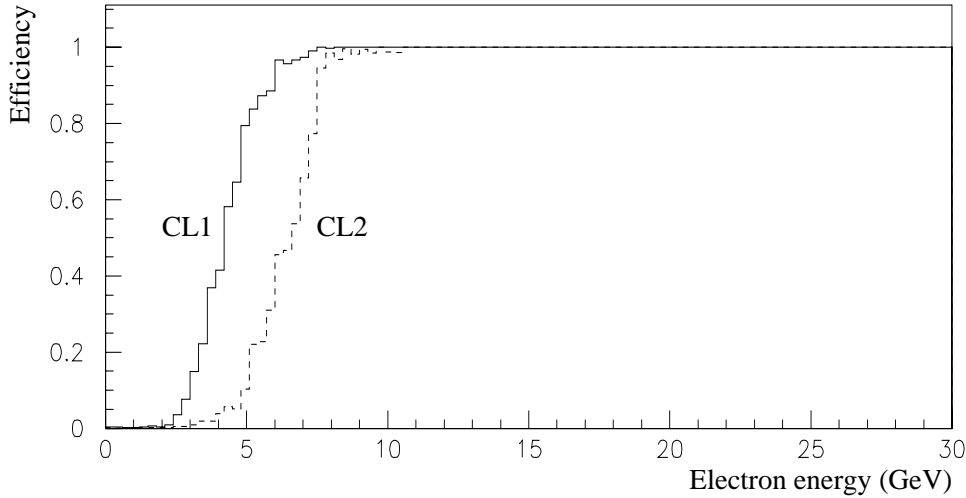


Figure 3.9: *BEMC single electron trigger efficiencies*

stacks were excluded⁴ from the trigger most of the time. In what follows this trigger configuration is referred to as the *closed triangles* configuration. Data taken during short luminosity periods with stable beam conditions and with inner triangle trigger allowed, is referred to as *open triangles data*. The shifted vertex data (SV) was taken with the *open triangles* configuration of the trigger.

Another source of false triggers was caused by charged particles or photons hitting directly the readout photodiodes. Most of these triggers were caused by synchrotron radiation. To reduce the high trigger rates caused by this process, the beam pipe region below the BEMC was equipped with lead shielding. In addition, the 16 innermost stacks were equipped with veto electronics⁵.

A further reduction of the trigger rate due to single diode interactions is performed at the L4 level for the stacks not equipped with veto electronics. Such events are identified after the full BEMC reconstruction, which includes individual wavelength shifter energies and cluster energy depositions.

A small fraction of the events caused by this false trigger survived the filters and was accepted in the final triggered data sample. These events formed one of the background sources for the low Q^2 DIS selection. Therefore, a special offline procedure has been developed, allowing for the identification and rejection of these events (see section 4.4.2, page 70).

Depending on the beam currents and on background conditions, the rate for the stand-alone trigger CL2 was in the range 5-12 Hz, to be compared to the genuine DIS event rate of ~ 0.5 Hz. This is due to backgrounds not vetoed by the ToF veto, to single diode false

⁴To be more precise, the high threshold is set to a very high value, preventing the cluster seed from the four innermost triangular stacks.

⁵The vetoing is based on the structure of the signal from wavelength shifters collecting the scintillation light in a stack. In the case of particle shower, the scintillation light is distributed between the four readout diodes. A trigger due to a high level signal in only one diode (single diode event) indicates that a photon has hit it directly and therefore this event is vetoed by a specially designed electronics.

triggers and to photoproduction events.

3.5 Data acquisition

The H1 data acquisition system is designed to read-out and digitise over 250 000 analog channels, resulting in some 3 Mbytes of raw digitised information for a triggered event.

Informations are digitised and read-out in parallel from many subdetectors and directed to the ‘central data acquisition’ (CDAQ) which coordinates the overall readout chain. They are merged together in the central memory buffer (event builder), in order to form a full H1 event. Data are compressed and formatted, reducing the event size to 50-100 Kbytes. The latter are sent to the L4 filter farm, and later to the central mainframe computer, which writes the data onto magnetic tapes.

At all stages, extensive data monitoring and detector controls are performed.

3.6 Monte Carlo simulation

The Monte Carlo data used for the present analysis rely on a full detector simulation program (H1SIM) based on the GEANT package [36]. The average simulation time is of the order of 600 s for one event on a SGI 4D/460 processor. Most of the CPU time is required for the simulation of the particle showers in the detector. Therefore, for massive simulations ($\sim 1\text{M}$ events) a special shower parameterisation, which is fast but accurate, was developed (H1FAST) leading to a reduction of the CPU time by a factor 10.

For the simulation of DIS-faking photoproduction events, a two step procedure (TURBO) has been developed: a fast parameterised simulation of the energy deposition in the BEMC is first performed. If this energy deposition exceeds 7 GeV (corresponding roughly to the CL2 threshold), then the full event is simulated. With this method only $\sim 1\%$ of the generated events is simulated, allowing sufficient statistics to be accumulated.

Chapter 4

Experimental method and DIS event selection

In this chapter, the experimental method used to measure the DIS cross-section and the structure function $F_2(x, Q^2)$ is introduced. The method is based on a comparison of the data with the results of a Monte Carlo simulation. Next, are briefly presented different ways of measuring the DIS event kinematics used in the present analysis. Finally, after a short discussion of backgrounds, the DIS event selection is described, followed by conclusions, summarising the selection criteria applied to the different data samples analysed.

4.1 Experimental procedure

The cross section for deep inelastic scattering is computed (in H1) as a function of the invariants x and Q^2 :

$$\int_{bin} \frac{d^2\sigma(x, Q^2)}{dx dQ^2} dx dQ^2 = \frac{N_{DIS}}{A\mathcal{L}} = \frac{N_{obs} - N_{\gamma p} - N_{bg}}{A\mathcal{L}} = \sigma_c \left(\frac{\sigma_c}{\int_{bin} \frac{d^2\sigma(x, Q^2)}{dx dQ^2} dx dQ^2} \right)^{-1}, \quad (4.1)$$

with

- A Detector acceptance estimated by Monte Carlo simulation, including smearing effects. It is defined as the ratio of the number of selected Monte Carlo events over the number of generated events in the given (x, Q^2) bin: $A = N_{rec}/N_{gen}$;
- \mathcal{L} Total integrated luminosity;
- N_{obs} Number of selected DIS (candidate) events;
- $N_{\gamma p}$ Estimated number of the ep photoproduction background events;
- N_{bg} Estimated number of the non ep interaction background events;
- σ_c Differential cross section $d^2\sigma/dx dQ^2 |_{x_c, Q_c^2}$, evaluated at the bin centre (x_c, Q_c^2) .

The differential cross section can be expressed in terms of the structure function F_2 :

$$\frac{d^2\sigma(x, Q^2)}{dx dQ^2} = \kappa(R) \cdot F_2(x, Q^2) \cdot (1 + \delta) \quad (4.2)$$

with

$$\kappa(R) = \frac{2\pi\alpha^2}{Q^4 x} \left(2(1-y) + \frac{y^2}{1+R} \right) \quad (4.3)$$

where $y = Q^2/xs$ and

- $1 + \delta$ electroweak radiative corrections to the pure one photon exchange (Born cross section σ_0). The Z^0 exchange can be safely neglected for the Q^2 range explored in the present thesis¹;
- R ratio between the longitudinal (σ_L) and transverse (σ_T) cross sections $R = \sigma_L/\sigma_T = F_2/2xF_1 - 1$. The contribution from R is negligible except at large y where assumptions have to be made until it can be measured. It is presently calculated by QCD².

Using 4.2, the F_2 structure function can be related to the measured cross section as:

$$F_2(x_c, Q_c^2) \cong \frac{1}{\kappa_c(R)} \sigma_c \left(\frac{\sigma_c}{\int_{bin} \frac{d^2\sigma(x, Q^2)}{dx dQ^2} dx dQ^2} \right)^{-1} \cdot RC \cdot BC \quad (4.4)$$

with

- $RC \cong 1/(1 + \delta)$ inverse of the radiative corrections to the Born cross section σ_0 ;
- BC corrections to be applied in order to take into account the finite bin size while F_2 is defined at the bin centre (x_c, Q_c^2) .

The latter corrections are defined as follows:

$$RC = \frac{\int_{bin} \frac{d^2\sigma_0(x, Q^2)}{dx dQ^2}(x, Q^2) dx dQ^2}{\int_{bin} \frac{d^2\sigma(x, Q^2)}{dx dQ^2} dx dQ^2} \quad (4.5)$$

and

$$BC = \frac{\sigma_0(x_c, Q_c^2)}{\int_{bin} \frac{d^2\sigma_0(x, Q^2)}{dx dQ^2} dx dQ^2} \quad (4.6)$$

The sign \cong accounts for the assumptions that the bin centre corrections are calculated using the Born cross section instead of the total DIS cross section (see 4.1) and the radiative corrections are averaged over the bin.

The ‘‘Monte Carlo method’’ used in the present thesis consists in evaluating the structure function F_2 from a starting function F_2^{MC} . One has:

$$F_2 \cong \frac{1}{\kappa(R)} \frac{N_{DIS}}{A\mathcal{L}} \frac{\sigma_0(x_c, Q_c^2)}{\int_{bin} \frac{d^2\sigma(x, Q^2)}{dx dQ^2} dx dQ^2} = \frac{N_{DIS}}{A\mathcal{L}} \frac{F_2^{MC}(x_c, Q_c^2)}{\int_{bin} \frac{d^2\sigma_{MC}(x, Q^2)}{dx dQ^2}(x, Q^2) dx dQ^2}, \quad (4.7)$$

where $F_2^{MC} = \sigma_0/\kappa(R)$ is the structure function parameterisation used for the Monte Carlo simulation³. If acceptance and radiative corrections are implemented correctly in the Monte Carlo simulation, the corresponding cross section is:

$$\int_{bin} \frac{d^2\sigma_{MC}(x, Q^2)}{dx dQ^2}(x, Q^2) dx dQ^2 = \frac{N_{rec}}{A\mathcal{L}_{MC}}, \quad (4.8)$$

¹ Effects due to Z^0 boson exchange are smaller than 3% even at the highest value of Q^2 presently reached, $Q^2 \sim 5000 \text{ GeV}^2$, which is far beyond the scope of the present analysis.

² The theoretical uncertainty on R is included in the systematic errors of the F_2 measurement. Note that a 20% error on R leads to a 2% uncertainty on F_2 at $y = 0.6$ for R of about 0.6.

³ In practice, F_2 is obtained from parton distribution functions, in a given renormalisation scheme.

where N_{rec} is the number of selected DIS Monte Carlo events in a given bin (including radiative events). Expression 4.7 becomes:

$$F_2 \cong \frac{N_{obs} - N_{\gamma p} - N_{bg}}{N_{rec}} \frac{1}{\epsilon} \frac{\mathcal{L}_{MC}}{\mathcal{L}} F_2^{MC}(x_c, Q_c^2), \quad (4.9)$$

where ϵ describes remaining corrections to be applied to the Monte Carlo simulation, because of an imperfect description of the detector.

Below, a synthetic overview is given of studies which were performed in order to estimate the variables used in (4.9). These studies are more or less accurately distributed in separate groups in an *ex-post* logical approach, yet in reality there are interconnections and feedbacks between them.

When a reliable description of the data by the Monte Carlo simulation is obtained, the extraction method based on a Monte Carlo simulation allows for reducing systematic uncertainties of the F_2 measurement, because the correlations between error sources are best taken into account. This is a major issue in view of the high statistics available, and consequently of low statistical errors.

A general prescription for the F_2 structure function measurement is:

1. Define the DIS selection criteria. This selection consists in the following groups of criteria:
 - run selection in order to obtain a data sample with uniform detector and background conditions;
 - electron identification⁴ and background rejection cuts;
 - fiducial cuts restricting the selection to the parts of apparatus allowing for reliable measurements and adequate description by the Monte Carlo simulation. The latest statement is crucial for the present method of F_2 extraction based on the comparison of the data with the result of a Monte Carlo simulation.
2. Data selection and detector efficiencies are studied and compared to the Monte Carlo simulation. Corrections are applied to the Monte Carlo if necessary (ϵ).
3. The quality of the detector calibration and resolution (energy calibration, angular measurements, etc.) is checked and improved if possible by a comparison of the Monte Carlo simulation with the data.

These studies (2-3) are essential to verify that the data description by the Monte Carlo simulation is reliable. We listed them as separate items, while in reality they are strongly correlated and done approximately in parallel. In general, several iterations were necessary to obtain the present understanding of the data and a fair Monte Carlo description.

4. The implementation of radiative corrections in the Monte Carlo simulation is verified. This point is essentially a pure Monte Carlo study and therefore we separate it from the above listed group. At the end, a comparison of F_2 measurements using different ways to reconstruct the kinematic variables (see section 4.2) provides to some extent a cross check of the reliability of the radiative correction implementation (see section 7.1.3).

⁴The identification of the scattered electron in the detector implies that the interaction happened in a defined Q^2 range.

5. The remaining background subtraction can be done using the data themselves (pilot bunches) for the non- ep interaction backgrounds (beam-wall, beam-gas interactions etc.). The ep photoproduction background is estimated using a Monte Carlo simulation.

At this point, all ingredients of expression (4.9) are defined.

6. Convenient binning and central values (x_c, Q_c^2) are defined.

Here again this can not be done independently of detector studies, since for example event migrations depend on the quality of the kinematics reconstruction, i.e. on calibrations and resolutions of the detector components.

7. The F_2 values are extracted.

8. The obtained F_2 measurements are parameterised, and the parameterisation is used as an input to the Monte Carlo simulation. Several iterations are necessary to exclude the dependence of the measured structure function F_2 on the Monte Carlo input structure function F_2^{MC} .

9. The systematic errors are studied and the kinematic range where F_2 can be meaningfully measured is defined for each kinematic reconstruction method.

10. The final measurement of the F_2 structure function is a combination of measurements using different kinematic reconstruction methods, providing a maximum coverage of the HERA kinematic range.

As a matter of fact, different items listed above do not have the same weight from the point of view of manpower and effort. The analysis presented here deals essentially with five items. The DIS event and run selections (1) and background elimination (5) will be presented in this section after a short introduction of the DIS event kinematics. Fiducial cut issues (1) will be mentioned in chapter 6 in parallel to selection and detector efficiency studies (2). Chapter 5 is dedicated to detector calibration and resolution studies (3). Finally, systematic errors (9) are treated all along chapters 5 and 6 and will be summarised in the last chapter 7, bringing together all preceding investigations towards an F_2 measurement.

4.2 Deep inelastic scattering kinematics

A typical low Q^2 ($5 \leq Q^2 < 200 \text{ GeV}^2$) DIS event is presented in Fig 4.1. The scattered electron is detected in the backward electromagnetic calorimeter BEMC. Its energy deposition is schematically represented by a square with a total area proportional to the detected energy. The event interaction vertex is determined from the charged particle tracks reconstructed in the central and/or the forward tracker. Trajectories of the detected particles are schematically represented by full curves originating from the interaction vertex. The scattered electron angle θ_e , defined with respect to the proton beam direction (z -axis), is measured from the reconstructed interaction vertex and the signal detected in the backward proportional chamber BPC situated right in front of the BEMC. A BPC signal (hit)

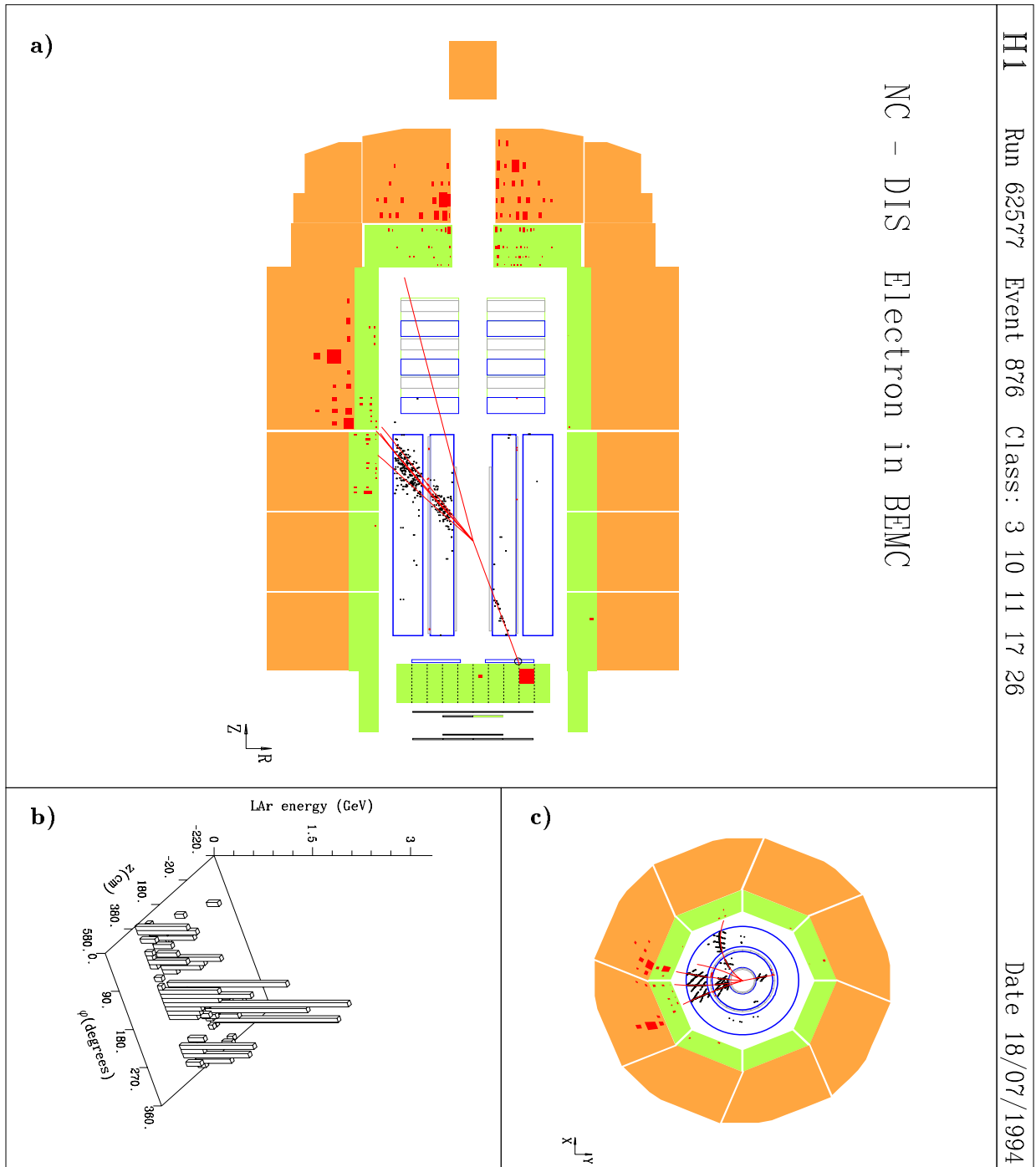


Figure 4.1: DIS event with the scattered electron detected in the BEMC. a) side view of the H1 detector (the instrumented iron is not shown); c) radial view of the H1 detector; b) Liquid argon calorimeter energy deposition in function of $z - \phi$.

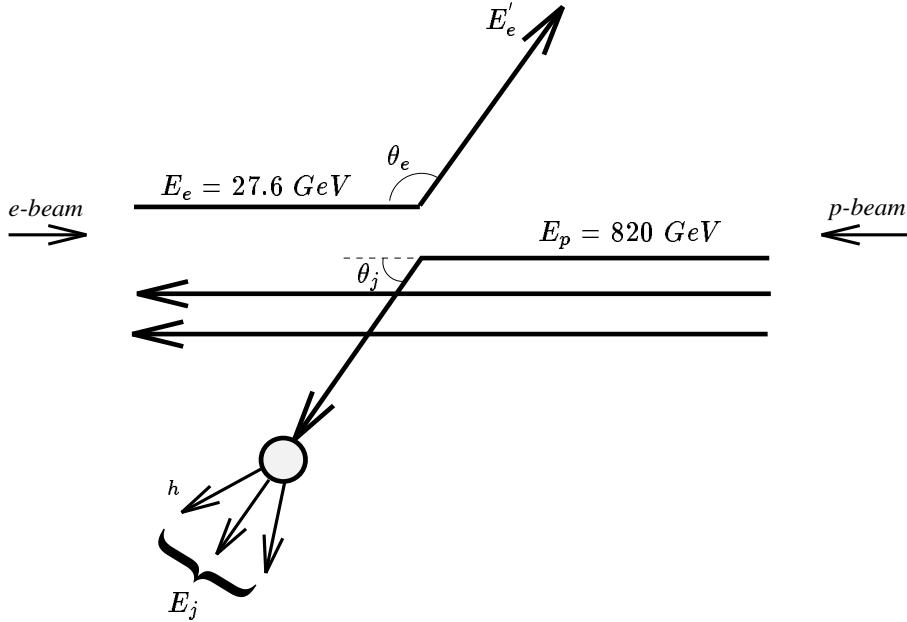


Figure 4.2: Schematic definition of the measured quantities in DIS.

is visible as a small circle. A particle jet from the hadronisation of the struck quark (“current jet”) is visible in the central part of the detector. The associated energy E_j and the polar angle θ_j are determined by combining tracker measurements for the low momentum charged particles and calorimeter informations. The energy deposition in the most forward part of the H1 detector corresponds to the proton remnant fragments.

The above mentioned quantities are defined schematically in Fig 4.2. The polar angles are measured with respect to the incident p -beam direction. Two of the four measured quantities ($E_e, \theta_e, E_j, \theta_j$) are sufficient to determine the event kinematics.

Given this redundancy in the measurement, the kinematic variables can be determined by different methods [14]. In the present analysis two methods are used: the “electron” method using only informations from the scattered electron and the “sigma” method, combining scattered electron and hadronic final state measurements. A third method, the so called “double angle” method, is used only for calibration purposes.

Electron method

The electron method is technically the simplest one. It uses only the energy E'_e and the polar angle θ_e of the scattered electron. The basic formulae are⁵:

$$y_e = 1 - \frac{E'_e}{E_e} \sin^2 \frac{\theta_e}{2} \quad Q_e^2 = 4E'_e E_e \cos^2 \frac{\theta_e}{2} = \frac{E_e'^2 \sin^2 \theta_e}{1 - y_e}. \quad (4.10)$$

The variable x is calculated as $x = Q^2/ys$, with s being the centre of mass energy squared of the ep collision. The iso-angle and iso-energy lines of the scattered electron in the (x, Q^2)

⁵In the following formulae, the electron and proton masses are always neglected

plane are shown in Fig 4.3-a. In the present analysis, the low Q^2 region corresponding to the acceptance of the BEMC-BPC detectors ($151 \leq \theta \leq 176^\circ$) is the matter of concern.

Straightforward calculations yield the following expressions for the relative errors:

$$\frac{\delta Q^2}{Q^2} = \frac{\delta E}{E} \oplus \tan \frac{\theta_e}{2} \delta \theta_e \quad (4.11)$$

$$\frac{\delta x}{x} = \frac{1}{y} \frac{\delta E}{E} \oplus \tan \frac{\theta_e}{2} \left(x \frac{E_p}{E_e} - 1 \right) \delta \theta_e \quad (4.12)$$

$$\frac{\delta y}{y} = \frac{1-y}{y} \frac{\delta E}{E} \oplus \frac{1-y}{y} \cot \frac{\theta_e}{2} \delta \theta_e \quad (4.13)$$

The precision of the Q^2 measurement is high for most of the HERA kinematic range, except at high θ_e where it starts to degradate due to the $\tan \theta_e/2$ factor in 4.11.

The y and x resolutions are poor for most of the HERA kinematic range due to the $1/y$ factor in 4.12, 4.13 except at high y -low scattered electron energy E_e (the iso-energy lines are parallel to the iso- y lines, see Fig 4.3-a).

The incoming e -beam energy (E_e) is fixed to its nominal value in formulae 4.10. If the effective incoming electron energy is reduced by emission of a real photon ($E_e = 27.6 - E_\gamma$), the effect is not taken into account in the former expressions, leading to a biased event kinematics for this type of events. Event migrations induced by this bias are unfolded using a Monte Carlo simulation which includes QED radiative effects. The electron method is therefore very sensitive to the treatment of the radiative corrections in the Monte Carlo simulation.

Σ method

It is possible to benefit from the redundancy of measured quantities and to constrain the incoming lepton energy by combining the electron and hadron final state measurements. This is realised using the sigma method [37].

The variable y_Σ is defined using the information of the hadronic final state only ([14]):

$$y_h = \frac{\Sigma}{2E_e}. \quad (4.14)$$

with

$$\Sigma = \sum_h (E_h - p_{z,h}). \quad (4.15)$$

Here E_h and $p_{z,h}$ are the energy and the longitudinal momentum component of particle h , and the sum is over all final state particles, except the scattered electron. From conservation of the total $\sum (E - p_z)$ of the event, and if no particle escapes detection, the incoming electron energy can be calculated from the final state measured quantities, independently from initial state radiation⁶:

$$2E_e = \sum_{total} (E - p_z) = \sum_h (E - p_z) + (E - p_z)_e = \Sigma + E_e'(1 - \cos \theta_e). \quad (4.19)$$

⁶Total energy and longitudinal momentum conservation imply:

$$x E_p + E_e = E_e' + \sum E_j \quad (4.16)$$

$$x E_p - E_e = E_e' \cos \theta_e + \sum E_j \cos \theta_j \quad (4.17)$$

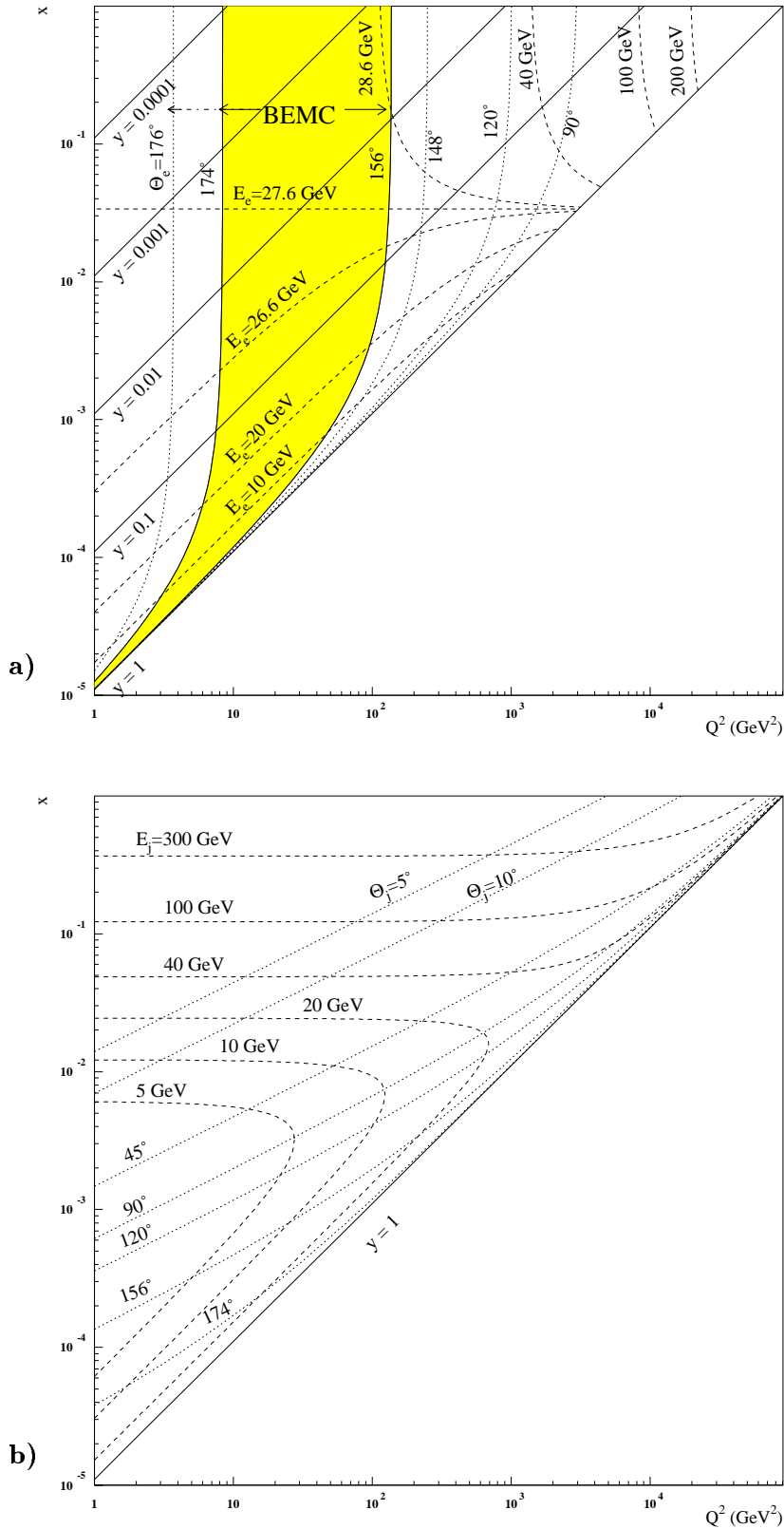


Figure 4.3: a) Iso-angle and iso-energy lines for the scattered electron. The acceptance region of the BEMC is shown hatched. The acceptance is increased down to $\theta_e \sim 176^\circ$ for the shifted vertex (SV) data. b) Iso-angle and iso-energy lines for the current jet.

We can now obtain for y_h a new expression y_Σ , which is independent of the incoming e -beam energy:

$$y_\Sigma = \frac{\Sigma}{\Sigma + E'_e(1 - \cos \theta_e)} \quad Q_\Sigma^2 = \frac{E_e'^2 \sin^2 \theta_e}{1 - y_\Sigma}. \quad (4.20)$$

In contrast to the electron method, the sigma method is not sensitive to the emission of a real photon before the interaction, since the incoming lepton energy does not appear explicitly in the formula of y_Σ . The sigma method kinematics is thus less biased by radiative effects (ISR). This is its main advantage with respect to the electron method. On the other hand, this method does not allow for a reliable kinematic measurement in the interesting high y (low x -low Q^2) region, where the hadronic final state is emitted mostly in the direction of the BEMC (see Fig 4.3-b), which is a purely electromagnetic calorimeter. The hadron measurement is thus poor, which introduces a large uncertainty on y_Σ .

One can formulate the sigma method resolution in terms of the electron method resolution quoted above. This allows for an easy comparison between them (in particular in the low Q^2 region $\theta_e \rightarrow \pi$):

$$\frac{\delta y_\Sigma}{y_\Sigma} \Big|_E = y_e \frac{\delta y_e}{y_e} \Big|_E, \quad (4.21)$$

$$\frac{\delta y_\Sigma}{y_\Sigma} \Big|_{\theta_e} = y_e \frac{\delta y_e}{y_e} \Big|_{\theta_e}. \quad (4.22)$$

y_Σ is more precise than y_e by a $1/y$ factor at small y (high E_e).

For Q^2 :

$$\frac{\delta Q_\Sigma^2}{Q_\Sigma^2} \Big|_E = 2 \frac{\delta Q_e^2}{Q_e^2} \Big|_E, \quad (4.23)$$

$$\lim_{\theta_e \rightarrow \pi} \frac{\delta Q_\Sigma^2}{Q_\Sigma^2} \Big|_{\theta_e} = (1 - y_e) \frac{\delta Q_e^2}{Q_e^2} \Big|_{\theta_e}, \quad (4.24)$$

The sigma resolution is in general worse by a factor two than the electron method resolution, except at high y ($y \rightarrow 1$) where the rising θ_e dependent resolution term for $\theta_e \rightarrow \pi$ is suppressed by the $(1 - y)$ factor.

For x :

$$\frac{\delta x_\Sigma}{x_\Sigma} \Big|_E = (2 - y_e) y_e \frac{\delta x_e}{x_e} \Big|_E, \quad (4.25)$$

$$\lim_{\theta_e \rightarrow \pi} \frac{\delta x_\Sigma}{x_\Sigma} \Big|_{\theta_e} = \frac{1 + y_e}{1 - y_e} y_e \frac{\delta x_e}{x_e} \Big|_{\theta_e}, \quad (4.26)$$

In the sigma method the x -resolution is improved by a factor y_e , compared to the factor $1/y_e$ for the electron method, and is therefore significantly better than the electron method at low y .

and then

$$\sum_{total} (E - p_z) = (xE_p + E_e) - (xE_p - E_e) = 2E_e. \quad (4.18)$$

Double angle kinematics

For the double angle method the formulae are:

$$y_{DA} = \frac{\tan \frac{\theta_h}{2}}{\tan \frac{\theta_e}{2} + \tan \frac{\theta_h}{2}} \quad Q^2_{DA} = 4E_e^2 \frac{\cot \frac{\theta_e}{2}}{\tan \frac{\theta_e}{2} + \tan \frac{\theta_h}{2}} \quad (4.27)$$

The method is rather insensitive to the energy response of the detector and used for the energy calibration purposes in the present thesis. The iso-angle (θ_h) and iso-energy (E_h) lines of the current jet in the (x, Q^2) plane are shown on Fig 4.3-b.

4.3 Event samples

Several data samples were taken by the H1 detector in 1994 (see chapter 2 table 2.3). A convenient combination of these samples insures a maximal coverage of the kinematic plane for the F_2 measurement. The event distribution in the (x, Q^2) plane is shown in Fig 4.4. The interaction vertices of the majority of the events are centred around $z \sim 3$ cm; in what follows they constituted the “nominal vertex” sample (shown as regions B,C and D in Fig 4.4). The corresponding integrated luminosity is 2.2 pb^{-1} ($\sim 150\,000$ events satisfying the DIS selection). Throughout this thesis, the low (high) Q^2 sample refers to events with the scattered electron detected in the BEMC (LAC calorimeter - zone D in Fig 4.4). For the low Q^2 kinematic region studied here, the nominal vertex sample is further subdivided into the “open triangle” data sample (B - $\mathcal{L} = 0.27 \text{ pb}^{-1}$) with the innermost BEMC stacks of triangular shape included in the trigger (see section 3.4.1) and the “closed triangle” sample (C - $\mathcal{L} = 1.93 \text{ pb}^{-1}$) with the innermost BEMC stacks excluded from the trigger. The shifted vertex ($\mathcal{L} = 58 \text{ nb}^{-1}$) and satellite bunch ($\mathcal{L} = 68 \text{ nb}^{-1}$) data samples (A; $\sim 15\,000$ events) increase the covered kinematic region towards small Q^2 . Finally, a sample of DIS radiative events was extracted with a hard photon ($E_\gamma \geq 4 \text{ GeV}$) emitted collinear with the incident e -beam, representing $\sim 2\%$ of all DIS events. Due to the reduced incident e -beam energy, this sample allows access to very low Q^2 values. The radiative sample is not shown on Fig 4.4 and will not be discussed here. For more details see [8].

We briefly discuss here the main background sources, because they will impose constraints on the event selection, which is presented in the rest of this chapter. The background estimates are presented in chapter 7.

4.3.1 Backgrounds

An important limitation in the exploration of the low Q^2 sample at high y (low E'_e - see Fig 4.3-a) results from the *background* contamination (on Fig 4.4 only the kinematic region with $y \leq 0.6$ is covered, corresponding approximately to $E'_e \geq 11 \text{ GeV}$).

Two major sources of background are:

- Quasi real *photoproduction* ($Q^2 \sim 0$) in ep interactions. In this process, the electron disappears in the beampipe, because $Q^2 \sim 0$ and $\theta_e \sim 180^\circ$. Secondaries from γp

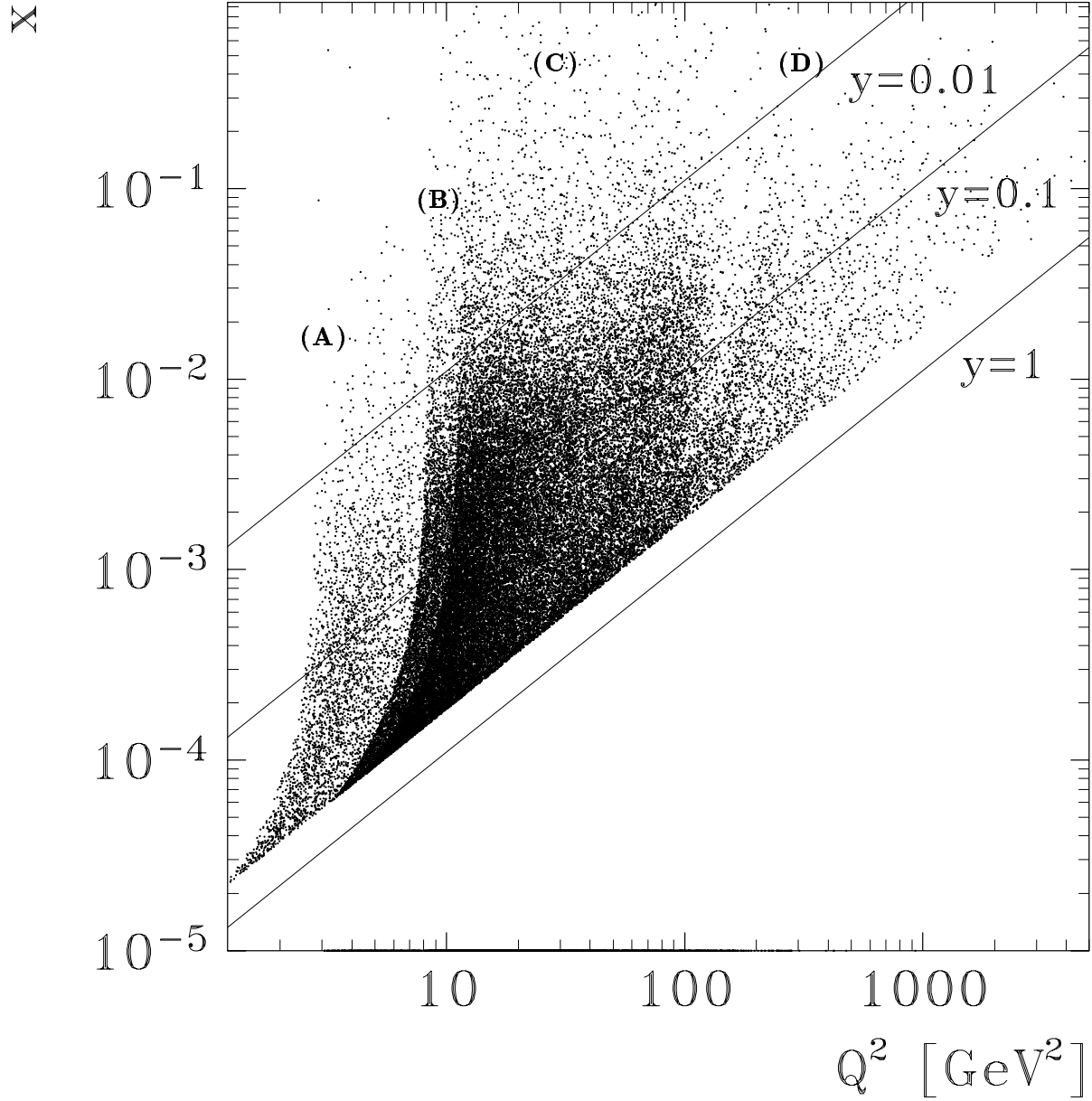


Figure 4.4: *Distribution of the event sample in the (x, Q^2) plane. The four visible regions (A,B,C,D) are A) the shifted vertex-satellite data samples; B-C) the nominal vertex interactions with the electron detected in the BEMC, subdivided into B) the “open triangle” sample, with the innermost BEMC stacks of triangular shape included in the trigger (see section 3.4.1) and C) the “closed triangle” sample, with the innermost BEMC stacks excluded from the trigger; D) high Q^2 events with the scattered electron detected in the LAC calorimeter. Only events from A,B,C are considered in the present thesis (from [8]).*

processes can deposite energy in the BEMC, faking an electron⁷ and leading to an over-estimate of Q^2 . The probability of a significant energy deposition in the BEMC is small⁸ but due to the high cross-section of this process with respect to the DIS cross-section, there is still significant contamination in the DIS event sample for $E'_e \leq 11\text{GeV}$.

- Non- ep background, caused by particles leaving the beam and interacting with the beam line elements (“beam-wall” interactions), or due to beam interactions with the residual gas (“beam-gas” interactions) or due to cosmic ray interactions in the detector.

As will be seen, both photoproduction and non- ep backgrounds increase strongly at low scattered electron (candidate) energies. They thus accumulate in the DIS kinematic (x, Q^2) plane in the high y region (see Fig 4.5), hardly accessible for the DIS analysis.

Photoproduction

The photoproduction is conveniently separated into a “soft” and a “hard” component. The dominant soft processes involve no large momentum transfer and can not be calculated in the framework of perturbative QCD. On the other hand, jet production is well described by perturbative QCD calculations (point-like or hard process) [38].

The total scattering cross-section is effectively parameterised and the following processes and Born graph cross-sections are distinguished:

- Resolved photon interaction, i.e. the photon fluctuates into a $q\bar{q}$ pair which interacts hadronically. This contribution is split into:
 - a soft component (Fig 4.6-c), which is commonly described in terms of the vector dominance model (VDM). In this picture, the photon couples to a vector meson V , ($V=\rho, \omega, \phi$), which interacts with the proton in a non-perturbative way ($\sigma_{VDM}^{\gamma p}$);
 - a hard component (Fig 4.6-d - $\sigma_{hard}^{\gamma p}$).
- Direct photon interaction, i.e. the photon participates directly in the scattering process. The two Born graphs for direct interactions are presented in Fig 4.6-a, b.

⁷As we will see later, the electron identification is based on the energy deposition in the BEMC together with a tracker signal (hit) in the BPC chamber. A $\gamma\pi^\pm$ overlap, for example, can fake an electron: the photon causes an electromagnetic energy deposit in the BEMC, while the charged pion is detected by the BPC.

⁸Energy conservation implies:

$$E_e + xE_p = E'_e + \sum E_j \quad (4.28)$$

For $x \leq 10^{-3}$ ($\theta_j \geq 156^\circ$) and hence for $xE_p \leq 1\text{ GeV}$, the current jet is detected in the BEMC and the total energy in the backward region is:

$$E'_e + xE_p \approx 27.6\text{ GeV}. \quad (4.29)$$

Since the quark energy is distributed among all the particles of the current jet, it is unlikely that one of these particles carries a substantial amount of the total energy. The misidentification probability is small above 6 GeV and it becomes negligible above 11 GeV.

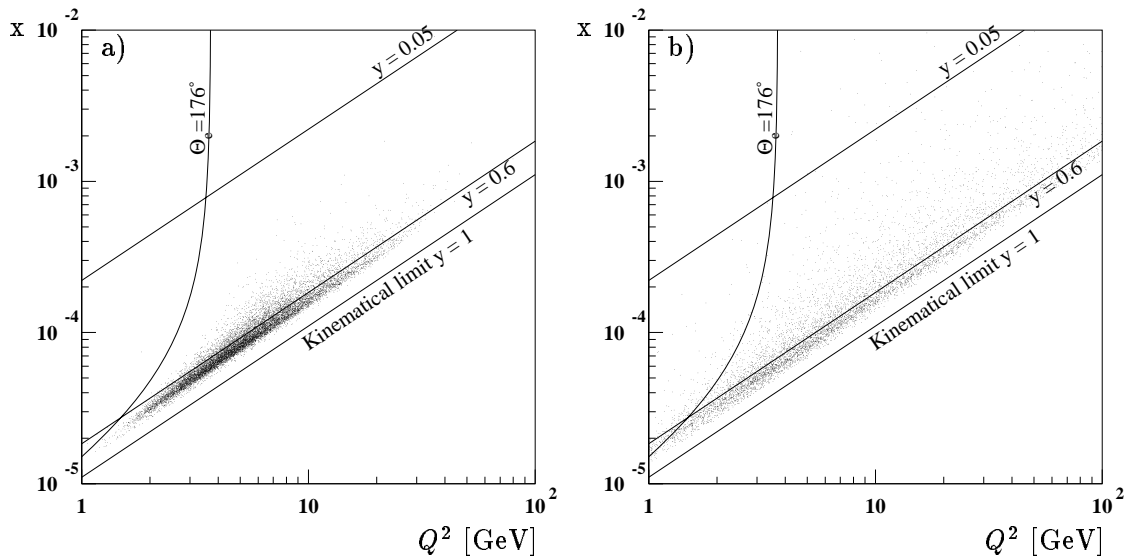


Figure 4.5: Accumulation of the background events in the (x, Q^2) plane in the high y region (low electron candidate energies) for the a) photoproduction background (Monte Carlo simulation) and b) non- ep background (pilot bunches).

The kinematics is computed from the “electron” variables. Due to the minimum energy requirement for the DIS trigger the region close to $y = 1$ is empty.

The total photoproduction cross section can be written as:

$$\sigma_{tot}^{\gamma p} = \sigma_{dir}^{\gamma p} + \sigma_{VDM}^{\gamma p} + \sigma_{hard}^{\gamma p}. \quad (4.30)$$

The photoproduction background contamination to DIS is estimated using a Monte Carlo simulation based on the PHOJET event generator. It includes both soft and hard mechanisms and allows for a continuous transition between them. Multiple (several photons exchanged) soft and hard interactions are included. More details on the ideas and methods used in the program PHOJET can be found in ref. [39].

The photoproduction background can also be estimated directly from the data: for a small fraction of the photoproduction events the electron can be detected in the electron tagger, allowing the measurement of the true event kinematics.

Non- ep background

The rate of non- ep interactions is much higher than the rate of DIS events, but an efficient reduction is provided already by the H1 trigger system, and further reduction is obtained during the DIS selection (see section 4.4.2). The residual background can be estimated by means of unpaired non-colliding particle bunches⁹ (“pilot bunches”). Since pilot bunches have no matching bunch to collide with, they can interact only with residual beam gas or beam line elements.

⁹By “bunches” we understand here packets of particles (electrons or protons) spaced in HERA by 96 ns. The word “bunch” has thus a different meaning here than in case of the satellite bunch (see section 2.2).

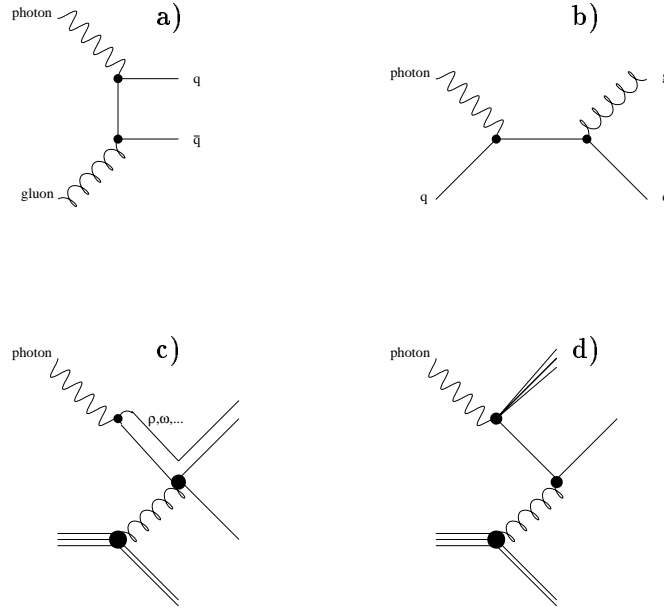


Figure 4.6: “Soft” (c) and “hard” (a, b, d) photoproduction processes.

Direct photon interactions: a) Photon-gluon fusion and b) QCD Compton scattering; the photon interacts with a $q\bar{q}$ pair in a pointlike way.

Resolved photon interactions: c) VDM interaction and d) hard component of the photon; the photon fluctuates into a $q\bar{q}$ pair which interacts hadronically.

The non-beam related background (as for example that due to cosmic ray interactions) can be estimated using the rate of interactions occurring in the empty (no beam) bunches¹⁰.

The total amount of non- ep background events for the ep -collision data sample is estimated as (see also expression 4.1):

$$N_{bg} = N_{p-pilot} \times \frac{n_{colliding}}{n_{p-pilot}} + N_{e-pilot} \times \frac{n_{colliding}}{n_{e-pilot}} + N_{empty} \times \frac{n_{colliding}}{n_{empty}}, \quad (4.31)$$

where $N_{p-pilot}$, $N_{e-pilot}$, N_{empty} are respectively the number of proton-pilot, electron-pilot and empty bunch events occurring in the final DIS event sample. $n_{p-pilot}$, $n_{e-pilot}$, n_{empty} and $n_{colliding}$ are respectively the number of proton-pilot, electron-pilot, empty and colliding bunches in the HERA beam. In 1994 the ratios $n_{colliding}/n_{pilot}$ were 9.0, 10.2 and 4.4 with a 1% precision for respectively p -pilot, e -pilot and empty bunches.¹¹

¹⁰ A bunch is considered *empty* if $I_e \leq 2\mu\text{A}$ and $I_p \leq 4\mu\text{A}$. Typical values of the bunch currents in 1994 were: $I_e = 90\mu\text{A}$ and $I_p = 240\mu\text{A}$. The total beam current is obtained by multiplying bunch currents by the number of bunches of corresponding type.

¹¹ A different interpretation of the pilot bunch background subtraction was given in [41]. According to this analysis, the e -pilots contain mostly “empty” events and, therefore, the “empty” event subtraction is included in the e -pilot (but also in the p -pilot) subtraction. A regression was performed on the data leading to the following values of $n_{colliding}/n_{pilot}$: 11.2, 11.3 and 0.0 for respectively p -pilot, e -pilot and empty bunch weights. Motivations and details can be found in ref. [41].

We’ll stick to the background subtraction according to (4.31). The difference between the two methods is irrelevant in view of present statistics.

4.4 DIS event selection

In the kinematic range studied in this thesis ($1.5 \leq Q^2 \leq 120 \text{ GeV}^2$) the scattered electron is detected in the backward calorimeter BEMC. We discuss here the electron identification, the background rejection and the run selection. Fiducial volume restrictions will be discussed later in chapter 6 in parallel to detector-related studies.

4.4.1 Electron identification

The electron is basically identified as the highest energy cluster in the BEMC (or in the LAC calorimeter for high Q^2 DIS selection) and the task is essentially completed by the BSET subtrigger which requires a minimum energy of 7.7 GeV (CL2) deposited in a BEMC cluster (see section 3.4.1). The leading energy cluster must satisfy some extra criteria, aiming to insure a good kinematic measurement (θ_e and E'_e for the electron method kinematics and in addition a good hadronic final state measurement for the sigma kinematic reconstruction method). All these criteria allow in addition for a significant background reduction, complemented by some pure background rejection cuts (see next section).

The basic criteria allowing identification of electrons scattered in the BEMC are:

1. *The scattered electron candidate is identified as the leading energy cluster in the BEMC with $E'_e \geq 11 \text{ GeV}$.*

This value is fixed as a compromise between the loss of statistics and background contamination, which strongly increases for lower electron candidate energies.

The 11 GeV value is well above the BSET trigger threshold (7.7 GeV for CL2) which avoids correcting the data for trigger efficiency effects.

2. *The vertex is reconstructed within $\pm 30 \text{ cm}$ in z ¹² ($\pm 20 \text{ cm}$ for the satellite bunch data¹³) around the average ep interaction position.*

The later is $z \approx +3 \text{ cm}$ for the nominal vertex data sample and $z \approx +67 \text{ cm}$ for the shifted vertex data sample ($z \approx +69 \text{ cm}$ for the satellite bunch sample). This value varies within a few cm due to slightly different HERA injection conditions.

¹²The interaction vertex is reconstructed by fitting reconstructed central (CJC-CIZ-COZ) and/or forward tracks to a common vertex. The transverse size (x, y -coordinates) of the interaction region is small (of the order of $0.5 \times 0.5 \text{ mm}^2$, see table 2.1) and permanently monitored by HERA. Events with a $x - y$ vertex outside the beams are considered *de facto* as background events and a $x - y$ vertex position cut is therefore applied at the reconstruction level. In practice, vertex reconstruction is performed using any tracks which sufficiently approach the beam direction on the $x - y$ plane. Non- ep background events occurring outside the beam can accidentally have one or more tracks satisfying this condition, thus defining a reconstructed vertex. Such vertices are randomly distributed in z .

The situation is different for the z -vertex position. The CJC chambers provide a high precision measurement in the $x - y$ transverse plane and a poor z -measurement, eventually improved by the CIZ-COZ chambers measurement. Furthermore, the length of the interaction region was $\sim 60 \text{ cm}$ along the z -axis in 1994, mainly due to the p -beam size. Therefore, the reconstruction program does not restrict the z -vertex position of the interaction.

¹³The level of the non- ep background contamination is significantly higher for the satellite bunch selection. A $\pm 20 \text{ cm}$ z -vertex cut allows for reducing the background contamination by $\approx 33\%$ with respect to a $\pm 30 \text{ cm}$ z -vertex cut, while for genuine DIS events it corresponds to a $2\sigma_z$ cut compared to a $3\sigma_z$ cut, leading to difference of $\approx 4\%$ of the events.

The average z -vertex position is available on a run-dependent basis from the H1 permanent data base [24] (see Table 7.1).

The vertex requirement suppresses most of the non- ep background, which has a small probability to originate from the interaction region (see next section). On the other hand, it insures a good θ -angle measurement of the scattered electron and of the hadronic final state, necessary for a reliable kinematic determination.

3. A BPC signal (hit) is associated to the electron candidate cluster, and the smallest distance from the closest BPC hit to the centroid of the electron cluster $EBPC \leq 5$ cm.

This criterion insures good θ_e reconstruction, determined by two points of the electron trajectory: the interaction vertex and the impact point in the BPC. It helps also to reject both photoproduction and non- ep background (see next section).

4.4.2 Background rejection

In 1994 the rate of genuine DIS events was less than 0.5 Hz compared to a $\times 1000$ higher non- ep background rate before the L1 trigger and to a $\times 20$ rate of the dominant physics process of photoproduction interactions. Triggers based on informations provided by the BToF detector, $x - y$ vertex position (see footnote 12), multiwire proportional chambers, fast calorimetric trigger, etc., efficiently reduce background contamination, so that the rate of events sent to the data storage media is ≤ 5 Hz.

At the DIS selection level, background contamination is significantly reduced by the requirement of minimum $E'_e \geq 11$ GeV, roughly restricting the selected kinematic region to $y \leq 0.6$.

The non- ep background is further effectively reduced by requiring the interaction vertex to lie within a limited region in z . z -vertex distributions of DIS and non- ep background events are shown on Fig 4.7-*a*, respectively as a solid line and a shaded histogram (arbitrary normalisation). As expected, the latter is almost not correlated¹⁴ with the real ep -interaction region around $z \sim 0$. Fig 4.7-*b* illustrates the effect of the vertex cut on the electron candidate energy distribution. The solid line corresponds to all events with a reconstructed vertex, while the shaded histogram corresponds to events with a reconstructed vertex lying within ± 30 cm around the interaction point (IP). An energy distribution of the non- ep background events is shown on the same figure as the dashed histogram.

The EBPC and ECRA estimator

Two estimators are used to reject photoproduction and non- ep background events: the smallest distance from the closest BPC hit to the centroid of the electron cluster, EBPC, and the cluster radius, ECRA.

For the BEMC cluster k , the centre of gravity is defined as:

$$x_{cog}^k = \frac{1}{E_{cluster}} \sum_{i=1}^n E_i x_i^k, \quad (4.32)$$

¹⁴The residual correlation is a feature of the vertex reconstruction algorithm, which first attempts to reconstruct a vertex in the ep -beam interaction region.

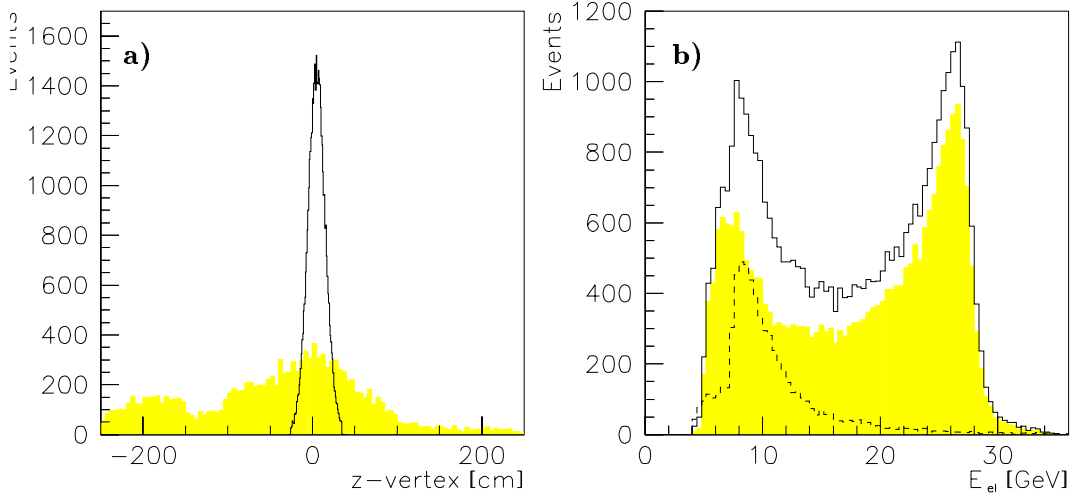


Figure 4.7: *Background reduction by the z-vertex requirement: a) z-vertex distribution of the DIS events with $-25.0 \leq z \leq 30$ cm (solid line) and of the non-ep background events (shaded histogram, arbitrary normalisation). b) Energy distribution of the selected DIS candidates: solid histogram: all DIS candidates with a reconstructed vertex, shaded histogram: DIS candidates with $-25 \leq z \leq 30$ cm; dashed line: non-ep background events.*

$$y_{cog}^k = \frac{1}{E_{cluster}} \sum_{i=1}^n E_i y_i^k, \quad (4.33)$$

where E_i is the energy collected in stack i and x_i^k, y_i^k are the x,y coordinates of stack i energy deposition centroid determined from the wave length shifter WLS readout (see section 3.2.1). The sum runs over the n stacks ($n \leq 9$) belonging to cluster k .

The precision obtained for the centre of gravity reconstruction is $\sigma_{x,y} = 0.7$ cm. A better precision for the measurement of the scattered electron angle θ_e can be obtained by using the impact point (hit) of the scattered electron in the BPC chamber, situated right in front of the BEMC.

The electron cluster-associated BPC hit identification is not always straightforward since an important fraction of events has preshowering of the scattered electron in the dead materials (mainly cables) between CJC and BPC. Several distinct hits are observed for such events in front of the electron candidate cluster. The hit closest to the electron cluster centroid is considered as the electron impact point into BPC (parallax effects being taken into account). The distance (in the BPC plane) between the position of this hit and the position of the cluster centroid defines the estimator EBPC.

The requirement $EBPC \leq 5.0$ cm has a twofold aim: to insure a good angle θ_e measurement and to reject background events. Fig 4.8-a shows the EBPC estimator distributions for a clean DIS sample (solid line, $E_e' \geq 11$ GeV), for a photoproduction background sample (shaded histogram - Monte Carlo simulation, $E_e' \geq 5$ GeV) and for non-ep background events (dashed line - pilot bunches, $E_e' \geq 5$ GeV). The relative normalisation is arbitrary.

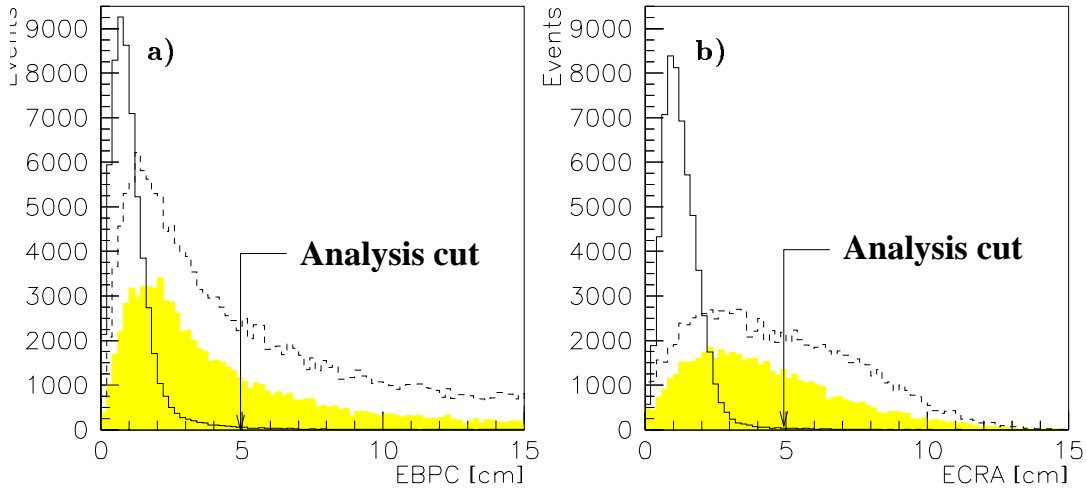


Figure 4.8: *a) EBPC and b) ECRA estimator distributions for the DIS event sample ($E_e' \geq 11$ GeV, solid line), for photoproduction background events (shaded histogram - Monte Carlo simulation, $E_e' \geq 5$ GeV) and for non-ep background events (dashed line - pilot bunches, $E_e' \geq 5$ GeV). The normalisation is arbitrary. This analysis cut is indicated.*

The energy-weighted cluster radius ECRA is defined as follows:

$$ECRA = \frac{1}{E_{cluster}} \sum_{i=1}^n E_i \times |r_i - r_{cluster}|, \quad (4.34)$$

where $r_{cluster}$ is the cluster centroid radius with respect to the coordinate origin, r_i is the centroid radius of the stack i energy deposition and E_i is stack i energy deposition. The distribution of the ECRA estimator is broader for clusters initiated by hadrons than by electromagnetic particles (see Fig 4.8-b). The requirement $ECRA \leq 5$ cm is safe for genuine DIS events and allows for additional background rejection.

Vertex type

An interaction vertex can be fitted from central tracks alone, from a combination of central and forward tracks or from forward tracks alone. The priority is always given to central tracks, due to the higher precision of their measurement and reconstruction compared to forward tracks.

The fraction of events with an interaction vertex fitted from forward tracks alone (forward vertex) is small, but increases strongly towards low- y (the so-called “kinematic peak”). Here, the current jet is emitted in the forward direction, leaving few or no tracks in the central tracker. It is interesting to include “forward vertex” events in the analysed DIS sample in order to increase the global vertex finding efficiency for the low- y region. However, this forward vertex sample contains a substantial amount of non-ep background events, as a direct consequence of the lower precision of the forward vertex fit¹⁵.

¹⁵Background events are usually characterised by a high track density (interactions on nuclei). The

An offline algorithm has been developed [45] providing the fraction of “good” forward tracks¹⁶ used in the vertex fit, compared to the total number of reconstructed forward tracks. A distribution of the thus defined quantity is presented on Fig 4.9-*a* for the DIS event selection (solid line) and for non-*ep* background events (shaded histogram). It clearly appears that background events have in general a smaller fraction of good vertex-fitted tracks, in agreement with the previously presented hypothesis (see footnote 15). A forward vertex event is therefore accepted if and only if the fraction of vertex-fitted tracks is greater than 0.4 ($ff \geq 0.4$)¹⁷.

Fig 4.9-*b* shows the corresponding z -vertex distributions: the shaded histogram is the z -vertex distribution for events with $ff < 0.4$ and the dashed line is for events with $ff \geq 0.4$. The latter clearly appear as dominantly composed of background events with a randomly reconstructed vertex. For comparison, the central z -vertex distribution (i.e. events satisfying the same selection criteria, except that a central vertex is required instead of a forward vertex) is shown on the same figure as the solid line. It should be noted that the width of the forward vertex distribution is increased with respect to the central vertex due to a less precise vertex fit: the latter is extrapolated over more than 1.5 m distance.

The distribution of the z -vertex fit error is shown on Fig 4.9-*c* for the central vertex fit as the solid line and for the forward vertex fit as the shaded histogram. Note that the scale is logarithmic and that the central vertex distribution is peaking at small values ($\delta z \leq 1.0$ cm), which correspond to events where it was possible to link track segments in CJC with those in CIZ and in COZ. The corresponding distribution is much broader for forward vertices.

The situation appears different for the shifted vertex data. First, the forward vertex fit is more precise since the interaction point is almost half closer along the z -axis to the forward tracker than in the nominal interaction point case. Second, the importance of the forward vertex is increased, emphasised by a globally less efficient central vertex due to the decreased acceptance of the central tracker to the current jet. The z -vertex distributions for central and forward vertices in case of the shifted vertex data are shown on Fig 4.9-*d* respectively as the solid line and the shaded histogram. The normalisation is absolute and the same criteria were used to select the event sample as on Fig 4.9-*b* for nominal interaction point data.

Concerning the use of the forward vertex, another point must be mentioned in addition to a substantial increase of the global vertex efficiency at low- y both for shifted and nominal vertex data samples. The aim of the SV data analysis is to increase the kinematic acceptance towards low Q^2 , low x . In this domain, the quark fragmentation is not measured yet, and it is possible that the vertex reconstruction efficiency, as described by the Monte Carlo simulation, is not correct. In this case, corrections based on Monte Carlo

probability of finding a forward track crossing the beam-axis in the $x - y$ plane and thus giving rise to a reconstructed z -vertex is high compared to the central tracker, due to the low $x - y$ measurement precision of the former. See also footnote 12.

¹⁶A “good” track is defined as one with at least one primary or secondary planar segment and with a planar segment in one of the first two supermodules [45].

¹⁷Another way to treat forward vertex events was proposed in ref. [41]. According to this study, forward vertex events increase the non-*ep* background contamination only in high- y region (low scattered electron energy). At low- y , the background is naturally suppressed by the minimum scattered electron energy requirement. On the other hand, it is at low- y that the use of the forward tracker increases substantially the global vertex efficiency. The forward vertex events are therefore accepted only for $y \leq 0.2$.

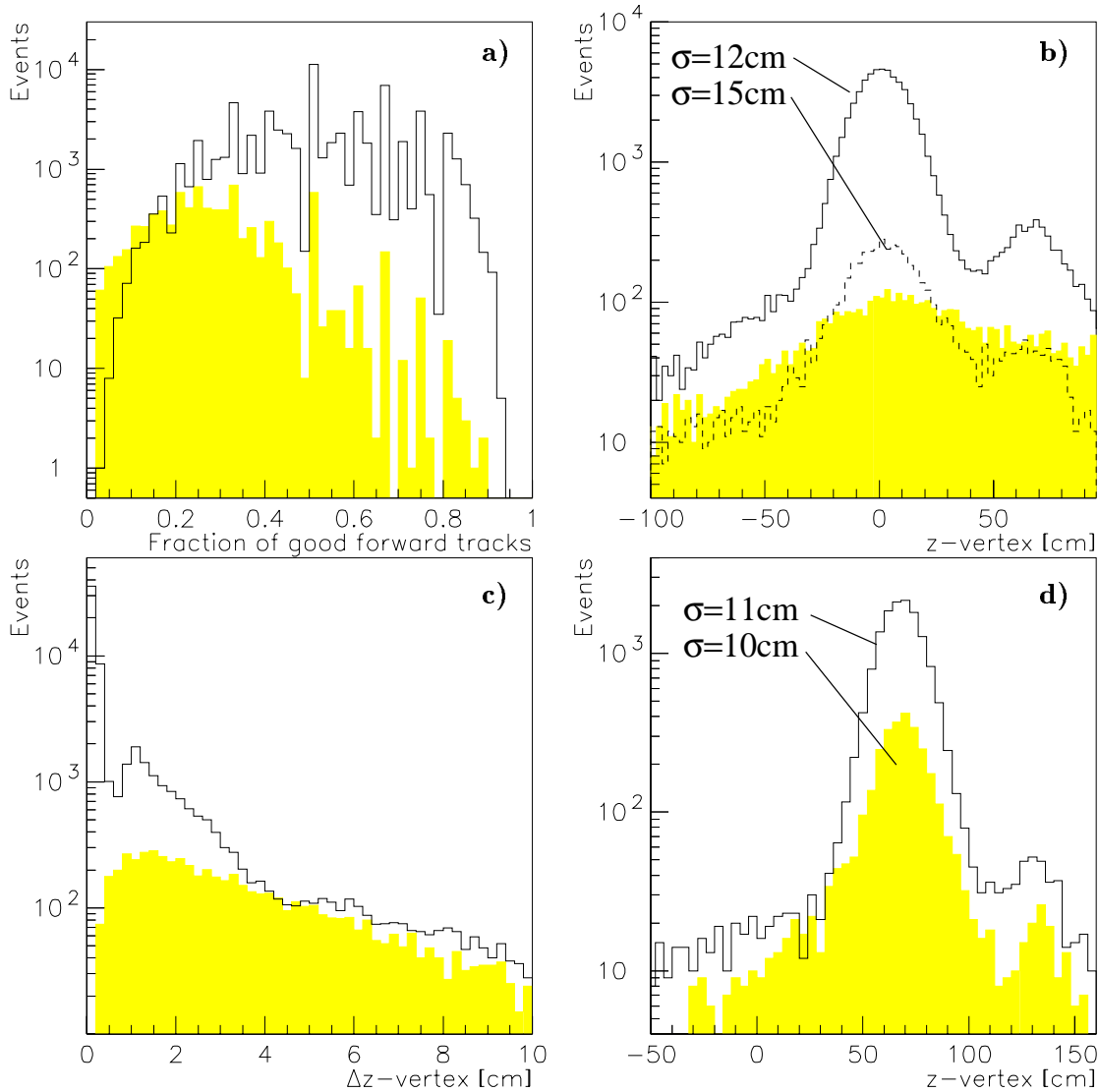


Figure 4.9: *a)* Fraction of good forward tracks used in the vertex fit: solid line: DIS event pre-selection; shaded histogram: non-ep background events (arbitrary normalisation). *b)* z-vertex distribution: solid line: central vertex distribution; shaded histogram: forward vertex distribution for events rejected by the "forward fraction" selection (see text), dashed line: events accepted by this selection (absolute normalisation). The indicated values of half-width are obtained by performing a Gaussian fit to the central part of the corresponding distributions. *c)* z-vertex fit error distribution: solid line: central vertex; shaded histogram: forward vertex. *d)* z-vertex distribution for the shifted vertex data sample: solid line: central vertex; shaded histogram: forward vertex (absolute normalisation).

simulations for detector acceptance would be wrong. It is therefore interesting to keep the vertex finding efficiency as high as possible in order to reduce corrections and thus possible systematic effects due the quark fragmentation models used in the Monte Carlo simulations.

The following conclusions result from the above listed arguments:

- Forward tracker vertices can be used if the fraction of “good” forward tracks used in the vertex fit is greater than 0.4 ($ff \geq 0.4$);
- Forward vertices are in general less precise than central vertices (leading to important event migrations in the kinematic plane due to θ smearing) but its proportion remains relatively small for the nominal interaction point data, except at low- y (in the kinematic peak region, which is anyhow less interesting in view of the bad x resolution (see section 4.2)). Therefore, using forward vertices for the nominal interaction point data sample does not in general lead to substantial benefits;
- The situation is quite different for the shifted vertex data. The forward vertex reconstruction is more precise and the proportion of forward vertex events is high. Using forward vertices is thus recommended for the SV data sample;
- We do not use forward vertices in case of the satellite bunch data sample for the following reason: forward vertices are affected by a large uncertainty in the bulk of the nominal vertex data, from which satellite bunch events are selected. It can happen that a main bunch event is reconstructed in the satellite bunch region along the z -axis. Since the satellite bunch intensity is only $\sim 3\%$ of the main bunch intensity, such migrations represent an important source of background for the satellite bunch event sample. We reduce these migrations by excluding events with no central but only a forward reconstructed vertex. Similarly, we apply a cut on the vertex fit error (provided by the reconstruction software) for the satellite bunch event sample ($\delta z \leq 5$ cm).

“ZORRO” estimator

The “ZORRO” estimator is defined as the average z -coordinate at the closest approach to the beam-axis for long CJC tracks. It was developed [46] during the 1993 data analysis (see also [47]) and adapted to the 1994 data analysis, based on the DST data format¹⁸.

¹⁸DTNV tracks satisfying the following criteria are used:

- More than 16 CJC hits;
- No forward segments are linked;
- Track transverse momentum $P_t \geq 300$ MeV.

then

$$ZORRO = \frac{1}{n} \sum_{i=1}^n Z_0^i, \quad (4.35)$$

where Z_0^i is the z -coordinate for track i of the closest approach to the beam-axis.

If the thus defined ZORRO value lies outside the allowed interaction region (± 30 or ± 20 cm around the nominal interaction point), than a second iteration is done without the track with the most negative (positive) Z_0 , depending on the sign of ZORRO. Indeed, it can happen that the ZORRO estimator is biased by a track due for instance to a cosmic muon; the second iteration is intended to validate such an event.

A distribution of the ZORRO estimator for the SV data sample is shown on Fig 4.10-*a*

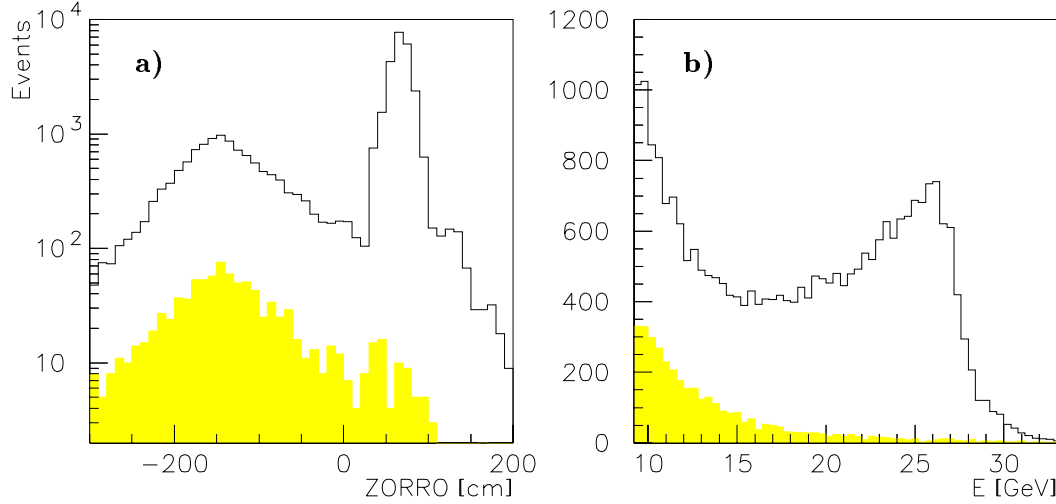


Figure 4.10: *a)* ZORRO estimator distributions for the shifted vertex event sample (solid line) and for non-*ep* background events (shaded histogram). *b)* Scattered electron energy distribution for SV events passing the vertex cut (solid line) and rejected by the $ZORRO \leq -40$ cm requirement (shaded histogram).

for all events (solid line) and for non-*ep* background events (shaded histogram). For the latter, the distribution peak is situated around $z = -150$ cm. This place is known as the position of *p*-beam “fixed target” collisions: a *p*-beam collimator is situated there, right below the BEMC, leading to an important rate of *p*-beam-collimator collisions. Some of these events, passing selection criteria including the vertex requirement, are found in the final DIS sample. A number of these events are efficiently identified by the ZORRO estimator, as can be seen on Fig 4.10-*a, b*. Fig 4.10-*b* presents the energy distribution for events passing the vertex requirement criterion (solid line) but rejected by $ZORRO \leq -40$ cm requirement (shaded histogram). The value -40 cm was chosen after a visual scanning, so that no good DIS event are lost. As expected, no kinematic peak is visible for the rejected events, confirming their non-DIS origin.

Single diode events background

These events are due to a invalid trigger caused by charged particles (beam-gas or beam-wall shower particles) or photons (synchrotron radiation photons) hitting directly one of the BEMC readout photodiodes (see page 47). Large energy deposition is then faked in the BEMC and if, by accident, this false trigger is validated by a reconstructed vertex and a BPC hit (both coming by accident from a non-*ep* background interaction occurring at the same time), the event is selected into the DIS event sample.

Most of these events are rejected already at the L1 level and further at the L4 level. However, a small fraction ($\sim 1\%$) appears in the DIS sample¹⁹, passing all selection criteria.

¹⁹The single diode events are not killed at the L1 or L4 level if one of the other three diodes of the same stack has an energy above 0.5 GeV, corresponding to approximately 4σ from the noise level. The probability to have noise fluctuations exceeding this limit is small but finite.

An offline procedure has been developed [40] and adapted to the DST data format, allowing the identification and proper treatment of these events. The treatment is based on the redundancy of information provided by the readout of the four long wave length shifters (WLS). Signals detected by the WLS depend on the impact point of the electron in the stack. However, each WLS contributes only a fraction (in average 0.25) to the total stack energy²⁰.

A single diode event is identified when an individual WLS contribution is greater than 0.8. For such events, the relevant WLS signal is set to the average deposited energy of the three other WLS.

Here is an example of a single diode event:

Run	Event	WLS-1	WLS-2	WLS-3	WLS-4	E_{stack}^{old}	E_{stack}^{new}
89929	1261	85.442	0.804	1.171	0.538	21.989	0.838

After setting the energy in WLS-1 from 85.442 GeV to 0.84 GeV, this event does not satisfy any more a minimum energy requirement and is therefore rejected.

4.4.3 Run selection

Run selection insures a uniform detector and stable background conditions for each data sample. It consists of the following requirements:

1. *Trigger phase 3 or 4.* There are four trigger phases corresponding to different sub-trigger (see section 3.4) prescaling factors²¹. For phases 1 and 2, most subtriggers are strongly prescaled. Phase 1 is set immediately after beam ramping end, when most H1 subdetectors are still not in operation. Phase 2 is set when the beams are still being tuned by the HERA crew, shortly after ramping end, to cope with high level false trigger rates due to beam-gas and beam-wall background interactions. Phases 3 and 4 are set for stable beam conditions. The difference between them is irrelevant for our purposes.
2. *Run quality: good or medium.* Each run is classified by the H1 shift crew as *good*, *medium* or *bad* depending on detector stability, i.e. the number of high voltage trips in the tracking detectors etc.
3. *High voltage status.* The fraction of time when the detector elements relevant for this analysis were in operation (nominal high voltage (HV) is supplied) is $\geq 80\%$. This criterion has a somewhat similar aim as the previous one. A low fraction of time with supplied nominal HV would mean that a given detector was unstable during this run. The following subdetectors are requested to have the nominal HV status:

²⁰The total stack energy is defined as an average over the four long WLS signals:

$$E_{stack} = \sum_{i=1}^4 WLS_i / 4. \quad (4.36)$$

²¹Prescaling means that only a fraction of events satisfying a given subtrigger condition is accepted. Prescaling factors are stored in the permanent data base.

BEMC, BPC, CIP, CIZ, CJC, LAC, ToF. The informations from all these detector elements were used during the event selection.

4. *BSET trigger status.* For some runs the background conditions were particularly bad and the BSET trigger (see section 3.4.1) was heavily prescaled to reduce the global dead-time of data taking. We do not consider these runs for the present analysis.
5. Only data collected during the e^+p collision period are used here.
6. *Events per luminosity unit.* Strict check of the run status is done based on the relative event yield study. Several runs are rejected (see next section).

4.4.4 Events per luminosity unit

The relative event yield (selected DIS events per nb^{-1} of integrated luminosity) is measured for each particular data sample for individual detector runs. Fig 4.11-*a* presents the yield for the closed triangle data sample after applying the run selection criteria 1 to 5 (see previous section). Only runs with more than 2 nb^{-1} are shown. The lower yield in the first period is due to classification problems at the L5 level. This period (all e^+p runs before run 84601), corresponding to a $\sim 8\%$ loss of luminosity, is not used in this analysis due to the impossibility of recovering missing events.

Several other runs were rejected due to known BSET trigger [44], detector or reconstruction [41] problems. Some of them are clearly visible and emphasised by a circle on the top figure.

The full list of rejected runs (after run 84601) is given in Appendix 1. Note that most of them are short and were rejected due to BSET trigger prescaling. Note also that the provided list includes bad quality and phase 1,2 runs, rejected anyhow in the run selection described previously.

Fig 4.11-*b* is obtained after rejecting all above mentioned runs. The remaining long-term structure (the yield slightly decreases around run number 60 and it increases again towards the end of data taking) is attributed to a slightly varying with time detector acceptance, due to varying along z nominal interaction position.

Fig 4.11-*c* illustrates the yield for short detector runs ($\mathcal{L} \leq 0.2 \text{ nb}^{-1}$). Most of these runs do not contain any DIS candidate. Since in general they correspond to unstable detector periods, one might suspect a different average yield. Short runs were grouped in bins of at least 1 nb^{-1} per bin in order to have a statistically significant measurement, and it clearly appears that the yield agrees with the long run yield.

Fig 4.12 illustrates yield measurements for the SV, open triangles and satellite bunch data samples. The latter was obtained by grouping the individual run luminosities in bins of at least 5 nb^{-1} (the average luminosity per run for the satellite bunch event sample is small and typically represents $\sim 3\%$ of the total run luminosity).

Note the different yield level for different data samples. It is due to increased Q^2 acceptances for the SV, satellite bunch and open triangles data samples.

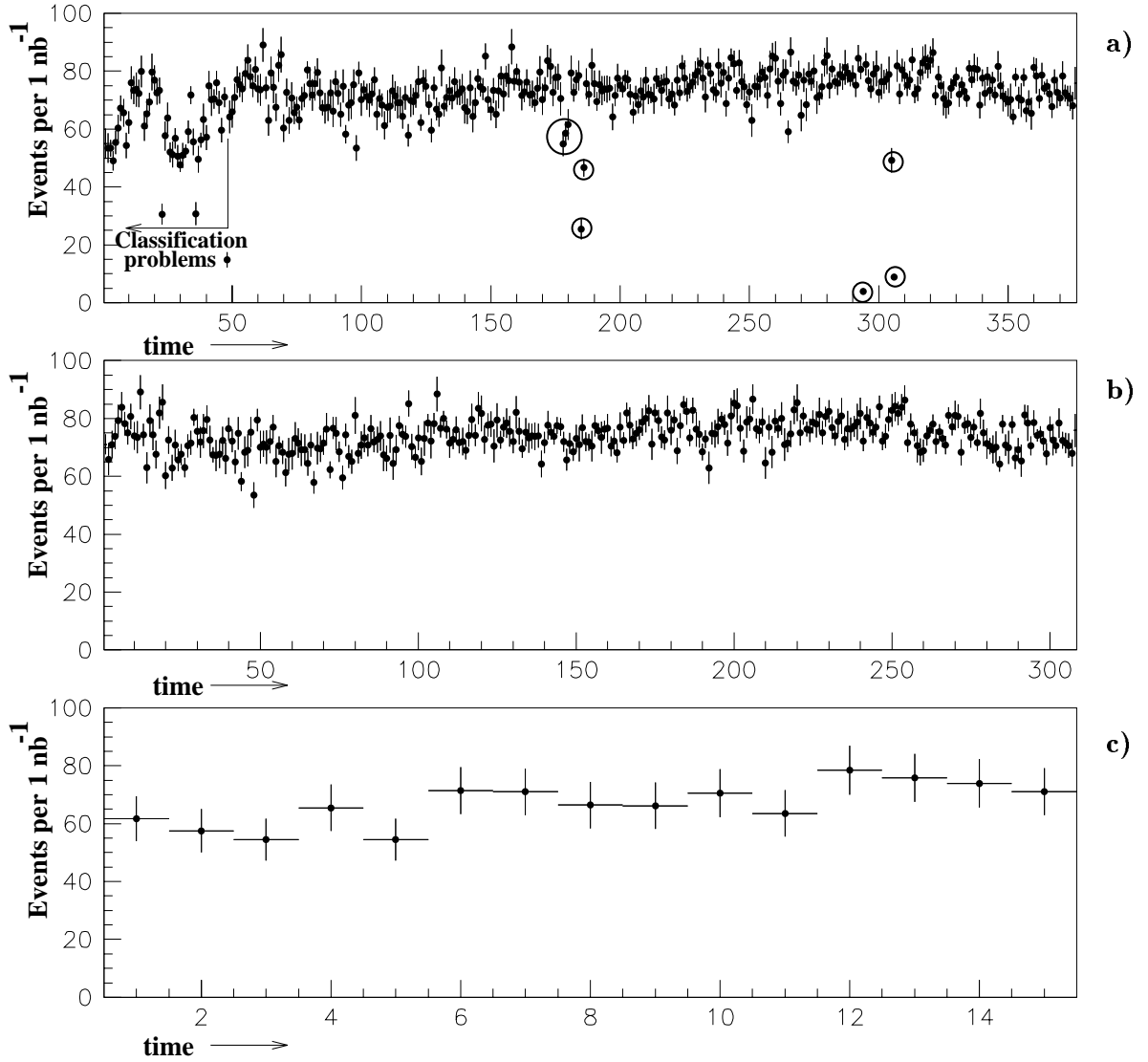


Figure 4.11: Yield of selected DIS events per nb^{-1} of integrated luminosity for the closed triangles data sample. Only runs with more than $2 nb^{-1}$ are shown: a) after applying the run selection criteria 1 to 5 (see text). The region indicated “classification problems” corresponds to a period with problems at the L5 level. b) after rejecting runs with a systematically low yield due to known trigger, detector or reconstruction problems (indicated by circles in a). c) yield for short runs ($\mathcal{L} \leq 0.2 nb^{-1}$) grouped in bins of $\geq 1 nb^{-1}$ of the integrated luminosity.

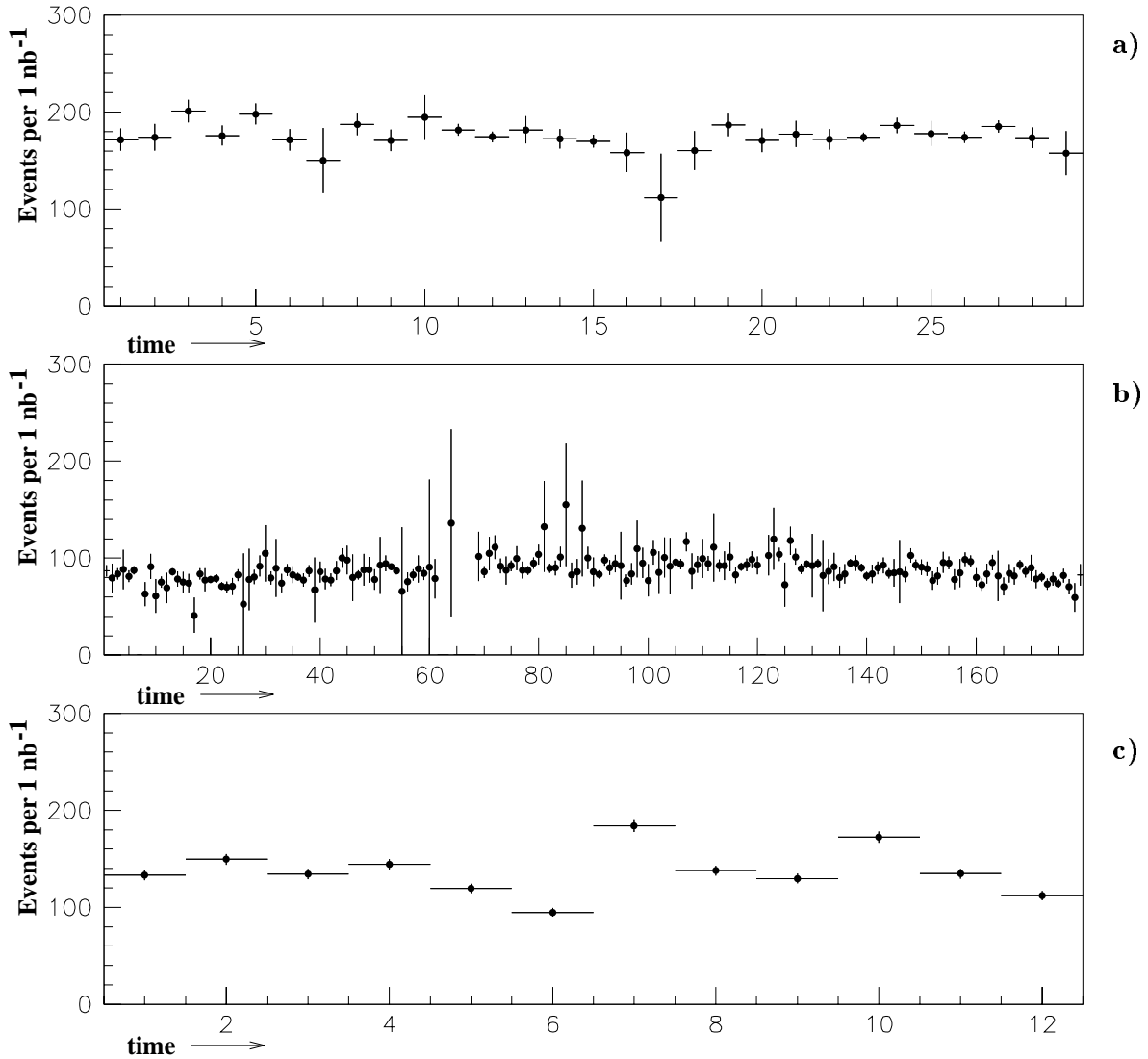


Figure 4.12: Yield of selected DIS events per nb^{-1} for: a) shifted vertex data sample; b) open triangles data sample; c) satellite bunch data sample. The individual run integrated luminosity being small (typically $\sim 3\%$ of the total run luminosity), individual runs were grouped in bins of $\geq 5 \text{ nb}^{-1}$ of the integrated luminosity per bin to produce a statistically significant measurement.

4.5 Summary

Run selection has been applied in order to obtain uniform data samples, with the following total integrated luminosities:

1. Closed triangle data sample: 1740 nb^{-1} , $\sim 130\,000$ events;
2. Open triangle data sample: 266 nb^{-1} , $\sim 20\,000$ events;
3. Shifted vertex data sample: 57.7 nb^{-1} , $\sim 8\,000$ events;
4. Satellite bunch data sample: 67.5 nb^{-1} , $\sim 7\,000$ events;

The following criteria are applied to select DIS candidate events:

1. Leading BEMC cluster energy $EBCFR$: ($11 \leq EBCFR \leq 32$) GeV;
2. Reconstructed vertex within ± 30 cm (± 20 for the satellite bunch sample) around the nominal interaction point;
3. Vertex type:
 - Closed triangle data sample: central vertex ($y \geq 0.2$) and central or forward vertex ($y \leq 0.2$), $\delta z \leq 6$ cm;
 - Open triangle data sample: idem;
 - Shifted vertex data sample: central vertex or forward vertex ($ff \geq 0.4$);
 - Satellite bunch data sample: central vertex, $\delta z \leq 5$ cm.
4. $EBPC \leq 5$ cm;
5. $ECRA \leq 5$ cm;
6. $ZORRO \geq -40$ cm for the SV and satellite bunch data samples and $ZORRO \geq -100$ cm for the nominal vertex data samples;
7. Events have to be explicitly triggered by the $BSET$ subtrigger for the closed triangle and satellite bunch data samples in order to exclude a few events with the electron scattered in one of the BEMC innermost stacks. Such events are in general not triggered by BSET but by a LAC or vertex subtrigger; they are excluded in order to avoid high corrections due to trigger inefficiencies in this region.

The remaining background contamination is estimated using the PHOJET Monte Carlo simulation as to the photoproduction background, and pilot bunches as to non- ep background events.

Chapter 5

Detector calibrations and resolutions

The studies presented here attempt to understand the systematics affecting the scattered electron energy, its angle and the hadronic final state measurements. These quantities are crucial for the precise measurement of the kinematic variables x and Q^2 and, ultimately, for the DIS cross-section and the F_2 structure function. When possible, their reconstruction is improved and the Monte Carlo simulation is tuned to data.

Effects of residual reconstruction and simulation miscalibrations are included in the systematic errors: first, discrepancies between data and Monte Carlo simulation are estimated; then, the estimated discrepancies are introduced artificially in the Monte Carlo simulation, producing a modified F_2 measurement. The ΔF_2 difference obtained in this way is taken as the systematic uncertainty to the F_2 measurement.

The following topics are studied here:

- Space point measurement in the BEMC;
- BEMC energy scale and crack corrections;
- Systematic effects affecting the θ_e measurement;
- y_Σ measurement and bias.

A detailed comparison with the standard H1 Monte Carlo simulation (H1SIM) will be shown as of here onwards.

5.1 Space point measurement in the BEMC

The main parameters of the BEMC were introduced in section 3.2.1.

The DIS event selection using the backward electromagnetic calorimeter BEMC (low Q^2) relies on the scattered electron energy and space point reconstruction. The latter is not used directly, but matched to a BPC signal (hit) of significantly higher space precision.

The aim of a precise cluster centroid reconstruction is to provide good matching with the BPC chamber for events with preshowering in cables in front of the BPC¹, which correspond to approximately half of the DIS event sample. The scattered electron impact point in the BPC is determined as the BPC hit closest to the cluster centroid projected onto the BPC plane (following a straight line between the cluster centroid and the event interaction vertex, i.e. parallax corrected). For events with no preshowering (Fig 5.1-a), the choice of the BPC hit is straightforward since it is unique. Several BPC hits

¹The amount of dead material the scattered electron encounters on its way to the BEMC, can be as large as one radiation length.

(sometimes up to 20), lying within a few centimetre spot, are reconstructed for events where preshowering has taken place (Fig 5.1-*b*).

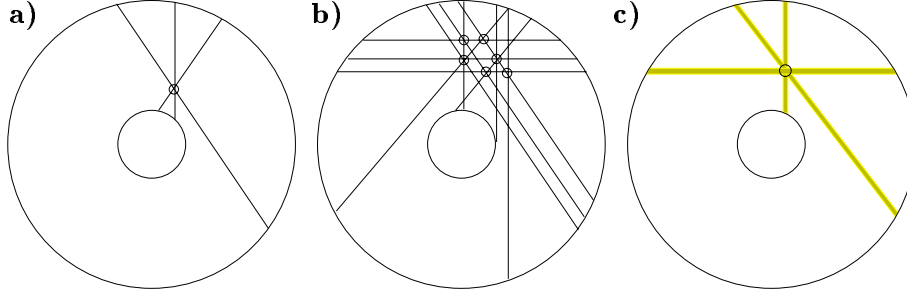


Figure 5.1: a) *BPC reconstruction in case of no preshowering: the hit is defined by crossing wires in at least three out of four BPC planes*; b) *BPC reconstruction when preshowering has taken place in front of it*; c) *if preshowering can not be resolved (when it is confined in a small solid angle), the BPC hit is defined by crossing bands of wires with detected signals*.

For events with no preshowering, the precision of space point reconstruction by the BPC is $\sigma \approx 2.0$ mm, compared to a mediocre $\sigma \geq 10.0$ mm for the BEMC. Such events can be used to study the cluster centroid reconstruction quality. For this, the additional requirement is imposed on the DIS sample, that only one BPC hit is reconstructed in front of the electron candidate cluster in the BEMC².

Fig 5.2-*a, b* (left column–data, right column–Monte Carlo simulation) shows the distribution of the quantity $y_{bpc} - y_{cog}$ versus y_{bpc} , where y_{cog} is the y -coordinate of the cluster centroid projection onto the BPC plane and y_{bpc} is the the y -coordinate of the associated BPC hit. Fig 5.2-*c, d* shows the result of a Gaussian fit to the quantity $y_{bpc} - y_{cog}$ in bands of 1.0 cm in y_{bpc} . A periodic structure is visible for both the data and the Monte Carlo simulation, and is more pronounced for data. In addition, Monte Carlo simulation presents a systematic slope. A similar slope is observed for the $x_{bpc} - x_{cog}$ distribution (not shown here) and is attributed to a bad parallax correction while projecting the cluster centroid onto the BPC plane. It can be removed by shifting the z -position of the cluster centroid by ≈ 1.4 cm towards the centre of the H1 detector (see Fig 5.2-*f*). This effect is interpreted as a bad simulation of the longitudinal extension of the electromagnetic shower in the BEMC³.

Both x - and y -coordinate structures repeat the periodic BEMC structure (with stack size is of 16×16 cm²). The bias in the cluster centroid position is correlated with the scattered electron impact point position in the stack. We did not try to understand in

²In fact, this requirement is only a partial guarantee of no preshowering. When preshowering is confined within a small solid angle, it is not resolved by the BPC chamber and the BPC hit is defined by crossing bands of wires composed of up to 10 wires with detected signals (Fig 5.1-*c*). However, these hits are easily identified by the large error affecting the position measurement, which is approximately half the width of the affected wire-band. An extra requirement of $\delta_{bpc} \leq 3$ mm is sufficient to exclude such events.

³The z -position of the scattered electron cluster is not measured in the BEMC. The shower depth is approximately parameterised with a logarithmic function of energy.

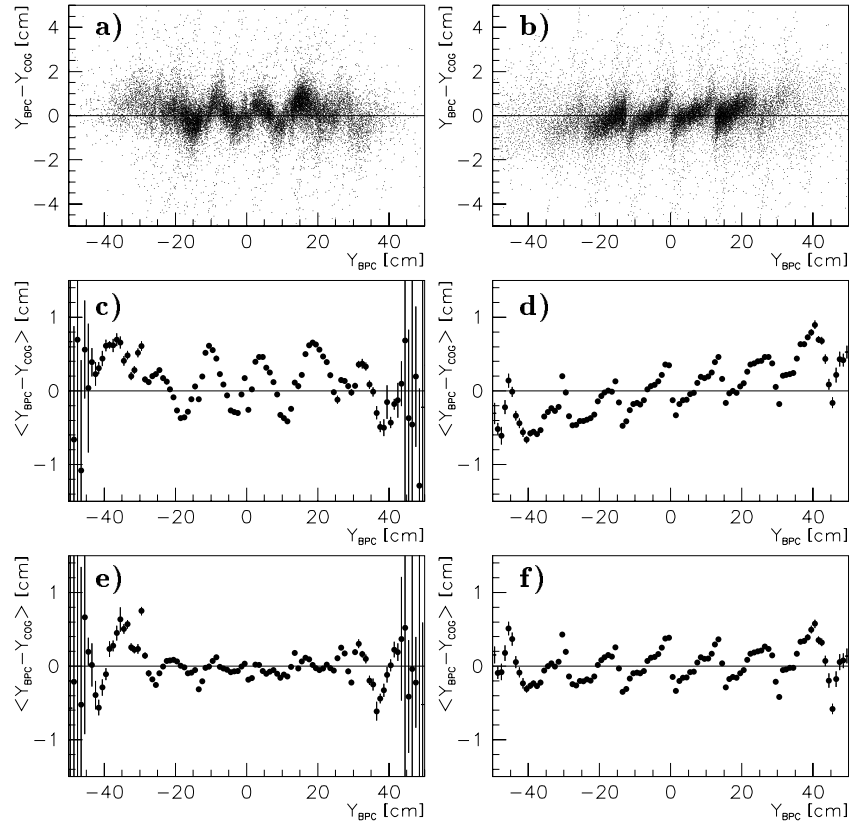


Figure 5.2: (a,b) Scatter plot (left column–data, right column–Monte Carlo simulation) and (c-f) mean value of a Gaussian fit to the quantity $y_{\text{BPC}} - y_{\text{COG}}$ versus y_{BPC} for DIS sample events with no preshowering: (c,d) before and (e,f) after applying detailed corrections to the cluster centroid position in the data (e) and shifting the z-position of the cluster centroid in the Monte Carlo simulation.

detail the origin of this phenomenon due to its irrelevance for the present analysis.

Corrections to x_{cog} and y_{cog} were defined in function of the impact position in the stack, divided in square cells of 1×1 cm². This cell-size corresponds approximately to the BEMC space point resolution. Detailed corrections are applied for $|x|, |y| \leq 32$ cm (first two quadratic stacks, where most of the statistics reside) to the data only⁴. The result is shown on Fig 5.2-*e* after applying the corrections for $y_{bpc} - y_{cog}$ versus y_{bpc} .

A small but significant improvement of the BEMC-BPC matching for events with preshowering is observed on Fig 5.3-*a* for the EBPC estimator distribution after applying the corrections (EBPC is the distance on the BPC plane between the cluster centroid and the closest BPC hit). A different BPC hit is selected for $\approx 8\%$ of events with preshowering.

A substantially better agreement between data and Monte Carlo simulation is observed after corrections for the distribution of the quantity $max_{x,y}$ (Fig 5.3-*b, c*), defined as the largest coordinate (in absolute value: $|x|$ or $|y|$) of the cluster centroid position. The remaining difference has limited impact on the kinematic reconstruction since the cluster centroid is not directly used for the θ_e polar angle measurement, but only through the choice of the associated BPC hit (see section 5.3.3).

5.2 BEMC energy scale and corrections

The precise knowledge of the BEMC energy scale and resolution is undoubtedly the most important source of systematic uncertainty to the F_2 measurement at low x and low Q^2 . As was introduced in section 3.2.1 (see also table 3.2), the primary BEMC energy calibration is performed using the kinematic peak method. The three relevant parameters, describing the quality of the BEMC energy reconstruction are resolution, linearity and geometrical uniformity of the energy response. Below, we will concentrate on the geometrical uniformity and particularly on the energy reconstruction in the crack region between the innermost triangular stacks and the first quadratic stacks (see Fig 3.3) since, as we will see later, the BEMC energy calibration undergoes there important fluctuations, poorly reproduced by the Monte Carlo.

The following topics are treated in this section:

- Basics of the double angle method, providing a scattered electron energy measurement independent of the BEMC reconstruction;
- Quality of the corrections to the BEMC energy deposition, accounting for energy loss in the cracks between BEMC stacks and for electron preshowering in cables between CJC and BEMC;
- Determination of new energy corrections, using the double angle method;
- Study of the BEMC energy resolution;
- Systematic error estimation.

⁴As we will see in section 5.3.3, the preshowering is not correctly reproduced by the Monte Carlo simulation due to the poor dead material description (cables, end-flange electronic boxes, etc.). As a consequence, the BPC hit multiplicity is low compared to data and the fraction of events with a unique BPC hit in front of the BEMC cluster is high. It is thus less important to apply similar corrections to the Monte Carlo simulation.

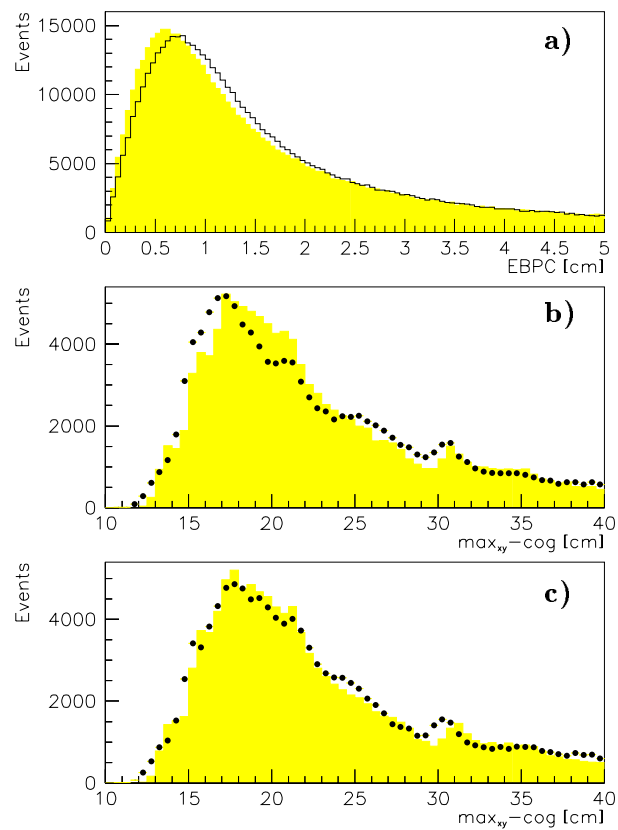


Figure 5.3: *a) EBPC estimator distributions before (solid histogram) and after (shaded histogram) applying corrections to the cluster centroid position. b, c) Data (points)–Monte Carlo simulation (shaded histogram) comparison of the quantity $\max_{x,y}$, defined as the largest coordinate (in absolute value: $|x|$ or $|y|$) of the cluster centroid position before (b) and after (c) applying the centroid position corrections.*

5.2.1 Double angle method

The double angle kinematics can be used to obtain an indirect scattered electron energy estimate, in order to check the energy reconstruction, calibration and resolution [48].

The e^- energy obtained by the double angle method is defined by:

$$E_{DA} = \frac{E_e(1 - y_h)}{\sin^2 \frac{\theta_e}{2}}$$

with

$$y_h = \frac{\tan \frac{\theta_h}{2}}{\tan \frac{\theta_e}{2} + \tan \frac{\theta_h}{2}}, \quad \theta_h = \arccos \frac{(P_t^h)^2 - (E^h - P_z^h)^2}{(P_t^h)^2 + (E^h - P_z^h)^2}$$

where

$$E^h - P_z^h = \sum_{hadrons} E^i - P_z^i$$

and

$$P_t^h = \left(\left(\sum_{hadrons} P_x^i \right)^2 + \left(\sum_{hadrons} P_y^i \right)^2 \right)^{\frac{1}{2}}$$

The summation is performed over all calorimeter clusters, excluding the electron candidate cluster, defined as the highest energy BEMC cluster.

The kinematic peak is selected by requiring the hadronic angle to be within ($15^\circ < \theta_h < 60^\circ$) (Fig 5.4-*a*). The distribution of the double angle energy E_{DA} after applying this cut is shown on Fig 5.4-*b* for the shifted vertex data and the Monte Carlo simulation. The normalisation is absolute, based on the luminosity measurement. The kinematic peak is shifted in the Monte Carlo simulation with respect to the data by ≈ 100 MeV ($\approx 0.3\%$). Half of the shift is attributed to a shift by 50 MeV of the incoming electron beam energy, used in the Monte Carlo simulation [41]. The additional 50 MeV shift is not understood, and is included as an extra 0.15% uncertainty to the double angle energy.

The quality of the double angle energy reconstruction is estimated from the Monte Carlo simulation, by comparison with the generated electron energy (Fig 5.5).

Fig 5.5-*a* shows the distribution of the quantity $(E_{da} - E_{gen})/E_{gen}$ versus $max_{x,y}$. The quantity $max_{x,y}$ is defined as the largest coordinate (in absolute value: $|x|$ or $|y|$) of the BPC hit associated to the electron candidate cluster. It describes the quadratic topology of the BEMC. For example, for ($14 < max_{x,y} < 16$) cm, the electron has been emitted in the region of the crack separating the inner triangles and the first quadratic stacks.

Fig 5.5-*b* shows the result of a Gaussian fit of the quantity $(E_{da} - E_{gen})/E_{gen}$ in bands of 0.5 cm in $max_{x,y}$.

One observes that the double angle energy E_{da} is well reconstructed, especially for the inner triangle region, which is of major interest for us. However, there is a slight bias, of the order of 0.2% for $max_{x,y} < 30.0$ cm, and 0.4% for $max_{x,y} > 30.0$ cm. This bias is included as a part of the uncertainty of the reconstructed energy scale.

5.2.2 Crack corrections

Energy corrections account for the fraction of the energy lost inside the cracks or in the dead material in front of the BEMC. Wrong corrections lead to a distortion and widening of the kinematic peak (quasi-elastic peak at the e -beam energy) shape. The corrections

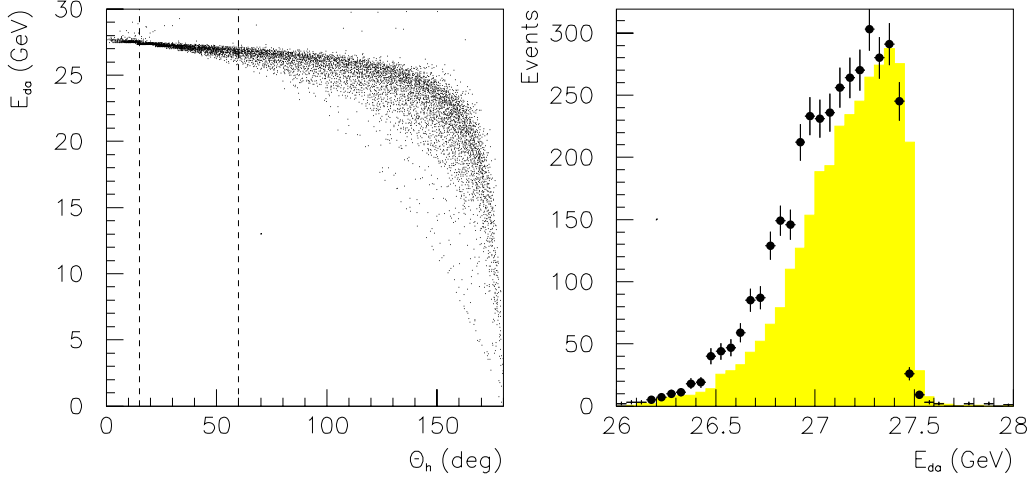


Figure 5.4: a) Scatter plot of the double angle energy E_{da} versus the hadronic angle θ_h . b) Double angle energy distribution for the events selected by requiring the hadronic angle with range $15^\circ < \theta_h < 60^\circ$ for the shifted vertex data (full points) and the Monte Carlo simulation (histogram). Absolute normalisation, based on the measured luminosity.

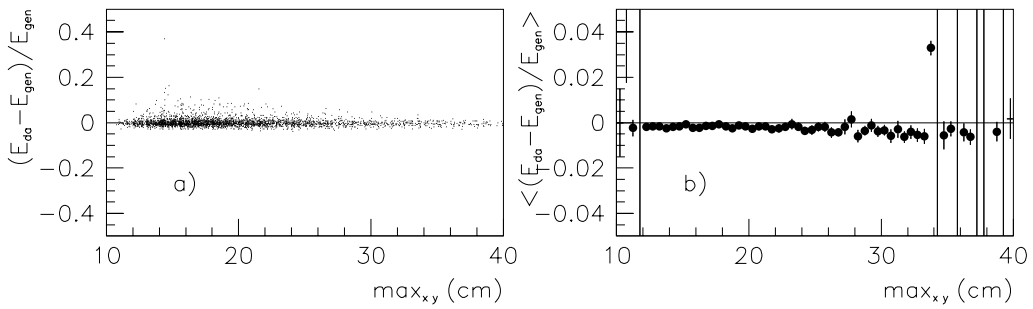


Figure 5.5: a) Scatter plot of the ratio $(E_{da} - E_{gen})/E_{gen}$ versus \max_{xy} (see text). b) Mean value for the Gaussian fit to the distribution of the quantity $(E_{da} - E_{gen})/E_{gen}$ in bands of \max_{xy} . The events are selected with $(15^\circ < \theta_h < 60^\circ)$.

are determined using the Monte Carlo simulation and are applied to the reconstructed visible energy (BCLR table), to obtain the final reconstructed energy (BCFR table).

Crack corrections have to be determined separately for the shifted and the nominal vertex interactions: the electron enters the crack under different angles, and for the same impact point can have more energy undetected in case of the shifted vertex interaction point than for nominal vertex interactions.

Fig 5.6 presents the distribution of the quantity $(E_{da} - E_{bcfr})/E_{da}$ versus $max_{x,y}$ for the shifted vertex data (a) and Monte Carlo simulation (b). The mean value and the standard deviation of a Gaussian fit of the distribution, in bands of $max_{x,y}$, are shown respectively on Fig 5.6-c, e for data and d, f for Monte Carlo.

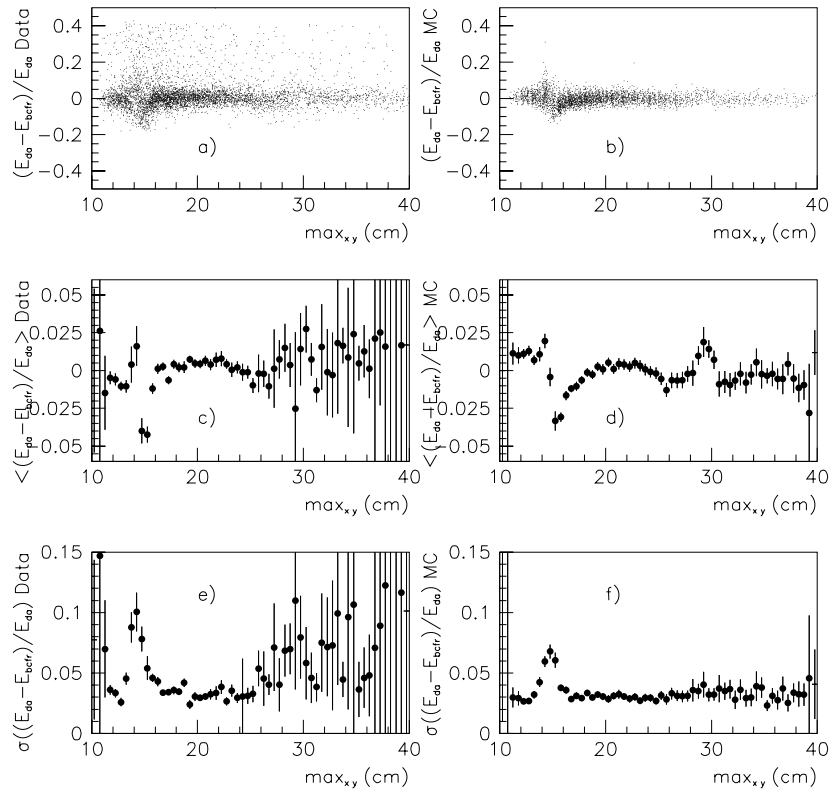


Figure 5.6: Scatter plot (a,b), mean value (c,d) and standard deviation (e,f) of a Gaussian fit to the ratio $(E_{da} - E_{bcfr})/E_{da}$ versus $max_{x,y}$. (Shifted vertex interactions; a - c - e: data, b - d - f: Monte Carlo).

One observes that the energy reconstruction is poor for the region of the crack separating the inner triangle region and the quadratic stacks, which corresponds approximately to the band $(14 < max_{x,y} < 16)$ cm. The effect is qualitatively reproduced by the Monte Carlo. In addition, inside the triangles, the energy is overestimated for the data by $\sim 1.0\%$, compared to the double angle energy, and underestimated by $\sim 1.0\%$ for the Monte Carlo.

The energy reconstruction is equally poor for the region of the crack separating the first and the second quadratic stacks ($28 < \max_{x,y} < 30$ cm). This however is less relevant as this analysis aims for the low Q^2 kinematic range, affected few by events with the electron scattered in this crack. In addition, in the affected Q^2 bins ($Q^2 \geq 15$ GeV²), the relative contribution of events originating from the crack remains small since the corresponding θ_e range is much wider than in case of the lowest Q^2 bins, affected by the first crack (see for example Fig 4.3).

An interesting observation is that the width (standard deviation) of the energy distribution in the band ($14 < \max_{x,y} < 16$ cm) is smaller for the visible BCLR energy (Fig 5.7) than for the final BCFR energy. This means that the energy at the BCLR level is less smeared (although it is underestimated) than the final reconstructed energy BCFR: the effect is observed both for data and Monte Carlo. The additional smearing is introduced by the crack corrections.

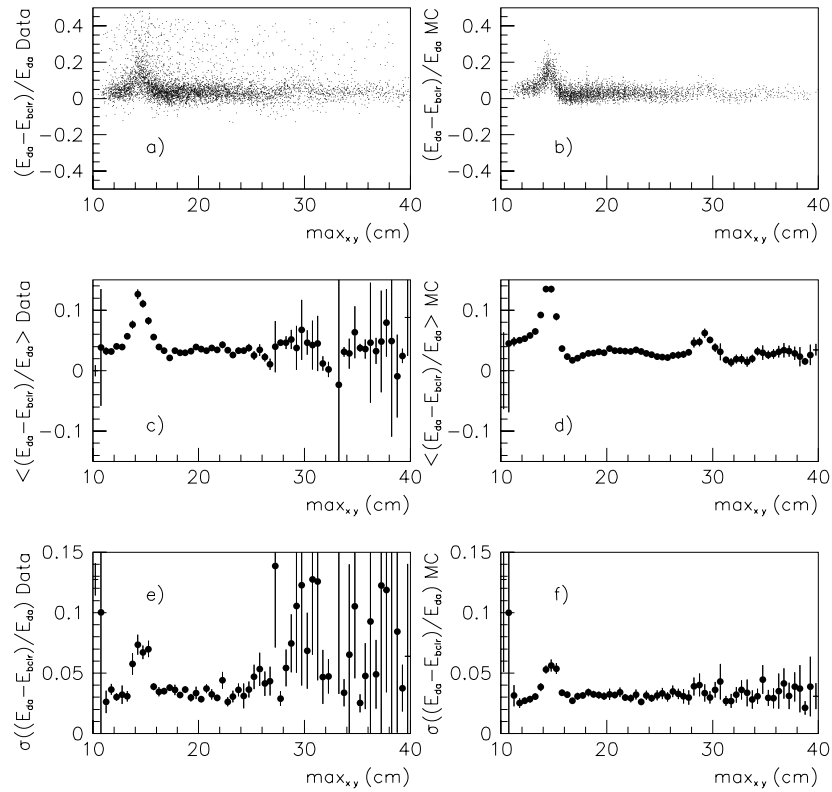


Figure 5.7: Same as for fig. 5.6 but BCLR instead of BCFR.

5.2.3 Double angle recalibration

Since the crack corrections fail to describe with satisfactory precision the first crack of the BEMC, we have proposed [49] to apply to the uncorrected visible energy BCLR, shown in Fig 5.7, a new correction, obtained from the comparison of the BCLR measurement and of the energy estimate obtained from the double angle method.

The corrections are thus directly applied to the BCLR energy to obtain a new final reconstructed energy BCFR in the region ($11 < \max_{x,y} < 17$) cm⁵. For $\max_{x,y} > 30$ cm, the reconstructed BCFR energy is used (because the statistics are too limited to use the double angle method). However, a closer look on Fig. 5.6 to the region of $\max_{x,y} > 30$ cm, corresponding to the outer BEMC stacks shows a systematic shift, upwards in the data and downwards in the Monte Carlo. An additional correction is thus applied on the final BCFR energy: +0.5% for the data and -0.5% for the Monte Carlo. A scatter plot similar to the one of Fig 5.6 but with the new corrections is shown on Fig 5.8.

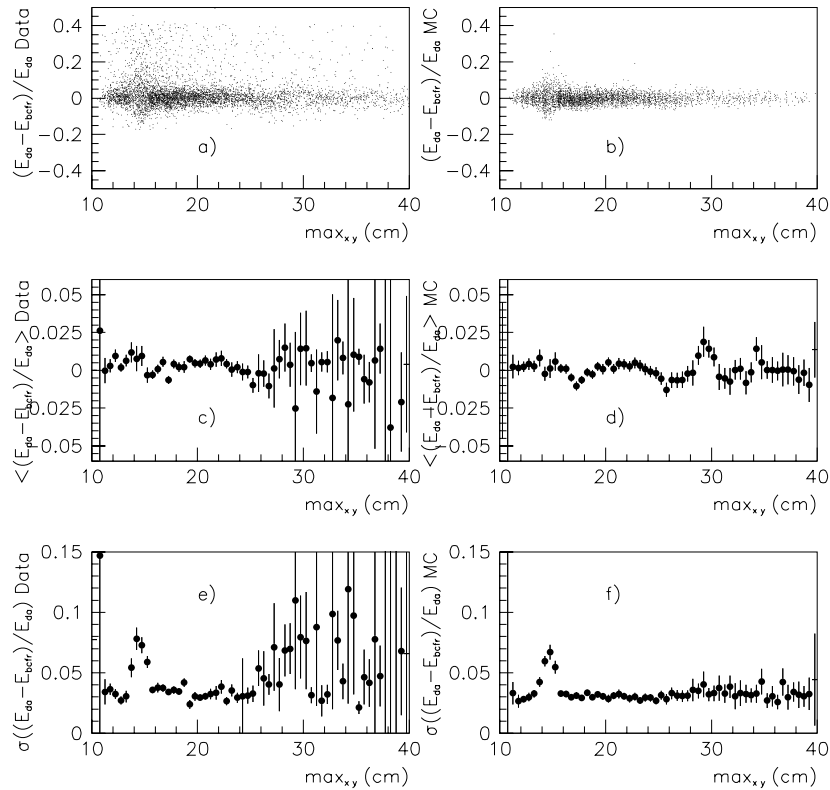


Figure 5.8: Same as for Fig 5.6 but after applying the energy correction obtained using the double angle method.

As designed, the bias in the energy reconstruction disappears inside the triangles and

⁵Crack corrections are considered in the first approximation to be energy independent

is less pronounced in the first crack (Fig. 5.8 c-d). The energy reconstruction in the first crack becomes also less smeared: the width of the distribution for $(E_{da} - E_{bcfr})/E_{da}$ (Fig. 5.8 e-f) is smaller than with the old crack corrections (Fig. 5.6 e-f).

It is also interesting to compare directly the shape of the energy distribution for the data and the Monte Carlo simulation before and after applying the new corrections (Fig 5.9). The distributions are presented in bands of $max_{x,y}$ for the shifted vertex data (full points) and Monte Carlo simulation (histogram).

A significantly better agreement between data and Monte Carlo simulation is observed.

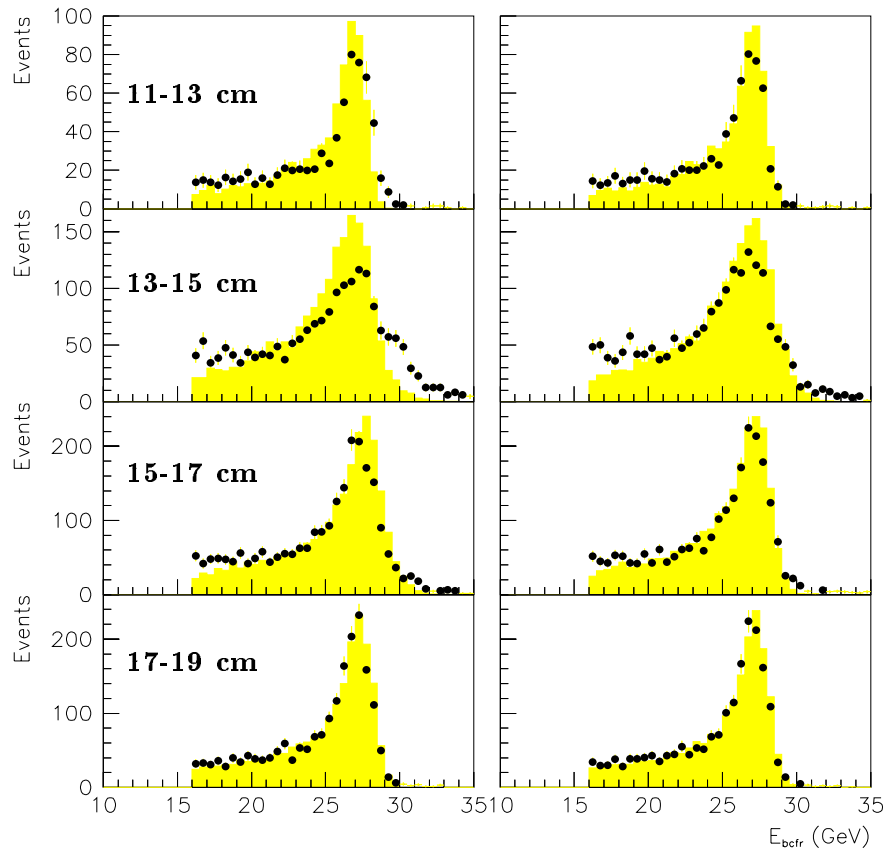


Figure 5.9: Energy distributions in bands of $max_{x,y}$ with the old crack corrections (left column) and with the new crack corrections (right column) for the shifted vertex data (full points) and the Monte Carlo simulation (histograms).

5.2.4 BEMC energy resolution

The BEMC energy resolution can be estimated directly from the data by comparing the final reconstructed energy (BCFR table) to the double angle energy measurement.

As shown above, the double angle energy resolution σ_{da}/E is estimated to be $\approx 1\%$ from

the Monte Carlo simulation (for $15^\circ < \theta_h < 60^\circ$). The resolution obtained by comparing the scattered electron energy to the double angle energy (see 5.8-*e, f*) is a convolution of the intrinsic BEMC energy resolution and the double angle energy resolution: $\sigma/E = \sigma_{bcfr}/E \oplus \sigma_{da}/E$. It is estimated by a linear fit to the flat part ($max_{x,y} \geq 17$ cm) of the distribution 5.8-*e*.

The BEMC energy resolution is then: $\sigma_{bcfr}/E = 0.030 \pm 0.002$ at $E = E_{beam} = 27.6$ GeV. This result agrees well with the value expected after the CERN beam tests (see section 3.2.1) as was shown on Fig 3.5.

5.2.5 Systematic uncertainty of the BEMC energy scale

As has already been pointed out in the introduction to this chapter, the systematic error of the energy scale is estimated from the *discrepancies* between the data and the Monte Carlo simulation. In other words, a systematic effect (as for example a systematic shift of the absolute energy scale) does not have any impact on the F_2 structure function measurement if it is correctly reproduced by the Monte Carlo simulation.

According to this definition, the energy scale uncertainty is estimated as the difference between data (Fig 5.8-*c*) and Monte Carlo simulation (Fig 5.8-*d*). The result is shown on Fig 5.10-*a* before and (*b*) after applying the new crack corrections.

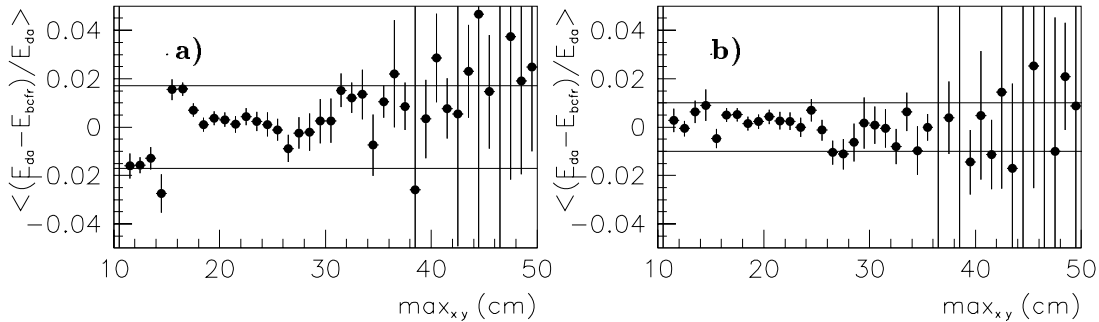


Figure 5.10: *Difference between the data and the Monte Carlo of the mean values on the fits of the $(E_{da} - E_{bcfr})/E_{da}$ in bands of $max_{x,y}$ for the shifted vertex interactions with the old crack corrections (a) and with the new crack corrections (b).*

The BEMC energy scale error of 1.7% quoted by the BEMC group for the 1993 data is indicated on Fig 5.10-*a*⁶. Fig 5.10-*b* shows that, with the new corrections, the energy scale is simulated to better than 1%.

Fig 5.11 presents the results of a similar analysis for the nominal vertex interactions data and Monte Carlo simulation [41]. Similarly to the shifted vertex data, the inner triangles and the first crack were recalibrated using the double angle method, and the overall corrections were applied to the BCFR energy for the outer BEMC stacks.

⁶In fact, this number seems too pessimistic, even before applying the new corrections, since for the first quadratic BEMC stack, where most of the statistics reside, the calibration has been performed in a very reliable way by the BEMC group.

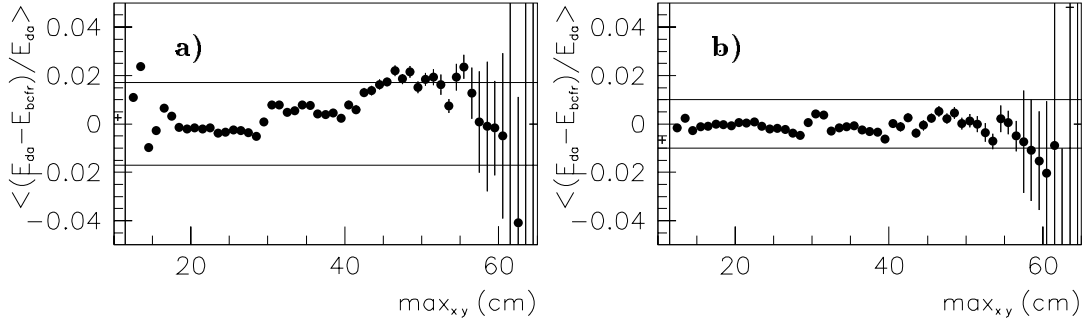


Figure 5.11: *Difference between the data and the Monte Carlo of the mean values on the fits of the $(E_{da} - E_{bctr})/E_{da}$ in bands of $max_{x,y}$ for the nominal vertex interactions with the old crack corrections (a) and with the new crack corrections (b) (from [41]).*

Finally, a 1% error is adopted [31] after applying the new corrections for the precision of the BEMC energy scale description by the Monte Carlo simulation, which is relevant for the systematic error studies, e.g. for the structure function analysis. It applies for both the shifted and the nominal vertex data samples.

5.2.6 Summary

Table 5.1 summarises the results obtained above.

	Shifted vertex		Nominal vertex [41]	
	data	Monte Carlo	data	Monte Carlo
Incoming electron beam energy		-50 MeV ⁷		-50 MeV
Double angle energy scale error	0.5%			
Double angle resolution σ_{da}/E_{da}	1%			
<i>Detailed corrections to BCLR:</i>				
Inner triangle stack	cf. [49]		cf. [41]	
<i>Overall corrections to BCFR:</i>				
First quadratic stack	-	-	-0.1%	+0.1%
Second quadratic stack	+0.5%	-0.5%	+0.36%	-0.36%
Outer stacks	-	-	+1.0%	-1.0%
Energy resolution σ_{bctr}/E_{bctr}	0.03 ± 0.002			
Energy scale error	1.0%			

Table 5.1: *Summary of the BEMC energy calibration parameters.*

⁷This correction applies to the value as it is written into the DMIS table.

5.3 Systematic effects affecting the θ_e measurement

The polar angle θ_e is measured as the angle of a straight line between the reconstructed vertex and the BPC hit with respect to the p -beam direction. The θ_e resolution is defined by the quality of the z -vertex and the BPC reconstructed impact point. There are two major systematic effects, degrading locally the polar angle θ_e reconstruction:

- Systematically biased z -vertex reconstruction in the particular case of vertex fits obtained only from the scattered electron track, crossing the whole length of the CJC chamber under large θ_e angle ($\theta_e \sim 170^\circ$);
- Systematically biased BPC hit reconstruction due to preshowering in the cables situated between CJC and BPC.

As usual, the systematic errors estimated in this section account for the *discrepancy* between the data and the Monte Carlo simulation.

5.3.1 θ_e resolution

Vertex fit resolution

The quality of the vertex fit is important for the θ_e resolution. A large proportion of events have a z -vertex with an error of less than 2 cm, which corresponds to the θ_e resolution of less than 1 mrad. Fig 5.12-*a, b* shows the distributions of the z -vertex fit error for the shifted vertex data (points) and Monte Carlo simulation (histograms) respectively for the purely central (*a*) and the purely forward vertex (*b*) fits (see section *Vertex type*, page 66). The normalisation is absolute, based on the luminosity measurement. On Fig 5.12-*a*, the peak at ~ 0.5 cm corresponds to vertices fitted with tracks containing CIZ and/or COZ segments of high z -precision (see chapter 4, footnote 12).

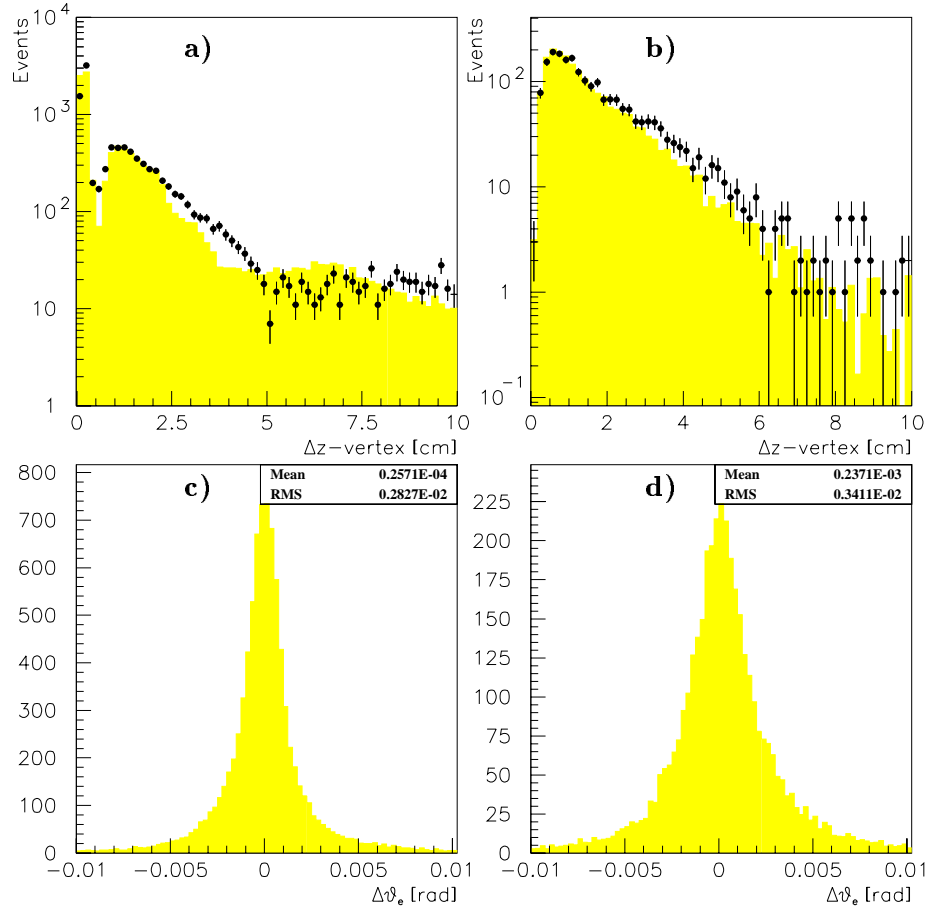
The Monte Carlo simulation describes the data with satisfactory precision although there is some disagreement in the range ($2.5 \leq \Delta z \leq 5.0$) cm, for pure central vertex fits (Fig 5.12-*a*).

BPC resolution

The intrinsic (hardware) BPC contribution to the θ_e resolution is of the same order of magnitude as the vertex fit contribution: approximately 50% of the events have a BPC hit error of ≈ 2 mm, corresponding to a θ_e resolution of 1 mrad. However, to reach this precision, it is essential to perform a precise alignment of the BPC chamber to the central tracker, in order to avoid a systematic displacement (e.g. horizontal/vertical shifts, rotation, inclination) of the BPC with respect to the central tracker, degrading the intrinsic BPC resolution⁸.

Two methods are available for the BPC chamber alignment and resolution estimate:

⁸The H1 detector is aligned to the CJC chamber, which is the main element of the H1 tracker. Other central tracker elements (CIZ, CIP, COZ and COP) are fixed to CJC. The CJC-referential is thus the basis of the H1 coordinate system. For the angular measurements with respect to the incoming e -beam direction (e.g. scattered electron polar angles), an eventual beam-tilt with respect to the CJC-axis has to be taken into account. In 1994 the average correction accounting for the beam-tilt was as large as 2 mrad.

Figure 5.12: θ_e resolution

Vertex fit error (data: points; Monte Carlo: shaded histogram, absolute normalisation) for central vertices (a) and forward vertices (b). $\theta_e - \theta_{simulated}$ for the shifted vertex interactions (Monte Carlo simulation) for an unique BPC hit in front of the scattered electron cluster (c) and several hits (d).

1. Extrapolation of the scattered electron track (CJC+CIZ) to BPC;
2. Extrapolation of the scattered electron track from the interaction vertex via CIP to BPC.

The first method was used for a 3-dimensional alignment of the BPC chamber with respect to the CJC-axis and to estimate the global θ_e resolution [41]. It turns out that BPC was displaced in x by 1.4 mm and in y by 2.4 mm, and that the global θ mismatch is less than 0.5 mrad. The θ_e resolution, measured for the nominal vertex high statistics data, turns out to be in average 2.3 mrad (RMS), in agreement with Monte Carlo simulation. The second method was used as an independent cross-check of the BPC alignment.

The θ_e resolution, as it is obtained from the Monte Carlo, is slightly worse for the shifted vertex interactions. Fig 5.12-*c, d* presents the distributions of $\theta_e - \theta_{simulated}$ for the event samples (SV) with a unique BPC hit in front of the scattered electron cluster (*c*) and with several BPC hits (*d*). Note, that the shape of the distribution is not Gaussian due to a non-Gaussian contribution of the z -vertex error. The resolution obtained is 2.8 mrad (RMS) in the first case (*c*-no preshowering) and 3.4 mrad (RMS) for events with preshowering (*d*).

In conclusion, the θ_e resolution is described with a satisfactory precision by the Monte Carlo simulation. Taking into account the residual difference between data and Monte Carlo and the uncertainty on the global BPC shift of 1.4 mm in x and 2.4 mm in y , we take 1 mrad as the systematic uncertainty of the θ_e measurement. This overall error does not include local effects, treated in the next two sub-sections.

5.3.2 Vertex bias for the shifted vertex data

A strong local bias of the z -vertex reconstruction is observed in case of the shifted vertex interactions. It affects events with the z -vertex fitted from a single track due to the scattered electron. The vertex position is systematically shifted by a few cm towards the centre of the H1-detector. The θ_e polar angle, defined from the z -vertex and the BPC hit, is then systematically underestimated, leading to an overestimated Q^2 measurement. As a consequence, events migrate from the low Q^2 region to higher Q^2 , the effect being emphasised by the $1/Q^4$ dependence of the DIS cross-section. Fortunately, only the $Q^2 \geq 15 \text{ GeV}^2$ kinematic range is affected, which is anyhow covered with much higher statistics by the nominal vertex data sample, not affected by this problem. However, we considered important to mention this effect, since quite a big effort was done by the CJC group to provide an explanation.

Fig 5.13-*a* presents the θ_e distribution for events with the z -vertex fit from a single track (data: full points, Monte Carlo: shaded histogram; absolute normalisation to the luminosity). The peak at $\theta_e \approx 170^\circ$ corresponds to the region where the scattered electron is observed within the CJC acceptance, defining a reconstructed vertex. The angular limit of the CJC acceptance for the backward scattered particles is $\theta \approx 172^\circ$ (SV interactions only). The second peak at $\theta_e \approx 175^\circ$ also corresponds to events with the z -vertex fit by a single track. However, the scattered electron being outside the CJC acceptance, the track defining a vertex is compulsory due to a current jet particle.

The bias in the z -vertex reconstruction for the first class of events with a vertex fitted by a single scattered electron track is demonstrated on Fig 5.13-*c, d*. Fig 5.13-*c* presents

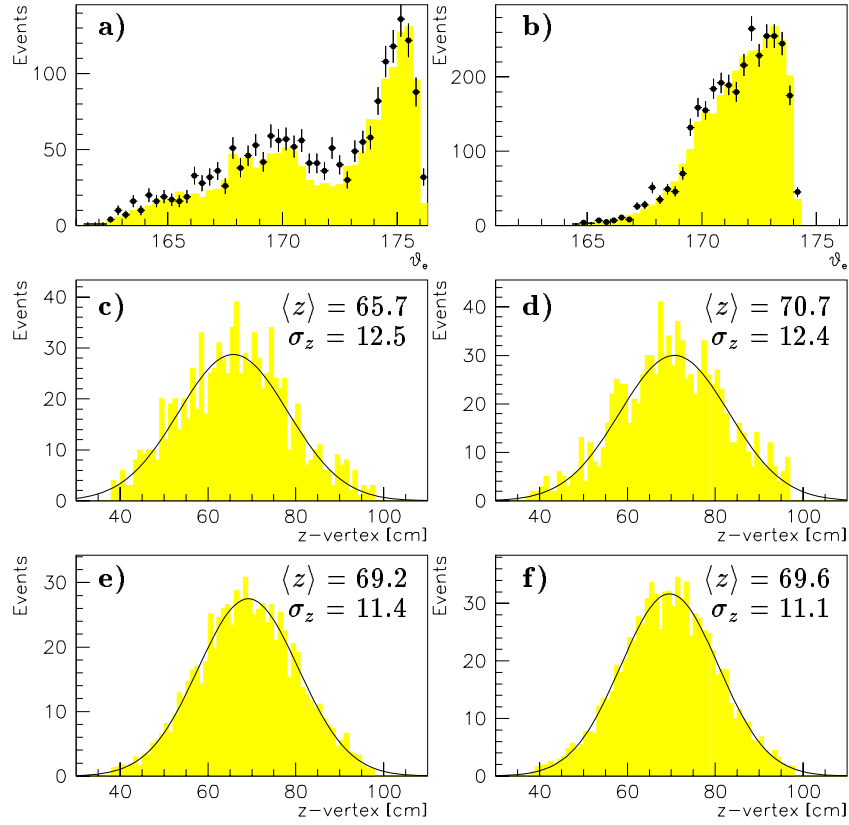


Figure 5.13: (a) θ_e distribution for events (SV) with vertex fit from a single track and (b) for all selected DIS events with $7.5 \leq Q^2 \leq 25 \text{ GeV}^2$ (data: dots; Monte Carlo: shaded histogram; absolute normalisation on the luminosity). z -vertex distribution and Gaussian fit for the shifted vertex data (c,d) and the Monte Carlo simulation (e,f) for events with a vertex fit from a single track with $\theta_e \leq 172.0$ (c,e) and with $\theta_e \geq 172.0$ (d,f).

the z -vertex distribution for the events with $\theta_e \leq 172.0$, while Fig 5.13-*d* corresponds to the events with $\theta_e \geq 172.0$ (right peak on Fig 5.13-*a*). A shift of ~ 5 cm is observed. Fig 5.13-*e, f* shows the similar distributions for the Monte Carlo simulation. In this case both distributions have approximately the same mean value of the Gaussian fit.

As to the origin of this phenomenon, we suppose it is due to the special character of the vertex fit with a single track, close to the edge of the CJC chamber: such tracks cross the whole length of the CJC chamber and are almost parallel to the CJC chamber wires. A saturation can thus occur as to the total charge collected by the affected wires, leading to a distortion in the charge division measurement, used for the hit z -position determination. As a consequence, the vertex fit is biased for this class of events in case of the shifted vertex interactions⁹.

Due to this phenomenon, an excess of events is observed in the final DIS sample, as can be seen on Fig 5.13-*b*. A bump is visible around $\theta_e \approx 170^\circ$, which is poorly described by the Monte Carlo simulation.

5.3.3 Preshowering and BPC-BEMC matching

Preshowering in front of the BPC

As it has already been introduced in section 5.1, a substantial fraction of events with the electron scattered in the BEMC is affected by preshowering, which occurs in the cables between CJC and BPC and in the tracker readout electronics, situated on its rear edge. The association of the BPC hit to the scattered electron cluster is evident in case of no preshowering, while it is not straightforward for events with a large solid angle preshowering, which produces several hits in the BPC (up to 20) in a few squared centimetre spot.

Fig 5.14-*a* shows the proportion of events with no preshowering¹⁰ in front of the BPC for the shifted vertex data (full points) and Monte Carlo simulation (crosses), in function of the scattered electron impact point radius in BPC with respect to the beam-axis. One immediately observes that there is on average twice as many events with no preshowering in the Monte Carlo simulation, compared to data. In addition, there is a pronounced peak in data at $R_{bpc} \approx 20.0$ cm, not even qualitatively described by Monte Carlo¹¹. The areas at $R_{bpc} \approx 17.5$ and $R_{bpc} \approx 21.0$ cm, squeezing the peak, correspond to the dead material accumulations due to the end-flange electronics of CIZ and of CIP respectively.

⁹The bias is not observed in case of the nominal vertex interactions for the following reasons: first, the CJC chamber is specially calibrated for these data; and second, the proportion of events with only one reconstructed CJC track due to the scattered electron is much lower than in case of the SV interactions (since the CJC acceptance is increased in the forward direction, allowing the current jet to be measured for most events)

¹⁰The definition of “no preshowering” depends on the resolution of the tracking detector, i.e. the BPC. Here, we use the following definition:

- One reconstructed BPC hit in front of the scattered electron cluster;
- Error of the BPC hit reconstruction $\sigma_{bpc} \leq 3$ mm, which fixes approximately the maximum size of the preshowering spot (see footnote 2).

¹¹A peak is present in Monte Carlo at $R_{bpc} \sim 23.0$ cm. However, it is significantly less pronounced than in data and displaced by ~ 3 cm.

The proportion of events with no preshowering increases again towards small values of R_{bpc} , as the scattered electron passes below the tracker and the end-flange electronics.

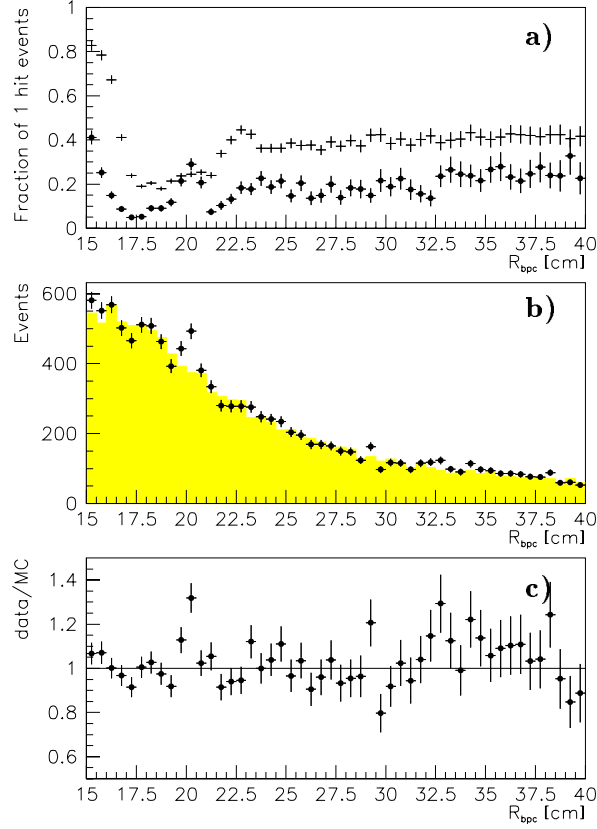


Figure 5.14: a) Fraction of events with no scattered electron preshowering in front of BPC for the shifted vertex data (full points) and Monte Carlo simulation (crosses) in function of R_{bpc} (the scattered electron impact point radius in BPC with respect to the beam-axis); b) Distribution of the DIS events in function of R_{bpc} : data—full points, Monte Carlo—histogram. Absolute normalisation; c) ratio of data over Monte Carlo from the previous distributions.

The straightforward conclusion is that the dead material description and therefore the electron preshowering is not correctly implemented in the Monte Carlo simulation. The question arises about the impact of this poor implementation on the structure function measurement.

Impact on DIS event sample. Migrations

The DIS event distribution in function of R_{bpc} for the data (full points) and the Monte Carlo simulation (histogram) is shown on Fig 5.14-b, together with the ratio of data over Monte Carlo (Fig 5.14-c).

A bump is present in the data around $R_{bpc} \approx 20.0$ cm and correlated with the increased fraction of events with no preshowering (see Fig 5.14-a). The effect is not present in the Monte Carlo simulation.

The following explanation as to the origin of this phenomenon is proposed:

- If a “wrong” BPC hit is chosen, the event eventually migrates “upwards” or “downwards” by a few cm (maximum ~ 2 cm) in R_{bpc} and thus to higher or lower reconstructed Q^2 . On the other hand, at $R_{bpc} \approx 20.0$ cm relatively few events undergo migrations due to a higher proportion of events with no preshowering (unique BPC hit);
- Events migrating from $R_{bpc} \approx 17.5$ and $R_{bpc} \approx 21.0$ cm areas can be reconstructed in the $R_{bpc} \approx 20.0$ cm area. Thus a surpopulation appears at $R_{bpc} \approx 20.0$ cm, while the areas at $R_{bpc} \approx 17.5$ and $R_{bpc} \approx 21.0$ cm are depopulated, not compensated by the inverse migrations from $R_{bpc} \approx 20.0$ cm.

Systematic error attribution

Correcting the Monte Carlo dead material implementation and resimulating the whole set of Monte Carlo files (more than 1.5M of events) did not appear as a reasonable solution. As the effect studied here has a local character, we decided to estimate its impact on the F_2 measurement only.

A procedure has been developed, reproducing artificially the described above migrations in the already simulated Monte Carlo files. The procedure consists in recalculating the individual event weight according to the shape of the experimental R_{bpc} distribution. The total number of Monte Carlo events is kept constant.

The systematic error is defined as the difference between the F_2 measurements obtained before and after R_{bpc} reweighting. The systematic error estimate is performed for the nominal vertex closed triangles data. The obtained result is shown in table 5.2 in function of the Bjorken invariants x and Q^2 . The errors are not negligible in case of the F_2

Q^2 (GeV ²) \ x	0.0002	0.00032	0.0005	0.0008	0.0013	0.002	0.0032	0.005
6.5	-0.5%							
8.5	-0.4%	-0.4%						
12.0		+0.7%	-0.5%	-0.7%	-0.5%			
15.0		+2.0%	+2.0%	+1.0%	0.0%	-0.6%	-0.5%	
20.0					+2.3%	+2.0%	+2.0%	
25.0					+1.0%	+2.0%	+2.3%	+2.5%
35.0					0.0%	0.0%	+0.3%	+0.4%

Table 5.2: Systematic error to F_2 in function of the Bjorken invariants x and Q^2 accounting for the bad Monte Carlo description of the dead materials in front of the BPC.

measurement with the nominal vertex high statistics data. They are however negligible in case of the shifted vertex data, since for a given Q^2 (θ_e) range, events are integrated over

a larger R range, compared to the nominal vertex case. Thus, the effect is “washed out” and is not taken into account in the shifted vertex and satellite bunch analyses.

5.4 y_Σ measurement

The variable y_Σ is defined starting from the purely “hadronic” y_h (see section 4.2). The latter is measured from a combination of central track momentum and calorimeter cell energies [51]. On Fig 5.15 the fraction of y_h measured from tracks, LAC and BEMC calorimeter contributions are given in function of $\log_{10} y_h$. An isolation criterion is used,

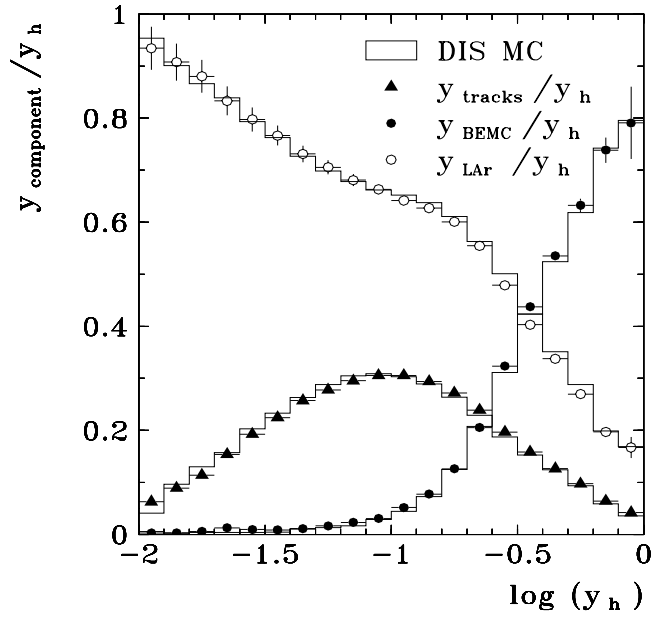


Figure 5.15: *Fraction of y_h originating from tracks, BEMC and LAC calorimeter contributions (From [51]).*

avoiding counting the LAC energy originating from a track already used in y_h . The Σ method being used for the kinematic reconstruction at low- y , the y_h measurement is dominated by the LAC and track contributions. At high y , the current jet is emitted in the backward direction and the BEMC contribution plays an increasing role.

The Monte Carlo simulation is shown on the same figure (histogram) for information. Note that the agreement of the Monte Carlo simulation with data is meaningless as for the description of the BEMC contribution: the Monte Carlo was globally tuned to the data, and the BEMC calorimeter being a purely electromagnetic calorimeter, large fluctuations can occur from event to event (see 3.2.1 and Fig 3.7).

y_Σ reconstruction and bias

The different contributions entering the hadronic y – tracks, LAC and BEMC cells – were tuned using the nominal vertex data. Dedicated studies [51] show that the reconstruction of the hadronic final state is unbiased and the Monte Carlo description is correct.

No special tuning of the hadronic y , i.e. crack corrections in LAC, is performed for the shifted vertex interactions. A different picture of the hadronic final state reconstruction can thus appear.

The only means to study the y_Σ reconstruction for the shifted vertex interactions in data and its Monte Carlo simulation description is to compare y_Σ to y_e in their overlap region, where both methods of kinematics reconstruction are available, i.e. at high y . On Fig 5.16-*a, b* y_e is compared to the generated y (y_{gen}). Fig 5.16-*a* is a scatter plot of $(y_{gen}^e - y_e)/y_{gen}^e$ in function of $\log y_{gen}^e$. Fig 5.16-*b* presents the result of a Gaussian fit of the left distribution in bands of y_{gen}^e . The error bars represent the spread (resolution) of y_e . As expected, the y_e reconstruction is not biased in the Monte Carlo and its resolution is excellent down to $y = 0.1$. We thus use y_e as the reference- y both for the data and the Monte Carlo simulation in the range ($1 \geq y_e \geq 0.1$) in order to check the y_Σ reconstruction. Unfortunately, this comparison can not be applied in the interval $y \leq 0.1$, where the importance of the Σ method increases.

Fig 5.16-*b - f* y_Σ shows a comparison of y_e for data (*c, d*) and Monte Carlo (*e, f*). As on Fig 5.16-*a, b*, the left one is the scatter plot of $(y_e - y_\Sigma)/y_e$ in function of $\log y_e$ and the right one is the result of the Gaussian fit with the error bars representing the spread (resolution).

The y_Σ resolution is correctly reproduced by the Monte Carlo simulation, but not its absolute value, which is systematically lower than y_e . This can be attributed to an underestimate of the hadronic final state energy in the reconstruction procedure: the flux of particles cross different detector parts than for the nominal vertex interaction position and the detector response can be modified (i.e. LAC crack corrections¹²).

If the Monte Carlo simulation had followed the data, the effect would cancelled for the F_2 measurement, and there would be no need for special corrections. However, there is a pronounced disagreement between the data and the Monte Carlo simulation (compare Fig 5.16-*d* and *f*). A systematic shift of y_Σ by $\sim 10\%$ would be necessary to cover the gap between data and Monte Carlo. In addition, the sigma method is used in the $y \leq 0.1$ range, not covered by this study. A global tuning of different components entering y_h is in fact needed for the shifted interaction vertex position. A 10% systematic error is thus attributed to y_h for the F_2 structure function measurement, when the sigma kinematics are used.

¹²The BEMC electromagnetic energy response was adapted to the shifted vertex interactions (see section 5.2).

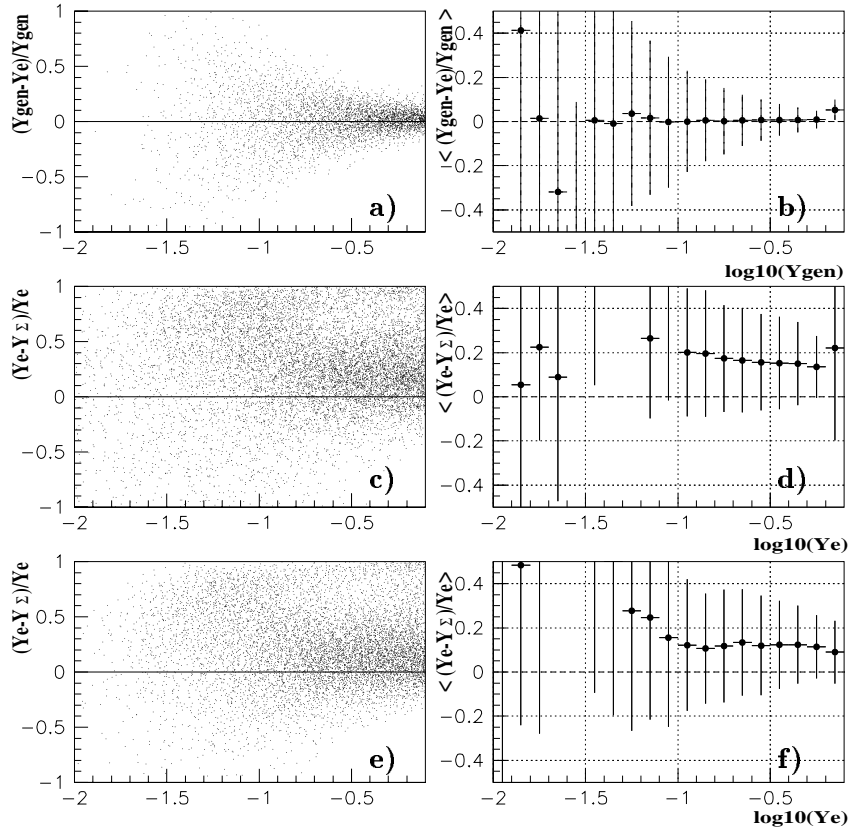


Figure 5.16: Quality of the y_Σ reconstruction (shifted vertex interactions):
a) $(y_{gen}^e - y_e)/y_{gen}^e$ as function of $\log y_{gen}^e$ (Monte Carlo); b) result of a Gaussian fit (error bars represent the spread (resolution)); c,d) $(y_e - y_\Sigma)/y_e$ as function of $\log y_e$ (data); e,f) $(y_e - y_\Sigma)/y_e$ as function of $\log y_e$ (Monte Carlo).

Chapter 6

Selection efficiencies

Two distinct steps can be found in the DIS selection procedure, with associated losses and efficiencies:

- *Hardware trigger and data acquisition:*
 1. BEMC trigger efficiency (BSET);
 2. Trigger losses due to the ToF veto;
 3. L4-farm filter losses;
- *Off-line selection:*
 4. Event classification losses;
 5. Vertex reconstruction efficiency and losses due to vertex error cuts;
 6. BPC hit association losses;
 7. ECRA requirement losses;
 8. ZORRO requirement losses.

The first group is “analysis independent”, i.e. is common to all DIS analyses of H1 data, and is studied outside the framework of the present thesis (BSET-trigger, see section 3.4.1; BToF, see section 3.3; L4, see section 3.4). A global 1% correction is applied, mostly to account for the BToF veto hardware and L4 reconstruction inefficiencies.

The second group is specific to the F_2 analysis and is not directly correlated with the first group.

The event classification and the ZORRO requirement turn out to be essentially loss-free (see respectively section 4.4.2, page 69). In this section, we discuss in detail the vertex efficiency, since it is most critical and less well known, and briefly the BPC and ECRA losses.

6.1 Vertex reconstruction efficiency

The vertex efficiency issue appears to be the faintest to understand and to handle effect, in the whole of the F_2 analysis. One could think that the vertex efficiency accounts primarily for the detector hardware properties, for the track finding efficiency and the vertex fit algorithm efficiency. Thus the vertex efficiency is at first sight a pure topological quantity and its definition would be: “the fraction of events with a reconstructed vertex for a given event topology, i.e. particle density and angular distribution.” However, the event topology description is delicate to handle in the context of the F_2 structure function

measurement. The latter is performed as a function of the x and Q^2 variables, and is based on comparisons between the number of DIS events in the data and in the Monte Carlo simulation. Thus the vertex efficiency has to be expressed as a function of x and Q^2 . Of course, it still solely depends on the event topology, but it is also strongly correlated with the underlying physics (choice of the input F_2 structure function and of the fragmentation process), which is *a priori* only known to some extent. So, even if the correlation between vertex efficiency and “event topology” is correctly reproduced by the Monte Carlo, this does not mean that it is correctly described in function of x and Q^2 . In addition, the measured x and Q^2 values are subject to QED radiation effects, which have also to be correctly modelised. This implies that the vertex efficiency description by the Monte Carlo is sensitive to the input parameterisation: taking a different parameterisation modifies the fraction of radiative events and hencefore the vertex efficiency. Finally, the global vertex efficiency for the F_2 measurement also depends on the relative contribution of “normal DIS” and “rapidity gap” DIS events. Hence different “physics” and thus different event topologies are mixed-up at the same measured x and Q^2 values.

Hence, if we observe discrepancies between data and Monte Carlo simulation, should we attribute them to a wrong hardware simulation, to a wrong quark fragmentation model used in Monte Carlo or to differences between the Monte Carlo input parameterisation and the “true” F_2 ? Those questions are not purely formal, as we have to apply corrections in the first two cases, while, as we will see later, the issue is less straightforward for the latter.

The above listed questions and problems do not fully encompass the vertex efficiency issue. Before developing it in details, let us emphasis again that our major difficulty was to disentangle the different sources of discrepancy between data and Monte Carlo simulation and, of course, to estimate them.

6.1.1 Vertex efficiency measurement

The vertex efficiency is defined as:

$$\mathcal{E}_{vertex} = \frac{N_{events\ with\ vertex}}{N_{total}} [3\sigma_z], \quad (6.1)$$

where $N_{events\ with\ vertex}$ is the number of DIS events with a reconstructed vertex lying within 3σ of the nominal z -vertex position and N_{total} is the total number of DIS events originating from the same z -vertex interval (as a function of (x, Q^2) or E'_e , etc.). The former quantity is measured directly, but the latter is more tricky to obtain for following three reason:

- The vertex requirement is a major background rejection criterion, and we have thus to deal with an important background contamination (essentially non- ep background) among the event sample with no reconstructed vertex;
- The satellite bunch contribution has to be corrected: while the satellite luminosity is small ($\approx 2 \div 2.5\%$ with respect to the main bunch luminosity), its larger Q^2 acceptance enhances its contribution compared to the main bunch. Hence, the satellite bunch contribution to the event sample with no reconstructed vertex can be as high

as $\approx 5\%$ (since we do not know if an event without reconstructed vertex comes from the nominal or satellite bunch), artificially decreasing the apparent vertex efficiency;

- The z -coordinate of the interaction point is needed to compute the polar angle of the scattered electron and thus the event kinematics.

Two methods are used to estimate the event losses due to the vertex requirement:

- One can use an alternative z -vertex reconstruction, using the CIP and BPC detectors (see Fig 6.1 and [52]). The advantage of this method is that it naturally avoids the quoted difficulties. However, it does not cover the low Q^2 kinematic range, because of the limited CIP detector geometrical acceptance.
- The second method [41] relies on the event sample obtained by applying more restrictive EBPC and ECRA requirements in order to reduce the background contamination. The remaining background is subtracted using the pilot bunches. The satellite correction is calculated analytically from the known satellite bunch luminosity and detector acceptance¹. Finally, the z -vertex position is set to its default nominal z -value of the interaction point for both the event samples with and without reconstructed vertex.

Both methods agree within 2% in their overlap region [41].

6.1.2 Vertex efficiency for the “electron” kinematics

Fig 6.2-*left* presents the vertex efficiency measured using the first method (CIP) for the shifted vertex data (full points) and obtained from two Monte Carlo simulations (the solid and dashed lines correspond respectively to the Monte Carlo simulations based on the result of the QCD fit to the H1 '94 F_2 measurement² and to the MRSDØ parameterisation [73]). The vertex efficiency is estimated in function of the scattered electron energy E_e' for three different θ_e ranges: (a) $165 - 170^\circ$, (b) $170 - 172.5^\circ$ and (c) $172.5 - 174^\circ$. The choice of the θ binning is motivated by the position of the scattered electron track with respect to CJC: (a) the electron track is within the CJC acceptance, a vertex is always reconstructed; (b) transition region (see also section 5.3.2) and (c) the scattered electron track is outside the

¹Consider a scattered electron candidate identified by its BEMC energy deposition E and a BPC hit at radius R . Since the interaction vertex was not reconstructed, it is not known whether it originates from the nominal or satellite bunch regions. The scattered electron energy and BPC impact radius are hence the only two measured quantities. The total number of events observed within the energy and radius intervals δE and δR is:

$$N(E, R) = (\mathcal{L}_{nominal} \frac{d^2\sigma_{nominal}}{dEdR} + \mathcal{L}_{satellite} \frac{d^2\sigma_{satellite}}{dEdR}) \delta E \delta R \quad (6.2)$$

One can thus define a probability that an electron observed at radius R with energy E comes from the nominal bunch region. This probability is used as a weight when counting the total number of events with no reconstructed vertex.

The differential cross section in (E, R) variables is obtained from the QCD structure function parameterisation by multiplying the differential cross section in (Q^2, x) variables by the corresponding Jacobian. The ratio of cross sections in (E, R) is about 2 for the satellite and the nominal bunch events [41].

²This simulation was originally performed using the GRV [76] structure function parameterisation. We reweighted it on an event by event basis to the H1 '94 fit (see section 7.1.2). Note that the GRV parameterisation describes anyway the H1 data with satisfactory precision.

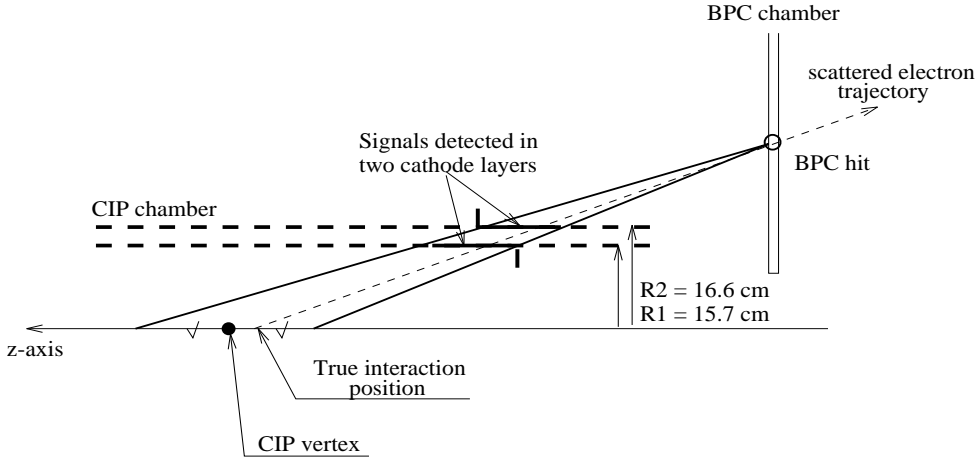


Figure 6.1: Sketch of the CIP vertex definition, using the BPC hit and two overlapping clusters of CIP pads with a detected signal.

CJC acceptance, the interaction vertex being reconstructed from the current jet particles only. Fig 6.2-*right* is the ratio of the efficiencies obtained using the data and obtained from the Monte Carlo (for the H1 '94 parameterisation). A linear fit is performed to the lower energy part ($E_e' \leq 25$ GeV) of the ratio and shown on the same figure.

Several conclusions can be drawn from Fig 6.2: (i) The adopted θ_e binning is observed to be pertinent, as the vertex efficiency evolves from $\sim 100\%$ in the first θ_e bin to significantly lower values when the scattered electron track is outside the CJC acceptance, especially for high E_e' ; (ii) As expected, a strong drop of the vertex efficiency is observed in the kinematic peak region, where the current jet is emitted in the forward direction, leaving no tracks in the CJC and when the electron itself does not reconstruct the vertex (*b* and *c*); (iii) The results obtained with the CIP method are described with acceptable precision (within 3%) by the Monte Carlo simulation (H1 '94 parameterisation), except in the kinematic peak, where the disagreement is more pronounced (mainly for θ_e between 172.5 and 174°); (iv) The vertex efficiency is not stable in the Monte Carlo simulation with respect to the input parameterisation: the MRSD \emptyset based Monte Carlo undershoots the efficiencies obtained from the data and the H1 '94 parameterisation simulation both at low energy and in the kinematic peak.

Concerning the latter point, the difference at low energy is understandable, since MRSD \emptyset is known to describe poorly the low Q^2 HERA data: its x evolution is essentially flat in x at low Q^2 , in contrast with a persistent F_2 rise, observed even for the lowest Q^2 values attained by H1 ($Q^2 \sim 1.5$ GeV 2). The DIS Born cross section is thus underestimated by MRSD \emptyset , while the radiative contribution to the cross section depends weakly on the choice of the F_2 parameterisation: the rate of QED radiative events at low energy is mostly determined by the F_2 behaviour in the kinematic peak, where all parameterisations presently available are similar, since they are tuned to the fixed target experiment results. Thus, at low energy we have relatively more “kinematic peak” radiative events in the case of the MRSD \emptyset than of the H1 parameterisations. Those events have the current jet in the forward direction, often outside the CJC acceptance (see Fig 4.3-*b*), leaving few or no

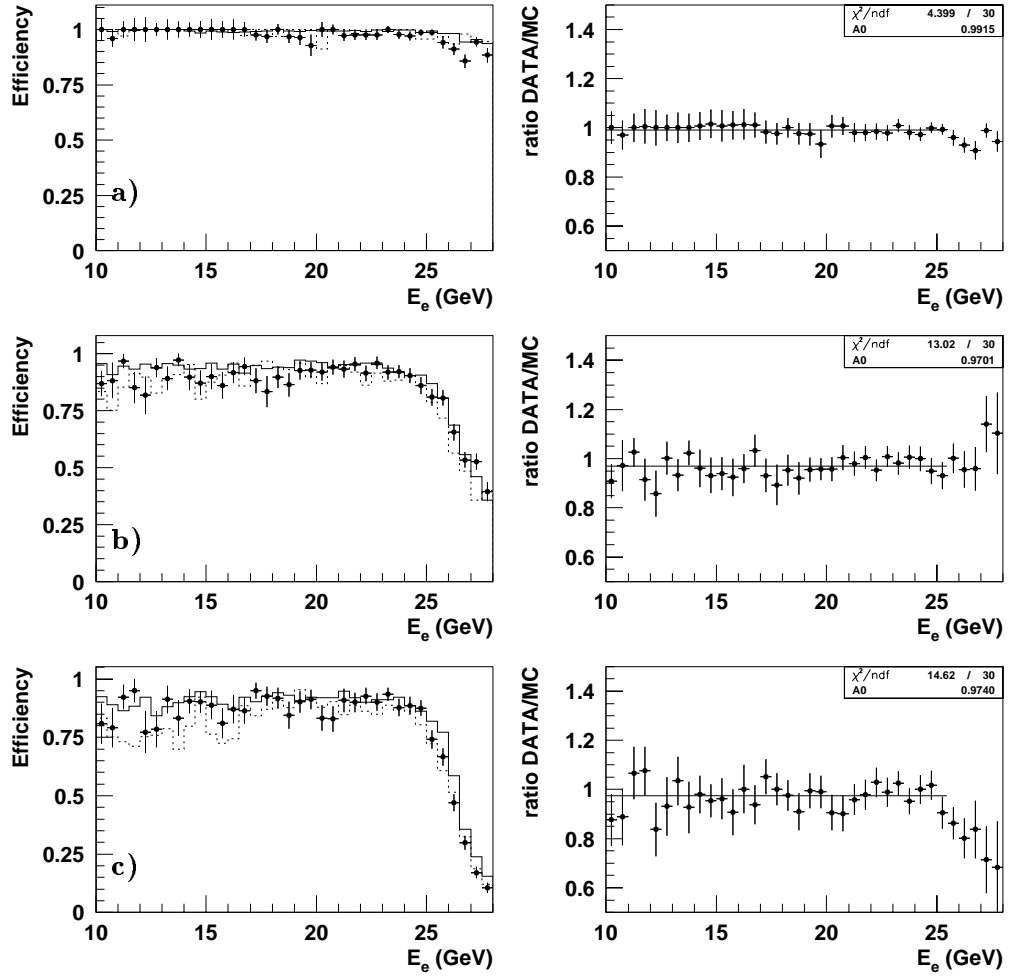


Figure 6.2: Vertex efficiency in function of the scattered electron energy E_e in slices of θ_e : a) $165 - 170^\circ$, b) $170 - 172.5^\circ$ and c) $172.5 - 174^\circ$. The left column shows the results of the vertex efficiency measurements for the shifted vertex data using the CIP method (full points) and for two Monte Carlo sets (solid line - H1 '94 parameterisation; dashed line - MRSD0 parameterisation [73]). The right column is the ratio of the efficiencies for data over Monte Carlo (H1 '94 parameterisation).

tracks in the CJC and increasing the proportion of events without reconstructed vertex.

This behaviour thus suggests that the vertex efficiency drop is mainly caused by radiative events. The vertex requirement reduces the span of radiative migrations in the kinematic plane, i.e. hard radiative events migrating from the kinematic peak to lower E'_e are mostly eliminated from the sample by the vertex requirement. We did not investigate this phenomenon deeper in the present analysis, since we choose rather to minimise radiative corrections using the Σ kinematics (see next section).

This intricate effect plays in favour of using the Monte Carlo method for the F_2 measurement, instead of the so-called “factorisation” method, where all efficiencies are explicitly factorised to correct for event losses: the vertex efficiency simply can not be factorised out, due to its strong correlation with radiative corrections. It provides an essential contribution to control the QED radiation.

As to the discrepancies in the kinematic peak - anyhow not used for the F_2 measurement - we think that two major effects are contributing: (i) different simulation conditions for the two Monte Carlo sets compared here: simulated vertex distribution, tracker simulation, detector calibrations, etc.³ The vertex efficiency falling sharply in the kinematic peak, it is very sensitive to the details of the simulation; (ii) the LEPTO generator [57] used for these simulations is known to suffer limitations at low W (γ^*p invariant mass). Events are not generated with $W \leq 2$ GeV (shifted vertex sample - $W \leq 5$ GeV), and the

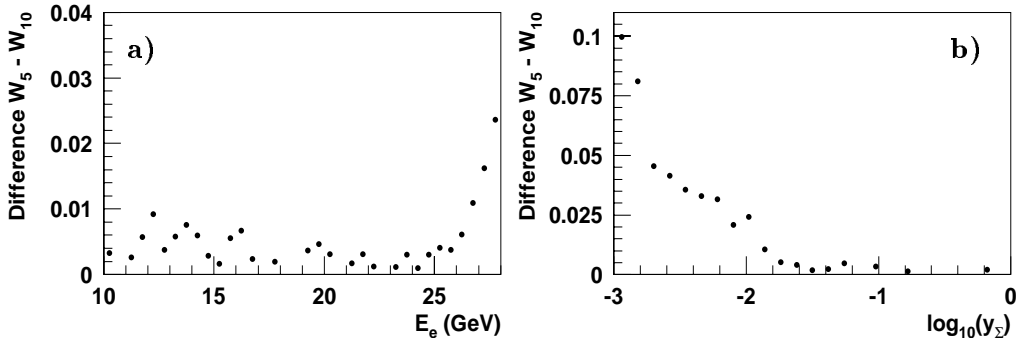


Figure 6.3: Influence of the W limitation on the vertex efficiency (shifted vertex Monte Carlo):

difference between vertex efficiencies obtained with a W generation cut at 5 and at 10 GeV: a) in function of E'_e ; b) in function of y_Σ . Statistical errors are not shown.

generation is done poorly for $2 \leq W \leq 4$ GeV⁴ ($y \leq 10^{-4}$) [41], because of difficulties in the scattered quark hadronisation. At first sight, there should be no problem, since we do not select events with $W \leq 5$ GeV. However, this effect can induce a lack of radiative events migrating inside the accepted sample mainly at low y , $y \leq 10^{-2} \sim 10^{-3}$, and therefore disturb the vertex efficiency description there. Besides, the amount of events lost can vary depending on the structure function set used for the Monte Carlo simulation, thus

³ A six months delay elapsed between the MRSDØ and the GRV Monte Carlo productions.

⁴ In fact we do not consider events with $W \leq 4$ GeV during the event selection.

leading to discrepancies in the vertex efficiencies between different Monte Carlo simulations. Fig 6.3 demonstrates for the shifted vertex Monte Carlo the difference ($0.01 \equiv 1\%$) in the vertex efficiencies obtained with a $W \geq 5$ and a $W \geq 10$ GeV generation cut, in function of E'_e and y_Σ (statistical errors are not shown). The effect is quite dramatic in the kinematic peak (high energy, $y_\Sigma \leq 10^{-2}$) and is almost absent at low energies (high y), as expected. It is interesting to note that the effect increases slightly towards the lowest energies, probably due to the pure “hard radiation” character of the vertex inefficiency there, which is due only to “kinematic peak” events migrating at lower energies. Of course the difference is amplified by comparing $W = 5$ to 10 GeV, while in our case it is only $W = 0$ to 4 GeV, but it is illustrative of a dangerous effect. High precision F_2 measurements in the coming years, extended towards very low y ($y \sim 10^{-3}$) in the low Q^2 kinematic range, will require further investigation of this problem.

To conclude: the $\theta_e - E_e$ context is not well suited for drawing definite quantitative conclusions as to the quality of the Monte Carlo description of the data, due its extreme sensitivity to the underlying physics, mainly through QED radiative migrations.

6.1.3 Vertex efficiency for the “sigma” kinematics

The Σ kinematic reconstruction being almost insensitive to QED radiations, it is thus natural to estimate the vertex efficiency as a function of y_Σ and not E'_e (or equivalently y_e : at high y , iso-energy lines are parallel to y lines, see Fig 4.3, section 4.2).

Fig 6.4 presents the result of the vertex efficiency measurement in function of y_Σ (right) compared to a similar measurement in y_e (left). As before, full points represent efficiencies obtained for the shifted vertex events, using the CIP method applied to the data, whereas the solid and dashed lines are obtained from Monte Carlo simulations, with respectively the H1 '94 and MRSDØ parameterisations. Fig 6.4-c, d present the ratio of efficiencies obtained from data over those extracted from the Monte Carlo simulations, for the MRSDØ (full points) and H1 '94 (solid line) parameterisations.

As expected, there is a significant difference between the vertex efficiencies obtained with these two parameterisations for the electron method, while both simulations are nicely consistent for the sigma method, making plain our hypothesis concerning the effect of radiation on the vertex efficiency.

The $\theta_e - y_\Sigma$ binning of the kinematic plane is most convenient for the vertex efficiency study, but at the condition that the y_Σ resolution be acceptable. We draw the attention to the fact that the latter is known to be limited: it is significantly worse than the y_e resolution for $y \geq 0.1$. Therefore, a local deterioration of the vertex efficiency would be simply “washed out” when measured in function of y_Σ .

Fig 6.5 (left) presents a comparison of the vertex efficiencies obtained from the data with the CIP method (full points) and given by the Monte Carlo simulation (H1 '94 - solid line) in function of y_Σ in θ_e slices, and their ratio (right). Statistics allow for a significant measurement at $y_\Sigma \geq 10^{-2}$. Data and Monte Carlo efficiencies agree within 3% for the $165 \leq \theta_e \leq 174^\circ$ range (limited by the CIP acceptance) studied here. We emphasise again that the observed agreement is meaningless for the very low y region (and probably also for the very high y region, see next section), where the vertex efficiency is a sharply falling function, particularly at the edge of the CJC acceptance for the current jet. An extension of the precise F_2 measurement towards very low y using the Σ method will

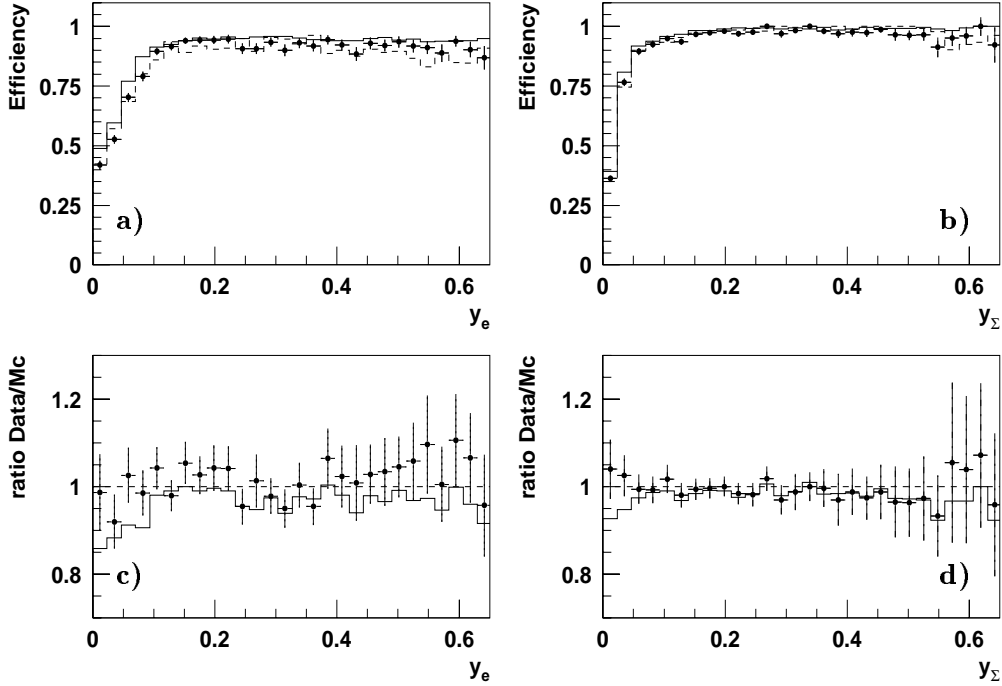


Figure 6.4: Vertex efficiency in function of y_e (a) and y_Σ (b). The full points, solid and dashed line correspond respectively to the efficiencies obtained using the CIP method applied to the data (SV), and from the Monte Carlo simulations with the H1 '94 and MRSDØ parameterisations. The bottom plots (c, d) show the efficiency ratios (data over Monte Carlo, histogram and dots being respectively for the H1 '94 and MRSDØ parameterisations).

require different tools for understanding the vertex efficiency. Meanwhile, we are satisfied with the present level of uncertainty of the vertex efficiency at low y , in view of the large errors from different other sources, dominating the F_2 measurement precision there.

6.1.4 Vertex efficiency at low x - low Q^2

For a small part of the kinematic plane covered by the H1 measurements, the scattered quark is ejected backwards, with θ_j approaching 180° , sometimes outside the CJC acceptance ($tg\theta_j/2 = tg\theta_e/2 \cdot y/(1-y)$, see also Fig 4.3-b, section 4.2). One could thus suspect a decrease of the vertex efficiency for such events. Unfortunately, the CIP method does not cover this part of the kinematic plane. We have thus to stick to the second method, with all underlying inconveniences and uncertainties.

Since we want to study the vertex efficiency behaviour for events with the current jet emitted backward, it is natural to measure it as a function of θ_j . We first need to make sure that the θ_j resolution is sufficient to observe possible local effects.

The quality of the θ_j reconstruction is summarised in Fig 6.6. The pronounced systematic shift was investigated earlier in section 5.4. The θ_j resolution is poor even for $y_\Sigma \geq 0.1$ and is $\sim 10^\circ$ as $\theta_j \rightarrow 180^\circ$. This is not sufficient to observe a sharp effect as θ_j

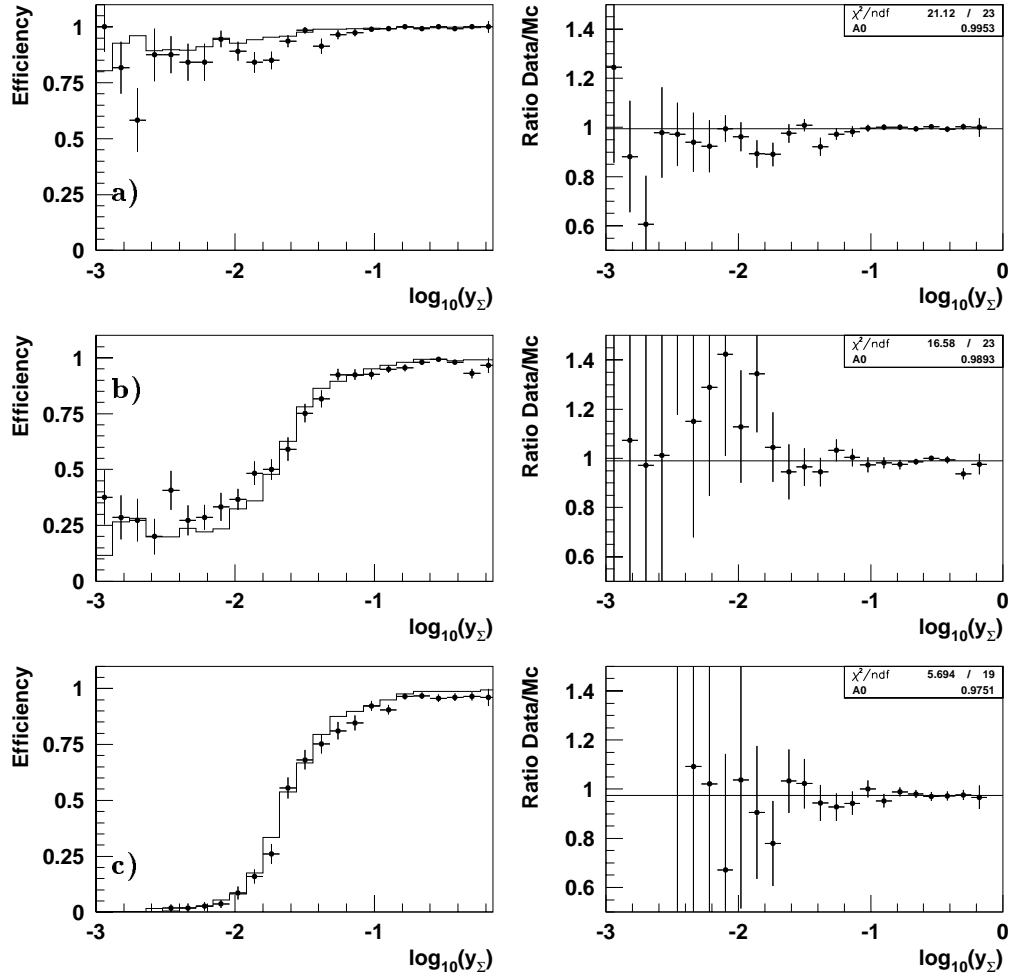


Figure 6.5: Vertex efficiency in function of y_{Σ} in slices of θ_e : a) $165 - 170^\circ$, b) $170 - 172.5^\circ$ and c) $172.5 - 174^\circ$. The left column shows the results of the vertex efficiency measurement for the shifted vertex data using the CIP method (full points) and the Monte Carlo simulation (H1 '94 parameterisation). The right column shows the ratio of these results.

approaches the CJC acceptance edges: such effect would however be visible as a smooth decrease for $\theta_j \geq 170^\circ$.

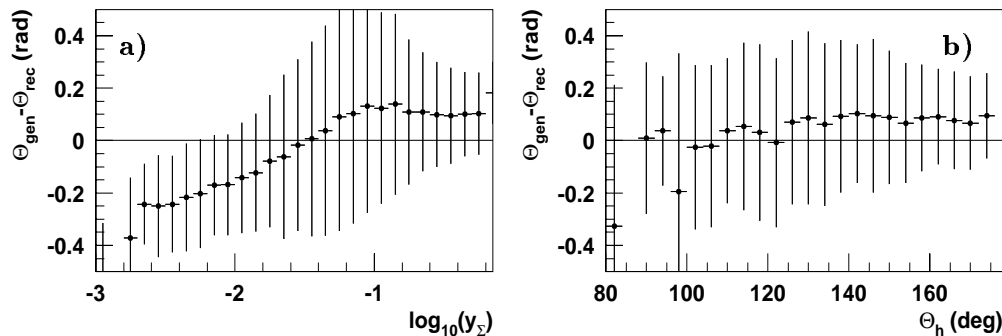


Figure 6.6: Quality of the θ_{jet} reconstruction:

- a) Systematic behaviour of the reconstructed θ_{jet} (θ_{rec}) with respect to the generated θ_{quark} (θ_{gen}) in function of y_Σ : the points are the result of Gaussian fits in slices of y_Σ , the error bars represent the spread (resolution). b) As in (a), but in function of θ_{jet} .

The event sample is selected with the additional requirement $y_\Sigma \geq 0.1$, which insures both a better θ_j resolution and an emphasis on the low x - low Q^2 part of the kinematic plane. Fig 6.7 presents the results in function of θ_j (left) and E'_e (right); the Monte Carlo simulation is performed with the H1 '94 parameterisation. There are only few non- ep background events among the sample with a reconstructed vertex, essentially at low E'_e and at high θ_j . The level of backgrounds (mainly non- ep background) is significantly higher in the sample with no reconstructed vertex, and the background subtraction is done statistically, using pilot bunch events (see section 4.3.1). Statistical fluctuations in the background subtraction can be large, which explains that the vertex efficiency exceeds 1.0 in some bins. The satellite bunch correction is not applied (it is approximately a global factor). The photoproduction background was not taken into account, but one would expect a feeble impact on vertex efficiency.

The two upper figures show the distribution of the selected DIS events with reconstructed vertex in function of θ_j and E'_e . Note that the sharply falling energy distribution around 23 GeV is not correctly reproduced by the Monte Carlo simulation because of the $y_\Sigma \geq 0.1$ cut, the y_Σ method being known to suffer of a systematic calibration bias.

The next two figures present the vertex efficiency measurements obtained from the data (full points) and from the Monte Carlo (solid line). The two bottom figures are the efficiency ratio (data over Monte Carlo), with a straight line fit superimposed. The result of the fit is close to that obtained before (see for example Fig 6.5-c). Note however that the satellite correction would bring it slightly up, in agreement with the previous results.

It is difficult to argue that a fall of the vertex efficiency does not exist for $\theta_j \geq 170^\circ$. It still may be a matter of background subtraction or a statistical fluctuation. There is a similar drop (while statistically less significant) at low E'_e . We thus do not exclude the possibility of a $\sim 5\%$ drop of the vertex efficiency at high θ_j .

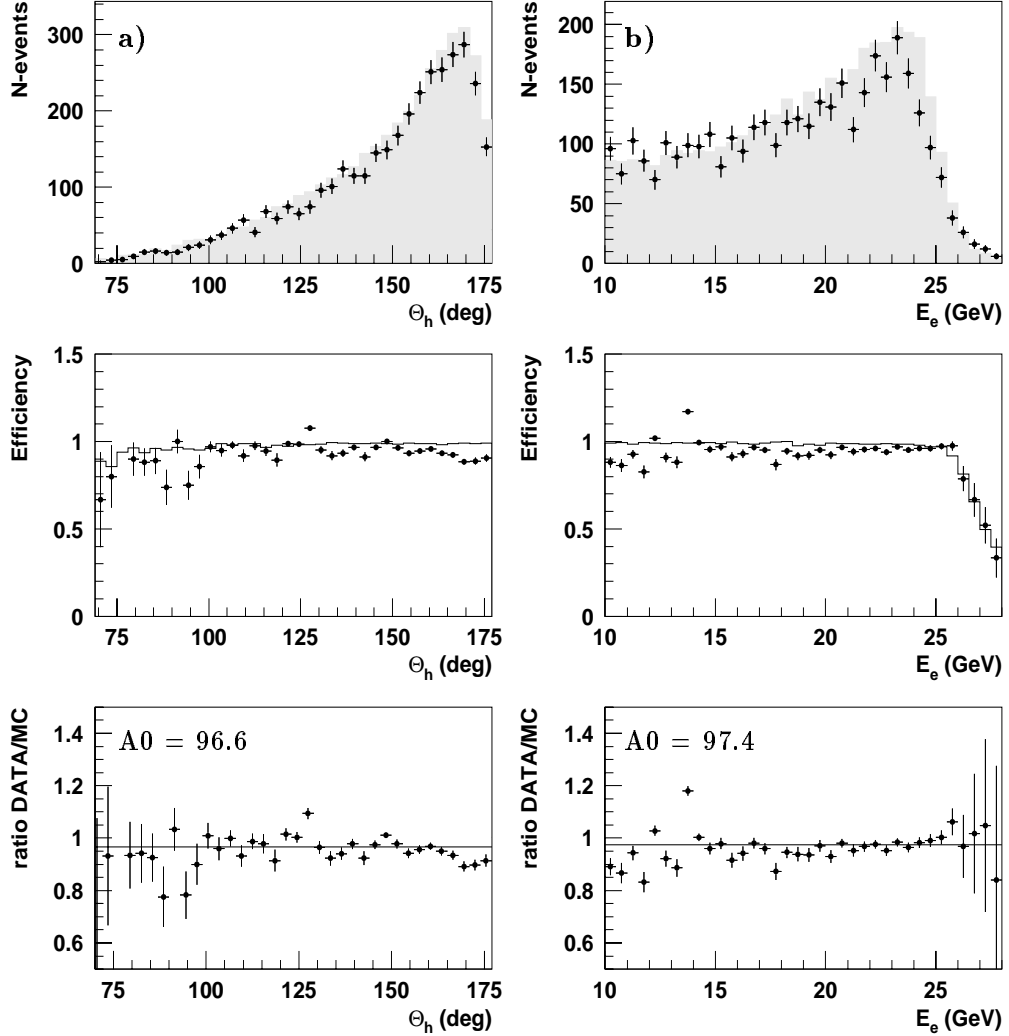


Figure 6.7: Vertex efficiency for the low Q^2 - low x sample ($0.1 \leq y_{\Sigma}$, $E_e' \geq 10$ GeV), with the current jet dominantly emitted in the most backward direction (the CJC acceptance is limited to $\sim 171^\circ$ in case of the shifted vertex data), in function of θ_{jet} (left) and E_e' (right). The two upper figures are the distributions of the selected events with a reconstructed vertex for the data (full points) and the Monte Carlo simulation (H1 '94 parameterisation, shaded histogram). The central figures are the vertex efficiencies obtained with the second method, after background subtraction using the pilot bunch events (data - full points, Monte Carlo - histogram). The bottom plots are the ratios of these efficiencies (data over Monte Carlo (full points) and a linear fit to them (solid line)).

It would be interesting to perform a similar analysis with the nominal interaction vertex data, where the CJC acceptance is smaller with respect to the backward-scattered quark and the effect should be more pronounced. Note however, that the effect is probably not very strong, even for the nominal vertex, because of the colour correlation in “normal DIS” events between the struck quark and the proton remnant: the central θ region is filled with hadronisation particles, paying off with a reconstructed vertex. This is presumably not true for the rapidity gap events. In this case, the effect may also depend on whether the pomeron is dominantly composed of gluons or quarks. In the latter case the hadronic jet tends to be confined in a small solid angle around the struck quark direction, while in the former case more hadrons are produced due to gluon radiation, weakly correlated with the struck quark direction. Tests performed with a Monte Carlo simulation [41], for a slightly higher Q^2 range (nominal vertex interactions, $Q^2 \geq 5 \text{ GeV}^2$) and for $y \geq 0.4$, showed that the vertex efficiency does not decrease if the pomeron is gluon-like, whereas there is a 10% decrease of the vertex efficiency if the pomeron is quark-like. Thus if rapidity gap events represent 10% of the total DIS bulk, the vertex efficiency will decrease by a mere 1%, yet integrated over the θ_j range corresponding to $Q^2 \geq 5 \text{ GeV}^2$ and $y \geq 0.4$. The latter class of events can thus induce a measurable vertex efficiency decrease in the kinematic region studied here. The remaining questions then concern the size of the rapidity gap contribution for the lowest Q^2 range, and the nature of the dominant pomeron component. The '95 SPACAL-calorimeter data analysis enlarges the kinematic plane coverage down to $Q^2 \sim 0.35 \text{ GeV}$ and $x \sim 6 \cdot 10^{-6}$, and will require a careful investigation of this phenomenon.

6.1.5 Forward vertex efficiency

In order to increase the global vertex efficiency at low y , it is interesting to include in the sample events with only a forward reconstructed vertex (see page 66, section 4.4.2).

Fig 6.8 shows the proportion of events with only a forward reconstructed vertex, compared to the total amount of DIS events, as a function of y_Σ (*a*) and θ_e (*b*). The full points correspond to the shifted vertex data, and the solid line to the Monte Carlo simulation (H1 '94 parameterisation). As expected, the forward vertex contribution increases at very low y , where the current jet is emitted outside the CJC acceptance but still inside the forward tracker acceptance (*a*). Furthermore, relatively few events with the scattered electron crossing the CJC have only a forward vertex (*b*). The Monte Carlo simulation tends to reproduce correctly the efficiency of the forward vertex reconstruction, without any significant bias.

6.2 BPC hit association losses

Two different aspects of the BPC hit association to the scattered electron cluster centroid are studied here: its energy dependence and the geometrical uniformity over the BPC volume. The BPC chamber was introduced in section 3.1.2 and the EBPC estimator was defined in section 4.4.2. To recollect, EBPC is the distance, in the BPC plane, between the cluster centroid projection onto it and the closest BPC hit. The intrinsic BPC efficiency (hardware and reconstruction efficiencies) is known to be independent of the electron energy and weakly dependent on the $r-\phi$ position (for more details, see [53]). However, the EBPC efficiency is expected to decrease at low scattered electron energy due to a worse cluster

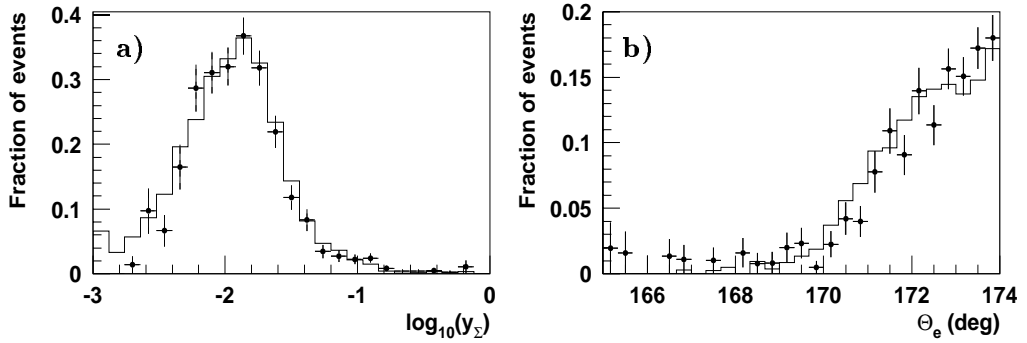


Figure 6.8: *Fraction of events with only a forward reconstructed vertex:*
a) in function of y_{Σ} (full points: data, solid line: Monte Carlo, H1 '94 parameterisation); b) in function of θ_e .

centroid resolution, i.e. the EBPC distribution is wide at low energy, and a measurable fraction of genuine DIS events can have an EBPC distance greater than 5 cm (our cut). However, an apparent EBPC inefficiency can be observed due to photoproduction and non- ep backgrounds (see Fig 4.8), which become important at low energy. As to the geometrical uniformity, particular attention has to be paid at the inner and outer BEMC and BPC edges, i.e. at $R \sim 14$ and ~ 64 cm.

The EBPC efficiency is estimated as:

$$\mathcal{E}_{EBPC} = \frac{N^{EBPC \leq 5 \text{ cm}}}{N^{EBPC \leq 5 \text{ cm}} + N^{other}}, \quad (6.3)$$

where $N^{EBPC \leq 5 \text{ cm}}$ is the number of events satisfying the $EBPC \leq 5$ cm requirement and N^{other} is the number of events with $EBPC > 5$ cm or without any reconstructed BPC hit in the vicinity of the identified electron candidate cluster. The latter number is difficult to estimate because of the background contamination (both photoproduction and non- ep backgrounds), particularly high at low scattered electron energy. The photoproduction background was simulated with the PHOJET generator and normalised absolutely, to the integrated luminosity. When studying the energy dependence of the EBPC requirement, an additional background filter, based on CIP detector signals⁵, was used. It allows for an efficient rejection of non- ep background events, and also to reduce the photoproduction contamination. Unfortunately, it is limited by the CIP detector geometrical acceptance and can not be used when studying the radius dependence of the EBPC efficiency. However, since the radius dependence is uncorrelated with energy, we avoid the background contamination by requiring $E_e' \geq 20$ GeV, without use the CIP filter.

Fig 6.9 presents the EBPC estimator efficiency as a function of the scattered electron energy and of the cluster centroid radius. The bottom plots (*c*, *d*) are the ratios of the

⁵It consists in requiring a CIP signal on the straight line between the interaction vertex and the scattered electron impact position in the BPC (or in the BEMC if there is no reconstructed BPC signal). For more details see [52].

efficiencies obtained from the data and using the Monte Carlo simulation, with a straight-line fit superimposed.

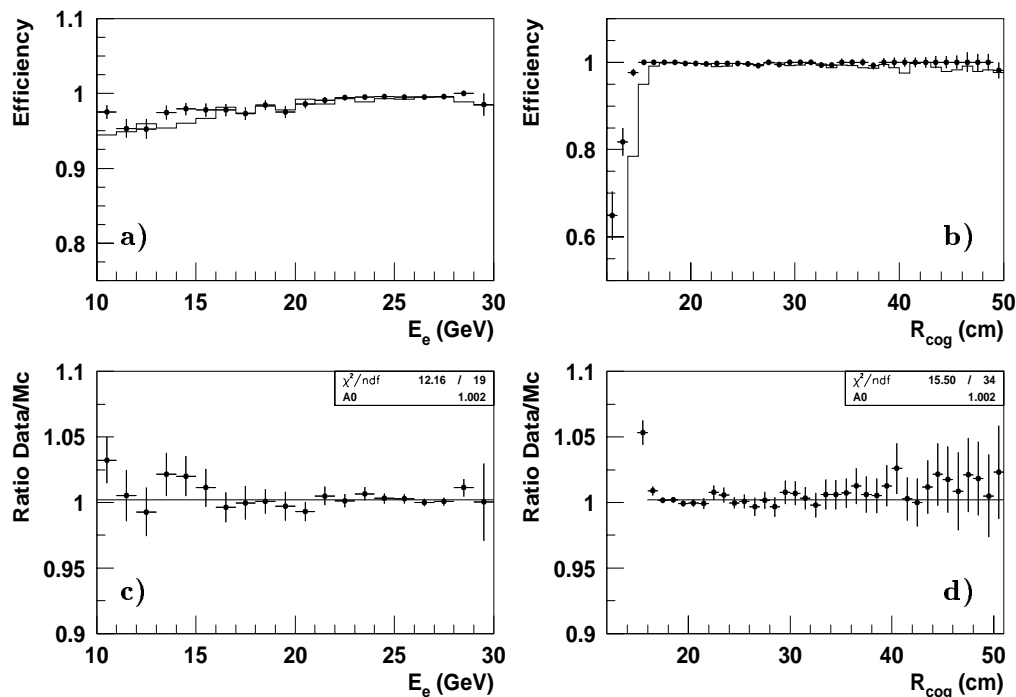


Figure 6.9: *EBPC* requirement efficiency in function of a) the scattered electron energy E'_e and b) the radius of the centroid position R_{cog} (full points: obtained from the data; solid line: using the Monte Carlo simulation). The bottom plots (c, d) are the corresponding ratios (data over Monte Carlo), with a straight-line fit superimposed onto it.

One can see that the E'_e -dependence of the *EBPC* efficiency is reproduced by the Monte Carlo simulation with satisfactory precision in the energy range shown here. Note however, that the photoproduction background description by the Monte Carlo is subject to a systematic uncertainty⁶, not shown on Fig 6.9, which could shift the simulated *EBPC* efficiency at low energy up or down by a few percent.

As to the R -dependence, a visible edge effect is observed for $R_{cog} \leq 16$ cm. This effect is attributed to a poor simulation. In order to avoid corrections, we limit the DIS selection to $R_{bpc} \geq 15$ cm (corresponding to $R_{cog} \geq 16$ cm after parallax correction). This is in fact the main limitation to the accessible fiducial volume at low Q^2 . A dedicated study of the outer BPC-BEMC edge was presented in [41]. It appears that the discrepancies between data and Monte Carlo are as high as 1 to 5% as R approaches 64 cm⁷.

⁶Using the control sample of electron tagged γp events, the uncertainty due to photoproduction background is estimated to be $\approx 30\%$ of the applied correction [43].

⁷The following corrections are applied to the Monte Carlo efficiencies, to account for discrepancies between data and Monte Carlo at the outer BPC edge [41]:

6.3 ECRA requirement losses

The ECRA estimator has been introduced in section 4.4.2. Here, we study the ECRA efficiency with respect to the scattered electron energy and the geometrical uniformity. The latter point is definitely less relevant than in the case of EBPC, since ECRA is mainly defined by the transversal spread of the electromagnetic shower, which has no reason to vary significantly within the BEMC volume.

Fig 6.10 presents the ECRA efficiency as obtained from the data and with the Monte Carlo. Again, as for EBPC, a small decrease of the ECRA efficiency (cut at 5 cm) is observed for low electron energies (see Fig 6.10-*a*). This feature is attributed to noise fluctuations in cells included in the BEMC cluster, which have a larger effect for low cluster energy and can thus induce an apparent widening of the cluster radius (ECRA) at low electron energy. In addition, the background contamination increases at low energy, and leads to an *apparent* decrease of the ECRA efficiency (see Fig 4.5 and Fig 4.8-*b*). The effect of the photoproduction background on the ECRA efficiency is illustrated on Fig 6.10-*a*. At 10 GeV, the ECRA efficiency compared using the Monte Carlo varies by $\sim 10\%$ (from 85% to 95%), depending on whether the photoproduction background (normalised to luminosity) is included or not in the Monte Carlo sample. Taking into account this systematic uncertainty, the Monte Carlo simulation describes the data well (note that only events with $y \leq 0.6$ or equivalently $E_e \geq 11$ GeV are used in the present analysis)

6.4 Summary

The vertex efficiency has been studied and compared with the results of Monte Carlo simulations. For the latter, it is shown that the vertex efficiency is strongly dependent on the F_2 input parameterisation, mainly through QED radiation. The pure “electron-like” vertex efficiency, i.e. estimated as a function of θ_e and E'_e , is the most sensitive to the QED radiative effect, and thus appears as inappropriate to draw quantitative conclusions on the agreement between the efficiencies estimated from the data and using the Monte Carlo. On the other hand, the “mixed” kinematics vertex efficiency, i.e. in θ_e and y_Σ , provides a less biased picture. It is less sensitive to radiative effects and provides a better context for global quantitative estimates of the quality of the data description by the Monte Carlo simulation. However, it does not allow for studying possible local effects, in particular at the CJC edges, because of the poor y_Σ resolution. Future high precision analyses based on SPACAL data extended towards low y at low Q^2 should study this matter thoroughly.

Using the CIP method to estimate the vertex efficiency in function of θ_e and y_Σ , it was found that there is a global agreement between the data and the Monte Carlo simulation. At low Q^2 , a $\leq 3\%$ systematic difference was observed. We stress again that the observed agreement is probably insignificant at the CJC edges with respect to the current jet direction, i.e. at low y (kinematic peak) or at low x and low Q^2 (see Fig 4.3-*a, b*), because of the poor y_Σ resolution.

Q^2 (GeV ²)	25.0	35.0	45.0	60.0	90.0	120.0	150.0
correction	1%	1%	2%	2.5%	3%	4%	5%

Note that for the Q^2 range used in the present thesis, only relatively low y values are reached for the F_2 measurement, and it is therefore equivalent to apply corrections in Q^2 or in θ_e .

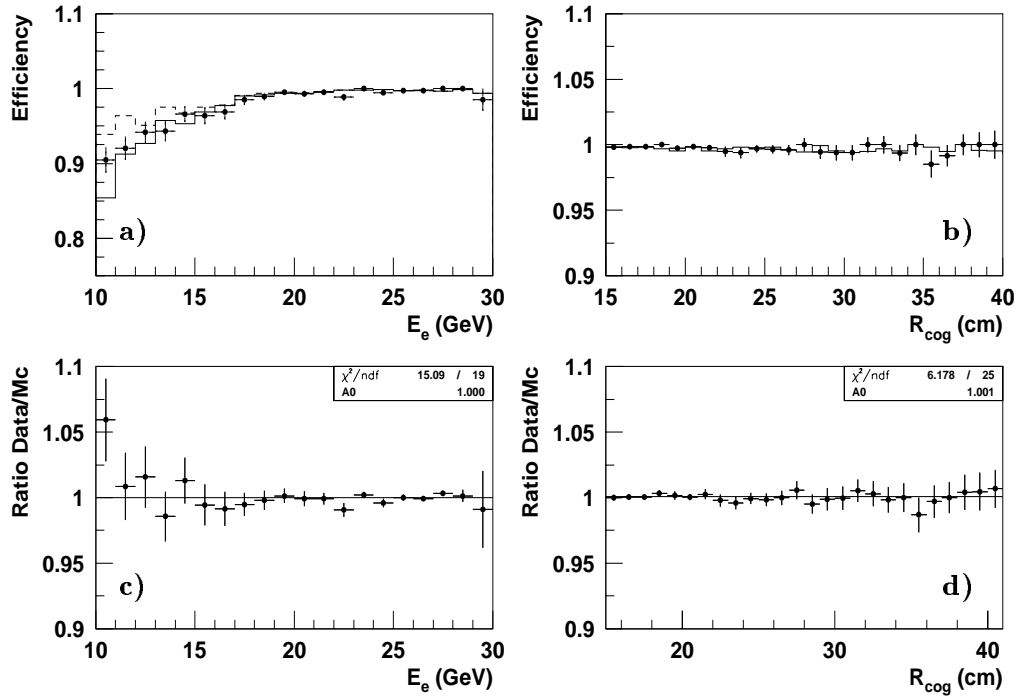


Figure 6.10: *ECRA requirement efficiency in function of a) the scattered electron energy E'_e and b) the radius of the centroid position R_{cog} (full points: data, solid line: Monte Carlo including photoproduction background, dashed line: Monte Carlo without photoproduction background). The plots (c, d) are the corresponding ratios (data over Monte Carlo including γp background) with a straight-line fit superimposed onto it.*

An attempt has been performed to improve the understanding of the vertex efficiency in the latter kinematic range by estimating it as a function of the purely topological quantities: θ_e and θ_j . The resolution of the latter quantity for $\theta_j \rightarrow 180^\circ$ is of $\sim 10^\circ$. Although this resolution is not sufficient to observe clearly a possible sharp fall of the vertex efficiency when the current jet leaves the CJC acceptance volume, a possible $\sim 5\%$ disagreement between the data and the Monte Carlo vertex efficiencies was found for $\theta_j \geq 170^\circ$. The effect is probably limited because of the colour correlation in “normal DIS” events between the struck quark and the proton remnant: the central θ region is filled with hadronisation particles, probably giving a vertex. An eventual vertex efficiency decrease can be attributed to the presence in the DIS sample of the rapidity gap events. The effect would be more pronounced since the dominant pomeron component is quark-like, while the gluon-like pomeron seems to have less or no impact on the vertex efficiency [41]. It would however require a better understanding with increasing statistics and a study extended towards very low Q^2 and x kinematic range. For instance, the rapidity gap contribution has to be included in the Monte Carlo event sample.

In the Monte Carlo simulation [41] the effects of the W limitation on the vertex efficiency was found to be small for the low Q^2 - low x part of the kinematic plane (less

than 0.5%), while it is not negligible at low y , and has to be investigated further for future analyses.

The EBPC and ECRA efficiencies were found to be correctly reproduced by the Monte Carlo simulation.

Taking into account similar results obtained for the nominal vertex data [41, 42, 51], an overall 2% error is assigned due to the imperfect description of the various efficiencies with the Monte Carlo simulation. In [8], a larger error was added to account for the vertex reconstruction efficiency at low Q^2 ($Q^2 \leq 8.5 \text{ GeV}^2$, up to 4%) and at large x (low y , up to 8% [42, 51]).

Chapter 7

F_2 measurement

In the previous chapters we have presented a detailed discussion of the available data, of the Monte Carlo simulation and the detector calibrations, resolutions, efficiencies and systematic effects. We are now ready to present the results of the F_2 structure function measurement, together with an accurate estimate of systematic errors. We start by impairing the “final touch” to the Monte Carlo simulation. Next, the kinematic range in which an F_2 measurement is possible is determined and the appropriate method for the kinematic reconstruction (i.e. “electron” or Σ) is discussed. The results of the F_2 measurement are presented and compared for different kinematic reconstruction methods and for different event samples, i.e. satellite bunch, shifted vertex, nominal vertex open and closed triangles data samples. The final F_2 measurement from the 1994 data [8] uses results obtained with these different data samples, allowing for a better coverage of the kinematic plane. This thesis contributes to the H1 '94 measurement [8] in the lowest Q^2 part ($1.5 \leq Q^2 \leq 6.5$ GeV²), using a combination of analyses of the satellite and the shifted vertex data sample.

7.1 Event samples and data to Monte Carlo comparisons

In this section we will first deal with the reweighting of the Monte Carlo vertex distribution, which did not reproduce with satisfactory precision the data in the original simulation. Then the reweighting procedure of the Monte Carlo events is presented, in view of minimizing the influence of the choice of the input parton distribution set (originally GRV [76]). This is an essential feature of our Monte Carlo based iterative method of F_2 extraction. Next, correctness of the implementation of radiative corrections in the DJANGO Monte Carlo simulation is verified. Finally, the achieved quality of the Monte Carlo simulation will be demonstrated by comparing the Monte Carlo predictions for various distributions with the data.

7.1.1 Reweighting of the z -vertex distribution

Fig 7.1-*a* presents the distribution of the z coordinate of the interaction vertex, for the shifted vertex data and for the original Monte Carlo simulation, together with the corresponding ratio and a straight-line fit to it (*c*). The Monte Carlo simulation reproduces poorly both the mean z -position and the width (σ) of the experimental z -vertex distribution. This means that the Monte Carlo simulation does not reproduce correctly the fraction of events lost because of the BPC-BEMC acceptance limitation. When using the Monte Carlo method for the F_2 measurement, it appears that even a shift of a few cm of the z -vertex distribution in the Monte Carlo leads to a measurable modification of F_2

(mostly at low Q^2 , where the bins are strongly affected by the acceptance limitation, see for example Fig 7.5).

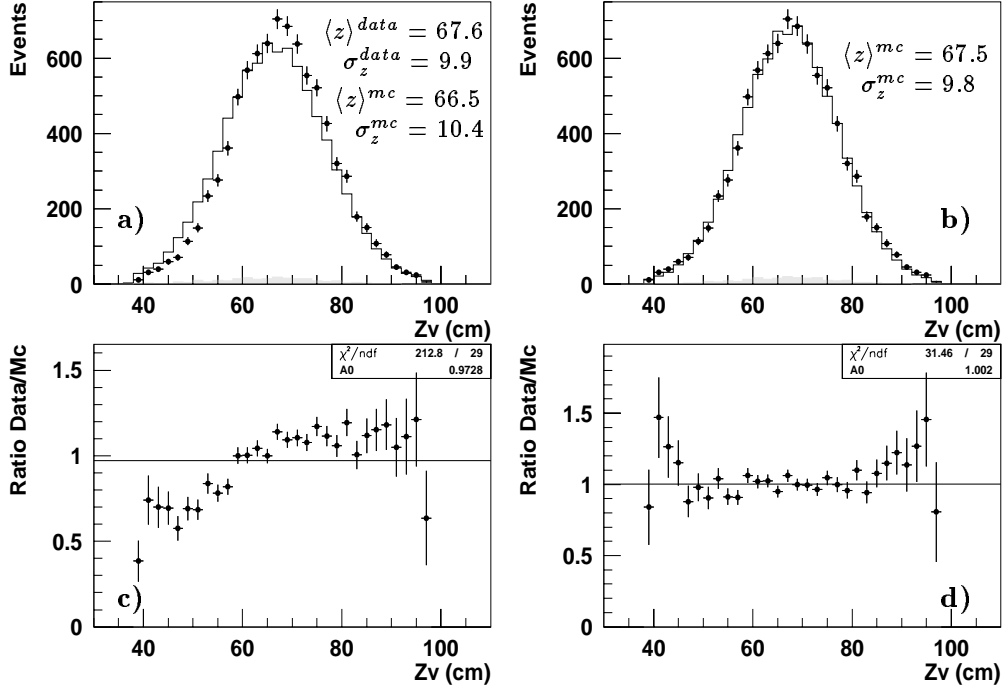


Figure 7.1: The z -vertex distribution for the shifted vertex data (full points) and Monte Carlo simulation (solid line: DIS (DJANGO); shaded histogram: photoproduction (PHOJET)) a) before and b) after reweighting (absolute normalisation to the total integrated luminosity). The bottom plots (c, d) show the ratio of the z -vertex distributions for the data and as obtained from the Monte Carlo, together with a straight-line fit to it.

To determine correctly the mean position and the width of the z -vertex distribution, one has to take into account the BPC-BEMC geometrical acceptance effect, which increases in the decreasing z -direction and biases the shape of the z -vertex distribution. The best solution would be of course to use a sample of events, selected without using the BPC-BEMC trigger, as for example the e -tagger triggered (photoproduction) events. For the time being, this was not done for technical reasons. A less “clean” solution, adopted here, is to restrict the sample of DIS events to the θ range where the scattered electron remains inside the BPC-BEMC acceptance for the whole z -vertex range of the event sample. Thus obtained (data and MC) z -vertex distributions can be reliably measured and the estimated unbiased width and central position are used to reweight the original Monte Carlo z -vertex distribution on an event by event basis (before the detector effects are included, i.e. generated distribution). Technically, each Monte Carlo event is assigned a weight proportional to the ratio of the two Gaussian distributions describing the vertex z -coordinate corresponding respectively to the Monte Carlo and the data. Of course, in order to preserve the total number of simulated Monte Carlo events, the surface beneath

End of run range	z_0 [cm]	σ [cm]
76344	0.000	11.000
78380	-0.900	10.800
82005	0.200	10.600
82960	0.200	10.600
83819	4.200	10.600
84040	7.400	10.400
84600	3.000	10.900
85300	1.800	12.100
86000	-3.500	10.300
86750	3.300	10.400
89468	5.700	10.400
89928	3.800	10.600
90003	65.900	10.000
90026	70.200	10.000
90419	5.200	10.100

Table 7.1: *H1* database lookup table of the nominal z -vertex for *H1* run ranges (from [20]).

The nominal ep interaction position and the longitudinal shape of the p -bunch (which determines the shape of the observed z -vertex distribution) were evolving in time due to slightly different HERA injection conditions.

the Gaussians must be kept constant. To be precise, one should also take into account that the fraction of events generated outside the BPC-BEMC acceptance and definitely lost, which varies depending on the generated z -vertex distribution. This is however a second order correction, which we discard here.

Fig 7.1-*b* presents the z -vertex distribution for Monte Carlo events, resulting from the procedure described above. As designed, the Monte Carlo reproduces the data much better. The reasons for the minor disagreement in the tails are the following: first, the z -vertex distribution is not exactly Gaussian (see subsection “FToF data analysis”, section 2.3.1); second, the remaining non- ep background, not included in the Monte Carlo, is approximately uniformly distributed along z (see Fig 4.7-*a*), producing an excess of events at the edges of the z -vertex distribution. The slightly different Monte Carlo normalisation after reweighting (see fit parameters, Fig 7.1-*c*, *d*) can be understood in view of the Q^2 cut used here to select the data and the Monte Carlo event samples ($Q^2 \geq 3.0 \text{ GeV}^2$), which induces more losses when the z -vertex distribution is shifted towards the BEMC (decreasing z -direction, i.e. before reweighting).

The z -vertex distribution is tuned in a similar way in the case of the satellite bunch data sample and in the case of the nominal vertex data sample. The latter was performed separately for data taking periods characterised by similar HERA injection parameters, reflecting in a similar width and mean position of the interaction region [41]. Table 7.1 [20] summarises the evolution of the z -vertex distribution over the whole '94 data taking period.

7.1.2 Reweighting of the input F_2 parameterisation

In the iterative procedure of the F_2 determination, the experimental F_2 measurement is introduced as an input of a new Monte Carlo simulation. However, it is not possible to resimulate the whole set of Monte Carlo files (> 1 M events), once the F_2 measurement is available. A different solution has been adopted here, consisting in reweighting the already simulated Monte Carlo set on an event by event basis, according to the F_2 parameterisation obtained from the latest obtained F_2 measurement.

To a good approximation the event weight is:

$$Weight(F_2^{MC}(x, Q^2), F_2^{MEAS}(x, Q^2)) = \frac{F_2^{MEAS}(x, Q^2)}{F_2^{MC}(x, Q^2)}, \quad (7.1)$$

where $F_2^{MC}(x, Q^2)$ is the original Monte Carlo simulation structure function (in our case obtained from the GRV parameterisation [76]) and $F_2^{MEAS}(x, Q^2)$ is the measured (new) structure function. This is sufficiently precise if y is not too high. At high y , however, the F_L contribution becomes significant, modifying the (x, Q^2) event distribution and thereby the DIS cross section. We discuss this in the following.

The DJANGO Monte Carlo program [55] uses the program HERACLES [56] to generate events at the parton level, which in turn are fragmented and hadronised using DJANGO routines based on LEPTO [57] and JETSET. The cross-section for deep inelastic scattering is defined in the one-boson exchange approximation and takes into account higher-order QCD corrections only in the leading order approximation (LO):

$$\frac{d^2\sigma}{dx dy}^{LO} = \frac{2\pi\alpha^2}{xyQ^2} [Y_+ F_2(x, Q^2) + Y_- F_3(x, Q^2)], \quad (7.2)$$

with

$$Y_{\pm} = 1 \pm (1 - y)^2. \quad (7.3)$$

Non-logarithmic $\mathcal{O}(\alpha_s)$ corrections are to be taken into account explicitly: in the DIS scheme, these corrections show up as a non-zero longitudinal structure function F_L . The longitudinal structure function is taken into account in the calculation of the cross section by HERACLES. The corrected DIS cross section is:

$$\frac{d^2\sigma}{dx dy}^{\mathcal{O}(\alpha_s)} = \frac{d^2\sigma}{dx dy}^{LO} - \frac{2\pi\alpha^2}{xyQ^2} y^2 F_L(x, Q^2). \quad (7.4)$$

The inclusion of F_L affects the (x, Q^2) distribution and thereby the cross section, but not the generation of the hadronic part of the event. The effect is up to 10% at high y in the lowest Q^2 bins. It can be defined as [57]:

$$F_L = F_L^{QCD}(x, Q^2) + F_L^{TM}(x, Q^2) + F_L^{HT}(x, Q^2), \quad (7.5)$$

where F_L^{QCD} , F_L^{TM} and F_L^{HT} are respectively the QCD contribution, the target mass correction and the higher twist contribution. The QCD contribution (leading twist) is to order α_s given by [58]

$$F_L^{QCD}(x, Q^2) = \frac{4\alpha_s(Q^2)}{3\pi} x^2 \int_x^1 \frac{dy}{y} F_2(x, Q^2) + \frac{2\alpha_s(Q^2)}{\pi} \sum_f e_f^2 x^2 \int_x^1 \frac{dy}{y^3} (1 - \frac{x}{y}) y g(y, Q^2), \quad (7.6)$$

where the sum runs over the quark flavours, and $g(y, Q^2)$ is the gluon density estimated from a QCD fit to the data. The first term originates from the gluon radiation diagram and the second from the photon-gluon fusion. F_L^{QCD} gives an important contribution at small x , where the gluon term dominates. The target mass correction to $\mathcal{O}(m_p^2/Q^2)$ is given by [58, 59]

$$F_L^{TM}(x, Q^2) = 4 \frac{m_p^2}{Q^2} x^3 \int_x^1 \frac{dy}{y^2} F_2(y, Q^2) - 2 \frac{m_p^2}{Q^2} x^2 F_2(x, Q^2). \quad (7.7)$$

Finally the (dynamical) higher twist contribution to $\mathcal{O}(1/Q^2)$ can be written as [58, 59]

$$F_L^{HT}(x, Q^2) = 8 \frac{\kappa^2}{Q^2} F_2(x, Q^2). \quad (7.8)$$

In the kinematic range studied here only F_L^{QCD} contributes significantly, and the two other contributions can be safely disregarded [60]. The longitudinal structure function can thus be parameterised using expression 7.6 and using the F_2 measurement and the gluon density g estimated from a QCD fit to the data:

$$F_L^{MEAS}(x, Q^2) = F_L^{QCD}(F_2^{MEAS}(x, Q^2), g(x, Q^2)). \quad (7.9)$$

The Monte Carlo event weight including the F_L effect is finally taken as:

$$Weight(F_2^{MC}, F_L^{MC}, F_2^{MEAS}, g, x, Q^2) = \frac{d^2 \sigma^{MEAS} / dx dy}{d^2 \sigma^{MC} / dx dy}, \quad (7.10)$$

where the differential cross section is calculated according to expressions 7.4 and 7.9, and x, Q^2 values are calculated at the hadronic vertex¹.

This procedure is equivalent to resimulate Monte Carlo files with a new input parton distribution set and is applied *on-line*, when running over Monte Carlo event files². Fig 7.2 presents the scattered electron energy distribution from the data (shifted vertex) and that obtained using the Monte Carlo simulations (*a*) using the original GRV parameterisation; *b*) reweighted according to the new parameterisation based on the H1 '94 measurements, according to the procedure described above.

¹The differential cross section calculated using the hadronic vertex kinematics is in a good approximation the Born cross section since the radiative corrections on the hadronic side are small. Furthermore, these radiative corrections do not depend on the structure function choice, as do the radiative corrections on the leptonic side.

²A powerful possibility is provided by the latest PAW [61] development - the dynamic shared libraries interface - allowing for subsequent calls to the external program libraries from *inside* a PAW interactive session. The Monte Carlo input structure function reweighting is thus done interactively, inside PAW sessions.

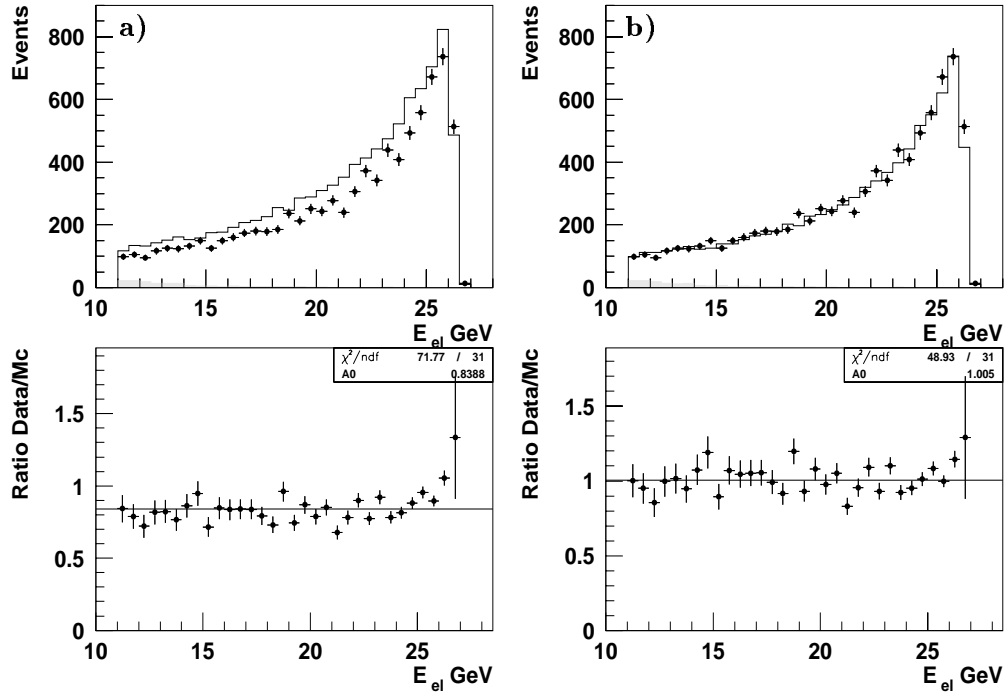


Figure 7.2: Distribution of the scattered electron energy E_e' for the data (shifted vertex, points) and obtained from the Monte Carlo simulation (histogram) a) before and b) after reweighting of the Monte Carlo input structure function (originally based on the GRV parton distribution set [76]), reweighted on an event by event basis to the H1 '94 QCD fit [8, 69, 70] and including the F_L effect; the normalisation is performed to the integrated luminosity. The lower range figures are the corresponding ratios (data over Monte Carlo) with a straight-line fit superimposed.

7.1.3 Implementation of the electroweak radiative corrections

The HERACLES [56] Monte Carlo generator includes $\mathcal{O}(\alpha)$ QED corrections due to photon radiation from both the lepton and the quark, as well as the complete one-loop virtual corrections. The accuracy of the implementation of radiative corrections in DJANGO was checked by comparing with the HECTOR [62] analytical calculations. The latter describe QED corrections up to order $\mathcal{O}(\alpha^2)$ in the leading logarithmic approximation (LLA).

Fig 7.3-a presents a comparison of the radiative corrections to the DIS Born cross section ($1 + \delta$) as obtained using the DJANGO Monte Carlo simulation (points) and the HECTOR package (lines), in function of y for three different Q^2 values: $Q^2 = 5, 15$ and 35 GeV^2 . Fig 7.3-b - d are the corresponding differences ($\delta_{Django} - \delta_{Hector}$) with a straight-line fit superimposed. The kinematics used are computed with the “electron” method and detector effects are not included. The HECTOR radiative corrections were calculated here only to order $\mathcal{O}(\alpha)$ for consistency with DJANGO. Note however, that in the kinematic range studied here the difference between calculations of orders $\mathcal{O}(\alpha)$ and $\mathcal{O}(\alpha^2)$ is insignificant.

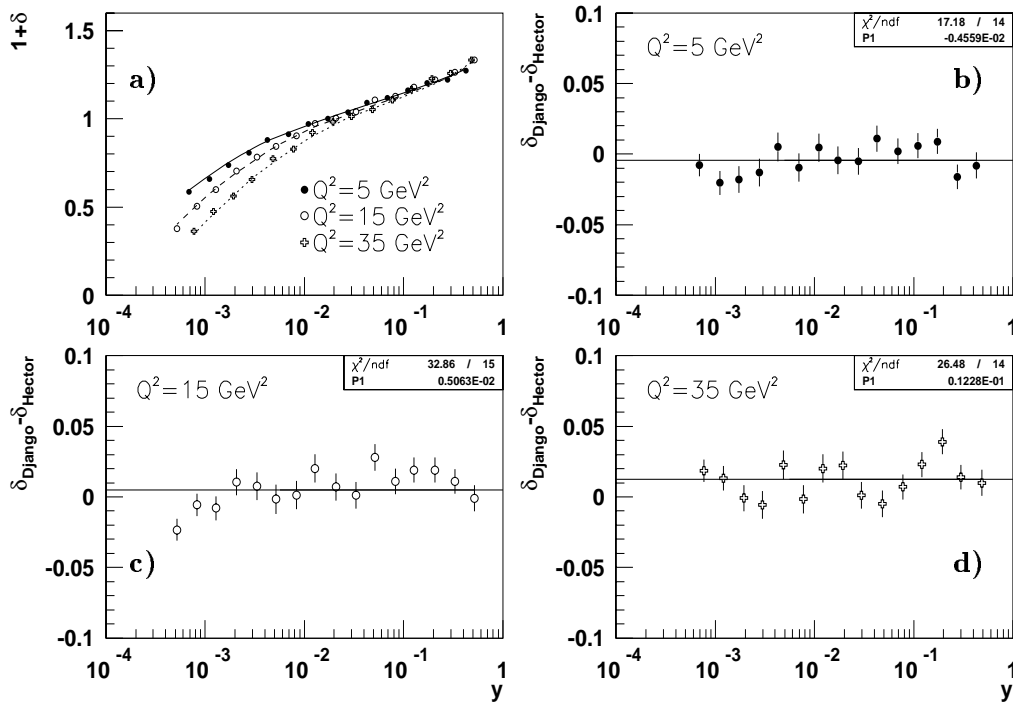


Figure 7.3: a) Electroweak radiative corrections as obtained using the DJANGO Monte Carlo simulation (points) and the HECTOR analytical program (lines) in function of y for three different Q^2 values ($Q^2 = 5, 15$ and 35 GeV^2); b-d) Corresponding differences between DJANGO and HECTOR radiative corrections, together with a straight-line fit superimposed (from [41]).

The obtained ratios of the total cross section to the DIS Born cross section are given for information in Table 7.5. The precision of the comparison presented here is limited by the amount of generated (but not simulated) DJANGO events (more than 10 M events [41]).

The DJANGO statistical error is typically $\sim 1\%$ (≈ 10000 events per point).

DJANGO and HECTOR agree to a few percent level, with a possible systematic effect increasing towards larger Q^2 values. An error of 2% was assigned to the DJANGO radiative corrections, in order to take into account a possible systematic effect in the total DIS cross section description [41].

7.1.4 Final Monte Carlo to data comparisons

Fig 7.4 presents the distributions of various quantities as obtained from the shifted vertex data (full points), and using the Monte Carlo simulation (the solid line represents the total DIS (DJANGO) + photoproduction (PHOJET) predictions, the shaded histogram the photoproduction alone). The distributions of the following quantities are shown: a) the scattered electron energy, b) the scattered electron polar angle θ_e ; c) the current jet polar angle $\theta_{hadrons}$; d) the z -coordinate of the interaction point; e) y_Σ and f) y_e . The event sample is restricted to the Q^2 range $Q^2 \geq 3.0 \text{ GeV}^2$, i.e. to the so-called “golden” region in case of the shifted vertex data. For $Q^2 < 3.0 \text{ GeV}^2$, events mainly originate from the region deep inside the BEMC inner triangles, undergoing an important edge effect, which is difficult to reproduce by Monte Carlo. The Monte Carlo description is therefore slightly worse for this part of the kinematic plane. Note that this is included in the systematic errors (10 to 20% for the $Q^2 = 1.5$ and 2.0 GeV^2 bins).

In general the Monte Carlo simulation describes the data well, except at the BPC-BEMC edges (inner and outer edges), where the agreement is slightly worse (for $Q^2 < 3 \text{ GeV}^2$ and $Q^2 \sim 100 \text{ GeV}^2$). The disagreement between Monte Carlo and data for $y_e \geq 0.6$ (see Fig 7.4-f) is due to the high level of non- ep backgrounds (see also Fig 4.5) not subtracted here.

It is interesting to note some features of the distributions shown here and allowing for the localisation of different systematic effects. For example, the background contamination (both photoproduction and non- ep) is enhanced in the high y_e part of the corresponding distribution, while it is smeared over a large range in the y_Σ and E'_e distributions. In general, the y_Σ distribution is less sensitive to variations of the Monte Carlo simulation parameters, i.e. energy calibration, input parameterisation, etc. Furthermore, in spite of an important y_Σ miscalibration, known *not to be reproduced by Monte Carlo* and studied earlier in section “ y_Σ reconstruction and bias” (see also Fig 5.16), Fig 7.4-e does not give any hint of a problem. It should be noted that Fig 7.4-a – c contain most interesting information as to the quality of the Monte Carlo simulation. The E'_e distribution not only allows for an “integrated” control over the whole selection scheme, i.e. z -vertex efficiency, fiducial y limitation, etc., but also controls the energy smearing description by the Monte Carlo (energy reconstruction and radiative effects), mostly by its shape in the kinematic peak region. The θ_e distribution is sensitive to the detector simulation implementation in general, and particularly to the z -vertex distribution simulation. Finally, the shape of the $\theta_{hadrons}$ distribution at low y (not emphasised here; the Fig 7.4-c distribution is performed for the “electron” selection, i.e. for $y \geq 0.05$) suggests that there may be some hadronic reconstruction miscalibration.

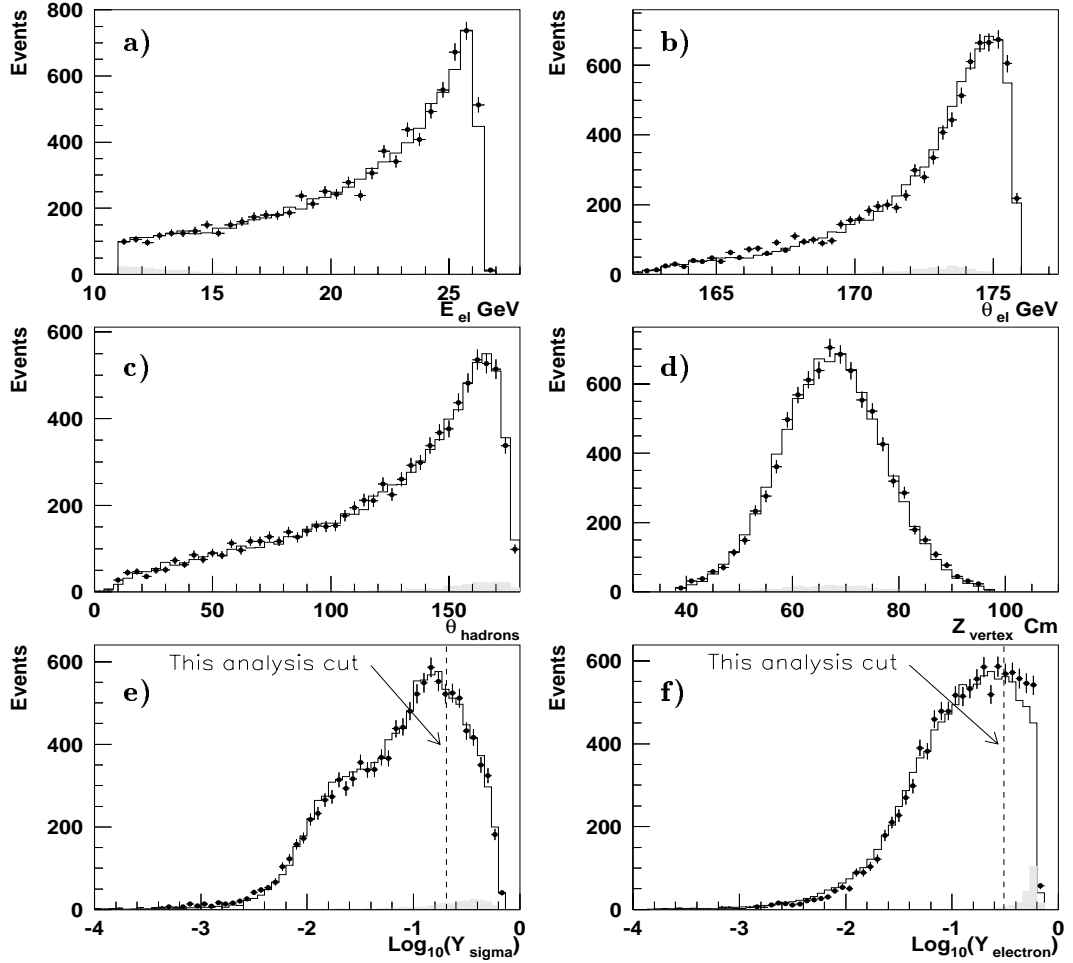


Figure 7.4: a) Distribution of the scattered electron energy as obtained from the shifted vertex data (points) and using the Monte Carlo simulation (solid line: DIS (DJANGO) + photoproduction (PHOJET); shaded histogram: photoproduction alone); b) the scattered electron polar angle θ_e ; c) the current jet polar angle $\theta_{hadrons}$; d) the z coordinate of the interaction position; e) y_Σ and f) y_e . Absolute normalisation to the integrated luminosity.

7.2 Kinematic plane coverage

7.2.1 Binning of the $x - Q^2$ kinematic plane

The following considerations are taken into account when choosing the bin size: (i) the relative ($\delta Q^2/Q^2$ and $\delta x/x$) kinematic resolutions are known to be approximately constant over more than 3 decades in x and two decades in Q^2 . The binning is therefore chosen logarithmically equidistant, for simplicity; (ii) the kinematic resolution (σ_{Q^2} , σ_x) has to remain well below the bin size, so that the bin to bin correlations remain small; (iii) statistics have to be reasonably high. This leads to the following choice of bin boundaries:

Q^2 :	1.334	1.778	2.371	3.162	4.217	5.623	7.499	10.00
	13.34	17.78	23.71	31.62	42.17	56.23	74.99	100.0
	133.4	177.8	237.1	316.2	421.7	562.3	749.9	1000.
x :				.0000251	.0000398	.0000631		
	.000100	.000158	.000251	.000398	.000631			
	.00100	.00158	.00251	.00398	.00631			
	.0100	.0158	.0251	.0398	.0631			
	.100	.158	.251					

The differential cross sections and therefor the F_2 structure function are measured for a discrete set of (x, Q^2) values. These “bin centre” values x_c, Q_c^2 are chosen to be:

Q_c^2 :	1.5	2.0	2.5	3.5	5	6.5	8.5	12
	15	20	25	35	50	65	80	120
	150	200	250	350	500	650	800	1200
x_c :				.000032	.00005	.00008		
	.00013	.0002	.00032	.0005	.0008			
	.0013	.002	.0032	.005	.008			
	.0130	.02	.032	.05	.08			
	.130	.2						

This choice of x_c, Q_c^2 is mainly dictated by the possibility of easy comparisons with other experiments (in particular ZEUS), as well as with earlier H1 measurements.

Fig 7.5 presents the binning of the low Q^2 part of the (x, Q^2) kinematic plane (“electron” method of kinematic reconstruction). The numbers of observed DIS candidate events for the shifted vertex data are indicated for bins where a significant DIS cross-section measurement is performed, together with the estimated background contamination (in brackets). The shaded area corresponds to the part of the kinematic plane affected by the BPC-BEMC acceptance limitation, which progressively deteriorates as θ_e approaches 176.5° .

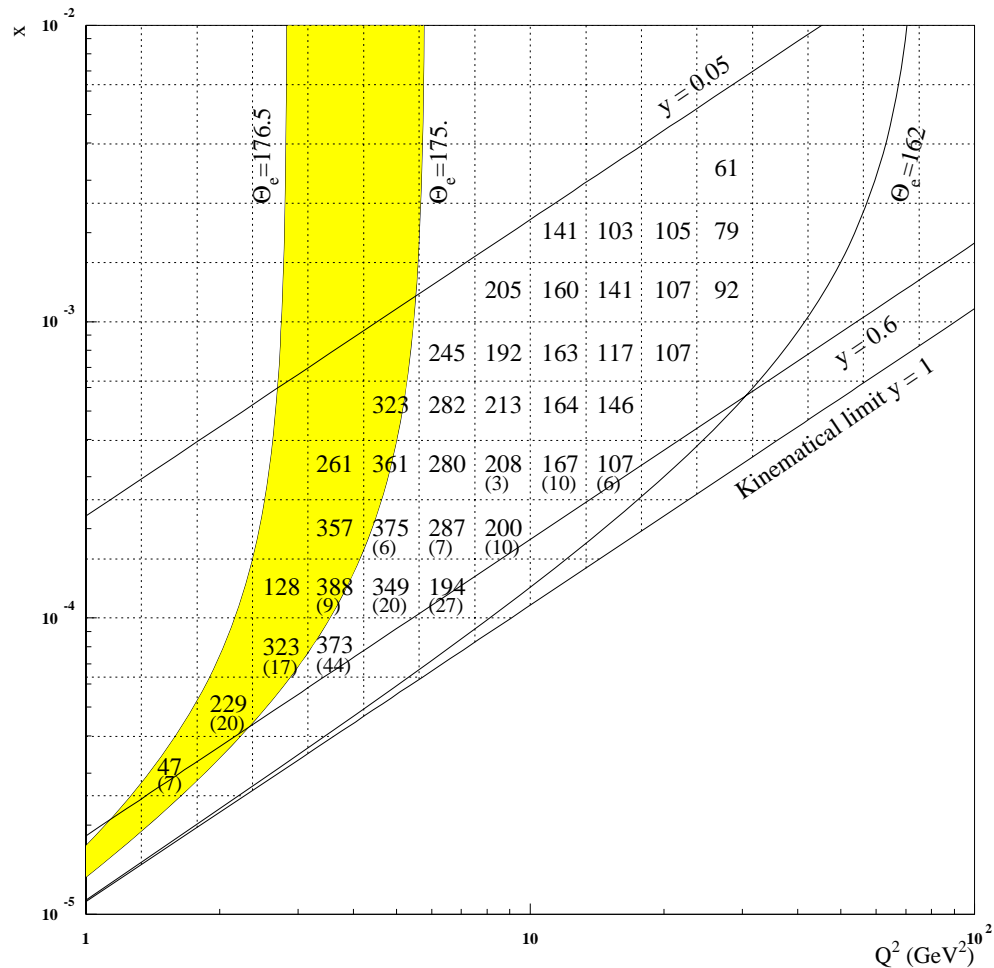


Figure 7.5: Binning of the kinematic plane used for the H1 '94 structure function F_2 measurement. The shaded area corresponds to the region with reduced fiducial volume because of the BPC detector acceptance limitation. The numbers of observed DIS candidates are indicated for bins where the DIS cross-section measurement is performed using the shifted vertex data (“electron” kinematics). In these bins, the number of background events is given in brackets (photoproduction (PHOJET) + non-ep background (from pilot bunches)); when not given, this number is < 1 .

7.2.2 Kinematic measurement resolution and systematic bias

The x and Q^2 resolutions were defined in section 4.2 for the “electron” and the Σ methods of kinematic reconstruction, as a function of the scattered electron energy and of the polar angle resolutions. Here an estimate of the kinematic resolution is presented, including effects of the full detector simulation, i.e. various inhomogeneities in the scattered electron and hadronic final state reconstructions. The estimate is performed separately for the shifted and for the nominal vertex Monte Carlo simulations. The electroweak radiative events are excluded from the Monte Carlo event sample used here. The statistics per bin is of the order of $\sim 100 \div 1000$ unweighted entries in case of the shifted vertex Monte Carlo simulation and approximately twice as high for the nominal vertex.

Fig 7.6 presents the x and Q^2 resolutions as obtained using the shifted vertex Monte Carlo simulation for the “electron” method of kinematic reconstruction. Full points correspond to the bins where the F_2 structure function measurement is performed using the “electron” method (the “electron”- Σ separation passes approximately at $y \sim 0.1 \div 0.15$). The horizontal and vertical error bars correspond respectively to one sigma of the Q^2 and x resolutions (σ_{Q^2} , σ_x). The “bin centres”, as defined in section 7.2.1, are indicated with small points. The error bars are made to cross at a point displaced with respect to the bin centre by the average systematic bias in the bin, due to the kinematic reconstruction.

As expected the Q^2 resolution in the case of the “electron” method is excellent, even at low Q^2 ($Q^2 \rightarrow 1.5 \text{ GeV}^2$). The x resolution is slightly worse, while still very good for $y \geq 0.15$. For high y bins, corresponding to the lowest x values at fixed Q^2 , the half-bin size corresponds to $\sim 2\sigma$ of the x and Q^2 resolutions, meaning that the bin by bin correlations remain small. The “electron” method reconstruction appears to be little biased.

Fig 7.7 presents similar results for the Σ method. Both the Q^2 and x resolutions are significantly worse than in the case of the “electron” method and the x and Q^2 reconstructions present an important systematic bias, particularly when the current jet is emitted backward, in the BEMC direction (see Fig 4.3). The (x, Q^2) binning is clearly too fine, even for $0.01 \leq y \leq 0.1$, where the Σ method is ordinarily used. In order to reduce the bin by bin correlations, we have grouped bins two by two in x , while the Q^2 binning is kept untouched. The following new bins and “bin centres” are defined:

$$\begin{aligned}
 Q^2 = 3.5 \text{ GeV}^2 : & \quad \underbrace{0.00158-0.00251 \quad 0.00251-0.00398}_{0.0025} \\
 Q^2 = 5.0 \text{ GeV}^2 : & \quad \underbrace{0.00251-0.00398 \quad 0.00398-0.00631}_{0.004} \\
 Q^2 = 6.5 \text{ GeV}^2 : & \quad \underbrace{0.00158-0.00251 \quad 0.00251-0.00398}_{0.0025} \quad \underbrace{0.00398-0.00631 \quad 0.00631-0.01}_{0.0063}
 \end{aligned}$$

The lower x bins (for $y \geq 0.1$) were kept untouched as the “electron” method is used there. For higher Q^2 values, the F_2 structure function measurement is performed using the nominal vertex data.

Fig 7.8, 7.9, 7.10 and 7.11 present results of a similar study using the nominal vertex Monte Carlo simulation. The x and Q^2 resolutions of the “electron” method are very close to that obtained for the shifted vertex interactions (see Fig 7.8). No bias is visible in the high y part of the kinematic plane (see Fig 7.10). The Σ method resolution is slightly

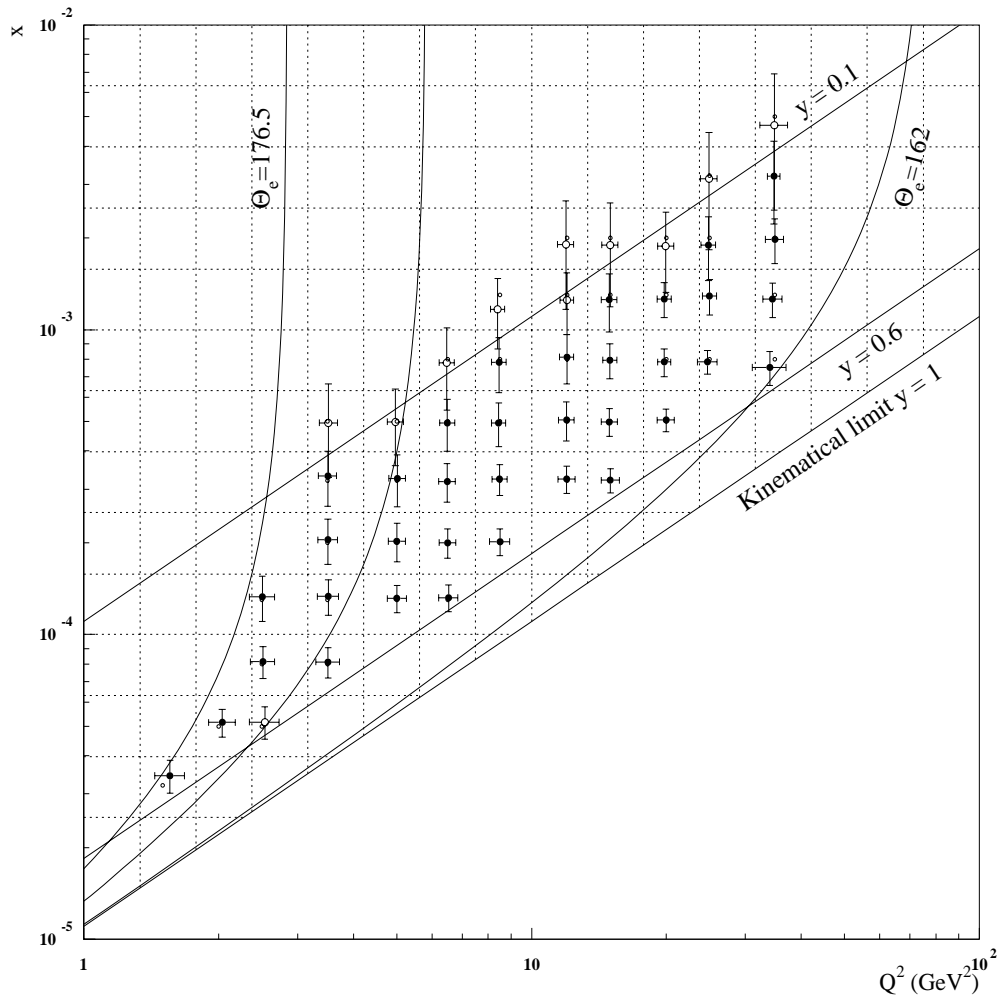


Figure 7.6: Resolution and systematic bias for the shifted vertex events, using the “electron” method of kinematic reconstruction.

The full points correspond to bins where the DIS cross-section is reliably measured using the “electron” method. The horizontal and the vertical error bars correspond respectively to one sigma of the Q^2 and x resolutions (σ_{Q^2} , σ_x). The “bin centres”, as defined in section 7.2.1, are indicated with small points. The error bars are made to cross at a point displaced with respect to the bin centre by the average systematic bias in the bin, due to the kinematic reconstruction.

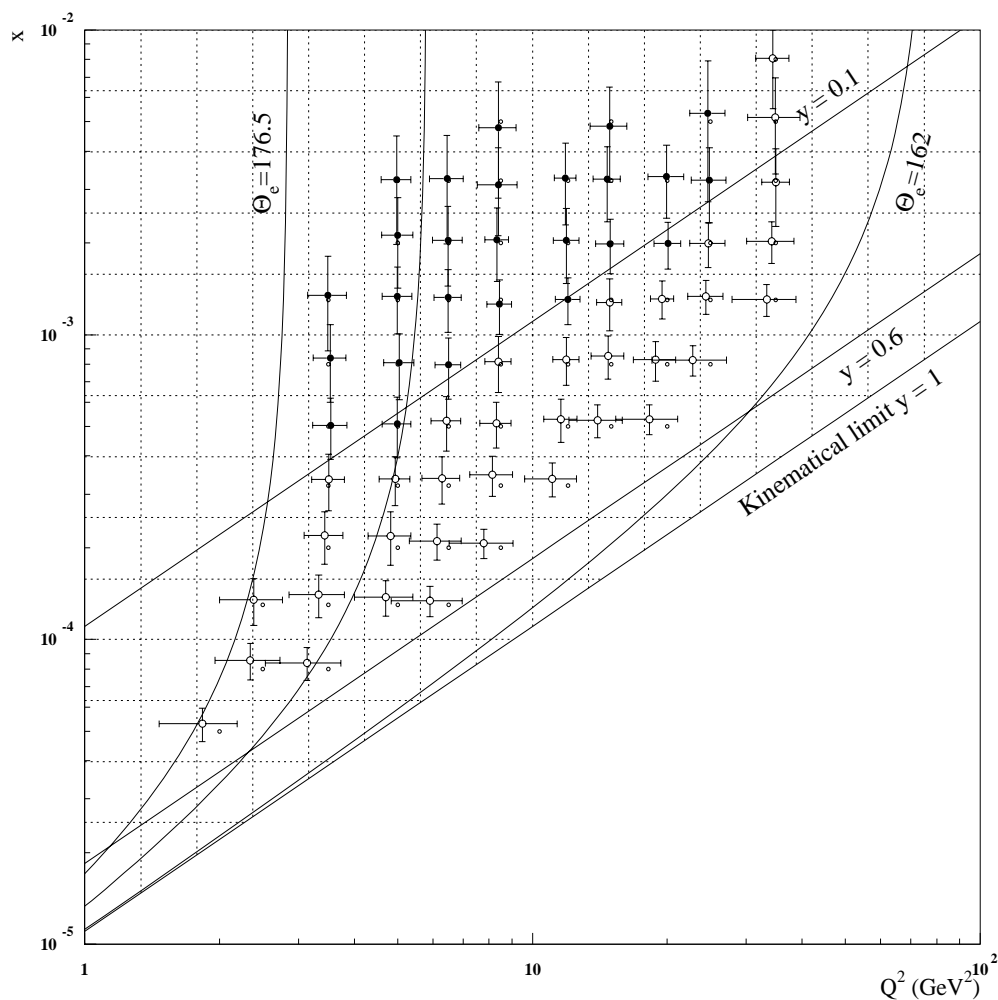


Figure 7.7: Resolution and systematic bias for the shifted vertex events, using the Σ method of kinematic reconstruction.

The full points correspond to bins where the DIS cross-section is reliably measured using the Σ method. The horizontal and the vertical error bars correspond respectively to one sigma of the Q^2 and x resolutions (σ_{Q^2} , σ_x). The “bin centres”, as defined in section 7.2, are indicated with small points. The error bars are made to cross at a point displaced with respect to the bin centre by the average systematic bias in the bin, due to the kinematic reconstruction.

better than in the case of the shifted vertex interaction position, which is understandable since the hadronic final state reconstruction was tuned for the nominal interaction position (see Fig 7.9). Similar to the SV data, a strong systematic bias exists at high y , where this method is not used in any case (see Fig 7.9 and Fig 7.11). It is interesting to note that no Σ measurement is possible for $\theta_e \simeq 162^\circ$ (the BPC acceptance edge). This is probably related to the particular way the Σ kinematics is defined there. We did not try to investigate further this phenomena.

Similar to the shifted vertex data, the binning adopted is clearly too fine. One can thus argue that *all* Σ bins have to be grouped two by two in x . This was however not done in [8].

7.2.3 Smeared acceptance, purity and stability

Apart from resolutions, several other parameters can be defined, providing information for each bin on the size of event migrations. Among them are:

- The smeared acceptance A_{smeas} :

$$A_{smeas} = \frac{|N_{gen}(\Delta x, \Delta Q^2) + N_{in}(\Delta x, \Delta Q^2) - N_{out}(\Delta x, \Delta Q^2)|}{N_{rec}(\Delta x, \Delta Q^2)}, \quad (7.11)$$

where N_{gen} , N_{in} , N_{out} and N_{rec} are respectively the number of events generated in the bin, migrating into the bin, out of the bin and the total number of events reconstructed in the bin;

- The purity P :

$$P = \frac{N_{stay}(\Delta x, \Delta Q^2)}{N_{rec}(\Delta x, \Delta Q^2)}, \quad (7.12)$$

where N_{stay} is the number of events *generated and reconstructed in the same bin*;

- The stability S :

$$S = \frac{N_{stay}(\Delta x, \Delta Q^2)}{N_{gen}(\Delta x, \Delta Q^2)}, \quad (7.13)$$

where N_{gen} is the number of events generated in the bin and *reconstructed somewhere inside the kinematic plane after applying fiducial cuts (y , θ_e and E'_e)*.

Fig 7.12 presents the stability S for the “electron” and Σ methods, for the shifted vertex interactions. In [8], a bin was accepted for the F_2 measurement if $S_{electron} \geq 0.5$ or $S_\Sigma \geq 0.3$. Similar studies have been performed using the nominal vertex Monte Carlo sample [51].

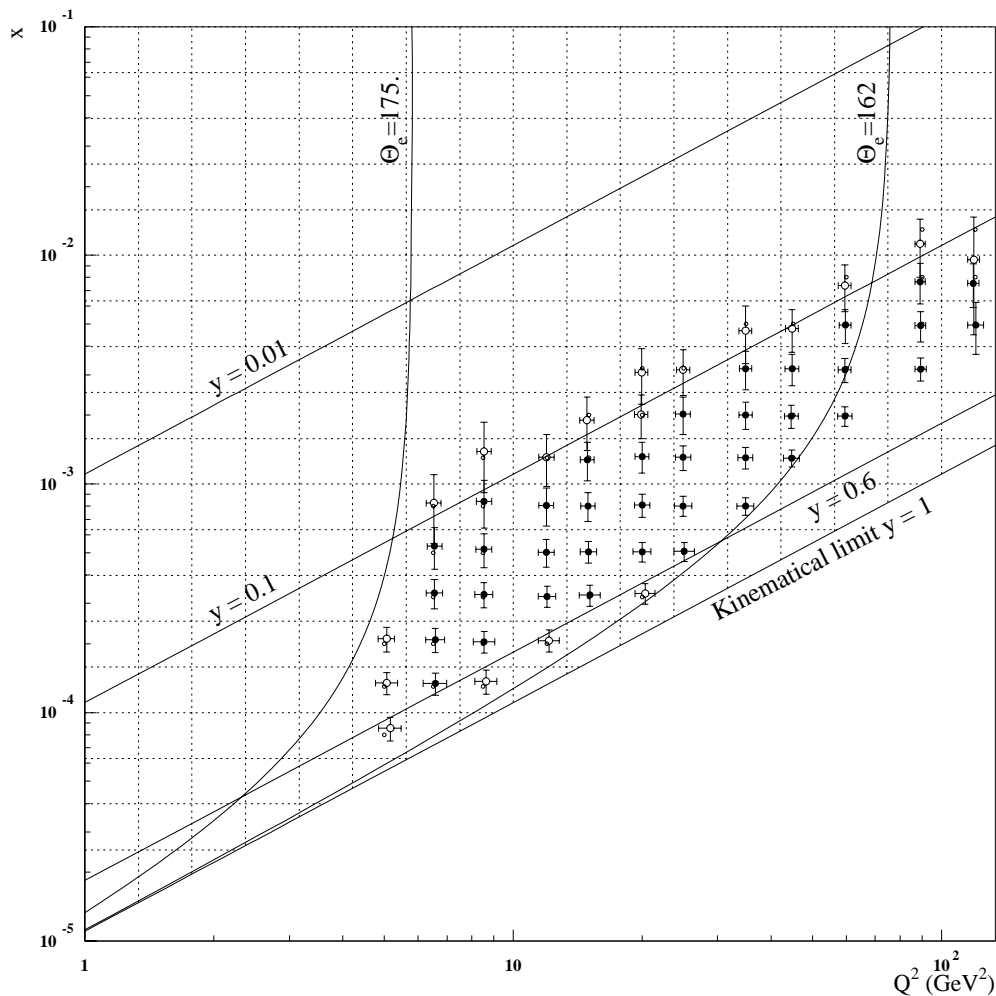


Figure 7.8: Resolution and systematic bias for the nominal vertex events, using the “electron” method of kinematic reconstruction.

The full points correspond to bins where the DIS cross-section is reliably measured using the “electron” method. The horizontal and the vertical error bars correspond respectively to one sigma of the Q^2 and x resolutions (σ_{Q^2} , σ_x). The “bin centres”, as defined in section 7.2, are indicated with small points. The error bars are made to cross at a point displaced with respect to the bin centre by the average systematic bias in the bin, due to the kinematic reconstruction (from [41]).

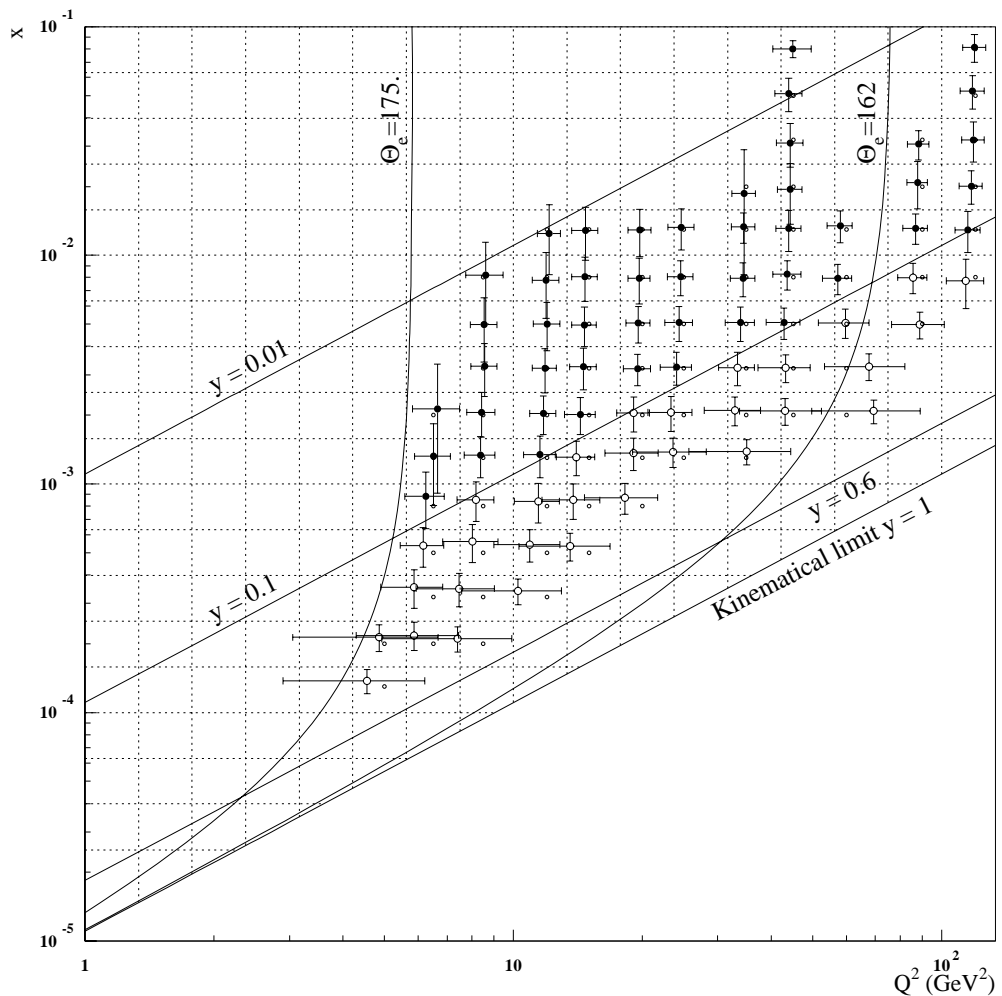


Figure 7.9: Resolution and systematic bias for the nominal vertex events, using the Σ method of kinematic reconstruction.

The full points correspond to bins where the DIS cross-section is reliably measured using the Σ method. The horizontal and the vertical error bars correspond respectively to one sigma of the Q^2 and x resolutions (σ_{Q^2} , σ_x). The “bin centres”, as defined in section 7.2, are indicated with small points. The error bars are made to cross at a point displaced with respect to the bin centre by the average systematic bias in the bin, due to the kinematic reconstruction (from [41]).

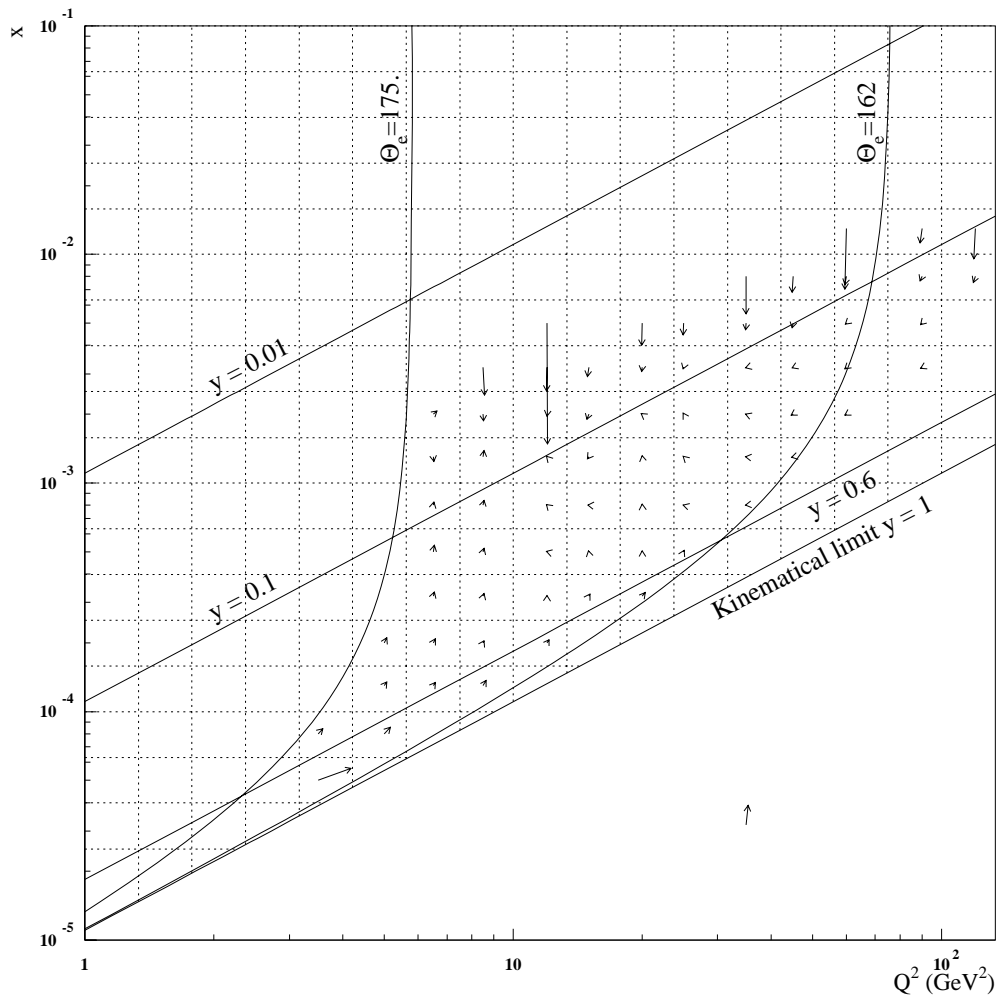


Figure 7.10: Systematic bias for the nominal vertex events, using the “electron” method of kinematic reconstruction.

The arrow size and direction correspond to the direction and the size of the average systematic bias in the bin, due to the kinematic reconstruction (nominal vertex).

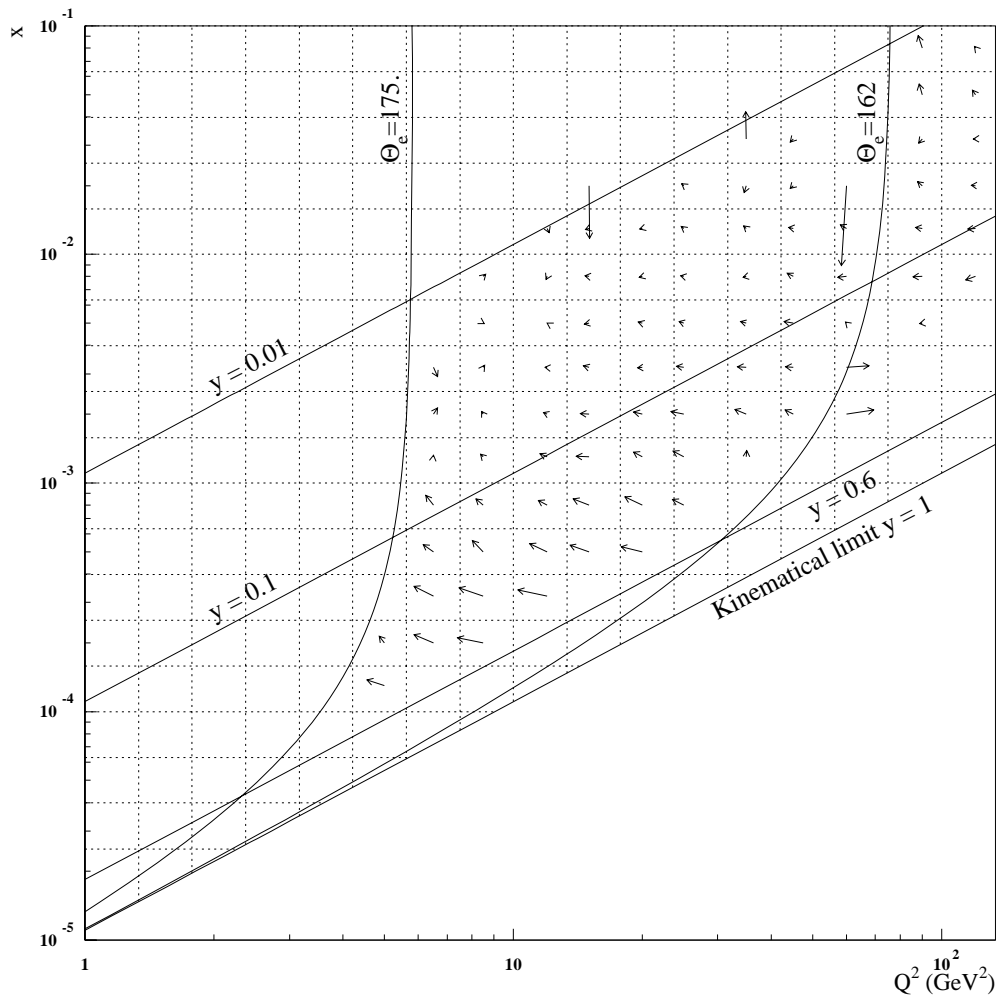


Figure 7.11: *Systematic bias for the nominal vertex events, using the Σ method of kinematic reconstruction.*

The arrow size and direction correspond to the direction and the size of the average systematic bias in the bin, due to the kinematic reconstruction (nominal vertex).

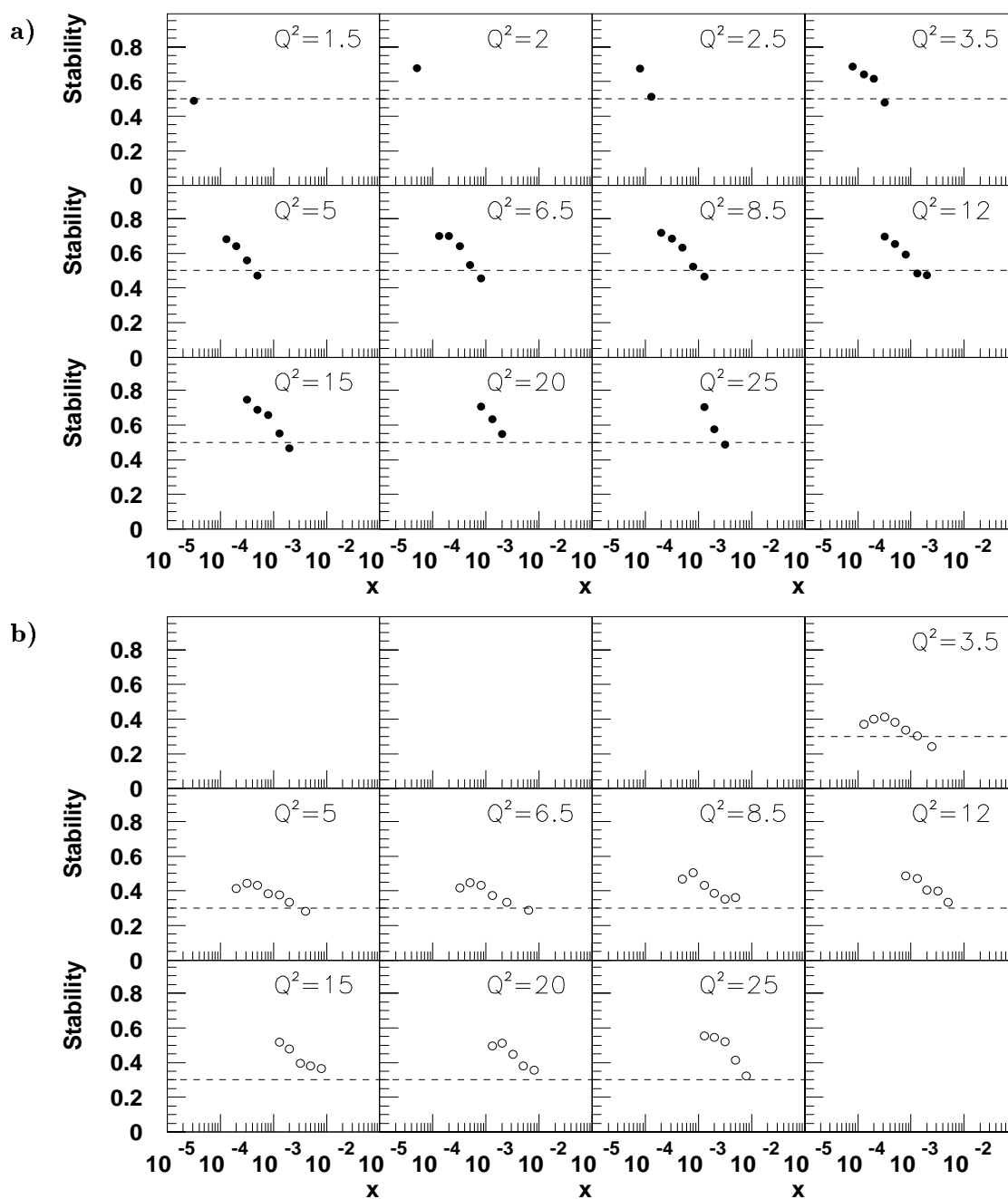


Figure 7.12: Bin stability for the shifted vertex interactions, using a) the “electron” and b) the Σ method of kinematic reconstruction (Monte Carlo statistical error bars are not shown). Note, that for the high x points at $Q^2 = 3.5, 5$ and 6.5 GeV^2 in case of the Σ method of kinematic reconstruction (bins grouped in x two by two), the values indicated correspond to the average stability over two bins before grouping. The actual values for the joint bins are of course higher, with $S > 0.3$. Lower x bins in case of the Σ method were not grouped as the “electron” method is used there.

7.3 F_2 measurement results

In this section the measurement of the structure function $F_2(x, Q^2)$ is presented, using the Monte Carlo based method of extraction.

7.3.1 Systematic errors

The F_2 structure function analysis was based on the shifted vertex, satellite bunch and the nominal vertex data samples with the scattered electron detected in the BEMC.

The following sources of systematic uncertainties were considered:

- The uncertainty in the BEMC electron energy scale: 1% (see section 5.2.5);
- An uncertainty of 1 mrad for the electron polar angle (see section 5.3.1). An extra systematic uncertainty is included for the nominal vertex data, accounting for the bad implementation of the dead material in Monte Carlo simulation (see section 5.3.3) and leading to local distortions of θ_e reconstruction;
- The uncertainty in the hadronic energy scale: the detailed study of y_h/y_e and of $p_{T,h}/p_{T,e}$ (p_T is the momentum transverse to the beam axis) led to the assignment of a 4% error on the hadronic energy deposited in the LAC calorimeter, a 15% error on the same quantity in the BEMC, and a 3% error on the y_h fraction carried by the tracks. These errors take into account the intrinsic energy scale uncertainty of each detector and the uncertainty of the sharing of the total hadronic final state energy between these subdetectors. These numbers also include uncertainties due to the treatment of the electronic noise in the LAC calorimeter and the BEMC [42, 51]. An extra 10% systematic uncertainty to y_h is added in case of the shifted vertex interactions (see section 5.4);
- An overall error of 2% was assigned due to the imperfect description of the various efficiencies (see chapter 6). A larger error was added to account for the variation of the vertex reconstruction efficiency at small y ($y \leq 0.01$, 8%) where jets get closer to the beam pipe in the forward direction [42, 51], and at small x and large θ ($Q^2 \leq 8.5 \text{ GeV}^2$, 4%) where H1 had no further tracking device besides the BPC (see section 6.4);
- An error of 2% in the radiative correction was assigned based on comparisons of the HECTOR [62] calculation with the DJANGO [55] Monte Carlo simulation results. The agreement (to the few percent level) between the structure function results obtained with the “electron” and the Σ methods is an additional cross check for the control of the radiative corrections.
- The structure function dependence of the Monte Carlo based F_2 measurement was kept below 1% by performing a two step iterative analysis (see section 7.1.2);
- Based on the control data sample of electron tagged γp events the uncertainty due to photoproduction background was estimated to be smaller than 30% of the correction applied [43];

Table 7.5 summarises the values of systematic errors due to the different sources. Statistical errors of the Monte Carlo simulation are added quadratically to the systematic error. The systematic errors are given point by point. However, some of them are strongly correlated over a large kinematic range. The systematic uncertainty for the shifted interaction position data samples is typically below 10%, and 5% for measurements obtained using the nominal vertex sample. It should be noticed that compared with the analysis of the 1993 data [6], many uncertainties have been reduced.

7.3.2 Structure function F_2 measurement from the SV and satellite bunch data samples

Fig 7.13 and 7.14 present the results of the structure function $F_2(x, Q^2)$ measurement using the shifted vertex (a) and the satellite bunch (b) data samples. The H1 '94 QCD fit [8, 69, 70] is superimposed as a solid line. The inner error bar is the statistical error, the outer corresponds to the full error resulting from adding quadratically the statistical and systematic error. The normalisation uncertainty, not included in the systematic error shown, is 3.9% for the shifted vertex data sample and 7.1% for the satellite bunch data sample (see section 2.3).

The kinematic range covered is:

$$\begin{aligned} \text{Shifted vertex, "electron"} &: Q^2 : 1.5 - 25.0 \text{ GeV}^2; \quad x : 3.2 \cdot 10^{-5} - 3.2 \cdot 10^{-3}; \\ \text{Satellite bunch, "electron"} &: Q^2 : 2.5 - 25.0 \text{ GeV}^2; \quad x : 3.2 \cdot 10^{-5} - 3.2 \cdot 10^{-3}; \\ \text{SV and satellite bunch, } \Sigma &: Q^2 : 3.5 - 25.0 \text{ GeV}^2; \quad x : 1.3 \cdot 10^{-4} - 8.0 \cdot 10^{-3}. \end{aligned}$$

The satellite bunch data do not allow the DIS cross-section measurement at $Q^2 < 2.5 \text{ GeV}^2$ because of the trigger limitation³. The available statistics become poor as $Q^2 > 25 \text{ GeV}^2$. The Σ method measurements at $Q^2 = 1.5 \div 2.5 \text{ GeV}^2$ are not shown because of the dramatic increase of the systematic uncertainties as Q^2 decreases.

It is interesting to note that the measurements using the shifted vertex and using the satellite bunch data have a similar systematic behaviour (see for example Fig 7.13, $Q^2 = 8.5 \text{ GeV}^2$). This behaviour is mostly determined by the inhomogeneities of the detector response and thereby has to be similar, since at a given (x, Q^2) , the SV and satellite bunch events enter the same detector parts. In addition, the same Monte Carlo sample is used for both analyses.

The relative normalisation of the F_2 measurement using the satellite bunch sample with respect to the F_2 measurement using the shifted vertex sample appears to be $\langle F_2^{sat}/F_2^{svx} \rangle = 1.00 \pm 0.02$ for the "electron" method and is 1.04 ± 0.02 for the Σ method. These values are consistent with an extra 5% luminosity uncertainty in case of the satellite bunch data sample, compared to the SV data sample (see section 2.3.1, Table 2.4). No systematic structure is observed for the F_2^{sat}/F_2^{svx} ratio plotted in function of x at fixed Q^2 (not shown here).

³The satellite bunch data sample is selected from data with the so-called *closed triangle* trigger configuration (see page 46).

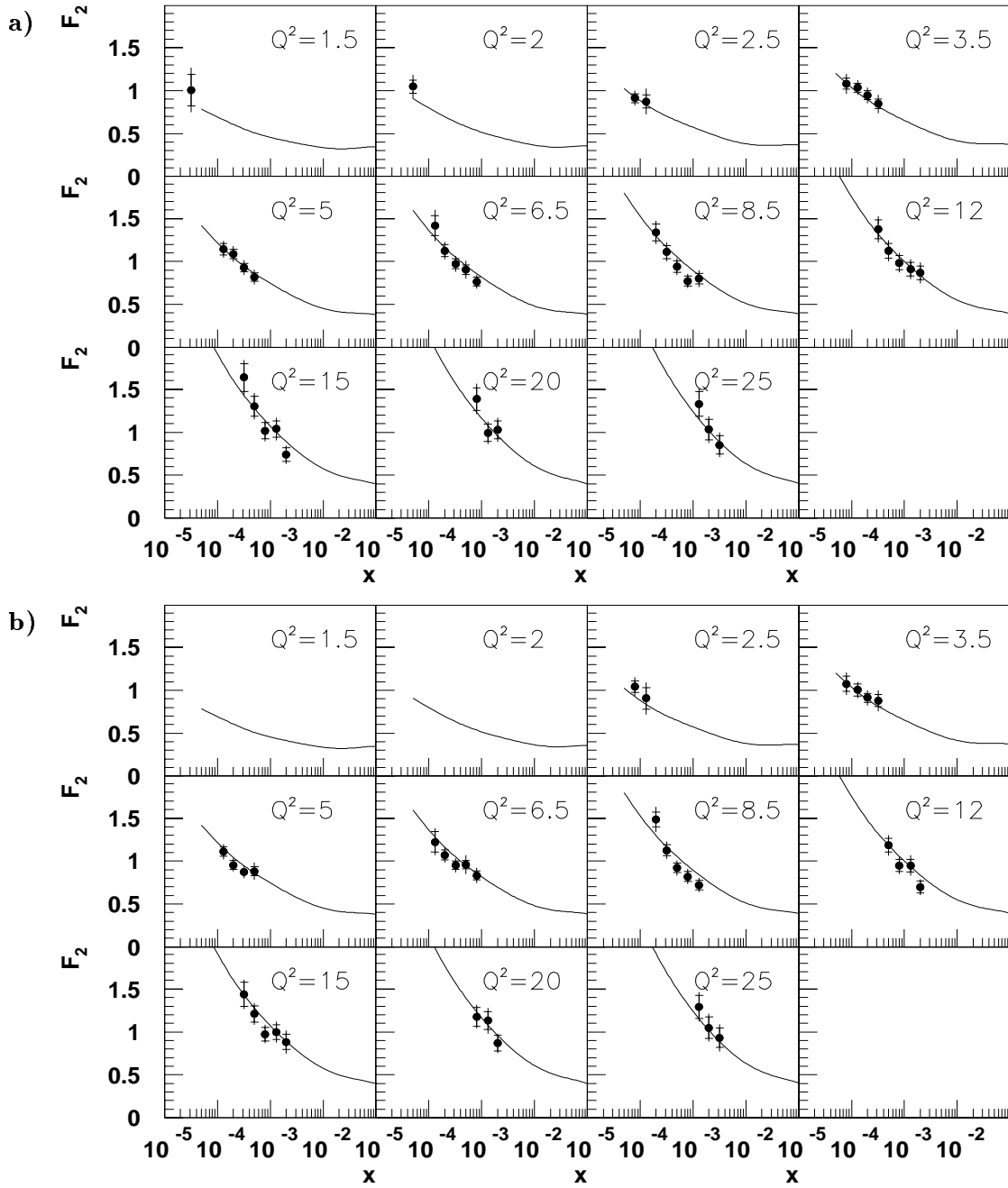


Figure 7.13: F_2 structure function measurement, as obtained using the shifted vertex (a) and the satellite bunch (b) data samples and the electron method of kinematic reconstruction. The H1 '94 QCD fit [8, 69, 70] is superimposed as a solid line. The inner error bar is the statistical error, the outer corresponds to the full error resulting from adding the statistical and systematic errors in quadrature. The normalisation uncertainty, not included in the systematic error, is 3.9% for the shifted vertex data sample and 7.1% for the satellite bunch data sample.

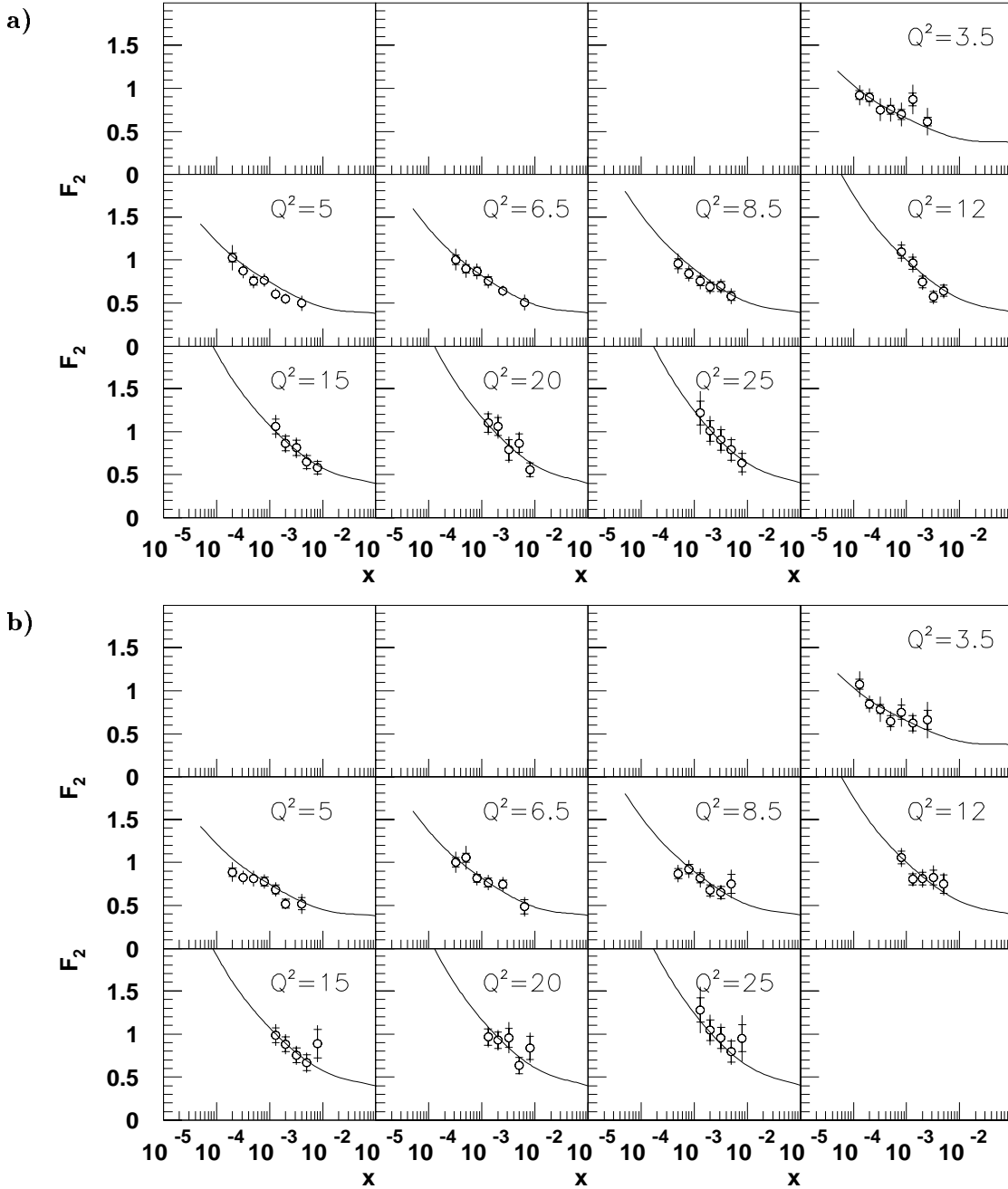


Figure 7.14: F_2 structure function measurement, as obtained using the shifted vertex (a) and the satellite bunch (b) data samples and the Σ method of kinematic reconstruction. The H1 '94 QCD fit [8, 69, 70] is superimposed as a solid line. The inner error bar is the statistical error, the outer corresponds to the full error resulting from adding the statistical and systematic errors in quadrature. The normalisation uncertainty, not included in the systematic error, is 3.9% for the shifted vertex data sample and 7.1% for the satellite bunch data sample. Note that only the Σ bins used for the final combined “electron”- Σ measurement are grouped two by two (the highest x bins at $Q^2 = 3.5, 5$ and 6.5 GeV^2).

7.3.3 Combining the SV and satellite bunch data samples

Since both the SV and the satellite bunch data samples undergo the same systematic effects and have approximately the same integrated luminosity ($\mathcal{L}_{svx} = 57.5 \text{ nb}^{-1}$, $\mathcal{L}_{sat} = 67.5 \text{ nb}^{-1}$), it is worth combining them, in order to increase the statistical significance of the F_2 measurement at low Q^2 . However, the event selection and the background subtraction are slightly different. Therefore, we combine directly the results of the DIS cross-section (or F_2) measurement. The combined F_2 is determined as a bin by bin average of F_2^{svx} and F_2^{sat} , weighted with the statistical uncertainties ΔF_2^{svx} and ΔF_2^{sat} . The only additional systematic error of the satellite bunch sample with respect to the SV sample - a 5% extra luminosity normalisation uncertainty - is included in the statistical errors when combining:

$$F_2^{combined} = \frac{F_2^{svx}/(\Delta F_2^{svx})^2 + F_2^{sat}/((\Delta F_2^{sat})^2 + (0.05 \cdot F_2^{sat})^2)}{1./(\Delta F_2^{svx})^2 + 1./((\Delta F_2^{sat})^2 + (0.05 \cdot F_2^{sat})^2)} \quad (7.14)$$

The statistical error is defined as:

$$\Delta F_2^{combined} = \sqrt{\frac{1.}{(\Delta F_2^{svx})^2} + \frac{1.}{(\Delta F_2^{sat})^2 + (0.05 \cdot F_2^{sat})^2}} \quad (7.15)$$

Tables 7.2, 7.3 and Fig 7.15-*a, b* summarise the structure function $F_2(x, Q^2)$ obtained in this way with respectively the “electron” and the Σ methods of kinematic reconstruction. The full error results from adding the statistical and systematic errors (see section 7.3.1) in quadrature. The normalisation uncertainty is not included in the systematic error.

The combined F_2 measurement is shown on Fig 7.16 (full points) and compared with the F_2 measurement using the nominal interaction position data (open circles; $Q^2 = 8.5 \text{ GeV}^2$: open triangle data sample; $Q^2 > 8.5 \text{ GeV}^2$: close triangle sample). The inner error bar is the statistical error, the outer corresponds to the full error. Note that the statistical errors in the case of the nominal vertex measurement are not visible (the statistical error does not exceed 3% for $Q^2 \leq 35.0 \text{ GeV}^2$). Both measurements nicely agree within errors.

Q^2 (GeV ²)	x	F_2^{svx}	ΔF_2^{stat}	F_2^{sat}	ΔF_2^{stat}	F_2^{com}	ΔF_2^{stat}	$\Delta F_2^{sys t}$	ΔF_2^{tot}
1.5	$3.2 \cdot 10^{-5}$	0.969	0.176			0.97	0.176	0.187	0.26
2.0	$5.0 \cdot 10^{-5}$	1.037	0.077			1.04	0.077	0.110	0.14
2.5	$8.0 \cdot 10^{-5}$	0.885	0.052			0.89	0.052	0.065	0.08
2.5	$1.3 \cdot 10^{-4}$	0.874	0.079	0.905	0.126	0.88	0.068	0.128	0.15
3.5	$8.0 \cdot 10^{-5}$	1.020	0.065	1.075	0.088	1.04	0.053	0.092	0.11
3.5	$1.3 \cdot 10^{-4}$	1.034	0.053	1.003	0.071	1.03	0.045	0.067	0.08
3.5	$2.0 \cdot 10^{-4}$	0.946	0.051	0.911	0.053	0.93	0.041	0.075	0.09
3.5	$3.2 \cdot 10^{-4}$	0.844	0.055	0.878	0.070	0.85	0.046	0.093	0.10
5.0	$1.3 \cdot 10^{-4}$	1.112	0.065	1.109	0.055	1.11	0.049	0.074	0.09
5.0	$2.0 \cdot 10^{-4}$	1.086	0.057	0.954	0.051	1.03	0.044	0.069	0.08
5.0	$3.2 \cdot 10^{-4}$	0.929	0.051	0.875	0.044	0.91	0.039	0.066	0.08
5.0	$5.0 \cdot 10^{-4}$	0.818	0.047	0.882	0.052	0.84	0.039	0.076	0.09
6.5	$1.3 \cdot 10^{-4}$	1.418	0.118	1.224	0.117	1.33	0.088	0.131	0.16
6.5	$2.0 \cdot 10^{-4}$	1.126	0.070	1.070	0.058	1.10	0.052	0.072	0.09
6.5	$3.2 \cdot 10^{-4}$	0.973	0.060	0.950	0.049	0.96	0.045	0.068	0.08
6.5	$5.0 \cdot 10^{-4}$	0.904	0.057	0.959	0.051	0.93	0.044	0.088	0.10
6.5	$8.0 \cdot 10^{-4}$	0.764	0.052	0.832	0.051	0.79	0.041	0.062	0.07
8.5	$2.0 \cdot 10^{-4}$	1.339	0.099	1.485	0.086	1.40	0.075	0.098	0.12
8.5	$3.2 \cdot 10^{-4}$	1.111	0.077	1.126	0.063	1.12	0.057	0.077	0.10
8.5	$5.0 \cdot 10^{-4}$	0.940	0.066	0.920	0.055	0.93	0.049	0.070	0.09
8.5	$1.3 \cdot 10^{-3}$	0.771	0.058	0.821	0.058	0.79	0.045	0.060	0.08
8.5	$8.0 \cdot 10^{-5}$	0.798	0.060	0.721	0.055	0.76	0.044	0.073	0.09
12.0	$3.2 \cdot 10^{-4}$	1.377	0.110	0.000	0.000	1.38	0.110	0.106	0.15
12.0	$5.0 \cdot 10^{-4}$	1.124	0.088	1.184	0.078	1.15	0.066	0.083	0.11
12.0	$8.0 \cdot 10^{-4}$	0.985	0.081	0.947	0.070	0.97	0.059	0.078	0.10
12.0	$1.3 \cdot 10^{-3}$	0.910	0.077	0.948	0.074	0.93	0.058	0.090	0.11
12.0	$2.0 \cdot 10^{-3}$	0.866	0.079	0.697	0.070	0.78	0.056	0.084	0.10
15.0	$3.2 \cdot 10^{-4}$	1.638	0.162	1.437	0.139	1.53	0.113	0.120	0.16
15.0	$5.0 \cdot 10^{-4}$	1.304	0.115	1.209	0.094	1.26	0.080	0.094	0.12
15.0	$8.0 \cdot 10^{-4}$	1.017	0.094	0.974	0.081	1.00	0.067	0.074	0.10
15.0	$1.3 \cdot 10^{-3}$	1.039	0.094	0.997	0.088	1.02	0.069	0.089	0.11
15.0	$2.0 \cdot 10^{-3}$	0.738	0.080	0.883	0.090	0.79	0.063	0.074	0.10
20.0	$8.0 \cdot 10^{-4}$	1.387	0.131	1.177	0.110	1.28	0.090	0.110	0.14
20.0	$1.3 \cdot 10^{-3}$	0.994	0.101	1.130	0.103	1.05	0.077	0.089	0.12
20.0	$2.0 \cdot 10^{-3}$	1.027	0.102	0.868	0.090	0.95	0.071	0.090	0.12
25.0	$1.3 \cdot 10^{-3}$	1.330	0.142	1.292	0.133	1.31	0.102	0.114	0.15
25.0	$2.0 \cdot 10^{-3}$	1.032	0.120	1.047	0.125	1.04	0.090	0.101	0.14
25.0	$3.2 \cdot 10^{-3}$	0.853	0.108	0.931	0.114	0.89	0.081	0.096	0.12

Table 7.2: F_2 measurement (electron method of kinematic reconstruction), combining the results of measurement with the shifted vertex and the satellite bunch data samples. The full error results from adding the statistical and systematic errors in quadrature. The normalisation uncertainty, not included in the systematic error, is 3.9% (the additional 5.0% normalisation uncertainty for the satellite bunch data sample is included in the satellite bunch statistical error when averaging).

Q^2 (GeV ²)	x	F_2^{svx}	ΔF_2^{stat}	F_2^{sat}	ΔF_2^{stat}	F_2^{com}	ΔF_2^{stat}	ΔF_2^{syst}	ΔF_2^{tot}
3.5	$1.3 \cdot 10^{-4}$	0.921	0.052	1.075	0.058	0.97	0.043	0.107	0.12
3.5	$2.0 \cdot 10^{-4}$	0.895	0.047	0.847	0.051	0.88	0.038	0.090	0.10
3.5	$3.2 \cdot 10^{-4}$	0.751	0.044	0.788	0.053	0.76	0.037	0.126	0.13
3.5	$5.0 \cdot 10^{-4}$	0.752	0.051	0.647	0.063	0.72	0.041	0.119	0.13
3.5	$8.0 \cdot 10^{-4}$	0.697	0.058	0.750	0.083	0.71	0.049	0.126	0.14
3.5	$1.3 \cdot 10^{-3}$	0.870	0.074	0.625	0.090	0.78	0.058	0.137	0.15
3.5	$2.5 \cdot 10^{-3}$	0.614	0.046	0.662	0.109	0.62	0.043	0.157	0.16
5.0	$2.0 \cdot 10^{-4}$	1.028	0.051	0.886	0.049	0.98	0.040	0.131	0.14
5.0	$3.2 \cdot 10^{-4}$	0.875	0.043	0.823	0.042	0.86	0.035	0.073	0.08
5.0	$5.0 \cdot 10^{-4}$	0.754	0.047	0.811	0.045	0.76	0.037	0.069	0.08
5.0	$8.0 \cdot 10^{-4}$	0.765	0.044	0.778	0.053	0.77	0.037	0.063	0.07
5.0	$1.3 \cdot 10^{-3}$	0.606	0.041	0.686	0.052	0.63	0.034	0.050	0.06
5.0	$2.0 \cdot 10^{-3}$	0.549	0.040	0.521	0.054	0.54	0.033	0.043	0.06
5.0	$4.0 \cdot 10^{-3}$	0.497	0.029	0.520	0.071	0.50	0.027	0.086	0.09
6.5	$3.2 \cdot 10^{-4}$	1.002	0.056	1.000	0.054	1.00	0.045	0.112	0.12
6.5	$5.0 \cdot 10^{-4}$	0.898	0.048	1.054	0.052	0.94	0.040	0.096	0.10
6.5	$8.0 \cdot 10^{-4}$	0.869	0.049	0.815	0.047	0.85	0.039	0.076	0.09
6.5	$1.3 \cdot 10^{-3}$	0.755	0.049	0.765	0.052	0.76	0.039	0.068	0.08
6.5	$2.5 \cdot 10^{-3}$	0.643	0.033	0.747	0.047	0.67	0.030	0.054	0.06
6.5	$6.3 \cdot 10^{-3}$	0.506	0.031	0.485	0.082	0.50	0.029	0.084	0.09
8.5	$5.0 \cdot 10^{-4}$	0.957	0.059	0.868	0.058	0.92	0.046	0.095	0.11
8.5	$8.0 \cdot 10^{-4}$	0.842	0.053	0.920	0.055	0.87	0.043	0.075	0.09
8.5	$1.3 \cdot 10^{-3}$	0.756	0.056	0.820	0.059	0.78	0.044	0.082	0.09
8.5	$2.0 \cdot 10^{-3}$	0.688	0.055	0.676	0.064	0.68	0.044	0.065	0.08
8.5	$3.2 \cdot 10^{-3}$	0.694	0.058	0.650	0.070	0.68	0.046	0.061	0.08
8.5	$5.0 \cdot 10^{-3}$	0.581	0.052	0.750	0.108	0.61	0.047	0.079	0.09
12.0	$8.0 \cdot 10^{-4}$	1.094	0.076	1.057	0.073	1.08	0.058	0.090	0.11
12.0	$1.3 \cdot 10^{-3}$	0.963	0.072	0.804	0.064	0.89	0.052	0.077	0.09
12.0	$2.0 \cdot 10^{-3}$	0.745	0.067	0.814	0.073	0.77	0.052	0.069	0.09
12.0	$3.2 \cdot 10^{-3}$	0.571	0.061	0.822	0.085	0.65	0.051	0.061	0.08
12.0	$5.0 \cdot 10^{-3}$	0.641	0.064	0.748	0.106	0.67	0.056	0.058	0.08
15.0	$1.3 \cdot 10^{-3}$	1.058	0.087	0.987	0.086	1.03	0.065	0.101	0.12
15.0	$2.0 \cdot 10^{-3}$	0.863	0.084	0.882	0.086	0.87	0.063	0.076	0.10
15.0	$3.2 \cdot 10^{-3}$	0.811	0.088	0.752	0.086	0.78	0.064	0.079	0.10
15.0	$5.0 \cdot 10^{-3}$	0.646	0.077	0.667	0.094	0.65	0.061	0.061	0.09
15.0	$8.0 \cdot 10^{-3}$	0.582	0.072	0.888	0.163	0.63	0.066	0.065	0.09
20.0	$1.3 \cdot 10^{-3}$	1.099	0.106	0.964	0.097	1.03	0.076	0.084	0.11
20.0	$2.0 \cdot 10^{-3}$	1.060	0.105	0.929	0.095	1.00	0.075	0.089	0.12
20.0	$3.2 \cdot 10^{-3}$	0.788	0.118	0.955	0.109	0.87	0.084	0.108	0.14
20.0	$5.0 \cdot 10^{-3}$	0.864	0.108	0.634	0.094	0.74	0.073	0.063	0.10
20.0	$8.0 \cdot 10^{-3}$	0.558	0.080	0.840	0.134	0.63	0.070	0.056	0.09
25.0	$1.3 \cdot 10^{-3}$	1.216	0.137	1.279	0.139	1.24	0.102	0.216	0.24
25.0	$2.0 \cdot 10^{-3}$	1.009	0.119	1.044	0.121	1.03	0.088	0.124	0.15
25.0	$3.2 \cdot 10^{-3}$	0.903	0.120	0.953	0.121	0.93	0.088	0.108	0.14
25.0	$5.0 \cdot 10^{-3}$	0.788	0.120	0.795	0.123	0.79	0.088	0.084	0.12
25.0	$8.0 \cdot 10^{-3}$	0.639	0.107	0.950	0.156	0.73	0.090	0.115	0.15

Table 7.3: F_2 measurement (Σ method of kinematic reconstruction), combining the results of measurement with the shifted vertex and the satellite bunch data samples. The full error results from adding the statistical and systematic errors in quadrature. The normalisation uncertainty, not included in the systematic error, is 3.9% (the additional 5.0% normalisation uncertainty for the satellite bunch data sample is included in the satellite bunch statistical error when averaging).

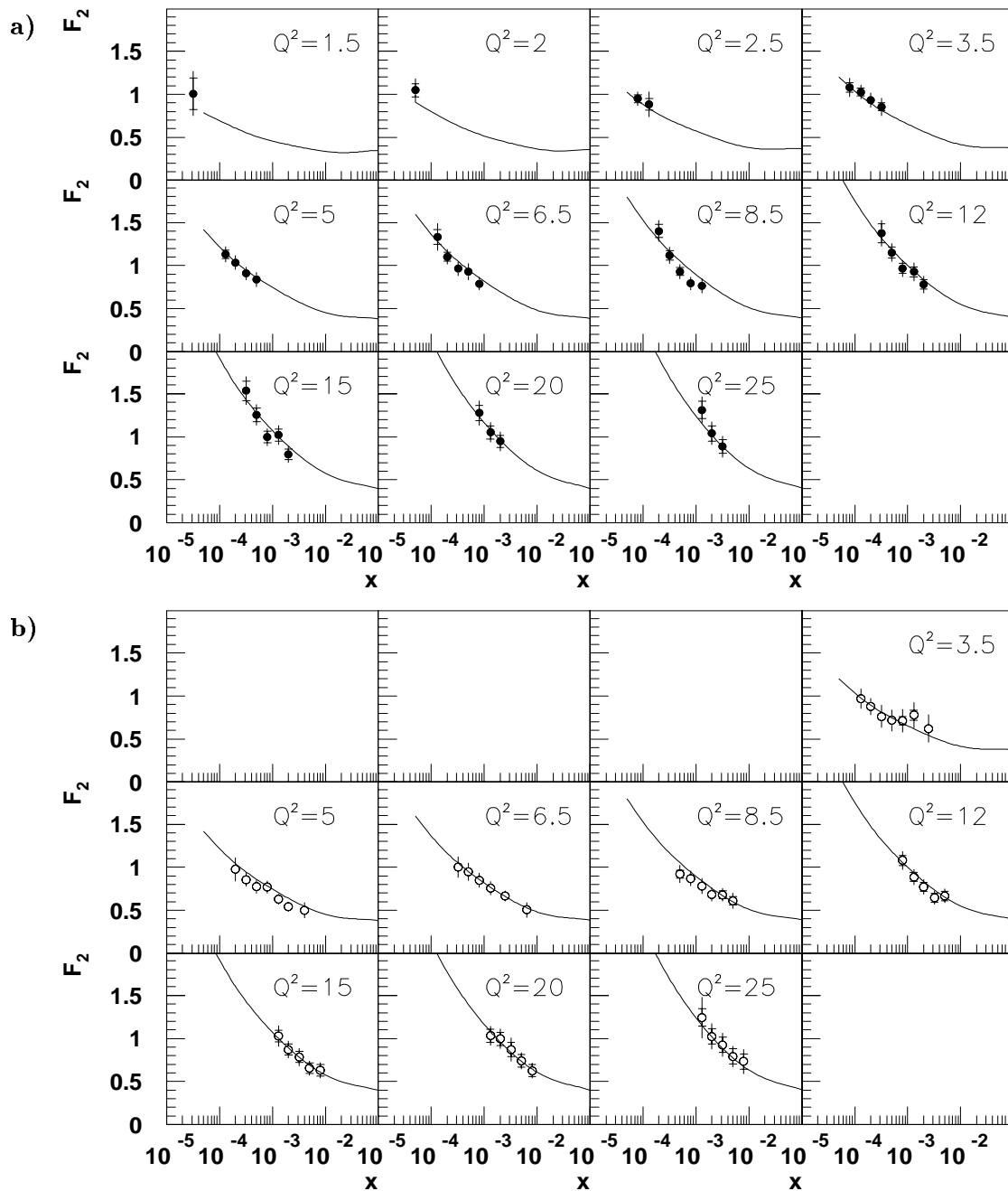


Figure 7.15: F_2 structure function measurement, as obtained by combining the results of the F_2 measurement using the SV and the satellite bunch data samples: a) electron method; b) Σ method. The inner error bar is the statistical error, the outer corresponds to the full error resulting from adding the statistical and systematic error in quadrature. The normalisation uncertainty, not included in the systematic error, is 3.9%.

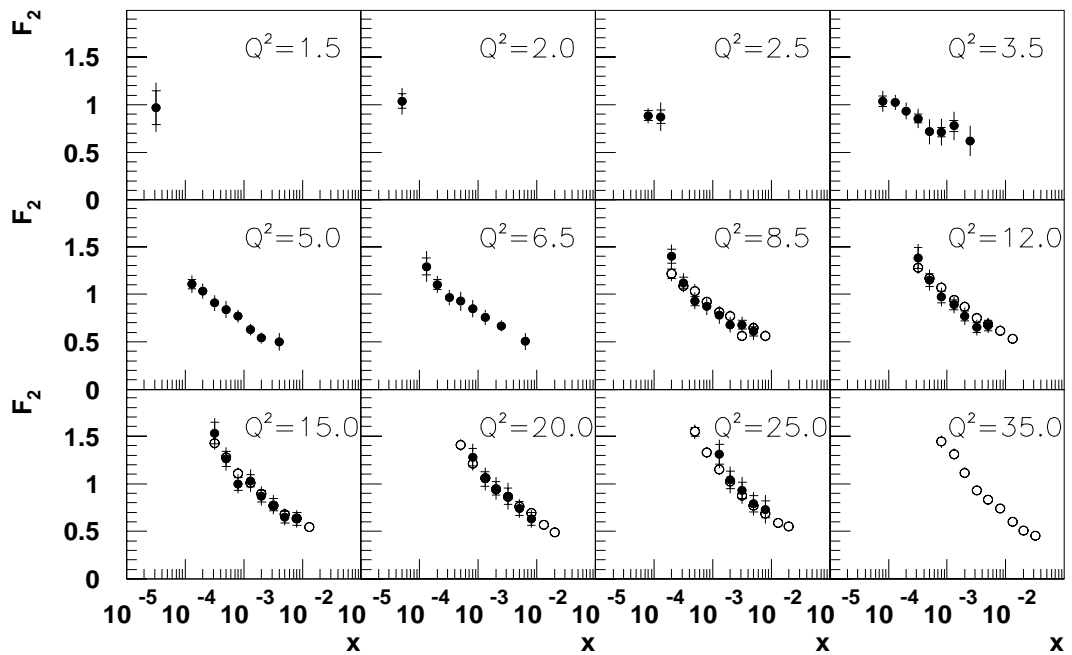


Figure 7.16: F_2 structure function measurement, as obtained by combining the results from the SV and the satellite bunch data samples (full points) and compared to the F_2 measurement from the nominal vertex data sample (open circles). For all Q^2 bins the “electron” method is used for the lowest x bins ($y \geq 0.1$), and the Σ method for the high x bins.

7.3.4 Final $F_2(x, Q^2)$ measurement results using the full combined 1994 data samples

Fig 7.17 presents the full Q^2 range H1 '94 $F_2(x, Q^2)$ measurement, as recently published [8], using the “electron” (full points) and Σ (open squares) method. This analysis contributes the measurement with $Q^2 \leq 6.5 \text{ GeV}^2$, except high x points at $Q^2 = 1.5$ and 2.5 GeV^2 , obtained from the radiative sample analysis [66, 67]; the Q^2 range $150 \leq Q^2 \leq 5000 \text{ GeV}^2$ corresponds to the so-called “high Q^2 ” DIS event selection, with the scattered electron detected in the LAC calorimeter. The inner error bar is the statistical error, the outer corresponds to the full error resulting from adding the statistical and systematic errors in quadrature. This comparison is intended to demonstrate that the systematic effects are estimated correctly, as the “electron” and Σ methods have different systematic behaviours and radiative corrections. A good mutual normalisation of both methods at low x (high y) is a cross-check of correctness of the radiative effect treatment for the “electron” method.

Fig 7.18 and 7.19 present the full H1 '94 measurement (full points: “electron” and Σ combined), respectively as a function of x at fixed Q^2 (Fig 7.18) and as a function of Q^2 at fixed x (Fig 7.19), together with results taken from the recent publication of the NMC [65] (open circles) and BCDMS [68] (open squares) Collaboration. The curves represent a NLO QCD fit [8, 69, 70], which includes data for $Q^2 \geq 5 \text{ GeV}^2$. The extension of the curves below 5 GeV^2 represents the backward evolution of the fit (from [8]).

Compared to the previous H1 analysis [6] the F_2 measurement has been extended to lower and higher Q^2 (from $4.5 - 1600 \text{ GeV}^2$ to $1.5 - 5000 \text{ GeV}^2$), and to lower and higher x (from $1.8 \cdot 10^{-4} \leq x \leq 0.13$ to $3 \cdot 10^{-5} \leq x \leq 0.32$).

7.3.5 Discussion

Fig 7.17, 7.18 and 7.19 clearly demonstrate the rise of F_2 with decreasing x . In Fig 7.20 the data from the eight lowest Q^2 bins are shown (this analysis contributes the measurement with $Q^2 \leq 6.5 \text{ GeV}^2$, except high x points at $Q^2 = 1.5$ and 2.5 GeV^2 , obtained from the radiative sample analysis [66, 67] (closed triangles). They are compared with recent data (open squares: ZEUS [63]; open circles: E665 [64]; open triangles: NMC [65]). The rise of F_2 towards low x is also present in the low Q^2 region. The measurement is in good agreement with the data from the ZEUS experiment and matches well with the data from fixed target experiments at higher x values.

The curves denoted MRSA', MRSG [74], CTEQ3M [75] and GRV [76] are obtained from parton distribution parameterisations. The MRS and CTEQ distributions assume an $x^{-\lambda}$ behaviour for $x \rightarrow 0$ at Q_0^2 4-5 GeV^2 . They were determined using also the 1993 HERA structure function data.

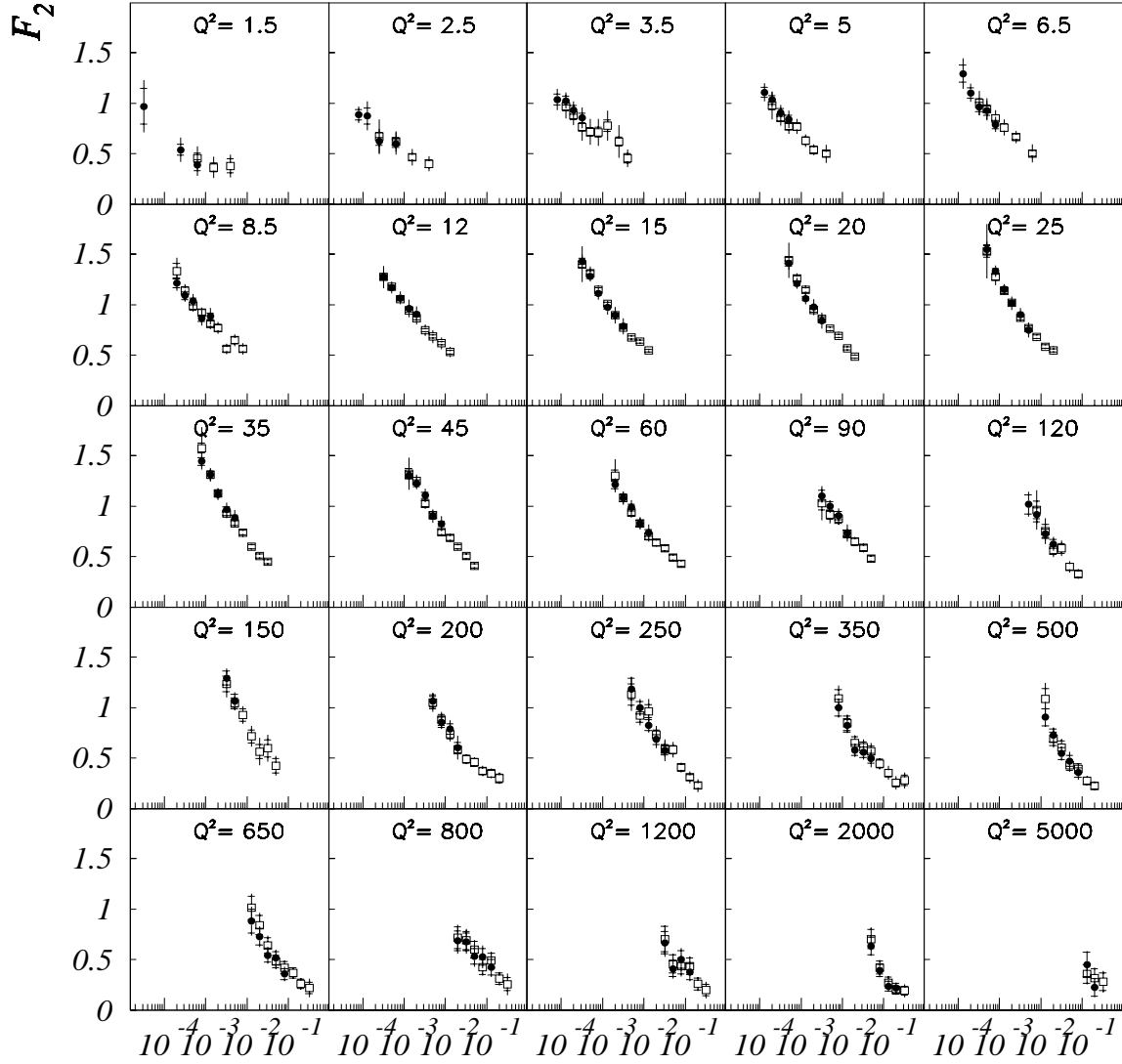
The GRV calculation assumes that all parton distributions at very low $Q_0^2 = 0.34 \text{ GeV}^2$ have a valence like shape, i.e. vanish for $x \rightarrow 0$. Assuming that the DGLAP equations can be used to evolve the parton distributions from this low Q_0^2 scale to larger Q^2 values, they predicted that the structure function F_2 should rise towards low x even for low values of $Q^2 \sim 1 \text{ GeV}^2$ [76]. The determination of the shape parameters of the distributions at the starting scale uses only data from fixed target experiments and not much freedom is left for further adjustments in the kinematic range of the HERA data. Small variations are connected with changes still possible in the starting Q_0^2 and the value

of the QCD parameter Λ . Fig 7.20 shows that the GRV distributions describe the data well, indicating that in this kinematic regime the sea quark distributions can be produced by QCD dynamics. The GRV and MRSA' parameterisations give a good description of the data in the range shown, with the possible exception of the first Q^2 bin for the latter. The MRSG and CTEQ3 distributions, which are not available for the lowest Q^2 values, describe the higher Q^2 data well.

Parameterisations motivated by Regge theory relate the structure function to Reggeon exchange phenomena which successfully describe the slow rise of the total cross section with the centre of mass system energy in hadron-hadron and γp interactions. Regge inspired models DOLA [71] and CKMT [72] lie below the data for $Q^2 \geq 2$ GeV at low x .

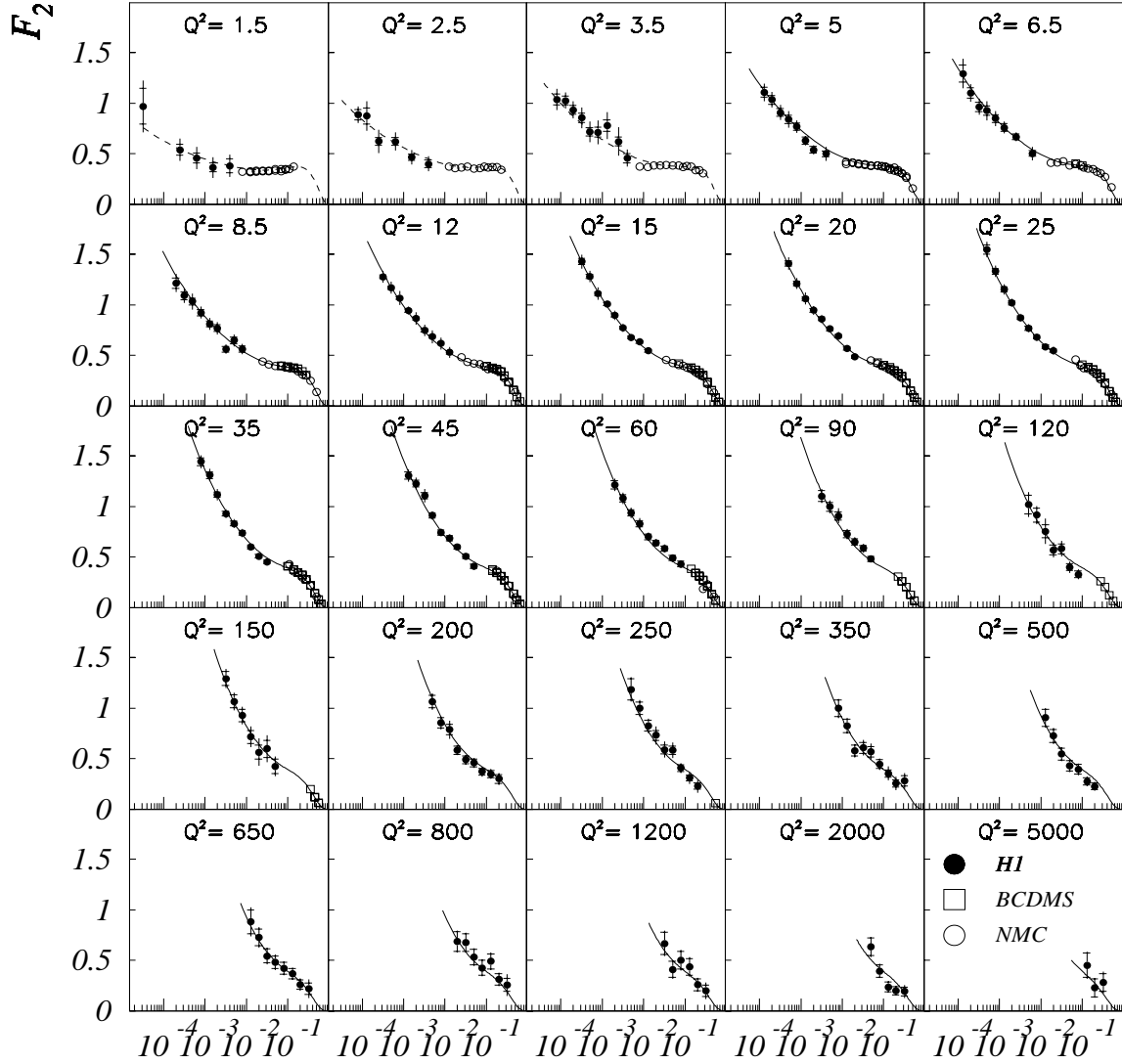
The final H1 '94 measurement results are tabulated in Table 7.4 (from [8]), providing the $F_2(x, Q^2)$ values together with statistical and systematic errors and the R values as used in the Monte Carlo simulation (see section 7.1.2⁴).

⁴The R ratio and the longitudinal structure function F_L are related by $R = F_L/2xF_1$ and $F_L = F_2 - 2xF_1$.



x

Figure 7.17: Measurement of the structure function by H1 with the electron (full points) and the Σ method. This analysis contributes to the points with $Q^2 \leq 6.5 \text{ GeV}^2$, except the high x points at $Q^2 = 1.5$ and 2.5 GeV^2 , obtained from the radiative sample analysis [66, 67]; the Q^2 range $150 \leq Q^2 \leq 5000 \text{ GeV}^2$ corresponds to the so-called “high Q^2 ” DIS event sample, with the scattered electron detected in the LAC calorimeter. The inner error bar is the statistical error, the outer corresponds to the full error resulting from adding the statistical and systematic error in quadrature. The normalisation uncertainty, not included in the systematic error, is 3.9% for $Q^2 \leq 6.5 \text{ GeV}^2$ and 1.5% for $Q^2 > 6.5 \text{ GeV}^2$ (from [8]).



x

Figure 7.18: Measurement of the structure function $F_2(x, Q^2)$ by H1 in function of x at fixed Q^2 . The full points are the results of the H1 '94 measurement, the open circles are results taken from the recent publication of the NMC [65] and the open squares results from BCDMS [68]. The H1 normalisation uncertainty, not included in the error, is 3.9% for $Q^2 \leq 6.5 \text{ GeV}^2$ and 1.5% for $Q^2 > 6.5 \text{ GeV}^2$. The curves represent a NLO QCD fit [8, 69, 70], which includes all data for $Q^2 \geq 5 \text{ GeV}^2$. The curves below 5 GeV^2 represent the backward evolution of the fit (from [8]).

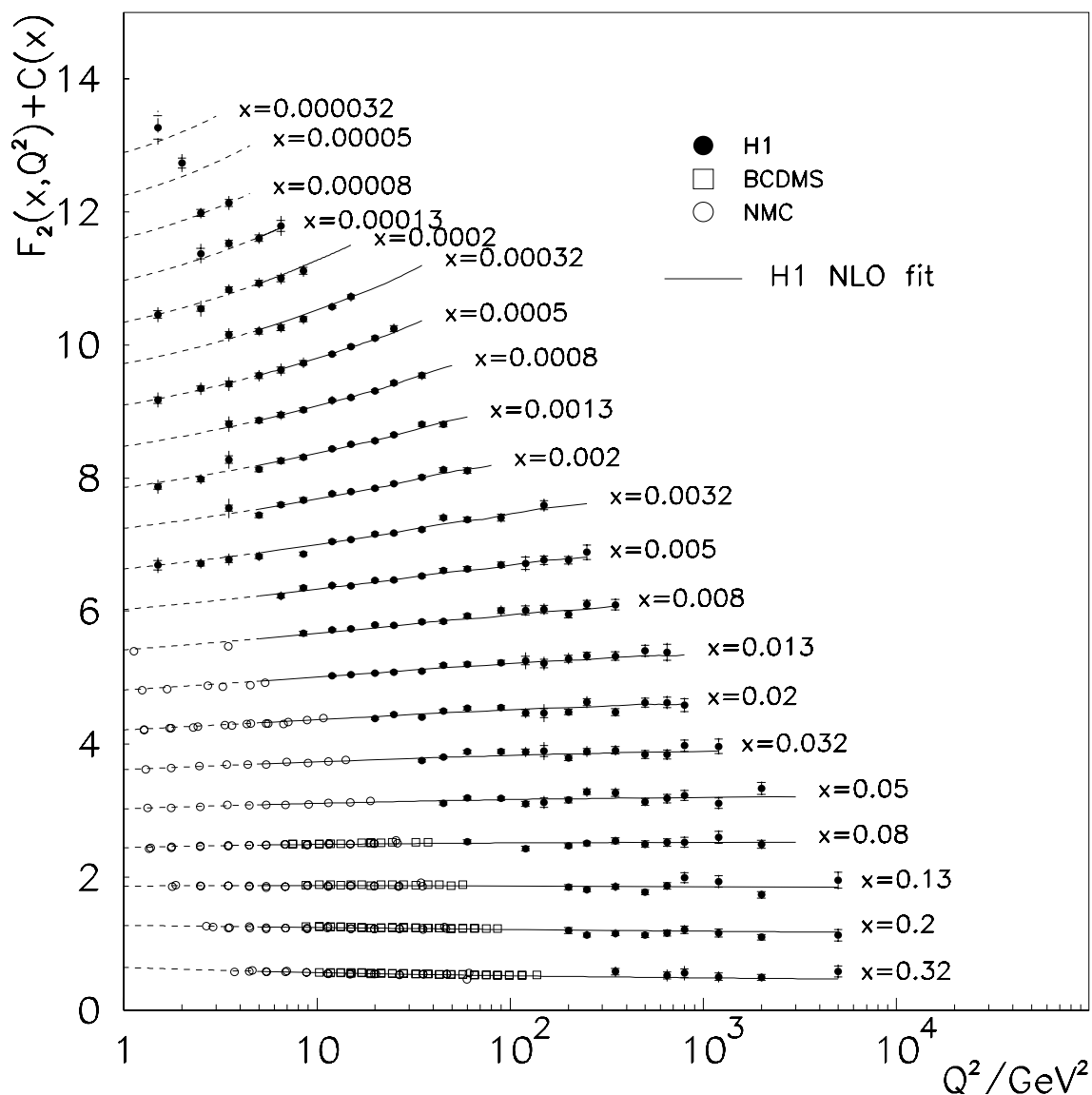


Figure 7.19: Same as for Fig 7.18 but as a function of Q^2 at fixed x . The F_2 values are plotted in a linear scale adding a constant $c(x) = 0.6(i - 0.4)$ where i is the x bin number starting at $i = 1$ from $x = 0.32$ (from [8]).

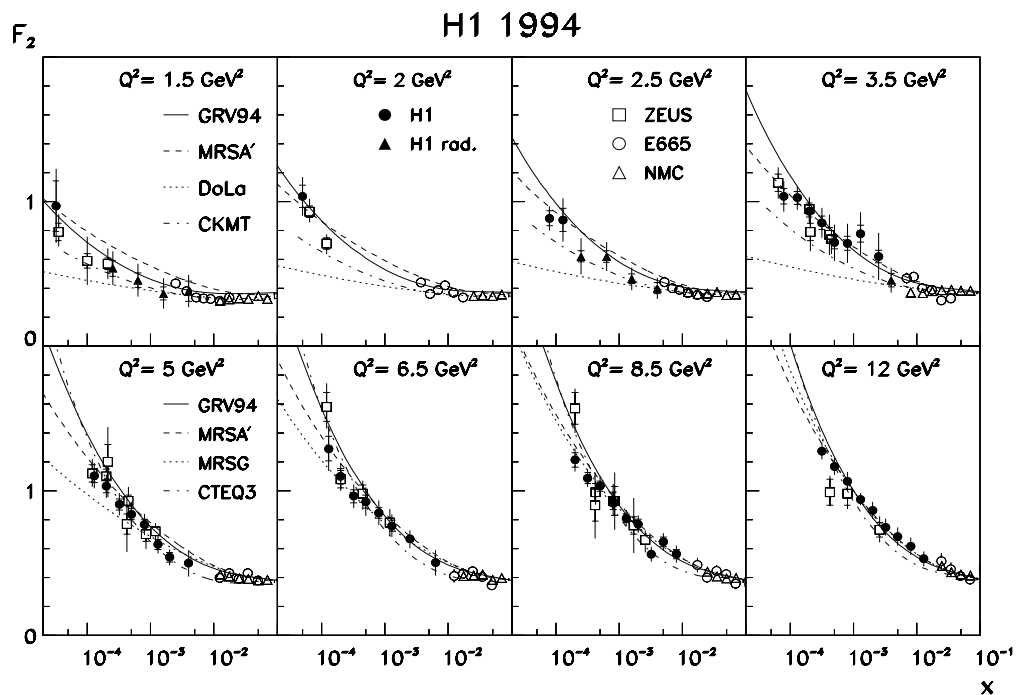


Figure 7.20: $F_2(x, Q^2)$ measurement in the low Q^2 region by H1 (closed circles: non-radiative events; closed triangles: radiative events [66]), together with results from ZEUS [63] (open squares), E665 [64] (open circles) and NMC [65] (open triangles) experiments. Different parameterisations for F_2 are compared to the data. The DOLA [71] and CKMT [72] curves are only shown for the upper row of Q^2 bins; CTEQ3M [75] and MRSG [74] are shown for the lower row; GRV [76] and MRSA' [74] are shown for the full Q^2 range (from [8]).

Q^2	x	F_2	δ_{stat}	δ_{syst}	R
1.5	.00003	0.969	0.176	0.187	0.71
1.5	.00025	0.540	0.055	0.104	0.75
1.5	.00063	0.458	0.050	0.101	0.74
1.5	.00158	0.365	0.045	0.095	0.70
1.5	.00398	0.381	0.070	0.087	0.63
2.0	.00005	1.037	0.077	0.110	0.65
2.5	.00008	0.885	0.052	0.065	0.80
2.5	.00013	0.874	0.079	0.127	0.80
2.5	.00025	0.622	0.037	0.119	0.80
2.5	.00063	0.621	0.039	0.093	0.79
2.5	.00158	0.466	0.033	0.072	0.75
2.5	.00398	0.402	0.039	0.062	0.65
3.5	.00008	1.036	0.053	0.092	0.64
3.5	.00013	1.026	0.045	0.067	0.64
3.5	.00020	0.934	0.041	0.075	0.64
3.5	.00032	0.854	0.046	0.093	0.64
3.5	.00050	0.716	0.041	0.119	0.64
3.5	.00080	0.712	0.049	0.126	0.63
3.5	.00130	0.778	0.058	0.137	0.61
3.5	.00250	0.621	0.043	0.157	0.59
3.5	.00398	0.458	0.046	0.075	0.54
5.0	.00013	1.106	0.049	0.074	0.54
5.0	.00020	1.033	0.044	0.069	0.54
5.0	.00032	0.907	0.039	0.066	0.54
5.0	.00050	0.839	0.039	0.076	0.53
5.0	.00080	0.769	0.037	0.063	0.53
5.0	.00130	0.630	0.034	0.050	0.51
5.0	.00200	0.540	0.033	0.043	0.50
5.0	.00400	0.500	0.029	0.086	0.46
6.5	.00013	1.292	0.085	0.127	0.49
6.5	.00020	1.101	0.052	0.072	0.48
6.5	.00032	0.963	0.045	0.068	0.48
6.5	.00050	0.926	0.044	0.088	0.48
6.5	.00080	0.848	0.038	0.076	0.47
6.5	.00130	0.759	0.039	0.068	0.46
6.5	.00250	0.667	0.029	0.054	0.43
6.5	.00630	0.504	0.029	0.084	0.37
8.5	.00020	1.215	0.050	0.062	0.44
8.5	.00032	1.089	0.038	0.048	0.44
8.5	.00050	1.033	0.034	0.062	0.43
8.5	.00080	0.923	0.031	0.038	0.43
8.5	.00130	0.811	0.030	0.047	0.42
8.5	.00200	0.770	0.034	0.049	0.40
8.5	.00320	0.562	0.028	0.043	0.38
8.5	.00500	0.648	0.033	0.051	0.36
8.5	.00800	0.564	0.032	0.049	0.33

Q^2	x	F_2	δ_{stat}	δ_{syst}	R
12.	.00032	1.276	0.020	0.055	0.39
12.	.00050	1.168	0.016	0.056	0.39
12.	.00080	1.067	0.015	0.061	0.38
12.	.00130	0.942	0.015	0.039	0.37
12.	.00200	0.866	0.016	0.057	0.36
12.	.00320	0.749	0.016	0.055	0.34
12.	.00500	0.685	0.016	0.061	0.32
12.	.00800	0.618	0.016	0.057	0.30
12.	.01300	0.531	0.017	0.049	0.26
15.	.00032	1.426	0.030	0.064	0.37
15.	.00050	1.280	0.020	0.050	0.36
15.	.00080	1.110	0.018	0.057	0.35
15.	.00130	1.008	0.016	0.033	0.35
15.	.00200	0.895	0.015	0.046	0.34
15.	.00320	0.773	0.014	0.036	0.32
15.	.00500	0.677	0.014	0.035	0.30
15.	.00800	0.634	0.014	0.031	0.28
15.	.01300	0.547	0.013	0.027	0.24
20.	.0005	1.407	0.026	0.054	0.34
20.	.0008	1.210	0.022	0.050	0.33
20.	.0013	1.061	0.020	0.055	0.33
20.	.0020	0.945	0.018	0.042	0.32
20.	.0032	0.861	0.017	0.038	0.31
20.	.0050	0.761	0.017	0.028	0.30
20.	.0080	0.693	0.016	0.035	0.28
20.	.0130	0.567	0.015	0.024	0.26
20.	.0200	0.487	0.015	0.025	0.22
25.	.0005	1.546	0.047	0.058	0.40
25.	.0008	1.330	0.028	0.051	0.39
25.	.0013	1.151	0.024	0.047	0.38
25.	.0020	1.019	0.022	0.035	0.37
25.	.0032	0.872	0.020	0.034	0.35
25.	.0050	0.768	0.019	0.034	0.33
25.	.0080	0.683	0.018	0.031	0.30
25.	.0130	0.585	0.017	0.028	0.26
25.	.0200	0.548	0.017	0.037	0.22
35.	.0008	1.442	0.038	0.051	0.36
35.	.0013	1.308	0.032	0.052	0.35
35.	.0020	1.116	0.027	0.052	0.33
35.	.0032	0.928	0.024	0.038	0.32
35.	.0050	0.832	0.023	0.040	0.30
35.	.0080	0.739	0.022	0.035	0.27
35.	.0130	0.600	0.019	0.025	0.24
35.	.0200	0.508	0.019	0.019	0.20
35.	.0320	0.452	0.019	0.026	0.16

./..

Q^2	x	F_2	δ_{stat}	δ_{syst}	R
45.	.0013	1.305	0.038	0.048	0.32
45.	.0020	1.225	0.034	0.049	0.31
45.	.0032	1.105	0.032	0.058	0.30
45.	.0050	0.912	0.028	0.033	0.28
45.	.0080	0.743	0.025	0.029	0.26
45.	.0130	0.686	0.024	0.031	0.22
45.	.0200	0.599	0.022	0.027	0.19
45.	.0320	0.505	0.021	0.023	0.15
45.	.0500	0.411	0.022	0.028	0.12
60.	.0020	1.213	0.042	0.048	0.29
60.	.0032	1.079	0.037	0.045	0.28
60.	.0050	0.937	0.033	0.043	0.26
60.	.0080	0.830	0.031	0.046	0.24
60.	.0130	0.701	0.028	0.029	0.21
60.	.0200	0.639	0.027	0.025	0.18
60.	.0320	0.586	0.026	0.028	0.14
60.	.0500	0.492	0.025	0.023	0.11
60.	.0800	0.432	0.027	0.023	0.08
90.	.0032	1.103	0.052	0.048	0.26
90.	.0050	0.997	0.045	0.047	0.24
90.	.0080	0.908	0.041	0.056	0.22
90.	.0130	0.726	0.035	0.040	0.19
90.	.0200	0.650	0.033	0.031	0.17
90.	.0320	0.587	0.030	0.034	0.13
90.	.0500	0.481	0.027	0.019	0.10
120.	.0050	1.018	0.094	0.076	0.23
120.	.0080	0.914	0.068	0.056	0.21
120.	.0130	0.755	0.063	0.111	0.18
120.	.0200	0.570	0.049	0.057	0.16
120.	.0320	0.582	0.048	0.060	0.13
120.	.0500	0.402	0.035	0.045	0.10
120.	.0800	0.330	0.032	0.034	0.07

Table 7.4: Measurement of the proton structure function $F_2(x, Q^2)$, with statistical and systematic errors. The normalisation uncertainty, not included in the systematic error, is 3.9% for $Q^2 \leq 6.5 \text{ GeV}^2$ and 1.5% for $Q^2 > 6.5 \text{ GeV}^2$ (from [8]).

Q^2 (gev^2)	x	y	F_2	$1 + \delta$ django	$1 + \delta$ hector	δ_{stat} %	δ_E (+)%	δ_E (-)%	δ_θ (+)%	δ_θ (-)%	δ_E^{had} (+)%	δ_E^{had} (-)%	δ_{bg} %	δ_{stat}^{cmc} %
1.5	3.2^{-5}	0.52	0.969	1.240	1.293	18.2	-3.0	2.3	-16.1	14.3			5.0	6.4
2.0	5.0^{-5}	0.44	1.037	1.284	1.307	7.1	-0.3	1.1	-6.5	5.2			6.0	3.6
2.5	8.0^{-5}	0.35	0.885	1.309	1.281	5.8	-2.7	0.2	-4.1	2.1			2.0	2.7
2.5	1.3^{-4}	0.21	0.874	1.225	1.239	9.0	0.7	7.7	-8.2	15.3			0.0	4.4
3.5	8.0^{-5}	0.48	1.036	1.292	1.303	5.1	-2.2	2.5	0.0	-0.8			6.0	2.7
3.5	1.3^{-4}	0.30	1.026	1.258	1.256	4.4	-3.2	2.3	-1.2	-0.2			1.0	2.5
3.5	2.0^{-4}	0.19	0.934	1.237	1.216	4.4	-4.3	4.0	-4.5	3.5			0.0	2.6
3.5	3.2^{-4}	0.12	0.854	1.200	1.177	5.4	-5.5	7.3	-7.4	5.7			0.0	3.2
3.5	5.0^{-4}	0.078	0.716			5.7	8.1	-4.5	-5.9	8.1	6.8	-8.1	2.8	2.2
3.5	8.0^{-4}	0.048	0.712			6.9	8.9	-5.4	-8.9	10.0	6.3	-10.0	0.9	2.4
3.5	1.3^{-3}	0.030	0.778			7.5	7.3	-8.1	-7.7	10.2	9.2	-8.5	0.0	3.2
3.5	2.5^{-3}	0.016	0.621			6.9	7.9	-13.9	-16.3	12.1	10.6	-11.2	2.4	2.0
5.0	1.3^{-4}	0.43	1.106	1.286	1.282	4.4	-1.2	1.8	1.8	-1.4			2.0	2.6
5.0	2.0^{-4}	0.28	1.033	1.237	1.237	4.3	-3.5	2.6	0.5	-1.8			0.0	2.5
5.0	3.2^{-4}	0.17	0.907	1.179	1.195	4.3	-3.8	5.1	2.4	1.2			0.0	2.6
5.0	5.0^{-4}	0.11	0.839	1.127	1.156	4.6	-7.9	5.8	-1.3	-2.3			0.0	2.7
5.0	8.0^{-4}	0.069	0.769			4.8	-2.4	-1.5	0.6	-2.5	2.7	-4.7	0.1	2.0
5.0	1.3^{-3}	0.043	0.630			5.4	0.7	0.8	0.4	1.6	1.7	-0.3	0.1	2.0
5.0	2.0^{-3}	0.028	0.540			6.1	2.6	0.5	0.0	-0.1	3.5	-2.9	0.0	1.7
5.0	4.0^{-3}	0.014	0.500			5.8	3.7	1.1	2.5	4.9	15.7	-5.3	0.1	1.2
6.5	1.3^{-4}	0.55	1.292	1.324	1.328	6.6	-0.5	3.4	3.7	0.4			6.0	3.9
6.5	2.0^{-4}	0.36	1.101	1.264	1.264	4.7	-2.9	1.8	0.9	-1.2			0.0	2.9
6.5	3.2^{-4}	0.22	0.963	1.211	1.217	4.7	-3.8	3.3	1.3	-2.6			0.0	2.8
6.5	5.0^{-4}	0.14	0.926	1.167	1.175	4.8	-4.2	10.2	0.5	2.2			0.0	2.9
6.5	8.0^{-4}	0.090	0.848			4.5	-1.6	3.6	4.4	-2.0	4.4	-3.3	0.1	2.4
6.5	1.3^{-3}	0.055	0.759			5.1	-1.1	1.6	3.2	-2.1	1.4	-0.4	0.1	2.2
6.5	2.5^{-3}	0.029	0.667			4.3	2.5	-1.0	-0.2	0.7	-2.2	1.0	0.1	1.7
6.5	6.3^{-3}	0.011	0.504			5.8	-4.8	1.9	3.5	-4.9	12.1	-7.1	0.0	1.4
8.5	2.0^{-4}	0.47	1.215	1.307	1.302	4.2	-1.5	1.7	-2.0	1.7			3.3	1.2
8.5	3.2^{-4}	0.29	1.089	1.243	1.244	3.5	-2.3	2.2	-1.7	2.7			0.3	1.1
8.5	5.0^{-4}	0.19	1.033	1.201	1.198	3.3	-5.6	4.1	-2.1	1.6			0.0	1.2
8.5	8.0^{-4}	0.12	0.923			3.3	-1.5	2.3	-1.4	0.7	-0.3	2.0	0.1	1.2
8.5	1.3^{-3}	0.072	0.811			3.7	-1.1	3.1	-0.8	3.7	-2.6	3.9	0.1	1.3
8.5	2.0^{-3}	0.047	0.770			4.4	-3.7	4.1	-0.9	0.9	-3.8	0.8	0.1	1.6
8.5	3.2^{-3}	0.029	0.562			4.9	-3.0	4.9	-1.0	0.5	-0.5	1.2	0.0	1.7
8.5	5.0^{-3}	0.019	0.648			5.1	-4.8	3.3	-1.6	0.2	-3.6	4.0	0.0	2.0
8.5	8.0^{-3}	0.012	0.564			5.7	-3.2	4.5	-1.6	0.6	-4.5	3.3	0.0	2.2
12.0	3.2^{-4}	0.41	1.276	1.289	1.278	1.5	-1.9	1.3	-2.8	2.0			1.3	1.1
12.0	5.0^{-4}	0.27	1.168	1.245	1.223	1.4	-2.8	3.6	-1.8	2.1			0.2	1.1
12.0	8.0^{-4}	0.17	1.067	1.187	1.178	1.4	-5.5	4.8	-1.8	1.3			0.0	1.2
12.0	1.3^{-3}	0.10	0.942			1.6	-2.5	0.2	0.2	-1.6	-2.9	2.5	0.1	1.4
12.0	2.0^{-3}	0.067	0.866			1.8	-4.2	3.4	3.0	-3.2	-2.3	4.8	0.1	1.6
12.0	3.2^{-3}	0.042	0.749			2.1	-6.0	4.2	3.2	-4.5	-2.2	2.2	0.1	1.8
12.0	5.0^{-3}	0.027	0.685			2.3	-6.8	6.5	4.4	-5.2	-2.0	2.0	0.0	2.1
12.0	8.0^{-3}	0.017	0.618			2.6	-5.8	6.3	6.1	-4.8	-1.9	3.7	0.2	2.3
12.0	1.3^{-2}	0.010	0.531			3.1	-8.0	4.6	3.7	-5.0	-4.6	3.2	0.0	2.8

./...

Q^2 (gev^2)	x	y	F_2	$1 + \delta$ django	$1 + \delta$ hector	δ_{stat} %	δ_E (+)%	δ_E (-)%	δ_θ (+)%	δ_θ (-)%	δ_E^{had} (+)%	δ_E^{had} (-)%	δ_{bg} %	δ_{stat}^{mc} %
15.0	3.2^{-4}	0.52	1.426	1.332	1.333	2.1	-2.2	3.2	0.2	0.9			1.7	1.3
15.0	5.0^{-4}	0.33	1.280	1.265	1.254	1.6	-1.8	2.2	-1.3	1.7			0.3	1.1
15.0	8.0^{-4}	0.21	1.110	1.222	1.203	1.6	-3.9	3.5	-1.4	2.3			0.1	1.1
15.0	1.3^{-3}	0.13	1.008			1.6	1.5	-1.7	-1.7	0.8	-0.2	-0.4	0.0	1.3
15.0	2.0^{-3}	0.083	0.895			1.7	4.0	-2.3	-2.0	3.3	-1.0	1.5	0.1	1.4
15.0	3.2^{-3}	0.052	0.773			1.8	2.9	-2.8	-2.2	1.9	-1.2	1.6	0.0	1.5
15.0	5.0^{-3}	0.033	0.677			2.0	2.9	-3.4	-2.5	2.7	-1.4	0.6	0.0	1.7
15.0	8.0^{-3}	0.021	0.634			2.1	3.0	-2.8	-2.2	2.6	-1.1	1.0	0.0	1.8
15.0	1.3^{-2}	0.013	0.547			2.4	3.1	-2.2	-1.2	2.8	-1.8	2.3	0.0	2.1
20.0	5.0^{-4}	0.44	1.407	1.308	1.298	1.9	-2.5	1.4	-1.6	0.8			0.6	1.2
20.0	8.0^{-4}	0.28	1.210	1.240	1.232	1.8	-3.2	2.0	-1.9	0.4			0.1	1.1
20.0	1.3^{-3}	0.17	1.061	1.200	1.183	1.9	-3.8	4.0	-1.5	1.8			0.0	1.2
20.0	2.0^{-3}	0.11	0.945			1.9	2.4	-3.0	-2.1	2.0	-1.4	0.2	0.1	1.3
20.0	3.2^{-3}	0.069	0.861			2.0	3.7	-1.7	-0.6	2.9	-0.5	1.5	0.0	1.5
20.0	5.0^{-3}	0.044	0.761			2.2	0.2	-2.5	-2.0	0.6	-2.0	1.0	0.0	1.6
20.0	8.0^{-3}	0.028	0.693			2.3	3.8	-1.9	-1.9	2.1	-1.7	2.8	0.0	1.8
20.0	1.3^{-2}	0.017	0.567			2.6	2.5	-1.5	-1.9	2.1	0.3	1.5	0.0	2.0
20.0	2.0^{-2}	0.011	0.487			3.0	1.2	-3.3	-2.8	1.3	-2.8	2.0	0.0	2.3
25.0	5.0^{-4}	0.55	1.546	1.393	1.380	3.0	0.1	0.5	-1.0	2.1			1.1	1.6
25.0	8.0^{-4}	0.35	1.330	1.290	1.268	2.1	-1.7	2.5	-1.0	1.1			0.2	1.1
25.0	1.3^{-3}	0.21	1.151	1.237	1.210	2.1	-2.6	1.5	-1.8	1.4			0.0	1.2
25.0	2.0^{-3}	0.14	1.019			2.1	2.0	-1.6	-1.3	1.0	-0.1	1.0	0.0	1.3
25.0	3.2^{-3}	0.087	0.872			2.2	1.6	-2.5	-2.4	1.1	-0.9	0.3	0.0	1.4
25.0	5.0^{-3}	0.055	0.768			2.5	2.6	-2.9	-1.1	1.6	-1.5	1.6	0.0	1.6
25.0	8.0^{-3}	0.035	0.683			2.6	3.1	-2.7	-1.6	1.8	-0.2	1.8	0.1	1.7
25.0	1.3^{-2}	0.021	0.585			2.9	3.5	-2.1	-1.0	2.6	-1.1	2.0	0.0	1.9
25.0	2.0^{-2}	0.014	0.548			3.1	5.5	-3.9	-2.2	1.8	-2.5	3.1	0.0	2.1
35.0	8.0^{-4}	0.48	1.442	1.333	1.323	2.6	-0.5	1.6	-0.7	2.0			0.4	1.3
35.0	1.3^{-3}	0.30	1.308	1.257	1.243	2.4	-2.1	2.0	-1.4	1.8			0.0	1.2
35.0	2.0^{-3}	0.19	1.116	1.229	1.190	2.4	-3.7	2.8	-1.6	1.0			0.0	1.2
35.0	3.2^{-3}	0.12	0.928			2.5	3.1	-2.2	-1.0	2.1	0.0	0.7	0.0	1.4
35.0	5.0^{-3}	0.078	0.832			2.7	2.6	-4.0	-2.3	1.6	-2.1	0.2	0.0	1.5
35.0	8.0^{-3}	0.049	0.739			2.9	3.6	-2.2	-2.1	2.4	-0.7	0.5	0.0	1.7
35.0	1.3^{-2}	0.030	0.600			3.2	2.4	-2.6	-1.0	1.1	-0.4	1.3	0.0	1.8
35.0	2.0^{-2}	0.019	0.508			3.6	1.4	-0.7	-0.6	2.1	-1.1	1.4	0.0	2.0
35.0	3.2^{-2}	0.012	0.452			4.1	4.4	-1.7	-0.8	2.0	-2.7	3.6	0.0	2.3
45.0	1.3^{-3}	0.38	1.305	1.312	1.287	2.9	-2.2	1.6	-1.1	-0.1			0.1	1.2
45.0	2.0^{-3}	0.25	1.225	1.240	1.221	2.7	-1.9	2.7	-1.0	1.7			0.0	1.2
45.0	3.2^{-3}	0.16	1.105	1.185	1.170	2.9	-4.5	3.8	-0.8	1.6			0.0	1.3
45.0	5.0^{-3}	0.10	0.912			3.0	2.1	-1.6	-1.1	0.8	-1.2	1.1	0.0	1.5
45.0	8.0^{-3}	0.062	0.743			3.4	2.8	-1.1	-0.4	1.2	-1.0	2.4	0.0	1.7
45.0	1.3^{-2}	0.038	0.686			3.5	3.4	-2.7	-1.4	1.5	-1.2	0.8	0.0	1.8
45.0	2.0^{-2}	0.025	0.599			3.7	1.9	-3.6	-1.5	1.8	-0.6	0.8	0.0	1.9
45.0	3.2^{-2}	0.016	0.505			4.1	3.0	-2.6	-0.7	1.5	-1.3	1.7	0.0	2.1
45.0	5.0^{-2}	0.010	0.411			5.2	3.2	-3.3	-1.2	2.0	-3.9	5.1	0.0	2.5

.. / ...

Q^2 (GeV^2)	x	y	F_2	$1 + \delta$ django	$1 + \delta$ hector	δ_{stat} %	δ_E (+)%	δ_E (-)%	δ_θ (+)%	δ_θ (-)%	δ_E^{had} (+)%	δ_E^{had} (-)%	δ_{bg} %	δ_{stat}^{mc} %
60.0	2.0^{-3}	0.33	1.213	1.291	1.259	3.4	-1.1	3.3	-0.3	1.9			0.0	1.3
60.0	3.2^{-3}	0.21	1.079	1.222	1.200	3.4	-2.4	2.6	-0.9	1.1			0.0	1.2
60.0	5.0^{-3}	0.13	0.937			3.5	2.6	-3.2	-1.4	1.7	1.6	-1.4	0.0	1.5
60.0	8.0^{-3}	0.083	0.830			3.7	4.0	-4.7	-1.7	1.3	-1.8	0.4	0.0	1.7
60.0	1.3^{-2}	0.051	0.701			4.0	2.5	-2.7	-1.6	0.8	-0.2	1.0	0.0	1.8
60.0	2.0^{-2}	0.033	0.639			4.2	2.8	-1.4	-0.5	1.1	-1.6	0.7	0.0	1.9
60.0	3.2^{-2}	0.021	0.586			4.3	4.0	-2.2	-0.9	1.5	-0.6	2.7	0.0	2.0
60.0	5.0^{-2}	0.013	0.492			5.0	2.0	-3.0	-0.6	1.7	-1.7	2.2	0.0	2.2
60.0	8.0^{-2}	0.0083	0.432			6.2	3.5	-2.8	-1.1	1.1	-0.8	3.5	0.0	2.7
90.0	3.2^{-3}	0.31	1.103	1.260	1.235	4.7	-1.9	1.5	-2.4	2.1			0.0	1.6
90.0	5.0^{-3}	0.20	0.997	1.199	1.179	4.4	-4.0	2.5	-1.7	0.7			0.0	1.4
90.0	8.0^{-3}	0.12	0.908	1.138	1.130	4.5	-5.3	7.0	-1.5	1.4			0.0	1.4
90.0	1.3^{-2}	0.077	0.726			4.8	3.7	-4.9	-1.1	1.8	0.0	0.9	0.0	1.9
90.0	2.0^{-2}	0.050	0.650			5.0	2.5	-4.1	-1.6	1.1	-0.3	0.3	0.0	2.0
90.0	3.2^{-2}	0.031	0.587			5.1	4.9	-4.2	-2.3	1.1	-0.3	-0.3	0.0	2.1
90.0	5.0^{-2}	0.020	0.481			5.5	3.3	-1.0	-0.1	1.3	-0.4	1.5	0.0	2.1
120.0	5.0^{-3}	0.27	1.018	1.240	1.213	9.2	-3.5	6.2	-3.0	4.8			0.0	3.1
120.0	8.0^{-3}	0.17	0.914	1.191	1.159	7.5	-5.6	3.3	-3.6	1.4			0.0	2.2
120.0	1.3^{-2}	0.10	0.755			8.4	14.0	-13.3	-3.4	3.2	0.0	-2.6	0.0	3.2
120.0	2.0^{-2}	0.067	0.570			8.5	8.1	-8.8	-3.1	3.1	2.0	-2.5	0.0	3.1
120.0	3.2^{-2}	0.042	0.582			8.2	9.5	-9.1	-2.3	2.5	0.0	1.0	0.0	3.2
120.0	5.0^{-2}	0.027	0.402			8.7	8.9	-10.9	-4.2	1.5	1.4	-1.6	0.0	3.0
120.0	8.0^{-2}	0.017	0.330			9.7	10.4	-8.2	-1.5	2.7	0.1	1.7	0.0	3.1

Table 7.5: Main sources of systematic errors to the $F_2(x, Q^2)$ structure function measurement.

Starting from the left are shown:

- event kinematics: Q^2 , x and y . Measurements obtained using the “electron” and the Σ method of kinematic reconstruction are separated by a horizontal line for each Q^2 ;
- F_2 measurement results obtained from the following data samples: $1.5 \leq Q^2 \leq 6.5 \text{ GeV}^2$ - shifted vertex and satellite bunch data samples, $Q^2 = 8.5$ - nominal vertex open triangle and $12.0 \leq Q^2 \leq 120.0 \text{ GeV}^2$ - close triangle data samples. They are separated with a double horizontal line;
- ratio of the radiative to the Born DIS cross-sections ($1 + \delta$), as obtained using the DJANGO Monte Carlo program and the HECTOR analytical package. Radiative corrections are given for the “electron” points only;
- δ_{stat} : statistical error;
- δ_E , δ_θ and δ_E^{had} : F_2 modification (in %) resulting from a systematic displacement of the scattered electron energy scale ($\pm 1\%$), of the scattered electron polar angle ($\pm 1 \text{ mrad}$) and of the hadronic energy scale (only Σ measurement is affected);
- δ_{bg} : systematic error of the background subtraction;
- δ_{stat}^{mc} : statistical error of Monte Carlo simulation.

Conclusions and Outlook

The analysis presented here has been performed at DESY, in the frame of the H1 collaboration, composed of more than 400 scientists from 12 countries throughout the world. A large particle detector is operated by H1 in the North Hall of the HERA accelerator, for studying collisions between 27.5 GeV electrons and 820 GeV protons. At HERA, the internal structure of the proton is being investigated with unprecedented accuracy by two experiments: H1 and ZEUS.

Deep Inelastic Scattering is a fundamental process for measuring quark and gluon densities in the proton and to make quantitative test of perturbative QCD. Compared to previous fixed-target experiments, the measured kinematic range is extended by two orders of magnitude at low x and high Q^2 . In this new domain, it is possible on one side to resolve structures down to 10^{-18} m (high Q^2), and on the other side to analyse a region of high parton density (low x), which is of special significance for the investigation of QCD effects. The latter domain is the subject of many speculations among theorists and appropriate experimental data are needed.

In deep-inelastic experiments the low x region is correlated, because of the overall limitation of the available energy, with low values of Q^2 . Thus the low x phenomenology cannot avoid investigating the transition from the structure function F_2 at small x to the photoproduction cross section at high energies. The interest is thus on the W -dependence at low Q^2 , since on one side for $Q^2 \sim 0$ the non-perturbative regime is successfully described by the Regge-inspired models, and on the other side for finite Q^2 , perturbative QCD predictions are given by the evolution equations.

A measurement has been presented here of the proton structure function $F_2(x, Q^2)$ based on data taken by the H1 experiment during the year 1994. The integrated luminosity is 2.7 pb^{-1} , which represents a tenfold increase in statistics compared to previous analysis based on the 1993 data. Low Q^2 values are reached using data with the ep interaction vertex shifted from the nominal position in special data taking period (SV data), and with the “satellite bunch” data sample. The data cover a kinematic range for Q^2 between 1.5 and 120 GeV^2 and x between $3.0 \cdot 10^{-5}$ and 0.32. The systematic effects affecting the F_2 measurement were in the focus of the present analysis, since statistical uncertainties become insignificant. The detailed technical studies presented here were aimed to backing the F_2 analysis results as recently published by H1 [8].

In order to increase the statistical significance of the low Q^2 F_2 measurement a special “proton satellite bunch” data sample was analysed here. This satellite bunch is a known feature of the HERA proton acceleration chain and is observed in the H1 detector at $z \approx +70$ cm with respect to the nominal interaction point, i.e. at the same position as the SV data sample. The total integrated luminosity of this satellite bunch for the 1994 e^+p collisions was estimated to be $73.8 \pm 5.2 \text{ nb}^{-1}$. The relatively small uncertainty on the integrated luminosity measurement for the satellite bunch ($\delta\mathcal{L}_{sat} = 7.1\%$, compared to $\delta\mathcal{L}_{sv} = 3.9\%$ for the shifted vertex data sample) made it possible to use these events for the F_2 measurement on a comparable basis as the SV data sample. Combining the satellite

luminosity estimate with an analysis of the Forward Time of Flight (FToF) scintillator data, a correction to the H1 luminosity accounting for the total satellite bunch effect was also provided.

The experimental method used for measurement of the DIS cross-section and the structure function $F_2(x, Q^2)$ is based on a comparison of the data with the results of a Monte Carlo simulation. The “electron” method of measuring the DIS event kinematics is known to be the best at high y and, in particular, at low x - low Q^2 . The kinematic range is extended at low y using the “ Σ ” method of kinematic reconstruction. The background contamination restricts the covered kinematic domain at high y to $y \leq 0.6$. The DIS event selection used here is based on the identification of the scattered electron in the backward calorimeter BEMC. The quality of the event selection was verified by measuring the relative event yield for each particular data sample for individual detector runs. Several runs were rejected due to known trigger, detector or reconstruction problems. 150 000 events were finally selected for the intermediate Q^2 values ($8.5 \leq Q^2 \leq 120 \text{ GeV}^2$) and ~ 15 000 events for the low Q^2 range ($1.5 \leq Q^2 < 8.5 \text{ GeV}^2$), corresponding respectively to an integrated luminosity of 2 000 and 125 nb^{-1} .

Among the systematic effects affecting the F_2 measurement at low Q^2 , the scattered electron energy and angle measurement uncertainties are undoubtedly the most important. The quality of the space point measurement in the BEMC was first investigated and improved. The BEMC energy calibration was then studied using the “double angle” method for the energy reconstruction. An essential improvement of the BEMC energy reconstruction could be achieved for the innermost triangular stacks and the crack region separating the inner triangles and the first quadratic stack. Global corrections to the BEMC energy scale were worked out for the outer BEMC stacks. The BEMC energy scale uncertainty is reduced to 1% after applying the corrections mentioned above, which is a substantial improvement compared to the 1.7% achieved for the 1993 data. The global quality of the determination of the polar angle θ_e was studied next. The θ_e resolution was found to be described with satisfactory precision by the Monte Carlo simulation. Taking into account the global BPC alignment uncertainty, 1 mrad was taken as the systematic error of the θ_e measurement. The θ_e measurement quality was found to be degraded locally by: (i) a systematic bias in the distribution of the reconstructed z -coordinate of the interaction vertex in the particular case of vertex fits obtained only from the scattered electron track and (ii) a systematic bias in the BPC hit reconstruction due to preshowering in the cables between the CJC and the BPC. The former effect is found to affect the $Q^2 > 15 \text{ GeV}^2$ kinematic range and only the SV data sample. At variance with the first effect the second one is not negligible in case of the nominal interaction point collisions, while it has few or no impact on the SV data sample. It should be noted that a better dead material description by the Monte Carlo simulation will be needed in the backward region for future high precision measurements at very low Q^2 . Finally, the hadronic final state reconstruction is found to be biased in case of the shifted vertex interactions, leading to a 10% systematic shift of y_Σ , not reproduced by Monte Carlo. Here again, an appropriate calibration has to be performed if more data are taken in the future.

The selection efficiencies were found to be globally reproduced by the Monte Carlo simulation with satisfactory precision. Among them, a particular attention was paid to the study of the vertex reconstruction efficiency, which is undoubtedly the faintest effect to understand and to handle, crystallising all the conceptual difficulties of the F_2

measurement. Comparing the vertex efficiency estimated directly from the data with the predictions of the Monte Carlo simulation, it was shown for the latter that the vertex efficiency is strongly dependent on the input F_2 parameterisation, mainly through QED radiation. The vertex efficiency “mixed” kinematics estimate, i.e. expressed in function of θ_e and y_Σ is proved to provide a better context for the vertex efficiency measurement than the pure “electron-like” vertex efficiency. Using the CIP method to estimate the vertex efficiency in function of θ_e and y_Σ , a global agreement between the data and the Monte Carlo simulation was found. At low Q^2 , a $\leq 3\%$ systematic difference was observed. However, due to its poor resolution, the “mixed” kinematics does not allow local effects to be resolved, in particular at the CJC edges, i.e. for the low Q^2 - low x kinematic domain. An attempt was performed to improve the understanding of the vertex efficiency in the latter kinematic range by estimating it as a function of the purely topological quantities: θ_e and θ_j . A possible $\sim 5\%$ disagreement between the data and the Monte Carlo vertex efficiencies was found for $\theta_j \geq 170^\circ$. When larger statistics will be available and/or lower Q^2 and x kinematic domain will be reached, a better understanding of this efficiency will be needed. The effects of the W limitation in the Monte Carlo simulation on the vertex efficiency was found to be small for the low Q^2 - low x part of the kinematic plane (less than 0.5%), while it is not negligible at low y , and has to be investigated further for future analyses. The EBPC and ECRA efficiencies were found to be correctly reproduced by the Monte Carlo simulation.

A correct description of the detector acceptance effects requires the Monte Carlo z -vertex distribution and input parton distribution set to be reweighted according to the experimental results. In order to define the kinematic range where the F_2 measurement is possible, the resolution and stability of the “electron” and Σ methods of kinematic reconstruction were estimated using the full detector simulation. The “electron” method is used at high y ($0.15 \leq y \leq 0.6$), complemented by the Σ method at low y ($0.01 \leq y < 0.15$). The adopted binning was found to be well suited for the “electron” method, while the binning is too fine in x for the Σ method of kinematic reconstruction. The Σ bins were thus grouped in x two by two, but only in case of the SV and satellite bunch data samples. No bins were grouped in case of the nominal vertex data sample analysis, and this should be done in the future. The results of the F_2 structure function measurements for different data samples, i.e. satellite bunch, shifted vertex, nominal vertex “open” and “closed triangles” data samples, were compared and the agreement between them was found good. The final F_2 measurement from the 1994 data is based on these different data samples, allowing for a better coverage of the kinematic plane. This thesis contributes directly to the H1 '94 measurement in the lowest Q^2 part ($1.5 \leq Q^2 \leq 6.5 \text{ GeV}^2$), from a combination of the satellite and the shifted vertex data sample analyses. The errors are decreased by a factor two as compared to the 1993 analysis.

The H1 measurement is found to be in good agreement with the one of the ZEUS experiment and matches well with the data from fixed target experiments at higher x values. The strong rise of F_2 at low x is confirmed, down to the lowest Q^2 values, $Q^2 \sim 1.5 \text{ GeV}^2$. The conventional DGLAP-based parameterisations (GRV and MRSA parton distribution sets) give a good description of the data for the whole kinematic range (with the possible exception of the first Q^2 bin for the latter), while parameterisations motivated by Regge theory lie below the data for $Q^2 \geq 2 \text{ GeV}^2$ at low x .

By the time this thesis was finalised, preliminary results on a measurement of the

structure function F_2 were reported by H1 [77] for momentum transfers down to $Q^2 \sim 0.35 \text{ GeV}^2$ and for Bjorken x values down to $6 \cdot 10^{-6}$. This extension in kinematic reach to lower x and Q^2 values has been achieved thanks to the 1995 upgrading of both the backward calorimeter and drift chamber. The angular acceptance of the new detectors is $< 177.8^\circ$ for collisions at the nominal vertex, increasing to 178.5° for collisions where the interaction vertex is shifted by 70 cm in the proton direction¹. The rise of F_2 observed at the smallest values reached for Q^2 is close to the one expected from Regge-motivated predictions. Hence these data cover the transition region from DIS to photoproduction.

Finally, a few words should be said about the future prospects which were discussed during the 1996 HERA Physics Workshop [78]. A challenging scenario of running HERA for many years has been developed. A luminosity of $> 2 \cdot 10^{31} \text{ cm}^{-2}\text{s}^{-1}$ is expected resulting in $\sim 180 \text{ pb}^{-1}$ per year of HERA delivered integrated luminosity (corresponding to $\sim 100 \text{ pb}^{-1}$ of H1 physics luminosity). The envisaged increase of luminosity will allow for further improvement of the detector calibrations and thus for reducing the systematic errors to the level of a few per cent ($\leq 3\%$) in almost the full accessible kinematic range. On the basis of these data high precision studies of QCD in the region of very small x and very large Q^2 can be carried out.

For instance: (i) for $Q^2 > 500 \text{ GeV}^2$ and both electron and positron beams running two neutral current and two charged current reactions can be measured, which will permit to extract various structure functions and combinations of parton densities. All these measurements require highest luminosities, $\mathcal{L} \geq 500 \text{ pb}^{-1}$, about equally shared between electron and positron runs; (ii) by using deuterons instead of protons in HERA the neutron structure functions can be measured and the up-down quark difference estimated; (iii) reducing the electron beam energy would permit to reach very low values of $Q^2 \ll 1 \text{ GeV}^2$; (iv) lowering E_p is also a necessity for measuring the longitudinal structure function F_L , which indeed requires a set of about four different proton beam energies with luminosities around $5 - 10 \text{ pb}^{-1}$ per energy setting; (v) finally, with a luminosity of several 100 pb^{-1} , the charm structure function will be measurable with an estimated accuracy of 10%. This will permit a detailed determination of the gluon distribution.

¹The effective angular acceptance of the previous BPC-BEMC detector was $< 173^\circ$ for collisions at the nominal vertex and $< 175.5^\circ$ for the shifted interaction vertex position.

Bibliography

- [1] J. Feltesse, DAPNIA-SPP-94-35(1994), Invited talk at the 27. International Conference on High Energy Physics, Glasgow, Scotland, 1994.
- [2] B. Badelek, J. Bartels, N. Brook, A. De Roeck, T. Gehrmann, M. Lancaster, A. D. Martin, A. Vogt *Working Group Report on the Structure of the Proton*, DTP/96/20, (1996);
To be published in Proc. of Durham Workshop on “HERA Physics: Proton, Photon and Pomeron Structure”, *J. Phys. G*.
- [3] B. Badelek, J. Kwieciński, *The low- Q^2 , low- x region in electroproduction* *Rev. Mod. Phys.* Vol. 68, No. 2, (1996) 445.
- [4] H1 Collaboration, I. Abt et al., *Nucl. Phys.* **B407** (1993) 515.
- [5] ZEUS Collaboration, M. Derrick et al., *Phys. Lett.* **B316** (1993) 412.
- [6] H1 Collaboration, T. Ahmed et al., *Nucl. Phys.* **B439** (1995) 471.
- [7] ZEUS Collaboration, M. Derrick et al., *Z. Phys.* **C65** (1995) 379.
- [8] H1 Collaboration, T. Ahmed et al., *A Measurement and QCD Analysis of the Proton Structure Function $F_2(x, Q^2)$ at HERA*, *Nucl. Phys.* **B470** (1996) 3.
- [9] T. Muta, *Foundations of Quantum Chromodynamics*, ed. World Scientific Publishing, Singapore (1987).
- [10] Yu. L. Dokshitzer, *Sov. Phys. JETP* **46** (1977) 641;
V. N. Gribov and L.N. Lipatov, *Sov. J. Nucl. Phys.* **15** (1972) 438 and 675;
G. Altarelli and G. Parisi, *Nucl. Phys.* **B126** (1977) 297.
- [11] Yu. L. Dokshitzer, V. A. Khoze, A. H. Mueller and S. I. Troyan, *Basics of Perturbative QCD*, ed. Frontière, France (1991).
- [12] E. A. Kuraev, L. N. Lipatov and V. S. Fadin, *Sov. Phys. JETP* **45** (1977) 199;
Y. Y. Balitsky and L.N. Lipatov, *Sov. J. Nucl. Phys.* **28** (1978) 822.
- [13] M. Ciafaloni, *Nucl. Phys.* **B296** (1988) 49;
S. Catani, F. Fiorani and G. Marchesini, *Phys. Lett.* **B234** (1990) 339; *Nucl. Phys.* **B336** (1990) 18.
- [14] *Proc. of the HERA workshop on Physics at HERA*, Hamburg (1991), eds. W. Buchmüller and G. Ingelman, DESY, Hamburg (1992), vol. 1,2,3.
- [15] B. H. Wiik, *HERA: Machine and Experiment*, in: *Proc. of the XXIV Int. Conf. on High Energy Physics*, ed. Springer-Verlag, Berlin (1989) 404–421.

-
- [16] F. Willeke, *HERA Proton Betrieb 1994*, in: *HERA Seminar Bad Lauterberg 1995*, preprint DESY-HERA 95-03 (1995) 177.
- [17] W. Scharf, *Particle Accelerators and their uses. Part I: Accelerator Design*, ed. Harwood Academic Publishers (1986).
- [18] F. Willeke, private communication.
- [19] G. Wiesenfeldt, *Diplomarbeit*, II Inst. Exp., Univ. Hamburg (1995), Hamburg preprint, März 1995.
- [20] S. Levonian, *Final analysis results. Report on H1 meeting, 1-Dec-94*, in: S. Levonian, <http://dice2.desy.de/h1/iww/iwork/ilumi/H1LUMI.PREC94.PS>.
- [21] S. Levonian, private communication.
- [22] Smaïn Kermiche, *Ph. D. Thesis*, Université de Paris-Sud, Centre d'Orsay, LAL 94-14 (1994).
- [23] L. Favart, *Ph. D. Thesis*, Université Libre de Bruxelles, IIHE (ULB-VUB) (1995).
- [24] S. Levonian, A. Panitch, *Treatment of the Proton Satellite Bunch in 1994 Data*, H1 internal report, H1-09/95-454 (1995).
- [25] H1 Collaboration, T. Ahmed et al., *Z. Phys.* **C66** (1995) 529.
- [26] M. Landon, *DDL description of the BRTQ bank*, in: /h1/h1banks.cmz library.
- [27] G. Lopez, private communication.
- [28] H1 Collaboration, T. Ahmed et al., *The H1 Detector at HERA*, preprint DESY H1-96-01 (1996).
- [29] G. Bertrand-Coremans et al., *Construction of a cylindrical MWPC for the central tracking detector of H1*, Nucl. Phys. B (Proc. Suppl.) **16** (1990) 518.
- [30] H1 Calorimeter Group, *The H1 liquid argon calorimeter system*, Nucl. Instr. and Meth. **A336** (1993) 460.
- [31] H1 BEMC Group, *The H1 Backward Calorimeter BEMC and its Inclusive Electron Trigger*, preprint DESY-95-177 (1995).
- [32] H1 BEMC Group, *Calibration and Reconstruction of the BEMC*, H1 internal report, H1-08/92-234 (1992).
- [33] M. Fleischer, E. Peppel, *BEMC energy calibration from quasi-elastic scattered electrons (1992 data)*, H1 internal report, H1-07/93-304 (1993).
- [34] C. Brune, U. Hölzke, K. Meier, *BEMC Calibration 1993*, H1 internal report, H1-04/94-352 (1994).
- [35] J. Ban et al., *The BEMC single electron trigger*, H1 internal report, H1-07/92-235 (1992).

- [36] R. Brun et al., *GEANT long write-up*, CERN Program Library, W5103, 1989.
- [37] U. Bassler and G. Bernardi, *Nucl. Inst. and Meth.* **A361** (1995) 197.
- [38] B. D. Burow, M. Erdmann, R. Kaschowitz, S. Levonian, L. Stanco, *Photoproduction Physics at HERA*, preprint DESY-94-215 (1994).
- [39] R. Engel, A. Rostovtsev, *PHOJET - A Monte Carlo Event Generator for Photoproduction*, H1 internal report, H1-01/95-420 (1995).
- [40] J. Ferencei, presentation to the ELAN group (1995).
- [41] A. Glazov, presentation to the ELAN group (1995).
- [42] U. Bassler, G. Bernardi, presentation to the ELAN group (1995).
- [43] G. Raedel, presentation to the ELAN group (1995).
- [44] J. Ferencei, private communication.
- [45] S. Burke, private communication.
- [46] F. Zomer, private communication.
- [47] P. Marage, A. Panitch, F. Zomer, *F₂ measurement at x-values around 10⁻⁴, using the satellite bunch*, H1 internal report, H1-07/94-396 (1994).
- [48] M. Goldberg, *Energy Calibration and the Resolution in BEMC*, H1 internal report, H1-05/93-292 (1993).
- [49] A. Panitch, *Energy calibration and resolution in the BEMC*, H1 internal report, H1-08/95-449 (1995).
- [50] E. Evrard, *Ph. D. Thesis*, Vrije Universiteit Brussel, IIHE (ULB-VUB) (1996), in litt.
- [51] B. Gonzalez-Pineiro, *Ph. D. Thesis*, Université de Paris (1996), in litt.
- [52] A. Panitch, P. Marage, *Vertex reconstruction using BPC and CIP in DIS events*, H1 internal report, H1-05/93-297 (1993).
- [53] K. Müller, *Ph. D. Thesis*, Universität Zürich (1994).
- [54] ELAN, internal communication (1995).
- [55] K. Charchuła, G. A. Schuler, H. Spiesberger, *DJANGO - version 6*, unpublished program manuel (1993);
the version 1.0 is described in G. A. Schuler, H. Spiesberger, *Proc. of the HERA Workshop on Physics at HERA*, vol. 3, eds. W. Buchmüller and G. Ingelman, DESY (1992) 1419.
- [56] A. Kwiatkowski, H. Spiesberger and H.-J. Möhring, *Computer Phys. Comm.* **69** (1992) 155;
Proc. of the HERA Workshop on Physics at HERA, vol. 3, eds. W. Buchmüller and G. Ingelman, DESY (1992) 1294.

- [57] *Proc. of the HERA Workshop on Physics at HERA*, vol. 3, eds. W. Buchmüller and G. Ingelman, DESY (1992) 1366.
- [58] R. G. Roberts, *The structure of the proton*, Cambridge University Press 1990.
- [59] J. L. Miramontes, J. Sánchez Guillén, *Nucl. Phys. B (Proc. Suppl.)* **7B**(1988) 141; J. Sánchez Guillén et al., *Nucl. Phys.* **B353** (1991) 337 and references therein.
- [60] M. Klein, ELAN communication (1996).
- [61] CERN Application Software Group, *PAW - Physics Analysis Workstation*, CERN, Geneva 1996.
- [62] A. Arbuzov et al., DESY preprint 95-185 (1995).
- [63] ZEUS Collaboration, M. Derrick et al., preprint DESY 95-193 (1995).
- [64] E665 Collaboration, M.R. Adams et al., FNAL-Pub-95/396-E (1995).
- [65] NMC Collaboration, M. Arneodo et al., *Phys. Lett.* **B364** (1995) 107.
- [66] H1 Collaboration, T. Ahmed et al., *Z. Phys.* **C66** (1995) 529.
- [67] L. Favart, M. Fleischer, M. Huette, Z. Zhang, DESY grey report 96-01 (1996).
- [68] BCDMS Collaboration, A.C. Benvenuti et al., *Phys. Lett.* **B223** (1989) 485; CERN preprint CERN-EP/89-06.
- [69] C. Pascaud and F. Zomer, LAL preprint LAL/94-42.
- [70] M. Virchaux and A. Milsztajn, *Phys. Lett.* **B274** (1992) 221.
- [71] A. Donnachie and P. V. Landshoff, *Phys. Lett.* **B296** (1992) 227.
- [72] A. Capella et al., *Phys. Lett.* **B337** (1994) 358.
- [73] A. D. Martin, W. J. Stirling and R. G. Roberts, *Parton distributions updated*, *Phys. Lett.* **B306** (1993) 145 and erratum *Phys. Lett.* **B309** (1993) 492.
- [74] A. D. Martin, W. J. Stirling and R. G. Roberts, *Phys. Lett.* **B354** (1995) 155.
- [75] CTEQ Collaboration, J. Botts et al., *Phys. Lett.* **B304** (1993) 15; CTEQ Collaboration, J. Botts et al. (to be published).
- [76] M. Glück, E. Reya and A. Vogt, *Z. Phys.* **C67** (1995) 433; A. Vogt, in: *Proc. of the Workshop on Deep Inelastic Scattering and QCD*, Paris (1995) 261.
- [77] H1 Collaboration, T. Ahmed et al., *A Measurement of the Proton Structure Function $F_2(x, Q^2)$ at Low x and Low Q^2 at HERA*, Contribution to the Warsaw Conference ICHEP'96, pa02-070, 1996, to be published.
- [78] J. Blümlein, A. T. Doyle, F. Hautmann, M. Klein and A. Vogt, *Structure Functions in Deep Inelastic Scattering at HERA*, Summary report of Working Group 1 of the 1996 HERA Physics Workshop, 1996, to be published.

List of Figures

2.1	Layout of HERA	10
2.2	Longitudinal proton bunch profile	12
2.3	Beam longitudinal phase space	13
2.4	Simulation of the bunch rotation technique, used to transfer protons from PETRA to HERA.	15
2.5	Longitudinal beam instability	16
2.6	Evolution of the bucket and the potential gap shapes, created by mixing the 52 and 208 rf systems in HERA	18
2.7	H1 luminosity system	19
2.8	z -vertex distribution for low Q^2 DIS events: nominal and shifted vertex data samples	24
2.9	FToF spectra	26
2.10	FToF data analysis: time evolution of the satellite bunch parameters	27
2.11	Ratio R_{tof} of the 4.8 ns to the +4.8 ns satellite currents as obtained from the FToF data in function of the luminosity run number	28
2.12	Satellite bunch correction to the measured luminosity in the H1 interaction region for different periods of 1994	29
3.1	Longitudinal view of the H1 detector	32
3.2	Radial view of the H1 central tracker	34
3.3	Transverse view of the backward electromagnetic calorimeter BEMC	36
3.4	Development of the electromagnetic shower in the BEMC	37
3.5	BEMC energy resolution	40
3.6	Space point reconstruction resolution for electrons scattered into the BEMC	41
3.7	BEMC response to hadronic particles	42
3.8	Proton related background identification using the BToF	44
3.9	BEMC single electron trigger efficiencies	47
4.1	DIS event with the scattered electron detected in the BEMC	53
4.2	Schematic definition of the measured quantities in DIS	54
4.3	Iso-angle and iso-energy lines in the (x, Q^2) plane for the scattered electron and for the current jet	56
4.4	Distribution of the event sample in the (x, Q^2) plane	59
4.5	Distribution of the background events in the (x, Q^2) plane	61
4.6	Schematic definition of soft and hard photoproduction processes	62
4.7	Background reduction by the z -vertex requirement	65
4.8	EBPC and ECRA estimator distributions	66
4.9	Forward/central vertex distributions	68
4.10	ZORRO estimator distributions	70

4.11	Yield of selected DIS events per nb^{-1} of integrated luminosity for the closed triangles data sample	73
4.12	Yield of selected DIS events per nb^{-1} for the shifted vertex, open triangles and satellite bunch data samples	74
5.1	BPC reconstruction in case of no preshowering and when preshowering has taken place	78
5.2	Cluster centroid reconstruction corrections-I	79
5.3	Cluster centroid reconstruction corrections-II	81
5.4	Double angle energy distributions	83
5.5	Comparison of the reconstructed double angle and the true (generated) electron energy	83
5.6	Reconstructed BCFR energy distributions	84
5.7	Reconstructed BCLR energy distributions	85
5.8	Reconstructed BCFR energy distributions after applying the energy correction obtained using the double angle method	86
5.9	Energy distributions in bands of $max_x y$ with the old and the new crack corrections	87
5.10	BEMC energy scale (shifted vertex data)	88
5.11	BEMC energy scale (nominal vertex data)	89
5.12	θ_e resolution (shifted vertex data)	91
5.13	Bias of the z -vertex reconstruction for events with a vertex fitted by a single scattered electron track	93
5.14	Preshowering in front of BPC	95
5.15	Fractions of y_h originating from tracks, BEMC and LAC calorimeter contributions	97
5.16	Quality of the y_Σ reconstruction	99
6.1	Sketch of the CIP vertex definition	104
6.2	Vertex efficiency in θ_e intervals in function of E_e	105
6.3	Influence of the W limitation on the vertex efficiency	106
6.4	Vertex efficiency in function of y_e and y_Σ	108
6.5	Vertex efficiency in θ_e intervals in function of y_Σ	109
6.6	Quality of the θ_{jet} reconstruction	110
6.7	Vertex efficiency at low Q^2 - low x	111
6.8	Fraction of events with only a forward reconstructed vertex	113
6.9	EBPC requirement efficiency	114
6.10	ECRA requirement efficiency	116
7.1	Reweighting of the z -vertex distribution in the Monte Carlo simulation	120
7.2	Reweighting of the Monte Carlo input parton distribution set	124
7.3	Electroweak corrections: DJANGO Monte Carlo simulation and HECTOR analytical calculations	125
7.4	Distributions of various kinematic quantities as obtained from the shifted vertex data and using the Monte Carlo simulation	127

7.5	Binning of the kinematic plane used for the H1 '94 structure function F_2 measurement	129
7.6	Kinematic resolution (shifted vertex, "electron" method)	131
7.7	Kinematic resolution (shifted vertex, Σ method)	132
7.8	Kinematic resolution (nominal vertex, "electron" method)	134
7.9	Kinematic resolution (nominal vertex, Σ method)	135
7.10	Systematic bias of kinematic reconstruction ("electron" method)	136
7.11	Systematic bias of kinematic reconstruction (Σ method)	137
7.12	Event stability: shifted vertex, "electron" and Σ methods	138
7.13	F_2 structure function measurement: shifted vertex and satellite bunch data samples, electron method	141
7.14	F_2 structure function measurement: shifted vertex and satellite bunch data samples, Σ method	142
7.15	F_2 structure function measurement: combined (shifted vertex and satellite bunch data samples) results	146
7.16	F_2 structure function measurement: comparison of results obtained using the shifted and the nominal vertex data samples	147
7.17	F_2 structure function measurement by H1: comparison of results obtained using the "electron" and the Σ methods of kinematic reconstruction	150
7.18	F_2 structure function measurement by H1 in function of x at fixed Q^2	151
7.19	F_2 structure function measurement by H1 in function of Q^2 at fixed x	152
7.20	F_2 structure function measurement by H1: low Q^2 part	153

List of Tables

2.1	Nominal HERA parameters	11
2.2	HERA proton acceleration system performance	11
2.3	Contributions to the experimental error on the luminosity	22
2.4	Contributions to the experimental error for the ‘forward’ satellite luminosity measurement	25
2.5	Contributions to the experimental error in the total satellite luminosity determination	28
3.1	Summary of H1-tracking detector parameters	33
3.2	Summary of the BEMC calorimeter parameters	42
5.1	Summary of the BEMC calibration parameters	89
5.2	Systematic error to F_2 accounting for the bad Monte Carlo description of the dead materials in front of the BPC	96
7.1	H1 database lookup table of the nominal z-vertex for H1 run ranges	121
7.2	F_2 measurement (electron) combined from the SV and the satellite bunch data samples	144
7.3	F_2 measurement (Σ) combined from the SV and the satellite bunch data samples	145
7.4	Proton structure function $F_2(x, Q^2)$ with statistical and systematic errors	155
7.5	Main sources of systematic errors to the $F_2(x, Q^2)$ structure function measurement	158

Appendix A

List of 1994 detector runs rejected due to the BSET trigger prescaling or partially reconstructed or affected by some other known problems:

84623 84624 84625 84626 84627 84628 85159 85161 85162 85163 85188 85192 85194 85263
85268 85277 85279 85280 86102 86141 86142 86146 86331 86332 86333 86334 86604 86620
86622 86623 86722 86754 86755 86793 86818 86841 86842 86844 86845 86846 86924 86926
86946 86965 87035 87036 87037 87093 87094 87095 87096 87098 87100 87101 87102 87170
87201 87203 87224 87246 87271 87290 87317 87318 87328 87408 87449 87450 87451 87454
87455 87511 87580 87582 87583 87586 87587 87593 87595 87599 87697 87699 87701 87702
87703 87704 87732 87764 87821 87822 87823 87824 87826 87840 87915 87916 87992 87994
88016 88082 88084 88086 88089 88102 88103 88105 88161 88164 88166 88167 88171 88172
88173 88209 88210 88232 88250 88252 88253 88254 88255 88258 88310 88312 88313 88314
88315 88361 88364 88435 88438 88439 88440 88441 88442 88443 88444 88445 88446 88447
88448 88449 88450 88452 88453 88455 88456 88458 88669 88671 88691 88721 88787 88809
88838 88839 88874 88911 88912 88913 88915 88916 88917 88957 88959 88989 89022 89023
89073 89074 89129 89136 89185 89186 89187 89210 89220 89228 89229 89252 89253 89254
89269 89414 89415 89416 89417 89427 89428 89430 89431 89432 89433 89435 89436 89437
89438 89439 89440 89441 89443 89445 89455 89469 89472 89475 89476 89492 89700 89701
89706 89707 89717 89822 89828 89830 89864 89896 89898 89899 89928 89929 89970 89972
89976 89981 90025 90152 90170 90171 90172 90174 90177 90233 90235 90236 90237 90264
90301 90303 90304 90345 90347 90348 90349 90351 90352 90354 90355 90356 90358 90363
90364 90365 90368 90369 90406 90407 90408 89449 90320 90286 90288 90290 88805 87233
87427 87472 84285 86974 87038 87044 87045 87046 87047 87048 87051 87053 87466 87469
87470 87482 87836 87837 87917 87921 88320 88694 84991 84892 85079 85276 87465 88362
84989 84990 84821

Acknowledgements

First of all I wish to thank sincerely Pr. Jean Sacton who offered me the possibility to work at the Inter-university Institute for High Energies (U.L.B.-V.U.B.) and who supported me since the end of my graduation studies in 1993.

Dr. Pierre Marage introduced me to high energy physics in the framework of the H1 experiment. I am very grateful for his continuous technical and moral support during the whole length of my stay at the I.I.H.E. His rich scientific and human experience, which he has never hesitated to share with me and his other students, never ceased to impress me. Thank you Pierre, for everything ...

I would like to thank all my colleagues from the 1994 ELAN analysis team: Ursula Bassler, Josef Ferencei, Beatriz Pineiro, Thomas Naumann and Peter Kostka. In particular I thank Gaby Raedel and Alexandre Glazov with whom I have shared most of the enjoyment and pains of the F_2 analysis. I have learned a lot from the ELAN ideologist Albert De Roeck and conveners Greg Bernardi and Max Klein.

I would like to thank Dr. Ghislaine Bertrand-Coremans, who was always there to provide advice, assistance and support, Dr. Daniel Bertrand, for his efforts in maintaining the I.I.H.E. computing in operation, and the whole H1 Brussels group: Patrick Van Esch, Robert Roosen, Denis Johnson, Laurent Favart, Barbara Clerbaux and Marie Barth. Particular thanks to Erik Evrard for his valuable advice of how to spend free time in Hamburg, and to Frank Botterweck, from the Antwerp group, for the constant assistance in computing during my first days at DESY and later, when he was teaching me the “elastic scattering” laws of billiards.

All my colleagues from H1 for their advice and support: Fabian Zomer, Witek Krasny, Serguey Levonian, Gerry Lopez, Christophe Royon, Corine and Georges Lobo, Sebastian Reinshagen, Jean-François Laporte, Silhacene Aid and many others ...

Monique Garnier, Myriam Pins and Danielle Peymans helped me a lot in all the organisational and practical aspects of my work at the I.I.H.E. My thanks also to Christain Wastiels and Etienne Lievens for all the jokes they supplied me in 3 years.

Finally, I would like to thank Gell-Mann for his discovery of quarks in 1964 and Feynman who introduced the parton model in 1969, and without whom this work would have never see the day ...